



Condition Monitoring of Mechanical Faults in Variable Speed Induction Motor Drives - Application of Stator Current Time-Frequency Analysis and Parameter Estimation

Martin Blödt

► To cite this version:

Martin Blödt. Condition Monitoring of Mechanical Faults in Variable Speed Induction Motor Drives - Application of Stator Current Time-Frequency Analysis and Parameter Estimation. Electric power. Institut National Polytechnique de Toulouse - INPT, 2006. English. NNT : . tel-00105482

HAL Id: tel-00105482

<https://theses.hal.science/tel-00105482>

Submitted on 11 Oct 2006

HAL is a multi-disciplinary open access archive for the deposit and dissemination of scientific research documents, whether they are published or not. The documents may come from teaching and research institutions in France or abroad, or from public or private research centers.

L'archive ouverte pluridisciplinaire **HAL**, est destinée au dépôt et à la diffusion de documents scientifiques de niveau recherche, publiés ou non, émanant des établissements d'enseignement et de recherche français ou étrangers, des laboratoires publics ou privés.

THÈSE

présentée
pour obtenir le titre de

DOCTEUR DE L'INSTITUT NATIONAL POLYTECHNIQUE DE TOULOUSE
Spécialité : Génie Électrique

par

Martin BLÖDT

Diplom-Ingenieur, Universität Karlsruhe (TH)

Ingénieur de l'École Nationale Supérieure d'Ingénieurs Électriciens de Grenoble

DEA Génie Électrique de l'Institut National Polytechnique de Grenoble

Condition Monitoring of Mechanical Faults in Variable Speed Induction Motor Drives

Application of Stator Current Time-Frequency Analysis and Parameter Estimation

soutenue le 14 septembre 2006 devant le jury composé de :

Mme.	Nadine	MARTIN	Président et rapporteur
M.	Jean-Pierre	ROGNON	Rapporteur
M.	Stefan	CAPITANEANU	Examineur
Mme.	Marie	CHABERT	Examineur
M.	Jérémi	REGNIER	Codirecteur de thèse
M.	Jean	FAUCHER	Directeur de thèse
M.	Pierre	GRANJON	Invité

Thèse préparée au Laboratoire d'Électrotechnique et d'Électronique Industrielle de
l'ENSEEIH
UMR CNRS N° 5828

Abstract

This Ph.D. thesis deals with condition monitoring of mechanical failures in variable speed induction motor drives by stator current analysis. Two effects of a mechanical fault are considered: load torque oscillations and airgap eccentricity. The analytical modelling using the magnetomotive force and permeance wave approach leads to two stator current models. The fault provokes amplitude or phase modulation of the fundamental current component. Suitable detection methods are spectral analysis and parameter estimation in steady state whereas time-frequency analysis is required during transients. Instantaneous frequency estimation, the Wigner Distribution and the spectrogram are studied. Simulation and experimental results validate the theoretical approach. Automatic extraction of fault indicators is proposed for an unsupervised monitoring system. Moreover, load torque oscillations and dynamic eccentricity can be discriminated with the proposed methods. The feasibility of an on-line monitoring system is demonstrated by a DSP implementation of the time-frequency analysis including indicator extraction.

Keywords

- Induction motor
- Mechanical faults
- Load torque oscillations
- Parameter estimation
- Instantaneous frequency
- Condition monitoring
- Eccentricity
- Time-frequency analysis
- Wigner Distribution

Résumé

Ce travail de thèse traite de la détection et du diagnostic de défaillances mécaniques par analyse du courant statorique dans les entraînements électriques à base de machine asynchrone. Deux effets d'un défaut mécanique, des oscillations de couple et une excentricité d'entrefer, sont supposés. La modélisation par approche des ondes de forces magnétomotrices et de perméance conduit à deux modèles analytiques du signal courant. La conséquence des défauts est soit une modulation de phase, soit une modulation d'amplitude du signal courant statorique. Ces phénomènes sont détectés par une analyse spectrale en régime permanent, ou des méthodes temps fréquence en régime transitoire. Les méthodes étudiées sont la fréquence instantanée, le spectrogramme et la représentation de Wigner-Ville. L'estimation paramétrique d'indices de modulation a également été traitée. Des résultats de simulation et expérimentaux permettent de valider les signatures et d'extraire de façon automatique des indicateurs de défaut. De plus, une méthode permettant la distinction des oscillations de couple d'une excentricité dynamique est proposée. L'étude est complétée par une implémentation sur DSP des méthodes temps-fréquence afin de démontrer la faisabilité d'une surveillance en ligne.

Mots-clefs

- Machine asynchrone
- Défauts mécaniques
- Oscillations de couple
- Estimation paramétrique
- Fréquence instantanée
- Surveillance et diagnostic
- Excentricité
- Analyse temps-fréquence
- Distribution de Wigner-Ville

Zusammenfassung

In dieser Arbeit wird die Entdeckung und Diagnose mechanischer Fehler in geschwindigkeitsvariablen Asynchronantrieben mittels Statorstromanalyse untersucht. Zwei Auswirkungen mechanischer Fehler auf die Asynchronmaschine werden vorausgesetzt: kleine, periodische Drehmomentschwankungen und Luftspaltexzentrizität. Das daraus resultierende Luftspaltfeld wird mittels der Durchflutung und des magnetischen Leitwerts analytisch und qualitativ berechnet. Der entsprechende Statorstrom zeigt kleine Amplituden- oder Phasenmodulationen infolge der mechanischen Fehler. Geeignete Signalverarbeitungsmethoden im stationären Betrieb sind Spektralanalyse und Parameterschätzung, wohingegen im geschwindigkeitsvariablen Betrieb Zeit-Frequenz-Analyse benötigt wird. Die Analyse der Momentanfrequenz, Wigner-Ville-Verteilung und Spektrogramm werden behandelt. Die vorgeschlagenen Methoden werden durch Simulationen und Versuchsergebnisse validiert. Die Ergebnisse zeigen, daß dynamische Exzentrizität und Drehmomentschwankungen unterschieden werden können. Um eine automatische und permanente Überwachung des Antriebes zu realisieren, werden verschiedene Indikatoren basierend auf Zeit-Frequenz-Analyse und Parameterschätzung vorgestellt. Die praktische Umsetzbarkeit der Algorithmen wird durch DSP Implementierung der Zeit-Frequenz-Analyse demonstriert.

Stichwörter

- Asynchronmaschine
- Mechanische Fehler
- Drehmomentschwankungen
- Parameterschätzung
- Momentanfrequenz
- Zustandsüberwachung
- Exzentrizität
- Zeit-Frequenz-Analyse
- Wigner-Ville-Verteilung

Acknowledgement - Remerciements

Bien que ce mémoire de thèse soit en langue anglaise, je me permets d'écrire ces remerciements en français. Les travaux présentés dans ce mémoire ont été réalisés au sein de l'équipe Commande et Diagnostic des Systèmes Electriques (CoDiaSE) du Laboratoire d'Electrotechnique et d'Electronique Industrielle (LEEI). Le laboratoire est situé à l'Ecole Nationale Supérieure d'Electrotechnique, d'Electronique, d'Informatique, d'Hydraulique et des Télécommunications (ENSEEIHT) de l'Institut National Polytechnique de Toulouse.

Tout d'abord, je voudrais remercier Messieurs Yvon Chéron et Maurice Fadel, directeurs du LEEI, ainsi que Pascal Maussion, responsable du groupe CoDiaSE, pour l'accueil qui m'a respectivement été réservé au sein du LEEI et du groupe CoDiaSE.

Ensuite, je voudrais remercier tous les membres du jury:

- Madame Nadine Martin, Directeur de Recherche CNRS au Laboratoire des Images et des Signaux, Grenoble, pour m'avoir fait l'honneur de présider le jury et d'être rapporteur. J'ai beaucoup apprécié son intérêt pour notre travail et les remarques très constructives que l'on a pu échanger.
- Monsieur Jean-Pierre Rognon, Professeur des Universités à l'ENSIEG, Grenoble, pour avoir accepté la lourde tâche de rapporteur et pour ses commentaires sur ce travail. Je voudrais également le remercier pour la grande qualité de ses enseignements dont j'ai pu profiter lorsque j'étais étudiant à l'ENSIEG.
- Monsieur Stefan Capitaneanu, Ingénieur à Schneider-Toshiba Inverter, d'avoir participé à ce jury en tant qu'examinateur, d'avoir porté autant d'intérêt à nos travaux et de nous avoir communiqué à travers son expérience industrielle son avis sur la pertinence de notre approche.
- Madame Marie Chabert, Maître de Conférences à l'ENSEEIHT, pour sa fructueuse collaboration pendant cette thèse. J'ai beaucoup apprécié de travailler avec elle, tant au niveau de la recherche, que pour les enseignements. Merci pour sa motivation, sa gentillesse, pour l'intérêt qu'elle a porté à notre sujet et pour sa rigueur lors des nombreuses relectures d'articles et de ce manuscrit.
- Monsieur Pierre Granjon, Maître de Conférences à l'ENSIEG, d'avoir participé à ce jury, pour ses commentaires et remarques constructives par rapport

au mémoire, pour son grand intérêt pour notre travail, pour sa gentillesse et sa sincérité. Un grand merci pour son encadrement lors de mon DEA, qui est à l'origine de mon intérêt pour le diagnostic et le traitement du signal.

- Monsieur Jérémie Regnier, Maître de Conférences à l'ENSEEIH, pour le co-encadrement de cette thèse. Je voudrais le remercier pour l'excellente ambiance de travail pendant les deux années, sa gentillesse, son intérêt et sa grande motivation pour un nouveau sujet qu'il a dû intégrer rapidement après son recrutement. J'ai toujours beaucoup apprécié nos échanges scientifiques ou non-scientifiques et c'était un plaisir de travailler ensemble.
- Monsieur Jean Faucher, Professeur des Universités à l'ENSEEIH, qui a dirigé ces travaux de thèse. Je voudrais lui exprimer toute ma gratitude pour la grande confiance qu'il m'a accordé tout au long de ces trois années. Merci de m'avoir proposé un sujet très enrichissant, de m'avoir laissé de la liberté et de m'avoir toujours soutenu. À part ses grandes qualités scientifiques, j'ai également beaucoup apprécié ses qualités humaines qui ont fait que tout s'est déroulé dans une ambiance très agréable.

Mes remerciements vont également au personnel technique du laboratoire: Jean-Marc Blaqui re, Jaques Luga, Didier Ginibri re et particuli rement Olivier Durrieu de Madron et Robert Larroche pour leur aide sur le banc d'essai. L'informatique est toujours un composante critique dans un tel laboratoire, donc merci   Jaques Benaoun, Jean Hector et Philippe Azema pour leur aide et leurs interventions. Je suis  galement reconnaissant envers le personnel administratif pour leur gentillesse et pour m'avoir facilit  de nombreuses t ches. Merci   Fatima Mebrek, Val rie Schwarz, Christine Bodden, Fanny Dedet, B n dicte Balon, Josiane Pionnie, Catherine Montels et Raymonde Escaig.

Parmi les autres permanents, je voudrais remercier Bruno Sareni (surtout pour sa disponibilit  et son aide par rapport   l'optimisation), Danielle Andreu (pour le bon d roulement de mes enseignements au sein de son d partement), Maria Pietrzak-David (pour sa gentillesse et sa disponibilit ), Fran ois Pigache, Ana Maria Llor et d'autres que je n'ai pas cit s.

Je voudrais saluer et remercier les doctorants avec lesquels j'ai eu le plaisir de partager le bureau international E113a, o  r gnait une ambiance toujours tr s agr able: Sylvain Canat, Lauric Garbuio, Paul-Etienne Vidal, Grace Gandanegara et particuli rement Gianluca Postiglione (pour le reste du temps dans un bureau un peu plus petit).

Un grand merci   de nombreux autres th sards qui ont contribu    une bonne ambiance dans le laboratoire. Je commence par les anciens: Guillaume Fontes, Nicolas Roux, Christophe Viguier ; suivi par mes coll gues J rome Faucher (pour les bons moments gastronomiques partag s), Ali Abdallah Ali (pour les nombreuses discussions autour d'un bon caf ), Mathieu Leroy, J r me Mavier, Anne-Marie, Bayram ; et les plus jeunes: les deux Fran ois, Marcos et Marcus, Valentin, Antony, Baptiste et de nombreuses autres personnes que je n'ai pas cit es.

Je voudrais également remercier mes amis qui m'ont encouragé et avec qui j'ai partagé des loisirs, en particulier Louis, Amandine, Pierre et Daniel pour les excursions en montagne, Benjamin pour ses relectures et les nombreuses dégustations et beaucoup d'autres que je ne cite pas ici.

Les derniers mots vont naturellement à ma famille. Je les remercie de leur soutien et leurs encouragements tout au long de mes études.

Contents

Abstract	i
Résumé	iii
Zusammenfassung	v
Acknowledgement - Remerciements	vii
List of Symbols	xxv
1 Introduction	1
1.1 Background	1
1.2 Problem Description	2
1.3 Literature Survey	3
1.4 Methodology and Outline	5
2 Harmonic Field Analysis	7
2.1 Introduction	8
2.2 MMF and Permeance Wave Approach	9
2.2.1 Simplifying Assumptions	9
2.2.2 Airgap Flux Density	11
2.2.3 Stator Current	11
2.2.4 Torque	12
2.3 Healthy Machine	13
2.3.1 Magnetomotive Force Waves	13
2.3.1.1 Definition	13
2.3.1.2 MMF of a Single Turn	14
2.3.1.3 MMF of a Three-Phase Winding	15
2.3.1.4 Rotor MMF	17
2.3.2 Airgap Permeance	20
2.3.2.1 Slotting	20
2.3.2.2 Saturation	22
2.3.3 Airgap Flux Density	22
2.3.4 Stator Current	24
2.3.5 Torque	25
2.4 Load Torque Oscillations	28
2.4.1 Mechanical Speed	29

2.4.2	Rotor MMF	30
2.4.3	Airgap Flux Density	32
2.4.4	Stator Current	32
2.5	Airgap Eccentricity	33
2.5.1	Airgap Length	35
2.5.2	Airgap Permeance	37
2.5.3	Airgap Flux Density	39
2.5.4	Stator Current	40
2.5.5	Torque	43
2.6	Summary	46
3	Introduction to the Employed Signal Processing Methods	49
3.1	Introduction	50
3.2	Basic Concepts	51
3.2.1	Classes of Signals	51
3.2.1.1	Deterministic Signals	51
3.2.1.2	Random Signals	52
3.2.2	Correlation	53
3.2.2.1	Deterministic Signals	53
3.2.2.2	Random Signals	54
3.2.3	Stationarity of Stochastic Processes	54
3.2.4	Fourier Transform	56
3.2.5	Sampling	56
3.2.6	Analytical Signal	57
3.2.6.1	Properties	57
3.2.6.2	Hilbert Transform	59
3.2.6.3	Hilbert Transform of Modulated Signals	60
3.3	Spectral Estimation	61
3.3.1	Definitions	62
3.3.2	Periodogram	63
3.3.3	Averaged Periodogram	64
3.3.4	Window Functions	65
3.4	Time-Frequency Analysis	66
3.4.1	Heisenberg-Gabor Uncertainty Relation	69
3.4.2	Instantaneous Frequency	70
3.4.3	Spectrogram	71
3.4.3.1	Definition	71
3.4.3.2	Properties	72
3.4.3.3	Examples	73
3.4.4	Wigner Distribution	74
3.4.4.1	Definition	74
3.4.4.2	Properties	75
3.4.4.3	Examples	76
3.4.5	Smoothed Wigner Distributions	78
3.4.5.1	Definitions	78
3.4.5.2	Examples	79

3.4.6	Discrete Wigner Distribution	81
3.4.7	Time-Frequency vs. Time-Scale Analysis	82
3.5	Parameter Estimation	83
3.5.1	Basic concepts	84
3.5.2	Estimator Performance and Cramer-Rao Lower Bound . . .	85
3.5.3	Maximum Likelihood Estimation	87
3.5.4	Detection	89
3.6	Summary	91
4	Fault Signatures with the Employed Signal Processing Methods	93
4.1	Introduction	94
4.2	Spectral Estimation	95
4.2.1	Stationary PM Signal	96
4.2.2	Stationary AM Signal	97
4.2.3	Simulation Results	98
4.2.4	Fault Indicator	99
4.3	Time-Frequency Analysis	103
4.3.1	Instantaneous Frequency	103
4.3.1.1	Stationary PM Signal	103
4.3.1.2	Transient PM Signal	104
4.3.1.3	AM Signal	105
4.3.1.4	Simulation Results	105
4.3.1.5	Fault Indicator	108
4.3.2	Spectrogram	111
4.3.2.1	Stationary PM and AM Signals	111
4.3.2.2	Transient PM and AM Signals	113
4.3.2.3	Simulation Results	113
4.3.3	Wigner Distribution	114
4.3.3.1	Stationary PM Signal	114
4.3.3.2	Transient PM Signal	119
4.3.3.3	Stationary AM Signal	120
4.3.3.4	Transient AM Signal	121
4.3.3.5	Simulation Results	122
4.3.3.6	Fault Indicator	123
4.4	Parameter Estimation	130
4.4.1	Stationary PM Signal	131
4.4.1.1	Choice of Signal Model	131
4.4.1.2	Cramer-Rao Lower Bounds	132
4.4.1.3	Maximum Likelihood Estimation	133
4.4.1.4	Numerical Optimization	135
4.4.1.5	Simulation Results	137
4.4.2	Stationary AM Signal	138
4.4.2.1	Simulation Results	139
4.5	Summary	140

5	Experimental Results	143
5.1	Introduction	144
5.2	Load Torque Oscillations	145
5.2.1	Spectral Estimation	145
5.2.2	Instantaneous Frequency - Steady State	147
5.2.3	Instantaneous Frequency - Transient State	148
5.2.4	Pseudo Wigner Distribution - Steady State	153
5.2.5	Pseudo Wigner Distribution - Transient State	157
5.2.6	Parameter Estimation	161
5.3	Load Unbalance	162
5.3.1	Spectral Estimation	162
5.3.2	Instantaneous Frequency - Steady State	164
5.3.3	Instantaneous Frequency - Transient State	166
5.3.4	Pseudo Wigner Distribution - Steady State	169
5.3.5	Pseudo Wigner Distribution - Transient State	171
5.3.6	Parameter Estimation	173
5.4	Dynamic Eccentricity	174
5.4.1	Spectral Estimation	174
5.4.2	Instantaneous Frequency - Steady State	176
5.4.3	Instantaneous Frequency - Transient State	177
5.4.4	Pseudo Wigner Distribution - Steady State	177
5.4.5	Pseudo Wigner Distribution - Transient State	180
5.4.6	Parameter Estimation	182
5.5	On-line Monitoring	182
5.5.1	Load Torque Oscillations - Steady State	183
5.5.2	Load Unbalance - Steady State	185
5.5.3	Load Torque Oscillations - Transient State	186
5.5.4	Load Unbalance - Transient State	186
5.6	Mechanical Fault Diagnosis	187
5.6.1	Steady State	187
5.6.2	Transient State	189
5.7	Summary	190
6	Conclusions and Suggestions for Further Work	193
A	Addition of Coil Voltages for PM and AM Cases	197
A.1	Addition of PM Coil Voltages	197
A.2	Addition of AM Coil Voltages	197
B	Elements of the Fisher information matrix	201
B.1	Monocomponent PM signal	201
C	Description of the Experimental Setup	203
C.1	General Description of the Test Rig	203
C.2	DSP Implementation	205
C.2.1	Downsampling	205

C.2.2	Hilbert Filtering	206
C.2.3	Discrete Implementation of the WD	207
Bibliography		209

List of Figures

2.1	Calculation of airgap flux density by MMF and permeance wave approach.	10
2.2	Illustration of Ampère's circuital law for the calculation of the airgap magnetic field.	13
2.3	MMF of a single coil	14
2.4	Decomposition of an alternating stationary wave into two opposite revolving waves.	15
2.5	Example of a two pole, two layer, fractional pitch winding.	16
2.6	Two-layer winding equivalent to a squirrel cage rotor.	18
2.7	Example of spatial sampling of a space harmonic of order 11 by a rotor with $N_r=12$ rotor bars. The resultant rotor wave has a pole pair number of -1.	19
2.8	Illustration of the stationary stator-fixed reference frame (S) and the rotating rotor-related reference frame (R).	20
2.9	Airgap length $g_{st}(\theta)$ and corresponding permeance $\Lambda_{st}(\theta)$ in the case of stator slotting.	21
2.10	Fundamental magnetic flux density $B(\theta)$, absolute value $ B(\theta) $ of the fundamental magnetic flux density and first saturation harmonic of the airgap permeance $\Lambda_{sa}(\theta)$ for a given time instant.	23
2.11	Torque-speed characteristic of an induction motor with asynchronous torque dip.	28
2.12	Schematic representation of static, dynamic and mixed eccentricity. \times denotes the rotor geometrical center, $*$ the rotor rotational center.	35
2.13	General case of rotor displacement and nomenclature.	36
2.14	Normalized permeance harmonic magnitudes with respect to degree of eccentricity.	38
3.1	Classification of signals.	52
3.2	Illustration of the effect of sampling on the Fourier transform with different sampling frequencies.	58
3.3	Illustration relative to the Bedrosian theorem.	61
3.4	Vector representation of an analytical signal $z(t)$ in the complex plane.	62
3.5	Illustration of signal segmentation and calculation of the averaged periodogram with $K = 4$	65
3.6	Periodogram and averaged periodogram ($K = 4$) of 256 samples of a sinusoid ($f = 0.2$) with additive zero-mean white Gaussian noise.	66

3.7	Power Spectral Densities of a 128-point sinusoidal signal ($f = 0.2$) analyzed with common window functions.	67
3.8	Two different chirp signals and the magnitudes of their Fourier transform.	68
3.9	Illustration of the instantaneous frequency of a chirp signal.	71
3.10	Illustration relative to the calculation of the short-time Fourier transform	72
3.11	Illustration of time and frequency resolution of the spectrogram with respect to window length: The long window leads to good frequency resolution and bad time localization whereas the short window provokes bad frequency resolution but good localization in time ($\Delta f_1 < \Delta f_2, \Delta t_1 > \Delta t_2$).	73
3.12	Spectrogram of 128 point sinusoidal signal with two different observation windows of length $N_w = 63$ and $N_w = 7$	73
3.13	Spectrogram of 128 point chirp signal with observation windows of different length N_w where $N_w = 23$ is the optimal window length.	74
3.14	Wigner Distribution of sinusoidal signal with constant frequency and WD of linear chirp signal.	77
3.15	Wigner Distribution of sum of two sinusoidal signals with constant frequency and WD of sinusoidal FM signal.	77
3.16	Pseudo Wigner Distribution of sinusoidal FM signal with smoothing windows of different length N_p	79
3.17	Wigner Distribution, Pseudo Wigner Distribution and Smoothed Pseudo Wigner Distribution of Dirac delta function.	80
3.18	Pseudo Wigner Distribution and Smoothed Pseudo Wigner Distribution of sum of two sinusoidal signals with constant frequency.	80
3.19	Illustration relative to the sampling of the Wigner Distribution.	82
3.20	Comparison of time and frequency resolution with the spectrogram and time-scale analysis.	83
3.21	Realization of DC level embedded in white Gaussian noise.	85
3.22	Illustration of the probability density function $p(x[0]; A)$ for different parameter values.	85
3.23	Illustration of probability density function of biased and unbiased estimator.	86
3.24	Example of likelihood function for parameter A after observation of one single sample $x[0]$	88
3.25	Probability density functions of $x[0]$ for hypothesis H_0 and H_1	89
3.26	Example of receiver operating characteristics (ROC).	91
4.1	Illustration of the Fourier transform magnitude of a PM stator current signal.	97
4.2	Illustration of the Fourier transform magnitude of an AM stator current signal.	98
4.3	Simulated PM and AM test signals.	99
4.4	Power Spectral Densities of simulated stator current PM signal analyzed with common window functions.	100

4.5	Periodogram of PM and AM signal.	101
4.6	Calculation of the spectrum based fault indicator IPSD.	102
4.7	Instantaneous frequency of simulated signals: signal without modulation, PM and AM signal.	105
4.8	Periodogram of instantaneous frequency of simulated PM and AM signals.	106
4.9	Instantaneous frequency of simulated transient PM and AM signals.	107
4.10	Spectrogram of instantaneous frequency of simulated transient PM and AM signals.	107
4.11	Calculation of the IF based fault indicator IIF1.	108
4.12	Spectrogram amplitude $A[n]$ and fault indicator IIF1 with respect to time for different PM modulation indices β	109
4.13	Comparison of indicators IIF1 and IIF2 with respect to different frequency sweep rates β_s of the supply frequency, modulation index $\beta = 0.1$	110
4.14	Calculation of the IF based fault indicator IIF2.	110
4.15	Fault indicator IIF2 with respect to time for different PM modulation indices β	111
4.16	Illustration relative to the spectrogram of a sinusoidal PM signal with different window lengths.	112
4.17	Spectrogram of simulated PM and AM signals with low modulation frequency ($f_c = 0.02$) and higher modulation indices ($\alpha = \beta = 0.5$), window length $N_w = 63$	113
4.18	Spectrogram of simulated PM and AM stator current signals, $f_c = 0.125$, $\alpha = \beta = 0.1$, different window lengths.	115
4.19	Spectrogram of simulated transient PM and AM stator current signals, $\alpha = \beta = 0.1$, different window lengths.	116
4.20	Illustration of the Wigner Distribution of a PM stator current signal with $\varphi_r = 0$ and $\varphi_\beta = 0$	119
4.21	Illustration of the Wigner Distribution of an AM stator current signal with $\varphi_\alpha = 0$	121
4.22	Wigner Distribution of simulated PM and AM signals with zoom on interference structure.	122
4.23	Pseudo Wigner Distribution of simulated PM and AM signals with zoom on interference structure.	123
4.24	Pseudo Wigner Distribution of simulated transient PM and AM signals with zoom on interference structure.	124
4.25	Calculation of the WD based fault indicator IWD1.	126
4.26	Fault indicator IWD1 with respect to time for different PM and AM modulation indices.	127
4.27	Calculation of the WD based fault indicator IWD2.	128
4.28	Example of extracted sideband signals from the PWD of simulated transient PM and AM stator current signals.	129
4.29	Absolute value and phase of complex fault indicator IWD2 for simulated transient PM and AM stator current signals.	130

4.30	Complex representation of fault indicator IWD2 for simulated transient PM and AM stator current signals with different modulation indices.	131
4.31	Theoretical Cramer-Rao lower bounds for $\text{var}\{\theta_3\}$ with respect to data record length N and SNR.	133
4.32	Example of function $ B(z_a, \underline{\theta}') $ in logarithmic scale with $\theta_5, \theta_6 = \text{const.}$ and typical data record $z_a[n]$	135
4.33	Scheme of the evolutionary optimization algorithm: $(\mu + \lambda)$ -evolution strategy.	137
4.34	Simulation results: mean estimated PM index vs. N and mean square estimation error together with CRLB vs. N , optimization with $(40 + 200)$ -evolution strategy.	138
4.35	Simulation results: mean estimated PM index vs. N and mean square estimation error together with CRLB vs. N , optimization with fixed grid search.	139
4.36	Simulation results: mean estimated AM index vs. N and mean square estimation error vs. N	140
5.1	Scheme of experimental setup	145
5.2	PSD of stator current with load torque oscillation $\Gamma_c = 0.14$ Nm vs. healthy case.	146
5.3	Average fault indicator IPSD vs. load torque oscillation amplitude Γ_c	147
5.4	Spectrogram of stator current IF with load torque oscillation $\Gamma_c = 0.14$ Nm vs. healthy case, 50% load.	148
5.5	Average fault indicator IIF2 vs. load torque oscillation amplitude Γ_c	149
5.6	Example of transient stator current during motor startup and its PWD.	150
5.7	PSD of stator current during speed transient with load torque oscillation $\Gamma_c = 0.22$ Nm vs. healthy case.	150
5.8	Example of transient stator current IF with strong load torque oscillation ($\Gamma_c = 0.5$ Nm) vs. healthy case, 25% load.	151
5.9	Spectrogram of transient stator current IF with load torque oscillation $\Gamma_c = 0.22$ Nm vs. healthy case, 10% load.	151
5.10	Fault indicator IIF2'(t) during motor startup with load torque oscillation $\Gamma_c = 0.22$ Nm vs. healthy case, 10% load.	152
5.11	Average fault indicator IIF2' vs. load torque oscillation amplitude Γ_c during speed transients.	153
5.12	Spectrogram of measured torque and PWD of stator current with appearing load torque oscillation $\Gamma_c = 0.05$ Nm, 25% load.	153
5.13	Fault indicator IWD1(t) for data record with appearing load torque oscillation $\Gamma_c = 0.05$ Nm, 25% load.	154
5.14	Absolute value and argument of fault indicator IWD2(t) for data record with appearing load torque oscillation $\Gamma_c = 0.05$ Nm, 25% load.	155

5.15	Average fault indicator IWD1 vs. load torque oscillation amplitude Γ_c	155
5.16	Complex representation of fault indicator IWD2 with load torque oscillations, 10% and 50% load.	156
5.17	PWD of transient stator current in healthy case and with load torque oscillation, 10% load.	157
5.18	Fault indicator IWD1'(t) during motor startup with load torque oscillation $\Gamma_c = 0.22$ Nm vs. healthy case, 10% load.	158
5.19	Absolute value and argument of fault indicator IWD2'(t) during motor startup with load torque oscillation $\Gamma_c = 0.22$ Nm vs. healthy case, 10% load.	158
5.20	Average fault indicator IWD1' vs. load torque oscillation amplitude Γ_c during speed transients.	159
5.21	Complex representation of fault indicator IWD2' with load torque oscillations during speed transients, 10% and 50% load.	160
5.22	Average PM and AM modulation indices with respect to load torque oscillation amplitude Γ_c , $N_b = 64$	162
5.23	Experimental ROC for threshold based detection of load torque oscillations using the estimated PM modulation index, $N_b = 64$	163
5.24	PSD of stator current with load unbalance $\Gamma_c = 0.04$ Nm vs. healthy case.	164
5.25	Average fault indicator IPSD vs. theoretical load torque oscillation amplitude Γ_c with load unbalance	165
5.26	Spectrogram of stator current IF in healthy case and with load unbalance ($\Gamma_c = 0.1$ Nm), 50% load.	166
5.27	Average fault indicator IIF2 vs. theoretical load torque oscillation amplitude Γ_c with load unbalance.	167
5.28	Fault indicator IIF2'(t) during motor startup with load unbalance of theoretical $\Gamma_c = 0.1$ Nm.	167
5.29	Average fault indicator IIF2' vs. theoretical load torque oscillation amplitude Γ_c with load unbalance during speed transients.	168
5.30	PWD of stator current in healthy case and with load unbalance ($\Gamma_c = 0.1$ Nm), 50% load.	169
5.31	Average fault indicator IWD1 vs. theoretical load torque oscillation amplitude Γ_c with load unbalance.	170
5.32	Complex representation of fault indicator IWD2 with load unbalance, 50% and 80% load.	170
5.33	Fault indicator IWD1'(t) during motor startup with load unbalance of theoretical $\Gamma_c = 0.1$ Nm.	171
5.34	Average fault indicator IWD1' vs. theoretical load torque oscillation amplitude Γ_c with load unbalance during speed transients.	172
5.35	Absolute value and argument of fault indicator IWD2'(t) during motor startup with load unbalance of theoretical $\Gamma_c = 0.1$ Nm.	172
5.36	Complex representation of fault indicator IWD2' with load unbalance during speed transients, no load and 50% load.	173

5.37	Average PM and AM modulation indices with respect to theoretical torque oscillation amplitude Γ_c with unbalance, $N_b = 64$	175
5.38	Experimental ROC for threshold based detection of load unbalance using the estimated PM modulation index, $N_b = 64$	175
5.39	PSD of measured torque with 40% dynamic eccentricity vs. healthy case.	175
5.40	PSD of stator current with 40% dynamic eccentricity vs. healthy case.	176
5.41	Fault indicator IIF2' with dynamic eccentricity during speed transient.	177
5.42	PWD of stator current in healthy case and with dynamic eccentricity, 10% load.	178
5.43	Complex representation of fault indicator IWD2 with dynamic eccentricity, 10% and 50% load.	179
5.44	Fault indicator IWD1' with dynamic eccentricity during motor startup, 10% load.	180
5.45	Absolute value and argument of fault indicator IWD2'(t) with dynamic eccentricity during motor startup.	181
5.46	Fault profile for Γ_c and indicator IPSD response vs. data record. . .	183
5.47	Comparison of fault indicator IPSD with $f_s = 25$ and 50 Hz.	184
5.48	PWD based indicators IWD1 and IWD2 vs. data records, $f_s = 50$ Hz.	184
5.49	Fault indicator IPSD with load unbalance	185
5.50	Fault indicators IWD1 and IWD2 with load unbalance	185
5.51	Considered speed profile: Supply frequency f_s vs. data records and corresponding torque oscillation amplitude Γ_c	187
5.52	Fault indicators IWD1' and IWD2' vs. data records during speed transients with load torque oscillations.	188
5.53	Fault indicators IWD1' and IWD2' vs. data records during speed transients with load unbalance of theoretical amplitude $\Gamma_c = 0.1$ Nm.	188
5.54	Complex representation of fault indicator IWD2 with load unbalance and 40% dynamic eccentricity, 50% average load.	189
5.55	Complex representation of fault indicator IWD2' during speed transients with load unbalance and 40% dynamic eccentricity, 50% average load.	190
C.1	Photo of the test rig	204
C.2	Photo of induction motor and DC motor	204
C.3	DC/DC converter for DC motor current control	205
C.4	Photo of DSP board with ADSP-21161	206
C.5	Preprocessing of stator current signal: lowpass filter $H(f)$, decimation and Hilbert filter $H_i(f)$	206

List of Tables

2.1	Synopsis of stator current frequency components	47
4.1	Summarized performances of the discussed signal processing methods	140
5.1	Average fault indicator IPSD ($\times 10^{-3}$) and standard deviation σ_{IPSD} ($\times 10^{-3}$) for load torque oscillations.	147
5.2	Average fault indicator IIF2 ($\times 10^{-3}$) and standard deviation σ_{IIF2} ($\times 10^{-3}$) for load torque oscillations.	149
5.3	Average fault indicator IIF2' ($\times 10^{-3}$) and standard deviation $\sigma_{\text{IIF2'}}$ ($\times 10^{-3}$) for load torque oscillations during speed transients.	152
5.4	Average fault indicator IWD1 ($\times 10^{-3}$) and standard deviation σ_{IWD1} ($\times 10^{-3}$) for load torque oscillations.	155
5.5	Average fault indicator IWD2 for load torque oscillations.	156
5.6	Average fault indicator IWD1' and standard deviation $\sigma_{\text{IWD1'}}$ for load torque oscillations during speed transients.	159
5.7	Average fault indicator IWD2' for load torque oscillations during speed transients.	160
5.8	Average estimated PM modulation index $E[\hat{\theta}_3]$ ($\times 10^{-3}$) and standard deviation $\sigma_{\hat{\theta}_3}$ ($\times 10^{-3}$) for load torque oscillations, $N_b = 64$. . .	161
5.9	Average estimated AM modulation index $E[\hat{\kappa}_2]$ ($\times 10^{-3}$) and standard deviation $\sigma_{\hat{\kappa}_2}$ ($\times 10^{-3}$) for load torque oscillations, $N_b = 64$. . .	161
5.10	Measured oscillating torque with load unbalance under different load conditions, $f_s = 50$ Hz.	163
5.11	Average fault indicator IPSD ($\times 10^{-3}$) and standard deviation σ_{IPSD} ($\times 10^{-3}$) for load unbalance.	165
5.12	Average fault indicator IIF2 ($\times 10^{-3}$) and standard deviation σ_{IIF2} ($\times 10^{-3}$) for load unbalance.	166
5.13	Average fault indicator IIF2' ($\times 10^{-3}$) and standard deviation $\sigma_{\text{IIF2'}}$ ($\times 10^{-3}$) for load unbalance during speed transients.	168
5.14	Average fault indicator IWD1 ($\times 10^{-3}$) and standard deviation σ_{IWD1} ($\times 10^{-3}$) for load unbalance.	169
5.15	Average fault indicator IWD2 for load unbalance.	170
5.16	Average fault indicator IWD1' and standard deviation $\sigma_{\text{IWD1'}}$ for load unbalance during speed transients.	171
5.17	Average fault indicator IWD2' for load torque oscillations during speed transients.	173

5.18	Average estimated PM modulation index $E[\hat{\theta}_3]$ ($\times 10^{-3}$) and standard deviation $\sigma_{\hat{\theta}_3}$ ($\times 10^{-3}$) for load unbalance, $N_b = 64$	174
5.19	Average estimated AM modulation index $E[\hat{\kappa}_2]$ ($\times 10^{-3}$) and standard deviation $\sigma_{\hat{\kappa}_2}$ ($\times 10^{-3}$) for load torque oscillations, $N_b = 64$. . .	174
5.20	Average fault indicator IPSD ($\times 10^{-3}$) and standard deviation σ_{IPSD} ($\times 10^{-3}$) for 40% dynamic eccentricity.	176
5.21	Average fault indicator IIF2 ($\times 10^{-3}$) and standard deviation σ_{IIF2} ($\times 10^{-3}$) for 40% dynamic eccentricity.	177
5.22	Average fault indicator IIF2' ($\times 10^{-3}$) and standard deviation $\sigma_{\text{IIF2'}}$ ($\times 10^{-3}$) for dynamic eccentricity during speed transients.	177
5.23	Average fault indicator IWD1 ($\times 10^{-3}$) and standard deviation σ_{IWD1} ($\times 10^{-3}$) for 40% dynamic eccentricity.	178
5.24	Average fault indicator IWD2 for dynamic eccentricity.	179
5.25	Average fault indicator IWD1' ($\times 10^{-3}$) and standard deviation $\sigma_{\text{IWD1'}}$ ($\times 10^{-3}$) for dynamic eccentricity during speed transients.	180
5.26	Average fault indicator IWD2' for dynamic eccentricity during speed transients.	181
5.27	Average estimated PM modulation index $E[\hat{\theta}_3]$ ($\times 10^{-3}$) and standard deviation $\sigma_{\hat{\theta}_3}$ ($\times 10^{-3}$) for dynamic eccentricity, $N_b = 64$	182
5.28	Average estimated AM modulation index $E[\hat{\kappa}_2]$ ($\times 10^{-3}$) and standard deviation $\sigma_{\hat{\kappa}_2}$ ($\times 10^{-3}$) for dynamic eccentricity, $N_b = 64$	182
5.29	Average estimated PM and AM modulation indices ($\times 10^{-3}$) for some cases of load torque oscillation, load unbalance and dynamic eccentricity, $N_b = 64$	190
C.1	Characteristics of induction and DC motor	204

List of Symbols

Γ	torque
Λ	airgap permeance
Φ	magnetic flux
Ω_r	pulsation of rotor flux density waves
Ω_s	pulsation of stator flux density waves
α	amplitude modulation index
α_s, α_c	initial frequencies of supply and fault pulsation during linear transients
β, β'	phase modulation index
β_s, β_c	frequency sweep rates of supply and fault pulsation during linear transients
$\delta(t)$	Dirac delta function
δ_d	relative degree of dynamic eccentricity
δ_s	relative degree of static eccentricity
θ	circumference angle in the stationary reference frame
θ'	circumference angle in the rotating rotor reference frame
θ_d	angle between two adjacent coils of a group of coils or a phase winding
θ_p	coil pitch, angle between two conductors of a coil
θ_r	rotor angular position
μ_0	magnetic permeability of free space
μ_r	relative magnetic permeability
μ_s	time harmonic order of stator MMF
ν_r	space harmonic order of rotor MMF
ν_s	space harmonic order of stator MMF
σ^2	variance
φ	a general phase angle
ω_c	fault characteristic pulsation
ω_r	rotor rotational angular frequency
ω_{rt}	pulsation of rotor currents
ω_s	pulsation of the fundamental supply voltage
\vec{A}	magnetic vector potential
B	magnetic flux density (or magnetic induction)
B_r	rotor contribution to the airgap magnetic flux density
B_s	stator contribution to the airgap magnetic flux density
E	energy
F_r	rotor magnetomotive force

F_s	stator magnetomotive force
$F_x^w(t, f)$	short time Fourier transform of signal x with window w
H	magnetic field (or magnetic field intensity)
I_1	fundamental stator current amplitude in AM model
$IF(t)$	instantaneous frequency
IIF	instantaneous frequency based fault indicator
IPSD	spectrum based fault indicator
IWD	Wigner Distribution based fault indicator
I_{rt}	amplitude of rotor-related current component in PM model
I_{st}	amplitude of stator-related current component in PM model
J	inertia
$J_k(x)$	k -th order Bessel function of the first kind
$K_{d\nu}$	winding distribution factor
$K_{p\nu}$	pitch factor
$K_x(t, \tau)$	Wigner Distribution kernel
N_r	number of rotor bars or rotor slots
N_s	number of stator slots
P	power
P_D	probability of detection
P_F	probability of false alarm
$\hat{P}_{per}(f)$	periodogram
$P_{xx}(f)$	power spectral density
$PW_x(t, f)$	Pseudo Wigner Distribution of signal x
R_0	mean airgap radius
R_r	outer radius of the rotor
R_s	inner radius of the stator
$R_{xy}(\tau)$	cross-correlation function
$S_x^w(t, f)$	spectrogram of signal x with window w
$SPW_x(t, f)$	Smoothed Pseudo Wigner Distribution of signal x
V_i	induced coil voltage
W_{mag}	magnetic field energy
$W_x(t, f)$	Wigner Distribution of signal x
f	frequency
f_c	fault characteristic frequency
f_r	rotor rotational frequency
f_s	supply frequency, sampling frequency in section 3.2.5
g	airgap length
g_0	mean airgap length
i_{am}	amplitude modulated stator current
i_{pm}	phase modulated stator current
j_s	current density along the stator periphery
k_c	Carter factor
l_m	length of the magnetic circuit of the motor
m_r	pole pair number of rotor flux density waves
m_s	pole pair number of stator flux density waves

p	motor pole pair number
$p(x; \underline{\theta})$	probability density function of x with respect to parameter vector $\underline{\theta}$
s	slip
$\Re\{\}$	real part of a complex
$\Im\{\}$	imaginary part of a complex
$E\{\}$	mathematical expectation
$\mathfrak{F}\{\}$	Fourier transform
$\mathcal{H}\{\}$	Hilbert transform
$\text{var}\{\}$	variance

Chapter 1

Introduction

1.1 Background

In a wide variety of industrial applications, an increasing demand exists to improve the reliability and availability of electrical systems. Popular examples include systems in aircraft, electric railway traction, power plant cooling or industrial production lines. A sudden failure of a system in these examples may lead to cost expensive downtime, damage to surrounding equipment or even danger to humans.

Monitoring and failure detection improves the reliability and availability of an existing system. Since various failures degrade relatively slowly, there is potential for fault detection at an early stage. This avoids the sudden, total system failure which can have serious consequences. It is important in the context of condition monitoring to distinguish fault detection from fault diagnosis. Fault detection is the decision if a fault is present or not while fault diagnosis provides more information about the nature or localization of the failure. This information can be used to minimize downtime and to schedule adequate maintenance action.

Electric machines are a key element in many electrical systems. Amongst all types of electric motors, induction motors are a frequent example due to their simplicity of construction, robustness and high efficiency. A growing number of induction motors operates in variable speed drives. In this case, the motor is no more directly connected to the power grid but supplied by an inverter. The inverter provides voltage of variable amplitude and frequency in order to vary the mechanical speed.

Common failures occurring in electrical drives can be classified as follows:

Electrical faults: stator winding short circuit, broken rotor bar, broken end-ring, inverter failure

Mechanical faults: rotor eccentricity, bearing faults, shaft misalignment, load faults: unbalance, gearbox fault or general failure in the load part of the drive

A reliability survey on large electric motors (>200 HP) revealed that most failures are due to bearing ($\approx 44\%$) and winding faults ($\approx 26\%$) [IEE85] [Eng95]. Similar results were obtained in an EPRI (Electric Power Research Institute) sponsored

survey [Alb87]. However, these studies concerned only the electric motor and not the whole drive. The present work investigates the detection of mechanical failures in the drive such as load unbalance, rotor eccentricity or load failures.

Generally, two approaches to monitoring and fault detection in electrical drives are distinguished:

Model based approach: A dynamic model is used in parallel to the real process.

Using identical inputs and comparing the model outputs to those of the real process, residuals for fault detection are generated. Alternatively, the numerical model parameters can be identified using common inputs and the process outputs. The parameter values then contain information on possible faults.

Signal analysis approach: No dynamic model of the real process is required.

The fault detection strategy is entirely based on measured physical quantities. They are analyzed to extract fault signatures for detection and diagnosis.

Disadvantages of the model based approach are the need for an accurate dynamic model and continuous simulation of the latter. Simple and fast models such as space vector models may not be very accurate for monitoring purposes whereas detailed models e.g. based on finite elements take too much computation time.

1.2 Problem Description

This work addresses the problem of condition monitoring of mechanical faults in variable speed induction motor drives. A signal based approach is chosen i.e. the fault detection and diagnosis is only based on processing and analysis of measured signals.

A common approach for monitoring mechanical failures is vibration monitoring. Due to the nature of mechanical faults, their effect is most straightforward on the vibrations of the affected component. Since vibrations lead to acoustic noise, noise monitoring is also a possible approach. However, these methods are expensive since they require costly additional transducers. Their use only makes sense in case of large machines or highly critical applications. A cost effective alternative is stator current based monitoring since a current measurement is easy to implement. Moreover, current measurements are already available in many drives for control or protection purposes. However, the effects of mechanical failures on the motor stator current are complex to analyze. Therefore, stator current based monitoring is undoubtedly more difficult than vibration monitoring.

Another advantage of current based monitoring over vibration analysis is the limited number of necessary sensors. An electrical drive can be a complex and extended mechanical systems. For complete monitoring, a large number of vibration transducers must be placed on the different system components that are likely to fail e.g. bearings, gearboxes, stator frame, load. However, a severe mechanical problem in any component influences necessarily the electric machine through load torque and shaft speed. This signifies that the motor can be considered as a

type of intermediate transducer where various fault effects converge together. This strongly limits the number of necessary sensors. However, since numerous fault effects come together, fault diagnosis and discrimination becomes more difficult or is sometimes even impossible.

A literature survey showed a lack of analytical models that account for the mechanical fault effect on the stator current. Most authors simply give expressions of additional frequencies but no precise stator current signal model. In various works, numerical machine models accounting for the fault are used. However, they do not provide analytical stator current expressions which are important for the choice of suitable signal analysis and detection strategies.

The most widely used method for stator current processing in this context is spectrum estimation. In general, the stator current power spectral density is estimated using Fourier transform based techniques such as the periodogram. These methods require stationary signals i.e. they are inappropriate when frequencies vary with respect to time such as during speed transients. Advanced methods for non-stationary signal analysis are needed.

1.3 Literature Survey

In this section, some examples of general literature related to stator current based condition monitoring are presented. More thorough discussions can be found in the corresponding sections.

An abundant literature dealing with condition monitoring of electrical machines exists. Tavner described in a textbook [Tav87] different monitoring strategies relying on the measurement of electrical, vibrational or chemical quantities. Stator current monitoring is only shortly mentioned. Vas [Vas93] dealt mainly with machine parameter estimation but included a section on condition monitoring of faults such as airgap eccentricity, rotor asymmetry, lamination insulation failure, inter-turn short circuits.

Examples of textbooks dealing with vibration monitoring of electric machines are [Tim89] [Mor92] [Big94]. They include description of rotating machines, different vibration sources, information on vibration measurement and condition monitoring.

A general review on condition monitoring of electrical equipment such as generators, transformers and motors is the work of Han [Han03]. Stator current based condition monitoring is considered in [Nan99] [Ben00] [Ben03]. Nandi [Nan99] reviews various motor faults and their stator current signatures. Expressions for additional frequencies depending on the fault type are given. Benbouzid [Ben00] [Ben03] also deals with stator current signature analysis but emphasizes on possible signal processing methods. Instantaneous power FFT, bispectrum analysis, wavelet analysis and high resolution spectral analysis are discussed in addition to classical spectral estimation.

Among various failures in induction motors, rotor asymmetry faults such as broken rotor bars or broken end rings received a lot of attention. Deleroi studied the influence of broken bars on the airgap magnetic field [Del84]. Kliman used

stator current spectrum analysis to detect broken rotor bars [Kli88]. A more recent work on modeling and detection of broken bars was carried out by [Did04].

Airgap eccentricity received also considerable attention. Cameron [Cam86] modelled the effect of static and dynamic eccentricity on the airgap field. Results with vibration and stator current measurements are presented. A more detailed study was conducted by Dorrell [Dor97] who presented experimental results with varying degrees of static and dynamic eccentricity under different load conditions. Nandi [Nan01] [Nan02] focused mainly on sidebands of the rotor slot harmonics for eccentricity detection. An alternative approach is the analysis of the stator current Park's vector, proposed by Cardoso in [Car93].

Compared to other failures, bearing faults received relatively little attention. This is certainly related to the difficulty of detecting them by stator current monitoring. Causes for bearing failures were analyzed and classified by Bonnett [Bon93]. A first work to detect bearing damage by current analysis was published by Schoen [Sch95b]. Characteristic bearing vibration frequencies were detected in the stator current spectrum as a consequence of single point defects. In contrast to single point defects, non-localized bearing faults were produced experimentally in [Sta04b] and their effect on vibration and current is studied. Stack [Sta04a] proposed a current based bearing fault detection scheme working with autoregressive models.

Load unbalance and shaft misalignment were extensively studied by Obaid [Oba03c] [Oba00]. The author used sidebands in the stator current spectrum for fault detection and studied the influence of fault severity and load on the sideband amplitudes.

The effect of time-varying load torques on the stator current spectrum was investigated by Schoen [Sch95a]. These effects were undesirable in the considered application of rotor fault detection and therefore, a method for removal was proposed. Legowski [Leg96] also examined the effect of time varying torque on the motor stator current and the instantaneous power spectrum. The time varying torque was supposed to result from mechanical abnormalities in the drive. Salles [Sal97] attempted the use of time-frequency methods such as instantaneous frequency and the Wigner Distribution for detection of stepped or periodic load torques. However, no theoretical study was presented and the obtained results do not encourage further use of the proposed approach.

Previous works in our laboratory were mainly focussed on modeling. Devanneaux [Dev02] established a detailed numerical induction motor model for monitoring and diagnosis purposes. The model is based on magnetically coupled electric circuit and allows the simulation of various failures such as inter-turn stator short circuits, broken rotor bars and eccentricity. However, the model did not yield satisfactory simulation results for precise signal analysis in the context of mechanical failures. The model was then adapted by Abdallah Ali [Ali06] for stator short circuit simulation in permanent magnet synchronous motors. Ben Attia [Att03] modeled gearbox failures and attempted a detection by stator current spectrum analysis.

1.4 Methodology and Outline

The organization of the present work is described in the following. Since there is a lack of adequate stator current models accounting for mechanical faults, chapter 2 entitled *Harmonic Field Analysis* proposes two analytical models. They are established using the classic magnetomotive force and permeance wave approach for calculation of the airgap harmonic field in electric machines. First, basic principles of this approach are discussed followed by a study of the healthy machine. The first considered fault effect are periodic load torque variations leading to shaft speed oscillations. The load torque oscillation may result from various mechanical failures such as load unbalance, shaft misalignment or a general load fault. Secondly, airgap eccentricity is studied as it may be a consequence of mechanical failures as well. The last section of this chapter is dedicated to torque oscillations resulting from eccentricity. Finally, two analytical stator current models with different modulations are obtained.

Most people dealing with electric machines and condition monitoring have a traditional training background as electric power engineers. However, the chosen condition monitoring approach requires not only a thorough knowledge of the object but also of suitable signal processing methods. Therefore, chapter 3 entitled *Introduction to the Employed Signal Processing Methods* reviews important concepts of signal processing such as Fourier transform, analytical signal or spectral estimation. In the following, various time-frequency methods for non-stationary signal analysis are presented. Since the modeling leads to stator current expressions with two different modulation types, amplitude and phase modulation, signal parameter estimation is discussed as alternative to non-parametric methods.

The following part of the work, chapter 4 entitled *Fault Signatures with the Employed Signal Processing Methods*, relates the two preceding chapters. The presented signal processing methods are applied to the analytical stator current models. Theoretical fault signatures with every method are obtained and directly validated with simulated synthesized signals. The knowledge about the signatures allows the extraction of suitable fault indicators which are quantities indicating the presence of a fault and, if possible, its severity. Tests with indicators in steady state and during transients complete the chapter.

Finally, chapter 5 entitled *Experimental Results* corroborates the preceding theoretical and simulation results. A particular experimental setup with an induction motor drive is used to study load torque oscillations, load unbalance and dynamic eccentricity. In a first time, stator current signals are measured and processed off-line. The theoretically predicted signatures could be observed and the fault indicators validated. To demonstrate the feasibility of permanent and automatic on-line monitoring, a time-frequency method is successfully implemented on a DSP board. The last section deals with mechanical fault diagnosis. Previously obtained results are compared to evaluate the signal processing method performances for fault discrimination.

The conclusion in chapter 6 summarizes important aspects of this work and proposes directions for further research.

Chapter 2

Harmonic Field Analysis

Contents

2.1	Introduction	8
2.2	MMF and Permeance Wave Approach	9
2.2.1	Simplifying Assumptions	9
2.2.2	Airgap Flux Density	11
2.2.3	Stator Current	11
2.2.4	Torque	12
2.3	Healthy Machine	13
2.3.1	Magnetomotive Force Waves	13
2.3.1.1	Definition	13
2.3.1.2	MMF of a Single Turn	14
2.3.1.3	MMF of a Three-Phase Winding	15
2.3.1.4	Rotor MMF	17
2.3.2	Airgap Permeance	20
2.3.2.1	Slotting	20
2.3.2.2	Saturation	22
2.3.3	Airgap Flux Density	22
2.3.4	Stator Current	24
2.3.5	Torque	25
2.4	Load Torque Oscillations	28
2.4.1	Mechanical Speed	29
2.4.2	Rotor MMF	30
2.4.3	Airgap Flux Density	32
2.4.4	Stator Current	32
2.5	Airgap Eccentricity	33
2.5.1	Airgap Length	35

2.5.2	Airgap Permeance	37
2.5.3	Airgap Flux Density	39
2.5.4	Stator Current	40
2.5.5	Torque	43
2.6	Summary	46

2.1 Introduction

This chapter analyzes theoretically the effects of mechanical faults on the airgap magnetic field and the stator current of induction machines. The result is an analytical stator current model that accounts for the mechanical fault. Then, these analytical expressions allow for suitable choices of signal processing methods for fault detection and diagnosis.

Mechanical faults are supposed to have two substantial effects on the induction machine:

Load torque oscillations: Load unbalance, shaft misalignment, gearbox faults or other failures in the load part of the drive produce periodic variations of the load torque or the inertia. These variations often relate to the mechanical rotor position. Load torque oscillations thus give rise to mechanical speed oscillations.

Airgap eccentricity: Bearing wear, misalignment or a bent shaft may lead to a non-uniform airgap.

The consequences of these phenomena are studied in theory using the traditional magnetomotive force (MMF) and permeance wave approach for calculation of the airgap magnetic flux density [Hel77] [Yan81] [Tim89]. Major advantages of this analytical approach are the simplicity and the obvious relationship to physical phenomena. However, this method cannot provide the exact harmonic amplitudes of the airgap magnetic field. Furthermore, the coupling phenomena between rotor and stator are difficult to take into account. Nevertheless, since the purpose of this chapter is to provide a qualitative stator current signal model valid for any induction motor, the approach is suitable.

Another approach would have been the use of finite element programs for a detailed computation of the airgap magnetic flux density. This numerical approach has two major drawbacks apart from time-intensive calculations. First, the model would only be valid for one particular machine with its winding distribution, rotor geometry, etc. which leads to a loss of generality. Secondly, the finite element simulation only provides a stator current waveform and not an analytical expression. The obtained current waveform still has to be analyzed using a particular signal processing method. The a priori choice of the analysis method may influence the results. For instance, a simple spectral analysis cannot clearly distinguish amplitude and frequency modulations under particular conditions. The analytical stator current expression on the other hand can directly provide this information.

The present chapter is organized as follows: First, a general description of the MMF and permeance wave approach is given. The method is then applied in 2.3 to the airgap field calculation in case of a healthy machine. This includes the derivation of the stator current and the electromagnetic output torque. Section 2.4 studies in a similar way the effect of an oscillating load torque on the airgap field and the stator current. Rotor eccentricity is discussed in 2.5 according to the same methodology.

2.2 MMF and Permeance Wave Approach

The MMF and permeance wave approach is used to calculate the magnetic flux density in the airgap of electrical machines. As mentioned previously, this approach gives only an approximation to the true flux density but it is sufficient in many cases. Oberretl used the method to calculate harmonic fields in a squirrel cage induction motor in a detailed way including higher order armature reactions [Obe65]. It is also commonly used in noise and vibration analysis of electrical motors [Yan81] [Tim89] or for identifying the consequences of faults that alter the airgap geometry e.g. airgap eccentricity [Cam86] [Hel77] or bearing faults [Blö04]. A schematic representation of the MMF and permeance wave approach is shown in Fig. 2.1. In the following, this approach is used to derive the airgap flux density. Subsequently, other relevant quantities for condition monitoring can be deduced from the flux density such as the non-supply frequency components in the stator current, the electromagnetic torque and radial forces acting on the stator frame which are one source of vibrations.

2.2.1 Simplifying Assumptions

The simplifying assumptions of the MMF and permeance wave approach are the following:

- The magnetic field calculations are based on the simplified Maxwell equations used in quasi-stationary conditions [Fey65b]. This means that the time-varying term $\partial E/\partial t$ is neglected. Only the contributions of current densities to the magnetic field are accounted for, the contributions from the time-varying electric field are neglected. These general assumptions hold because the time variations are relatively slow since electric machines are supplied by alternating currents of low frequencies. Consequently, the studied object is of small dimensions compared to the corresponding wavelength which is about 6000 km with 50 Hz.
- The relative permeability of iron is assumed infinite ($\mu_r = \infty$), saturation effects are neglected.
- The magnetic fields are only studied in two dimensions i.e. the machine is supposed to be part of a machine with infinite length. Boundary and end effects are not accounted for.

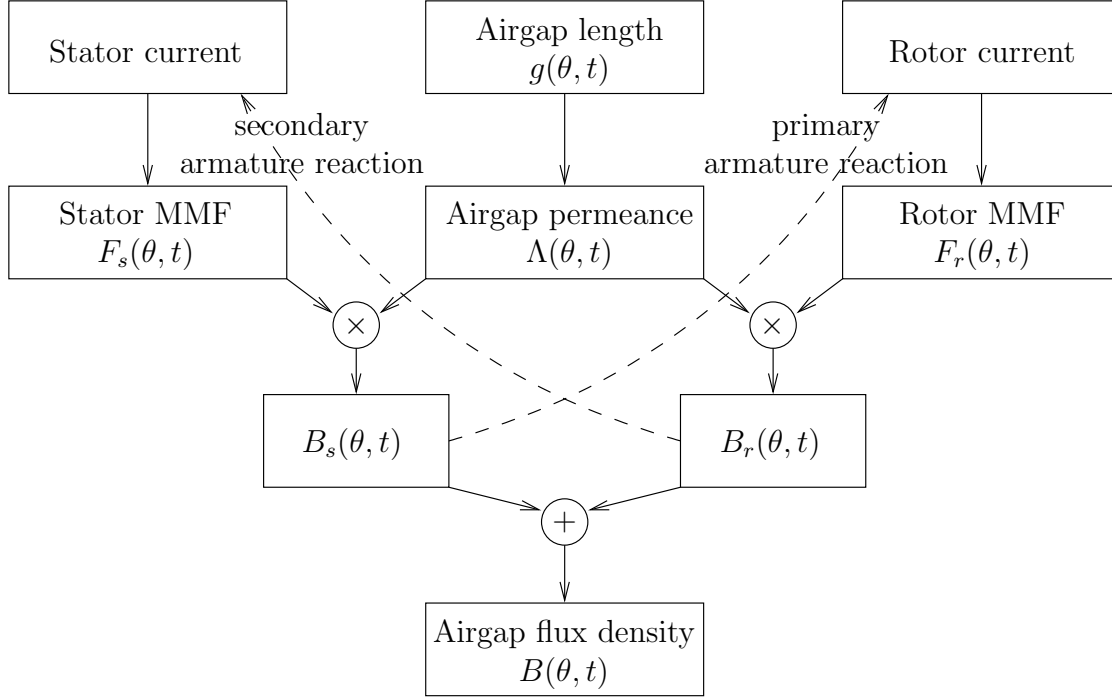


Figure 2.1: Calculation of airgap flux density by MMF and permeance wave approach.

- Only the radial airgap field is considered and it does not vary with respect to the radius r^1 , i.e. the airgap is supposed small compared to the machine diameter.

These are the traditional assumptions made for the calculation of the airgap field in steady state i.e. at constant speed and supply frequency [Hel77]. However, variable speed drives are considered in this work where the supply frequency varies. Nevertheless, the steady state magnetic field calculations are also valid in transient state when the speed and supply frequency transients are considered slow compared to the electrical time constants in the machine. These time constants concern the relation between applied voltages and resulting currents and they are generally determined by the ratio of inductance to resistance. If these time constants are small, the current resulting from an applied voltage can be considered instantaneous.

Similarly, if the supply frequency variations are slow compared to the electrical time constants, the supply frequency and speed can be considered quasi-stationary for the magnetic field calculations. Often, the supply frequency variations are related to the mechanical time constant of the drive i.e. the ratio of inertia to the friction coefficient. It can therefore be concluded that the following calculations are valid in transient state if the speed and frequency transients are slow compared to the electrical transients.

¹Consequently, $\text{div} \vec{B} = 0$ is not respected.

2.2.2 Airgap Flux Density

Assuming that the motor is supplied by a symmetric and sinusoidal three phase voltage system, sinusoidal currents will flow in the stator windings. Their amplitude depends on the winding impedance if the rotor influence is neglected in a first approximation. The structure of the three-phase winding leads to a rotating MMF wave (see following section for exact definitions). The currents are distributed in discrete slots along the circumference angle θ . Thus, they give rise to a stepped MMF wave that can be considered as the superposition of a fundamental MMF wave and its space harmonics.

The airgap geometry influences the magnetic flux density through the airgap length g . For simplification, it is often considered constant. However, rotor and stator slotting and eccentricity lead to airgap length variations with respect to θ and the rotor position θ_r . The airgap permeance $\Lambda(\theta, t)$, proportional to the inverse of the airgap length $g(\theta, t)$, is therefore a combination of rotating waves.

The airgap magnetic flux density is obtained by multiplying the MMF and permeance waves. The rotating flux density waves $B_s(\theta, t)$ induce voltages in the squirrel cage rotor that drive the rotor currents. This phenomenon is termed the *primary armature reaction*. The rotor currents themselves produce rotating rotor MMF waves. These interact with the airgap permeance and lead to a new set of flux density waves $B_r(\theta, t)$. These rotor-related flux density waves react on the corresponding stator-related waves of equal order. This is the *secondary armature reaction*. Other rotor-related waves can induce voltages of other than supply frequency in the stator windings. They drive currents of other than supply frequency for which the stator appears short-circuited. These currents are only limited by the stator and line impedance. New MMF waves, generated by the non-supply frequency currents, interact with the airgap permeance and produce consequently additional flux density waves that induce currents in the rotor, etc. The process continues until the steady-state flux distribution is established. For simplification, mostly the primary armature reaction will be considered in the following.

2.2.3 Stator Current

Stator current components at non-supply frequency are interesting for condition monitoring purposes. The rotating airgap flux density waves $B(\theta, t)$ lead to a time-varying flux $\Phi(t)$ in a phase winding. This flux can either be calculated by surface integration of the flux density $B(\theta, t)$ or by application of Stoke's theorem and calculation of the line integral of the magnetic vector potential \vec{A} :

$$\Phi(t) = \iint_{(S)} \vec{B}(\theta, t) \cdot d\vec{S} = \oint_l \vec{A} \cdot d\vec{l} \quad (2.1)$$

S denotes the surface limited by the turns of the winding, \vec{A} is the vector potential defined by $\vec{B} = \text{rot} \vec{A}$ and \vec{l} is the closed loop delimiting the surface S i.e. \vec{l} corresponds to the geometrical location of the conductors in a phase. According

to the simplifying assumptions, the vector potential has only a component in the axial z -direction. Hence, the integration can only be performed along each slot where a conductor of the corresponding winding is present.

The flux derivation yields the induced phase voltage that drives corresponding currents. If the induced voltage frequency is different from the supply frequencies, the stator appears short-circuited and the currents are only limited by the stator winding and line impedance \underline{Z}_s . Then, the corresponding stator current $i_s(t)$ is

$$i_s(t) = \frac{1}{\underline{Z}_s} \frac{d}{dt} \Phi(t) \quad (2.2)$$

The stator current components at non-supply frequency are therefore related to the airgap flux density by integration with respect to the angle θ , followed by time derivation. These operations do not modify the frequency of existing components. Thus, it can be concluded that the stator current contains the same frequencies as the airgap flux density.

2.2.4 Torque

The torque Γ acting between the rotor and the stator can be calculated according to the principle of virtual work [Fey65a] by considering the change in magnetic field energy W_{mag} with respect to the rotor angular position θ_r [Hel77]:

$$\Gamma = -\frac{\partial W_{mag}}{\partial \theta_r} \quad (2.3)$$

Note that since W_{mag} is a function of several variables, all of them except θ_r are supposed constant with this approach. With the simplifying assumptions, all the magnetic energy is concentrated in the airgap. Supposing a smooth airgap, the magnetic energy W_{mag} is:

$$W_{mag} = \frac{1}{2\mu_0} l_m R_0 g_0 \int_0^{2\pi} B^2(\theta, t) d\theta \quad (2.4)$$

where l_m denotes the magnetic circuit length, R_0 the mean airgap radius and g_0 the mean airgap length.

The airgap flux density $B(\theta, t)$ can be considered as the sum of a stator and a rotor related component, denoted $B_s(\theta, t)$ and $B_r(\theta, t)$. Furthermore, the stator flux density waves do not depend on θ_r , which leads finally to:

$$\Gamma = -\frac{1}{\mu_0} l_m R_0 g_0 \int_0^{2\pi} [B_s(\theta, t) + B_r(\theta, t)] \frac{\partial}{\partial \theta_r} B_r(\theta, t) d\theta \quad (2.5)$$

This expression shows that the torque is generated from interactions of the stator flux density waves and the derivatives of the rotor flux density waves on the one hand, on the other hand from interactions of rotor flux density waves with the derivatives of the rotor flux density waves.

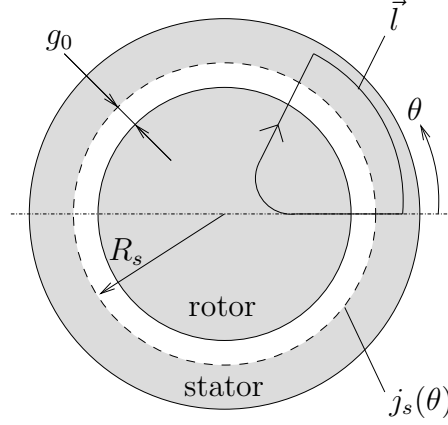


Figure 2.2: Illustration of Ampère's circuital law for the calculation of the airgap magnetic field.

2.3 Healthy Machine

2.3.1 Magnetomotive Force Waves

2.3.1.1 Definition

The magnetic field intensity \vec{H} in the airgap of the machine can be determined using Ampère's circuital law. Considering a current density $j_s(\theta)$ along the periphery of the airgap, the expression becomes:

$$\oint_l \vec{H} d\vec{l} = \int j_s(\theta) r d\theta \quad (2.6)$$

where l is a closed loop over the stator, airgap and the rotor and $r = R_s$ the inner radius of the stator (see Fig. 2.2).

Assuming the infinite relative permeability of iron, the stator current density magnetizes only the airgap. In the first instance, a smooth airgap of length g_0 is supposed. The radial airgap field $H_r(\theta)$ is therefore given by [Hel77]:

$$g_0 H_r(\theta) = \int_0^\theta j_s(\theta) r d\theta + g_0 H_r(0) \quad (2.7)$$

where $g_0 H_r(0)$ is an integration constant ensuring that no unipolar flux crosses the airgap:

$$\int_0^{2\pi} H_r(\theta) r d\theta = 0 \quad (2.8)$$

For the purpose of separating the effects of the airgap geometry and the winding distribution on the airgap magnetic field and flux density, the magnetomotive force (MMF) distribution $F(\theta)$ is commonly used. It is defined as the integral of the

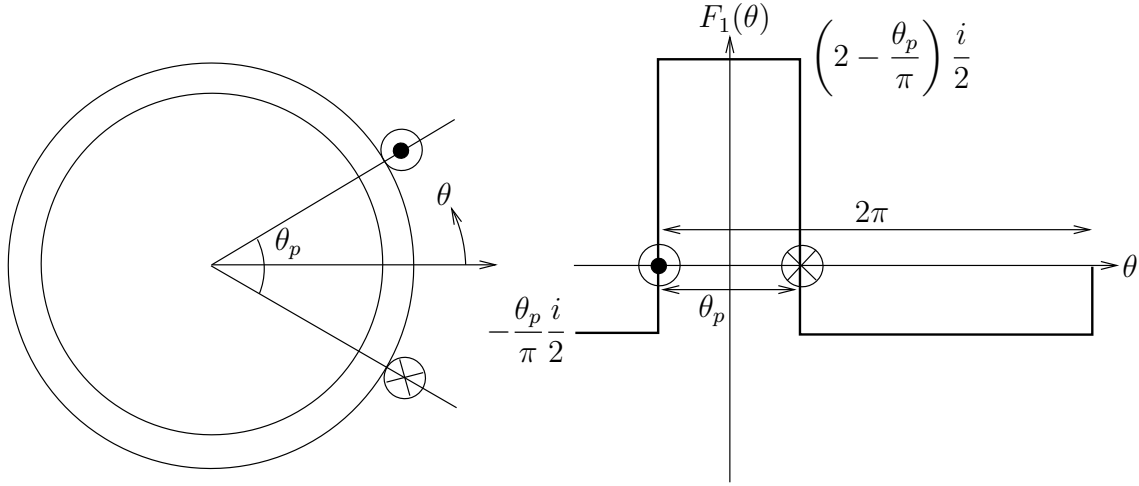


Figure 2.3: MMF of a single turn carrying a current i .

current distribution $j_s(\theta)$:

$$F(\theta) = \int_0^\theta j_s(\theta) r d\theta + F_0 \quad (2.9)$$

where F_0 is chosen such that $\int_0^{2\pi} F(\theta) r d\theta = 0$.

2.3.1.2 MMF of a Single Turn

The MMF $F_1(\theta)$ of a single turn consisting of two conductors spaced by the angle θ_p is displayed in Fig. 2.3 [Alg95] [Hel77]. A direct current i flowing in this turn provokes a uniform magnetic field over the turn under the assumption of a smooth airgap. The produced flux returns uniformly over the airgap i.e. the area of the two rectangles in Fig. 2.3 is the same. Therefore, the MMF has also a rectangular shape and is directly proportional to the magnetic field. Note that the currents are supposed to be concentrated in infinitely small slots i.e. they are distributed as Dirac generalized functions along the circumference.

This rectangular MMF waveform can be decomposed into a Fourier series as follows:

$$F_1(\theta) = \frac{2i}{\pi} \sum_{\nu_s=1}^{\infty} \frac{1}{\nu_s} \sin\left(\frac{\nu_s \theta_p}{2}\right) \cos(\nu_s \theta) \quad (2.10)$$

Note that $F_1(\theta)$ contains space harmonics of all ranks ν_s . Only if the turn had a full pitch ($\theta_p = \pi$), the even harmonics would disappear. The fact that the harmonic amplitudes depend on the turn pitch θ_p leads to the definition of the pitch factor $K_{p\nu_s}$ for a space harmonic of rank ν_s [Hel77]:

$$K_{p\nu_s} = \sin\left(\nu_s \frac{\theta_p}{2}\right) \quad (2.11)$$

If the turn is carrying alternating current instead of direct current, i is simply replaced in equation (2.10) by $i(t)$. Supposing $i(t) = I \cos(\omega_s t)$, a stationary alternating wave is obtained. With the trigonometric identity $\cos \alpha \cos \beta =$

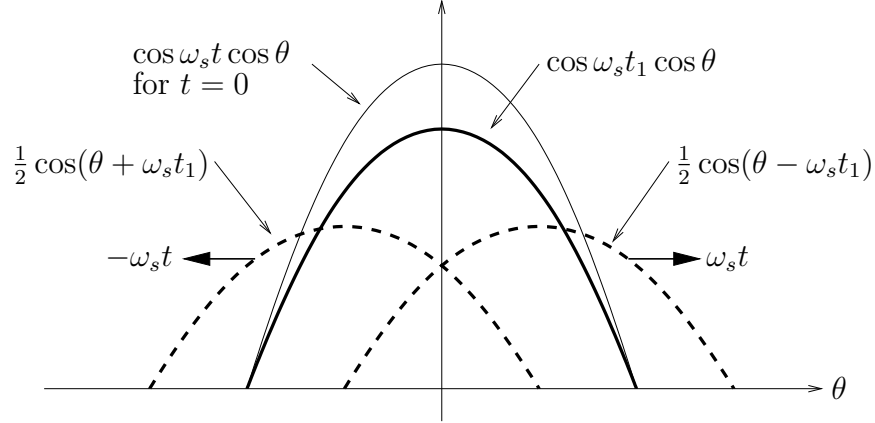


Figure 2.4: Decomposition of an alternating stationary wave into two opposite revolving waves.

$\frac{1}{2} [\cos(\alpha - \beta) + \cos(\alpha + \beta)]$, (2.10) becomes:

$$F_1(\theta, t) = \frac{I}{\pi} \sum_{\nu_s=1}^{\infty} \frac{1}{\nu_s} K_{p\nu_s} [\cos(\nu_s \theta - \omega_s t) + \cos(\nu_s \theta + \omega_s t)] \quad (2.12)$$

This relation shows that a stationary alternating MMF wave can be decomposed into a forward and a backward revolving wave of equal amplitude [Alg95]. This is graphically illustrated in Fig. 2.4 for a stationary sinusoidal wave $\cos \omega_s t \cos \theta$ at time instants $t = 0$ and $t = t_1$.

2.3.1.3 MMF of a Three-Phase Winding

First, the MMF of one phase winding is studied. The MMF of a three-phase winding can then be obtained by addition of the MMFs of the three phases.

Consider a phase winding which is formed by a group of N coils, each of them of pitch θ_p and carrying the same current i . The angle between two adjacent coils is denoted θ_d . The MMF $F_{1ph}(\theta)$ of this group of coils is then obtained by addition of the MMFs of N single coils [Hel77]:

$$F_{1ph}(\theta) = \frac{2Ni}{\pi} \sum_{\nu_s=1}^{\infty} \frac{1}{\nu_s} K_{p\nu_s} K_{d\nu_s} \cos(\nu_s \theta) \quad (2.13)$$

where $K_{d\nu_s}$ denotes the winding distribution factor, defined as:

$$K_{d\nu_s} = \frac{\sin(\nu_s N \frac{\theta_d}{2})}{N \sin(\nu_s \frac{\theta_d}{2})} \quad (2.14)$$

Assuming a motor with one pole pair $p = 1$, a conductor at $\theta = \theta_i$ of a phase winding always has an opposite conductor of the same phase winding at $\theta = \theta_i + \pi$ carrying the opposite current. Generally, a phase winding can therefore be considered as a combination of full pitch coils. Actually, the connection of the different coils is of no importance for the MMF generation as they are all

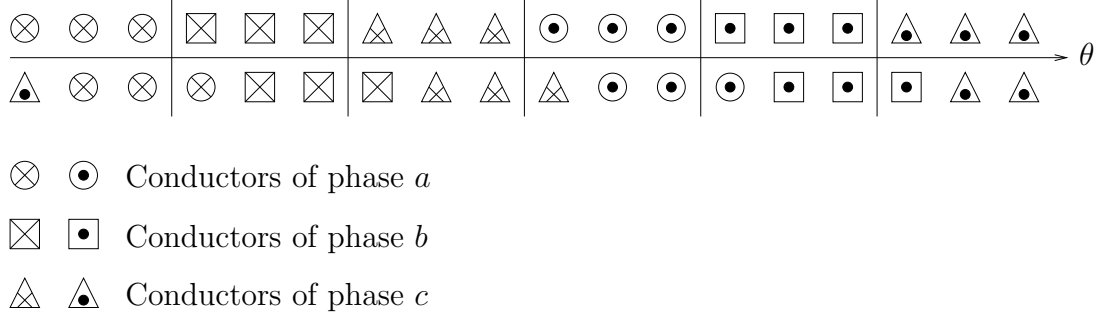


Figure 2.5: Example of a two pole, two layer, fractional pitch winding.

carrying the same current. This can be seen in Fig. 2.5 where the conductors of a fractional pitch two layer winding are shown. In consequence of the full pitch coils, even harmonics cancel out and only odd space harmonics remain [Kos69]. This also becomes clear considering the symmetry of the resulting MMF waveform: the MMF of a phase winding with e.g. $p = 1$ is symmetric according to $F(\theta + \pi) = -F(\theta)$. Thus, the coefficients of even rank of its Fourier series development are zero [Bro99].

In a three-phase winding with $p = 1$, the three groups of coils are mutually displaced in space by the angle $2\pi/3$. Assuming a balanced and sinusoidal supply, the alternating currents in the three phase windings are of equal amplitude with a phase shift of $2\pi/3$. Each phase produces forward and backward rotating MMF waves. The three forward rotating fundamental waves ($\nu_s = 1$) add up whereas the corresponding backward rotating waves cancel out. When the third order space harmonics are added, they completely vanish. This is true for all space harmonics with ranks being multiples of 3. For $\nu_s = 5, 11, 17, \dots$ the forward rotating waves cancel out and the backward rotating ones add up whereas the opposite is true for $\nu_s = 1, 7, 13, \dots$ [Kos69].

After generalization to p pole pairs, the stator MMF $F_s(\theta, t)$ of a three phase machine with sinusoidal supply can be expressed as follows [Hel77]:

$$F_s(\theta, t) = \frac{3}{\pi} NI \sum_{c=-\infty}^{\infty} \frac{1}{p(6c+1)} K_{p\nu_s} K_{d\nu_s} \cos[(6c+1)p\theta - \omega_s t] \quad (2.15)$$

where N is the number of series coils per phase, I is the current amplitude and ω_s the supply pulsation. The harmonic order is $\nu_s = p(6c+1) = p(\dots, -5, 1, 7, \dots)$ with $c \in \mathbb{Z}$. The notation with negative harmonic orders is chosen because the direction of rotation is directly obvious by the sign of the space harmonic (see e.g. [LG61] [Ric54]).

The angular velocity of the rotating waves can be determined considering a point along the periphery where the wave amplitude is constant. This point is described by the condition:

$$\cos[(6c+1)p\theta - \omega_s t] = \text{const.} \quad \Leftrightarrow \quad (6c+1)p\theta - \omega_s t = \text{const.} \quad (2.16)$$

The angular velocity ω_{ν_s} of the MMF waves is obtained by differentiation of this expression:

$$\omega_{\nu_s} = \frac{d\theta}{dt} = \frac{\omega_s}{p(6c+1)} = \frac{\omega_s}{\nu_s} \quad (2.17)$$

From (2.17), it can be concluded that waves of order $\nu_s = -5p, -11p, -17p, \dots$ move $1/(6c+1)$ times slower than the fundamental in the opposite direction. Waves with $\nu_s = 7p, 13p, 19p, \dots$ revolve $1/(6c+1)$ times slower than the fundamental in the same direction as the fundamental [Hel77]. The sign of the space harmonic order therefore indicates the direction of rotation of the corresponding wave.

Up to now, a sinusoidal supply voltage has been supposed that consequently leads to sinusoidal currents flowing in the windings. If the induction motor is supplied by a voltage inverter or connected to a grid with a significant level of voltage harmonics, current time harmonics will consequently be present. These harmonic currents also generate MMF waves. Their expression is simply obtained by replacing the fundamental pulsation ω_s by the corresponding harmonic pulsation $\mu_s \omega_s$ where μ_s denotes the order of the time harmonic. The MMF of a three phase winding including the effects of time harmonics can be written as [Yan81]:

$$F_s(\theta, t) = \frac{3}{\pi} N \sum_{\mu_s=1}^{\infty} \sum_{c=-\infty}^{\infty} \frac{1}{p(6c+1)} K_{p\nu_s} K_{d\nu_s} I_{\mu_s} \cos [(6c+1)p\theta - (\pm|_{\mu_s} \mu_s \omega_s) t] \quad (2.18)$$

where I_{μ_s} denotes the amplitude of the corresponding current time harmonic. The notation $\pm|_{\mu_s}$ is used to distinguish the sign of the pulsation with respect to the time harmonic order μ_s of the corresponding wave:

$$\pm|_{\mu_s} = \begin{cases} + & \text{if } \mu_s = 3n + 1 = 1, 4, 7, 10, \dots \\ - & \text{if } \mu_s = 3n - 1 = 2, 5, 8, 11, \dots \end{cases} \quad n \in \mathbb{N}_0 \quad (2.19)$$

The detailed calculation of the three-phase winding MMF shows that the components with $\mu_s = 3n + 1 = 1, 4, 7, \dots$ give rise to MMF waves rotating in the positive direction. Thus, notation $\pm|_{\mu_s}$ is used in the following to distinguish the direction of rotation. If $\mu_s = 3n - 1 = 2, 5, 8, \dots$, the corresponding MMF waves rotate in the negative direction [Ség96]. In general, even time harmonics are of smaller amplitude than odd harmonics. Current time harmonics of order $3n$ have not been considered as they cannot circulate in star-connected windings.

The general angular velocity ω_{ν_s, μ_s} of a MMF wave is obtained as follows:

$$\omega_{\nu_s, \mu_s} = \pm|_{\mu_s} \frac{\mu_s \omega_s}{p(6c+1)} \quad , \quad c \in \mathbb{Z} \quad (2.20)$$

Hence, it can be noted that higher order time harmonics move faster than the fundamental whereas higher order space harmonics move slower.

2.3.1.4 Rotor MMF

The MMF of a squirrel cage rotor can be derived in two ways. First, the rotor can be considered equivalent to a m -phase two layer winding according to Fig. 2.6 [Hel77]. A turn is formed by the conductors in the top layer of one slot and the bottom layer of the adjacent slot. The current I_{ring} flowing in the turn is the current in the end ring between the two slots. The number of phases in such a winding would be $m = N_r/p$ where N_r denotes the number of rotor bars. The

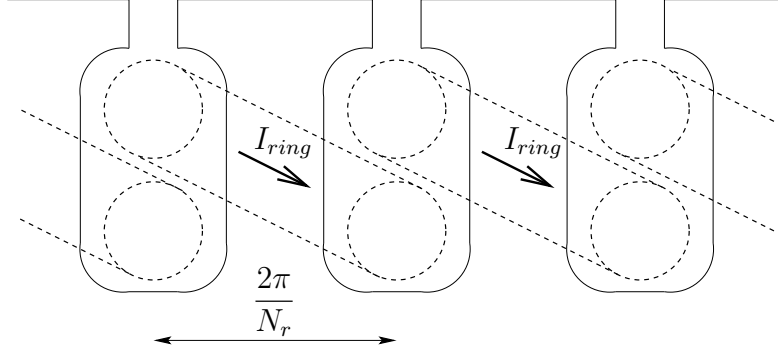


Figure 2.6: Two-layer winding equivalent to a squirrel cage rotor.

phase shift between the currents in two adjacent turns is $\varphi = 2\pi/m = 2\pi p/N_r$ since the rotor bars are spaced by the angle $2\pi/N_r$.

On the other hand, the rotor MMF can be calculated from the current flowing in each bar. Each slot leads thus to a step in the MMF curve. Detailed calculations with both methods can be found in [Hel77]. Let θ' denote the circumference angle θ' in the rotor reference frame. The final expression of the rotor MMF $F_r(\theta', t)$ is:

$$F_r(\theta', t) = \frac{N_r I_{bar}}{2\pi} \sum_{\nu_r=-\infty}^{\infty} \frac{1}{\nu_r} \cos(\nu_r \theta' - \omega_{rt} t - \varphi_{\nu_r}) \quad (2.21)$$

where I_{bar} denotes the amplitude of the rotor bar currents, ω_{rt} their pulsation and φ_{ν_r} the phase angle of the corresponding harmonic.

The pole pair numbers ν_r of the rotor MMF waves cannot take any integer value but only the following [LG61] [Ric54]:

$$\nu_r = cN_r + \nu_s \quad , \quad c \in \mathbb{Z} \quad (2.22)$$

This signifies that the interaction between the squirrel cage rotor and a stator space harmonic of order ν_s results in rotor space harmonics of order $cN_r + \nu_s$. This fact can be illustrated by considering the effect of the rotor bars as a spatial sampling [Nan01]. According to signal processing theory, the sampling of a sinusoidal signal of frequency f_0 results in additional frequency components in its spectrum at $cf_{sample} + f_0$. Similarly, the sampling of an order ν_s space harmonic by N_r rotor bars leads to additional space harmonics of order $cN_r + \nu_s$. An example is given in Fig. 2.7 where a space harmonic of order 11 interacts with $N_r=12$ rotor bars. The result is, amongst others, a harmonic of pole pair number -1. Therefore, the interaction between higher order space harmonics and the squirrel cage rotor may also produce harmonics of low order.

The origin of the rotor currents are induced voltages, themselves resulting from the airgap flux density. For simplification, only the flux density waves produced by the stator MMF waves according to (2.18), i.e. under the assumption of a smooth airgap, are considered. The relative angular velocity $\omega_{r\nu_s, \mu_s}$ of these waves with respect to the rotor is:

$$\omega_{r\nu_s, \mu_s} = \omega_{\nu_s, \mu_s} - \omega_r = \pm \left|_{\mu_s} \frac{\mu_s \omega_s}{\nu_s} - \omega_r \right. \quad (2.23)$$

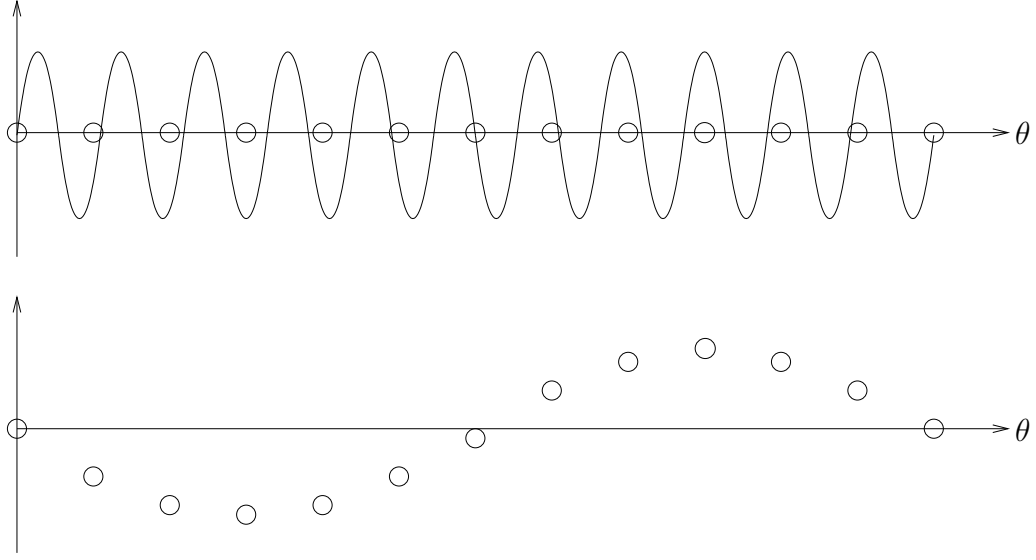


Figure 2.7: Example of spatial sampling of a space harmonic of order 11 by a rotor with $N_r=12$ rotor bars. The resultant rotor wave has a pole pair number of -1.

where ω_r denotes the rotor angular rotational frequency. These waves, having ν_s pole pairs, induce currents of pulsation ω_{rt} in the rotor with [Hel77]:

$$\omega_{rt} = \nu_s \omega_r \nu_{s,\mu_s} = \pm |\mu_s \mu_s \omega_s - \nu_s \omega_r| \quad (2.24)$$

The rotor MMF in equation (2.21) can also be expressed in the stationary reference frame related to the stator. The transformation between the rotating rotor related reference frame and the stationary reference frame is illustrated in Fig. 2.8 and mathematically described by:

$$\theta = \theta' + \theta_r = \theta' + \omega_r t \quad (2.25)$$

This leads to:

$$\begin{aligned} F_r(\theta, t) &= \frac{N_r I_{bar}}{2\pi} \sum_{\nu_r=-\infty}^{\infty} \frac{1}{\nu_r} \cos [\nu_r (\theta - \omega_r t) - \omega_{rt} t - \varphi_{\nu_r}] \\ &= \frac{N_r I_{bar}}{2\pi} \sum_{\nu_s=-\infty}^{\infty} \sum_{\nu_r=-\infty}^{\infty} \sum_{\mu_s=1}^{\infty} \frac{1}{\nu_r} \cos [\nu_r \theta - \nu_r \omega_r t - (\pm |\mu_s \mu_s \omega_s t - \nu_s \omega_r t) - \varphi_{\nu_s \nu_r}] \end{aligned} \quad (2.26)$$

When spatial sampling is neglected, the rotor space harmonic is of the same order as the stator space harmonic at its origin and $\nu_s = \nu_r$ with $c = 0$. The rotor MMF can then be expressed in a more familiar form with the same pulsations as the stator MMF:

$$F_r(\theta, t) = \frac{N_r I_{bar}}{2\pi} \sum_{\nu_r=-\infty}^{\infty} \frac{1}{\nu_r} \sum_{\mu_s=1}^{\infty} \cos [\nu_r \theta - (\pm |\mu_s \mu_s \omega_s t) - \varphi_{\nu_s \nu_r}] \quad (2.27)$$

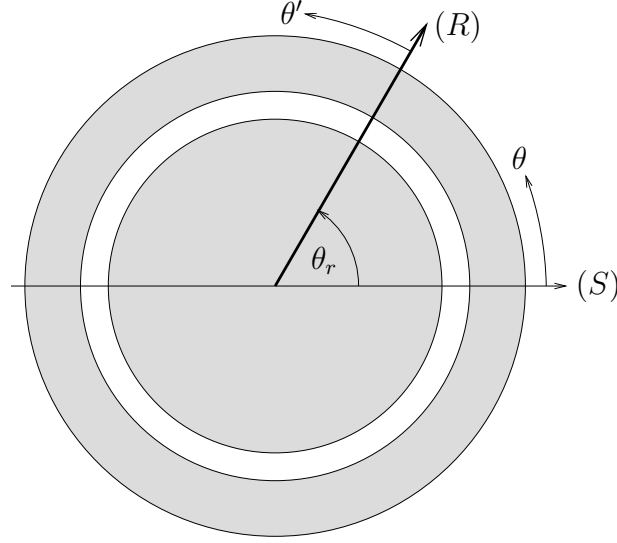


Figure 2.8: Illustration of the stationary stator-fixed reference frame (S) and the rotating rotor-related reference frame (R).

2.3.2 Airgap Permeance

The airgap permeance Λ is defined as the inverse of the airgap length g multiplied with the permeability of free space μ_0 [Yan81]:

$$\Lambda = \frac{\mu_0}{g} \quad (2.28)$$

In simplified considerations, the airgap length is supposed constant and the airgap permeance is therefore also a constant. When slotting, eccentricity or saturation effects are studied, the airgap varies with respect to time and the circumference angle θ . In these cases, the permeance also depends on these parameters and may take the expression of travelling waves similar to the MMF waves.

2.3.2.1 Slotting

In the preceding sections, the airgap has been supposed constant. However, when the rotor or stator are slotted, the airgap length varies with respect to time and space which consequently leads to variations in the airgap flux density.

A simple approach to account for slotting is the introduction of the *Carter factor*. Let B_0 denote the mean flux density without slotting. This mean value drops to B'_0 when slotting is considered. This flux density variation is equivalent to a fictional increase of the airgap from g_0 to g'_0 by a factor k_c , called the Carter factor:

$$B'_0 = \frac{1}{k_c} B_0 \quad , \quad g'_0 = k_c g_0 \quad \text{with } k_c > 1 \quad (2.29)$$

The Carter factor depends on the slot geometry and the airgap length. Various expression for k_c can be found in [Hel77].

The Carter factor globally models the mean airgap flux density but does not take into account local effects. This can be realized by considering a variable airgap

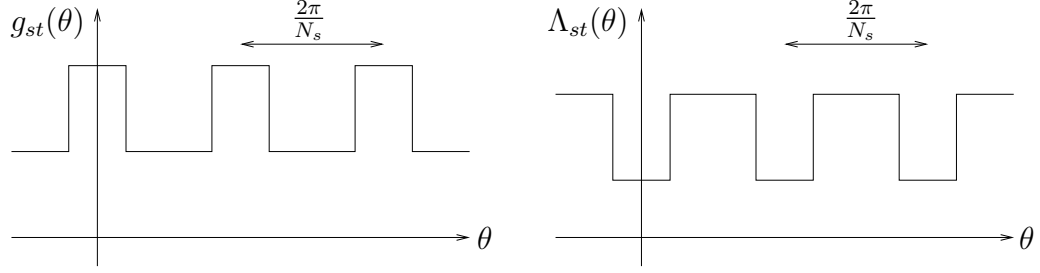


Figure 2.9: Airgap length $g_{st}(\theta)$ and corresponding permeance $\Lambda_{st}(\theta)$ in the case of stator slotting.

length $g(\theta)$. In presence of rectangular stator slots and a smooth rotor, the airgap length takes a rectangular shape as illustrated in Fig. 2.9. The number of stator slots is denoted N_s . This representation is simplified because it does not model the effective length of the magnetic field lines which is different from the considered rectangular function. However, a different shape only alters the magnitude of the Fourier series coefficients. These coefficients will not be calculated because our aim is only a quantitative analysis. Analytical expressions for the Fourier coefficients and further discussions on this topic can be found in [Hes92].

The airgap permeance $\Lambda(\theta)$ is obtained by inversion of $g(\theta)$ and is illustrated in Fig. 2.9. This waveform can be developed into a Fourier series:

$$\Lambda_{st}(\theta) = \sum_{n_{st}=0}^{\infty} \Lambda_{n_{st}} \cos(n_{st}N_s\theta) \quad (2.30)$$

When the rotor is slotted and the stator is supposed smooth, the permeance $\Lambda_{rt}(\theta')$ takes the following expression in the rotor reference frame:

$$\Lambda_{rt}(\theta') = \sum_{n_{rt}=0}^{\infty} \Lambda_{n_{rt}} \cos(n_{rt}N_r\theta') \quad (2.31)$$

This leads to the following equation for the permeance $\Lambda_{rt}(\theta, t)$ in the stationary reference frame:

$$\Lambda_{rt}(\theta, t) = \sum_{n_{rt}=0}^{\infty} \Lambda_{n_{rt}} \cos(n_{rt}N_r\theta - n_{rt}N_r\omega_r t) \quad (2.32)$$

The permeance due to rotor slotting is therefore a series of rotating waves with pole pair numbers $n_{rt}N_r$ and pulsations $n_{rt}N_r\omega_r$.

The total airgap permeance $\Lambda_{st,rt}$ when the rotor and the stator are slotted is the inverse of the total airgap length according to [Yan81]:

$$\Lambda_{st,rt} = \left(\frac{1}{\Lambda_{st}} + \frac{1}{\Lambda_{rt}} - \frac{1}{\Lambda_0} \right)^{-1} = \frac{\Lambda_{st}\Lambda_{rt}\Lambda_0}{\Lambda_{rt}\Lambda_0 + \Lambda_{st}\Lambda_0 - \Lambda_{st}\Lambda_{rt}} \quad (2.33)$$

where $\Lambda_0 = \mu_0/g_0$ denotes the permeance of a smooth airgap. The variable terms Λ_{st} and Λ_{rt} are relatively small compared to the constant term Λ_0 . The preceding

expression can therefore be approximated by the product of the variable terms and a constant C [Yan81]:

$$\Lambda_{st,rt}(\theta, t) = C\Lambda_{st}\Lambda_{rt} = \sum_{n_{st}=0}^{\infty} \sum_{n_{rt}=0}^{\infty} \Lambda_{n_{st},n_{rt}} \cos [(n_{st}N_s \pm n_{rt}N_r) \theta - n_{rt}N_r\omega_r t] \quad (2.34)$$

The airgap permeance in the presence of stator and rotor slotting is therefore a combination of rotating waves with pole pair numbers $n_{st}N_s \pm n_{rt}N_r$ and pulsations $n_{rt}N_r\omega_r t$. It should be noted that the pole pair numbers of these waves can be relatively small depending on the number of stator and rotor slots.

2.3.2.2 Saturation

Until now, the permeability of iron was supposed infinite and therefore, saturation effects were neglected. The permeance wave approach offers a simple possibility to account for basic saturation phenomena. In regions with iron saturation (especially the stator teeth), the airgap flux density is no more linear with respect to the MMF. Increasing the current and therefore the MMF leads to a smaller increase in the flux density than without saturation. This effect can be modelled by a virtually larger airgap i.e. a smaller permeance in regions where the iron is saturated [Yan81] or a larger slot opening [Hel77]. The saturated regions are located where the absolute value of the flux density is high. This fact is illustrated in Fig. 2.10 where the fundamental flux density wave $B(\theta)$ and its absolute value are displayed for a given time instant. Supposing a smooth airgap, the corresponding permeance function $\Lambda_{sa}(\theta)$ is shown with its first harmonic. The permeance decreases in regions with high absolute values of B .

Mathematically, the permeance including saturation effects can be represented by a Fourier series. The first saturation harmonic has twice the pole pairs of the fundamental wave. It revolves at the same speed and in the same direction as the fundamental flux density i.e. its pulsation is $2\omega_s$. Including higher harmonics, the permeance waves with saturation can be expressed as:

$$\Lambda_{sa}(\theta, t) = \sum_{n_{sa}=0}^{\infty} \Lambda_{n_{sa}} \cos (2n_{sa}p\theta - 2n_{sa}\omega_s t) \quad (2.35)$$

When saturation effects and slotting are considered together, equations (2.34) and (2.35) can be combined to yield:

$$\Lambda_{rt,st,sa}(\theta, t) = \sum_{n_{st}=0}^{\infty} \sum_{n_{rt}=0}^{\infty} \sum_{n_{sa}=0}^{\infty} \Lambda_{n_{st},n_{rt},n_{sa}} \cos [(n_{st}N_s \pm n_{rt}N_r \pm 2pn_{sa}) \theta - n_{rt}N_r\omega_r t \pm 2n_{sa}\omega_s t] \quad (2.36)$$

2.3.3 Airgap Flux Density

It has been demonstrated in [Hel77] that in case of a variable airgap, the airgap flux density $B(\theta, t)$ at a certain point can be determined with good approximation

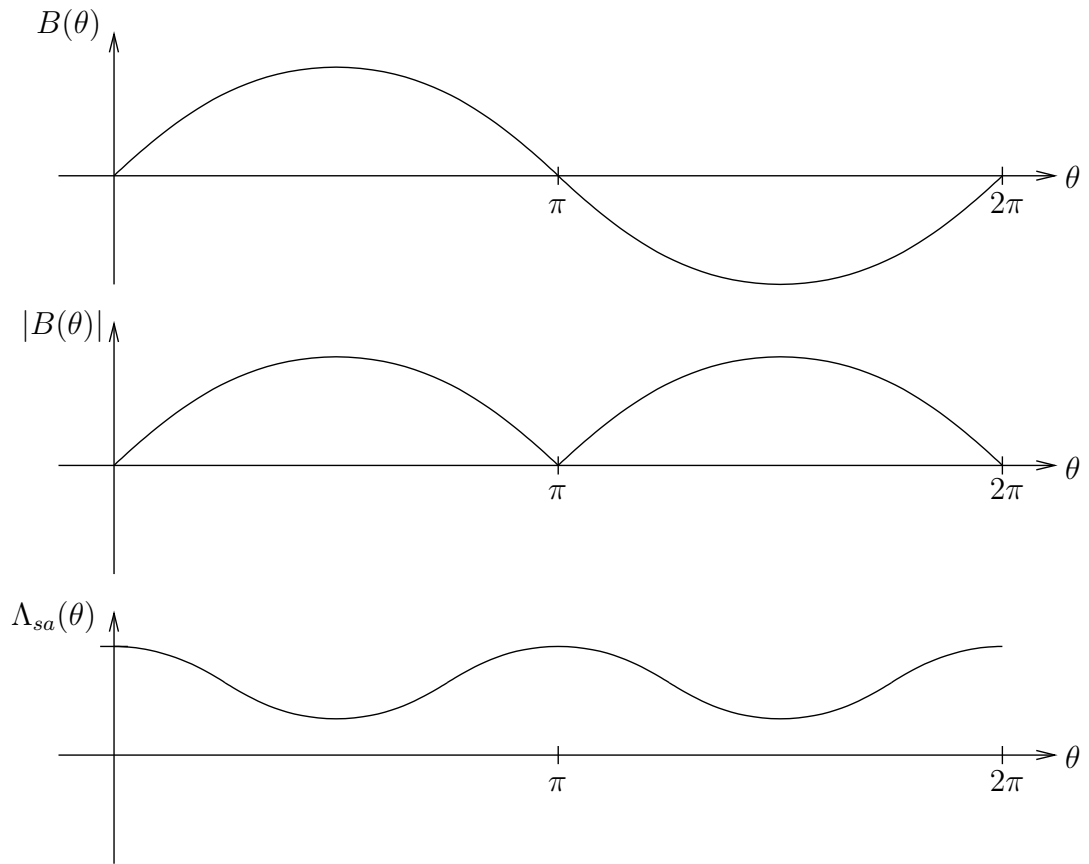


Figure 2.10: Fundamental magnetic flux density $B(\theta)$, absolute value $|B(\theta)|$ of the fundamental magnetic flux density and first saturation harmonic of the airgap permeance $\Lambda_{sa}(\theta)$ for a given time instant.

by the product of the instantaneous MMF and the airgap permeance at that point:

$$B(\theta, t) = \frac{\mu_0}{g(\theta, t)} F(\theta, t) = \Lambda(\theta, t) F(\theta, t) \quad (2.37)$$

If only the stator MMF and the rotor MMF due to the primary armature reaction are considered (higher order armature reactions are neglected), the resulting stator and rotor related flux densities $B_s(\theta, t)$ and $B_r(\theta, t)$ can be calculated by separate multiplication of the corresponding MMFs (equations (2.18) and (2.26)) with the permeance waves from (2.36). Then, the stator and rotor MMF $F_s(\theta, t)$ and $F_r(\theta, t)$ can be written in a general form:

$$F_s(\theta, t) = \sum_{\nu_s=-\infty}^{\infty} \sum_{\mu_s=1}^{\infty} F_{\nu_s, \mu_s} \cos(\nu_s \theta - (\pm |\mu_s| \mu_s \omega_s) t) \quad (2.38)$$

$$F_r(\theta, t) = \sum_{\nu_s=-\infty}^{\infty} \sum_{\nu_r=-\infty}^{\infty} \sum_{\mu_s=1}^{\infty} F_{\nu_s, \nu_r, \mu_s} \cos[\nu_r \theta - \nu_r \omega_r t - (\pm |\mu_s| \mu_s \omega_s t - \nu_s \omega_r t) - \varphi_{\nu_s \nu_r}] \quad (2.39)$$

Therefore, the corresponding flux density $B(\theta, t)$ is:

$$\begin{aligned} B(\theta, t) &= B_s(\theta, t) + B_r(\theta, t) \\ &= F_s(\theta, t) \Lambda_{rt, st, sa}(\theta, t) + F_r(\theta, t) \Lambda_{rt, st, sa}(\theta, t) \\ &= \sum_{m_s, \Omega_s} B_{m_s, \Omega_s} \cos(m_s \theta - \Omega_s t) + \sum_{m_r, \Omega_r} B_{m_r, \Omega_r} \cos(m_r \theta - \Omega_r t - \varphi_{m_r, \Omega_r}) \end{aligned} \quad (2.40)$$

where m_s and m_r denote the possible pole pair numbers of the stator and rotor flux density waves, Ω_s and Ω_r are the corresponding pulsations. These are obtained considering all the possible combinations from the multiplication of the permeance and the MMF waves:

$$m_s = \nu_s \pm n_{st} N_s \pm n_{rt} N_r \pm 2pn_{sa} \quad (2.41a)$$

$$\Omega_s = \pm |\mu_s| \mu_s \omega_s \pm n_{rt} N_r \omega_r \pm 2n_{sa} \omega_s \quad (2.41b)$$

$$m_r = \nu_r \pm n_{st} N_s \pm n_{rt} N_r \pm 2pn_{sa} \quad (2.41c)$$

$$\Omega_r = \nu_r \omega_r - \nu_s \omega_r \pm |\mu_s| \mu_s \omega_s \pm n_{rt} N_r \omega_r \pm 2n_{sa} \omega_s \quad (2.41d)$$

2.3.4 Stator Current

The non-supply frequency stator current components in a phase winding are obtained through a calculation of the magnetic flux and its derivative as described in 2.2.3. The following calculation consider one particular flux density wave $B_i(\theta, t)$ with pole pair number m_i , pulsation Ω_i and phase angle φ_i :

$$B_i(\theta, t) = B_i \cos(m_i \theta - \Omega_i t - \varphi_i) \quad (2.42)$$

The corresponding flux Φ_i through a stator coil formed by two conductors at angular positions θ_1 and θ_2 is:

$$\begin{aligned}\Phi_i(t) &= l_m \int_{\theta_1}^{\theta_2} B_i(\theta, t) r d\theta \\ &= \frac{B_i}{m_i} R_s l_m [\sin(m_i \theta_2 - \Omega_i t - \varphi_i) - \sin(m_i \theta_1 - \Omega_i t - \varphi_i)]\end{aligned}\quad (2.43)$$

Using $\sin \alpha - \sin \beta = \cos \frac{\alpha+\beta}{2} \sin \frac{\alpha-\beta}{2}$, the following flux expression is obtained:

$$\Phi_i(t) = \frac{B_i}{m_i} R_s l_m \sin \left(m_i \frac{\theta_2 - \theta_1}{2} \right) \cos \left(m_i \frac{\theta_1 + \theta_2}{2} - \Omega_i t - \varphi_i \right) \quad (2.44)$$

This expression shows that the pitch factor of the considered coil K_{pm_i} (see (2.11)) affects the flux amplitude. Consequently, the induced voltage $V_i(t)$ in the coil is obtained as:

$$V_i(t) = \frac{d}{dt} \Phi_i(t) = \frac{B_i}{m_i} R_s l_m K_{pm_i} \Omega_i \sin \left(m_i \frac{\theta_1 + \theta_2}{2} - \Omega_i t - \varphi_i \right) \quad (2.45)$$

The total induced voltage in a phase winding is the sum of the induced voltages in the coils. The induced voltage of non-supply frequency leads to a circulating current that is only limited by the winding and line impedance because the stator appears short-circuited to currents of such frequencies.

The preceding calculations therefore show that the pulsations Ω_i of the flux density waves (see equations (2.41b) and (2.41d)) can also be found in the stator current. Their amplitude will depend on the winding structure, the pulsation Ω_i , the corresponding space harmonic order m_i and of course the amplitude of the initial flux density wave B_i .

2.3.5 Torque

The electromagnetic torque Γ of the induction motor can be calculated from expression (2.5) using the previously calculated stator and rotor flux density waves.

$$\Gamma = -\frac{1}{\mu_0} l_m R_0 g_0 \int_0^{2\pi} [B_s(\theta, t) + B_r(\theta, t)] \frac{\partial}{\partial \theta_r} B_r(\theta, t) d\theta \quad (2.46)$$

However, it should be noted that this expression assumes that the stator flux density does not depend on the rotor angular position θ_r because only the rotor flux density is differentiated. If rotor slotting is taken into account, this assumption is no longer valid because the permeance waves depend on the rotor position. Consequently, the stator flux density depends on it as well. This can be seen in equation (2.41b) where the term $n_{rt} N_r \omega_r$ is present.

The derivative of the rotor flux density from (2.40) can be written in a general form as:

$$\frac{\partial}{\partial \theta_r} B_r(\theta, t) = \sum_{m'_r, \Omega'_r} B'_{m'_r, \Omega'_r} \sin(m'_r \theta - \Omega'_r t - \varphi_{m'_r, \Omega'_r}) \quad (2.47)$$

Using this expression and supposing a smooth rotor, equation (2.46) becomes with the general expression from (2.40):

$$\begin{aligned} \Gamma = -\frac{1}{\mu_0} l_m R_0 g_0 \left\{ \int_0^{2\pi} \sum_{m_s, \Omega_s} B_{m_s, \Omega_s} \cos(m_s \theta - \Omega_s t) \right. \\ \sum_{m'_r, \Omega'_r} B'_{m'_r, \Omega'_r} \sin(m'_r \theta - \Omega'_r t - \varphi_{m'_r, \Omega'_r}) d\theta \\ + \int_0^{2\pi} \sum_{m_r, \Omega_r} B_{m_r, \Omega_r} \cos(m_r \theta - \Omega_r t - \varphi_{m_r, \Omega_r}) \\ \left. \sum_{m'_r, \Omega'_r} B'_{m'_r, \Omega'_r} \sin(m'_r \theta - \Omega'_r t - \varphi_{m'_r, \Omega'_r}) d\theta \right\} \end{aligned} \quad (2.48)$$

Using the trigonometric identity $\cos \alpha \sin \beta = \frac{1}{2} [\sin(\beta - \alpha) + \sin(\alpha + \beta)]$, all the integrals take the following general form with $k \in \mathbb{Z}$:

$$\int_0^{2\pi} \sin(k\theta + \psi) d\theta = \begin{cases} 2\pi \sin \psi & \text{if } k = 0 \\ 0 & \text{for all other } k \end{cases} \quad (2.49)$$

k results from addition or subtraction of the pole pair numbers $m_s \pm m'_r$ or $m_r \pm m'_r$ of the two multiplied waves. A necessary condition for a non-zero value of the integral is thus $k = 0$.

It can therefore be concluded that a torque can only arise from a combination of flux density waves having equal pole pair numbers in terms of the absolute value. According to equation (2.48), the torque can result on the one hand from an interaction of a stator flux density wave with a rotor flux density wave of same pole pair number. On the other hand, two rotor flux density waves with equal pole pair numbers but different pulsations and phase angles can also produce a non-zero torque.

Including the condition of equal absolute value of the pole pair numbers, equation (2.48) can be written in a compact form as:

$$\begin{aligned} \Gamma = -\frac{\pi}{\mu_0} l_m R_0 g_0 \left\{ \sum_{|m_s|=|m'_r|, \Omega_s, \Omega'_r} B_{m_s, \Omega_s} B'_{m'_r, \Omega'_r} \sin(\Omega_s t \pm \Omega'_r t \pm \varphi_{m'_r, \Omega'_r}) \right. \\ + \sum_{|m_r|=|m'_r|, \Omega_r, \Omega'_r} B_{m_r, \Omega_r} B'_{m'_r, \Omega'_r} \sin(\Omega_r t \pm \Omega'_r t + \varphi_{m_r, \Omega_r} \pm \varphi_{m'_r, \Omega'_r}) \left. \right\} \end{aligned} \quad (2.50)$$

According to this expression, the electromagnetic torque generally varies sinusoidally with time. The torque is independent of time only if the pulsations verify

$$\Omega_s = \Omega'_r \quad \text{or} \quad \Omega_r = \Omega'_r \quad (2.51)$$

In order to illustrate the various mechanisms of torque production, several cases will be discussed in the following. The main part of the electromagnetic motor torque results from the interaction between the fundamental stator and rotor MMF. These waves have $m_s = m'_r = p$ pole pair number and pulsations $\Omega_s = \Omega'_r = \omega_s$. The calculation yields:

$$\begin{aligned}\Gamma &= -\frac{1}{\mu_0} l_m R_0 g_0 \int_0^{2\pi} B_{1s} \cos(p\theta - \omega_s t) B'_{1r} \sin(p\theta - \omega_s t - \varphi_1) d\theta \\ &= \frac{\pi}{\mu_0} l_m R_0 g_0 B_{1s} B'_{1r} \sin \varphi_1\end{aligned}\quad (2.52)$$

This equation illustrates the well-known fact that the average motor torque is a function of the product of stator flux density amplitude B_{1s} , rotor flux density amplitude B'_{1r} , and the sine of their phase difference φ_1 .

Let us now consider interactions between higher order space harmonics: The stator MMF contains e.g. a space harmonic of order $7p$ with the fundamental pulsation ω_s . This space harmonic is also present in the stator-related flux density wave. It induces rotor currents that lead to a rotor MMF wave with $7p$ pole pairs and the same angular velocity as the corresponding stator MMF wave, but with a different initial phase angle. The flux density waves related to the two MMF waves interact with each other because of the equal pole pair number. The pole pair numbers and pulsations of the corresponding waves take the following values according to (2.41):

$$\begin{aligned}m_s &= m'_r = 7p \\ \Omega_s &= \omega_s \\ \Omega'_r &= 7p\omega_r - 7p\omega_r + \omega_s = \omega_s\end{aligned}$$

As the considered flux density waves have the same pulsations Ω_s and Ω'_r , the resultant torque is independent of time for a given speed. However, if the speed varies with constant supply frequency e.g. during a motor start-up, the amplitude of considered torque varies since the corresponding rotor MMF amplitude changes with the relative speed of the rotor to the stator MMF with $7p$ pole pairs. The relative speed of the rotor with respect to this wave is zero if $\omega_r = \omega_s/7p$. In this case, the rotor MMF with pole pair number $7p$ will be zero as well as the considered torque component. The torque-speed curve of this particular component is similar to the main torque-speed curve but with a zero at $\omega_r = \omega_s/7p$ as illustrated on Fig. 2.11.

Hence, these torques influence the torque-speed characteristic of an induction motor and cause torque dips at low speeds (see Fig. 2.11). They arise generally from interactions of stator space harmonics with rotor space harmonics where the latter has been induced by the stator space harmonic itself. This is similar to the production of the main torque and characteristic for the induction motor. Therefore, these torques are called *asynchronous torques* (see [Hel77] and [Ric54] for more details).

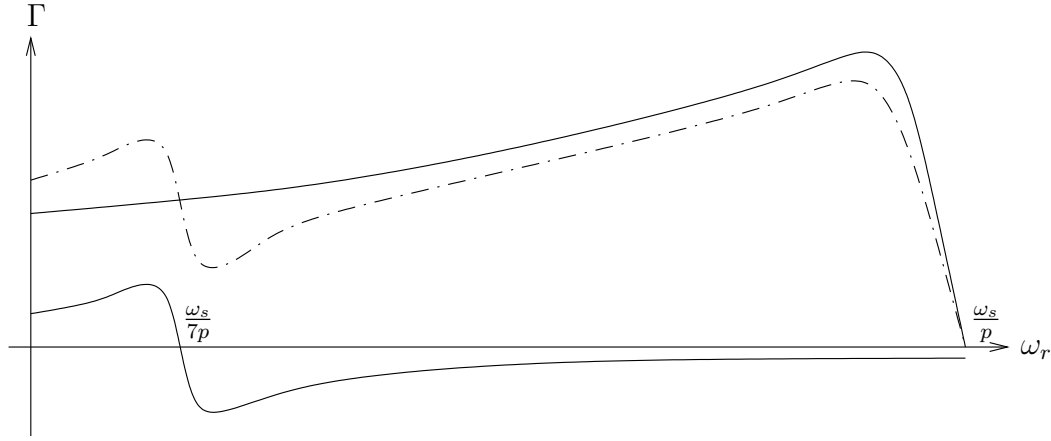


Figure 2.11: Torque-speed characteristic of an induction motor with asynchronous torque dip.

Another kind of torque arises if stator space harmonics interact with rotor space harmonics resulting from a different stator flux density wave. Consider the following example of a four pole motor with $N_r = 28$ rotor bars: The stator fundamental flux density wave with $\nu_s = p = 2$ pole pairs generates rotor waves with $\nu_r = cN_r + p = \dots, -26, 2, 30, 58, \dots$. Another stator space harmonic of order $13p = 26$ can therefore interfere with the rotor wave with $\nu_r = -26$. Consider the following values:

$$m_s = +26$$

$$m'_r = -26$$

$$\Omega_s = \omega_s$$

$$\Omega'_r = \nu_r \omega_r - \nu_s \omega_r + \omega_s = -26\omega_r - 2\omega_r + \omega_s = -28\omega_r + \omega_s$$

In order to calculate the corresponding torque from equation (2.50), the positive sign must be used to add up the pulsations, because the interacting waves had pole pair numbers with opposed signs. The resulting torque is:

$$\Gamma(t) = -\frac{\pi}{\mu_0} l_m R_0 g_0 B_{m_s, \Omega_s} B'_{m'_r, \Omega'_r} \sin(-28\omega_r t + 2\omega_s t - \varphi_{m'_r, \Omega'_r})$$

Therefore, this example demonstrates that a time-varying torque can arise if flux density wave combinations with different pulsations are considered. Different pulsations are obtained for the same pole pair numbers if the rotor flux density wave has been induced by a stator wave different from the interacting one. The arising torques are similar to those found in synchronous machines because they are constant only for a certain rotor speed; for all other speeds, they are sinusoidally varying with respect to time. Therefore, these torques are designated *synchronous torques* in literature (see [Hel77] and [Ric54]).

2.4 Load Torque Oscillations

Some classes of mechanical faults e.g. gearbox faults, shaft misalignment, load unbalance or bearing faults may generate periodic variations in the load torque

and consequently speed oscillations.

Thomson mentioned in [Tho94] the potential of stator-current analysis to detect purely mechanical faults. Cases are studied where shaft speed oscillations caused changes in the current spectrum. In the same way, characteristic gearbox frequencies could be detected in the stator current spectrum [Tho03].

Schoen et al. studied the effects of time-varying loads on the stator current using a space phasor model [Sch95a]. It was demonstrated that a periodic load torque at frequency f_c leads to sidebands in the stator current at $f_s \pm f_c$. A method to eliminate these effects in a current-based condition monitoring system was proposed in [Sch97].

An amplitude modulation of the stator current as a consequence of torque oscillations was supposed by Legowski et al. in [Leg96]. Simulation and experimental results confirmed the characteristic sidebands at $f_s \pm f_c$ in the current spectrum.

Salles et. al used a space phasor model of an induction machine and associated transfer functions for the theoretical study of torque oscillations [Sal97] [Sal00]. In consequence, they supposed an amplitude modulation of the stator current. Simulation and experimental results for periodic and non-periodic torque variations were presented [Sal98].

Extensive experimental investigations on stator current based detection of mechanical faults such as misalignment and load unbalance were carried out by Obaid et al. in [Oba00] [Oba03a] [Oba03b] [Oba03c]. The influence of fault severity and varying load levels on stator current frequencies at $f_s \pm f_r$ was studied. The consequences of shaft misalignment on various quantities such as stator current, axial flux and airgap torque were studied in [Cab96]. Kral et al. [Kra04] analyzed the instantaneous motor power for detection of varying levels of eccentricity and load imbalance. This technique requires three voltage and three current transducers, though. Angular fluctuations of the current space vector were used for detection of bearing faults and shaft misalignment in [Ark05].

The following theoretical considerations study the effect of a periodic, time-varying load torque on the airgap flux density and the stator current using the previously presented MMF and permeance wave approach. The theoretical development has been published in a shortened form in [Blö05b] and has been applied to bearing fault related torque oscillations in [Blö04].

2.4.1 Mechanical Speed

An arbitrary periodic load torque variation $\Gamma(t)$ with zero mean can mathematically be described by a Fourier series:

$$\Gamma(t) = \sum_{k=1}^{\infty} \Gamma_k \cos(k\omega_c t) \quad (2.53)$$

where ω_c denotes the fault characteristic pulsation. Without loss of generality, the torque oscillation is supposed to be an even function. As the effects of mechanical faults are often related to the shaft speed ω_r or the angular position θ_r , ω_c may often be equal to ω_r or an integer multiple of ω_r . More generally, depending on the presence of a gearbox in the drive, ω_c can be any rational multiple of ω_r .

In the following, the effect of the periodic torque variation on the mechanical speed and the mechanical rotor position is studied. This involves two integration operations i.e. the amplitudes of higher order terms of the Fourier series with higher frequencies are considerably attenuated. Therefore, only the first term of the variable components Fourier series is accounted for in the following, which is equivalent to considering a sinusoidal load torque variation.

The total load torque Γ_{load} including an average torque Γ_0 and a sinusoidal component of amplitude Γ_c can therefore be expressed as:

$$\Gamma_{load}(t) = \Gamma_0 + \Gamma_c \cos(\omega_c t) \quad (2.54)$$

The following mechanical equation relates the difference between the electromagnetic motor torque $\Gamma_{motor}(t)$ and the load torque $\Gamma_{load}(t)$ to the angular speed ω_r :

$$\begin{aligned} \sum \Gamma(t) &= \Gamma_{motor}(t) - \Gamma_{load}(t) = J \frac{d\omega_r}{dt} \\ \Rightarrow \omega_r(t) &= \frac{1}{J} \int_t [\Gamma_{motor}(\tau) - \Gamma_{load}(\tau)] d\tau \end{aligned} \quad (2.55)$$

where J is the total inertia of the machine and the load. It should be noted that friction torques are neglected.

In steady-state operation without load torque oscillations, the electromagnetic torque provided by the motor Γ_{motor} is equal to the constant load torque $\Gamma_{load} = \Gamma_0$. Since the oscillating term has zero mean, this is also true if the considered periodic load torque variations are present. The angular speed $\omega_r(t)$ therefore expresses as:

$$\begin{aligned} \omega_r(t) &= -\frac{1}{J} \int_{t_0}^t \Gamma_c \cos(\omega_c \tau) d\tau + C \\ &= -\frac{\Gamma_c}{J\omega_c} \sin(\omega_c t) + \omega_{r0} \end{aligned} \quad (2.56)$$

The integration constant is the angular speed in steady state denoted ω_{r0} . The mechanical speed in presence of load torque oscillations consists therefore of a constant component ω_{r0} and an additional sinusoidally varying one.

2.4.2 Rotor MMF

In order to derive the effect of the load torque oscillation on the rotor MMF, the angular rotor position θ_r is first calculated by integration of the angular speed.

$$\theta_r(t) = \int_t \omega_r(\tau) d\tau = \frac{\Gamma_c}{J\omega_c^2} \cos(\omega_c t) + \omega_{r0} t \quad (2.57)$$

The integration constant is assumed to be zero. In contrast to the healthy machine where $\theta_r(t) = \omega_{r0}t$, the angular rotor position consists of an additional oscillating term at the fault characteristic frequency.

The oscillations of the mechanical rotor position θ_r influence the rotor MMF. Considering only the fundamental, the rotor MMF with respect to the rotor reference frame is a wave with p pole pairs and pulsation $s\omega_s$, given by:

$$F_r(\theta', t) = F_r \cos(p\theta' - s\omega_s t - \varphi_r) \quad (2.58)$$

where s denotes the slip. This wave can be expressed in the stationary reference frame using equation (2.25) combined with expression (2.57) which defines the time-varying rotor angular position $\theta_r(t)$ with load torque oscillations. The transformation between the reference frames is therefore defined by:

$$\theta' = \theta - \omega_{r0}t - \frac{\Gamma_c}{J\omega_c^2} \cos(\omega_c t) \quad (2.59)$$

The following relation links slip, supply frequency and mean angular rotor speed:

$$\omega_{r0} = \omega_s \frac{(1-s)}{p} \quad (2.60)$$

Thus, the rotor MMF given in (2.58) is described in the stationary reference frame by:

$$F_r(\theta, t) = F_r \cos(p\theta - \omega_s t - \beta' \cos(\omega_c t) - \varphi_r) \quad (2.61)$$

with:

$$\beta' = p \frac{\Gamma_c}{J\omega_c^2} \quad (2.62)$$

Equation (2.61) clearly shows that the torque oscillation at frequency f_c leads to a phase modulation (PM) of the rotor MMF in the stationary reference frame. This phase modulation is characterized by the introduction of the term $\beta' \cos(\omega_c t)$ in the phase of the MMF wave. The parameter β' is generally called the PM modulation index. In most cases, the modulation index β' will be small ($\beta' \ll 1$) considering reasonable values for J , Γ_c and ω_c .

Until now, only the fundamental rotor MMF wave has been considered. However, the phase modulation also affects higher order space and time harmonics. This can easily be deduced from transforming the general rotor MMF in the rotating reference frame (see equation (2.21)) to the stationary reference frame using expression (2.59). The general expression for the rotor MMF as a consequence of torque and speed oscillations is therefore given by:

$$F_r(\theta, t) = \sum_{\nu_s=-\infty}^{\infty} \sum_{\nu_r=-\infty}^{\infty} \sum_{\mu_s=1}^{\infty} F_{\nu_s, \nu_r, \mu_s} \cos \left[\nu_r \theta - \nu_r \omega_r t - \nu_r \frac{\Gamma_c}{J\omega_c^2} \cos(\omega_c t) - (\pm |_{\mu_s} \mu_s \omega_s t - \nu_s \omega_r t) - \varphi_{\nu_s \nu_r} \right] \quad (2.63)$$

The fault has no direct effect on the stator MMF if higher order armature reactions are neglected. Therefore, considering only the fundamental, the stator MMF takes the following form:

$$F_s(\theta, t) = F_s \cos(p\theta - \omega_s t) \quad (2.64)$$

The general expression for the stator MMF waves taking into account various harmonics is given in equation (2.38).

2.4.3 Airgap Flux Density

The airgap flux density $B(\theta, t)$ is the product of the sum of stator and rotor MMF waves and the airgap permeance Λ . If slotting effects and iron saturation are neglected in a first time, the airgap permeance is supposed constant. Then, the airgap flux density takes the following expression:

$$\begin{aligned} B(\theta, t) &= [F_s(\theta, t) + F_r(\theta, t)] \Lambda_0 \\ &= B_s \cos(p\theta - \omega_s t) + B_r \cos(p\theta - \omega_s t - \beta' \cos(\omega_c t) - \varphi_r) \end{aligned} \quad (2.65)$$

The fundamental airgap flux density is therefore a sum of two components: The component resulting from the rotor MMF is modulated with a sinusoidal phase modulation at the fault characteristic frequency f_c , the stator MMF related component is unchanged.

The general expression for the airgap flux density waves taking into account higher order space and time harmonics, slotting and saturation is identical to (2.41). Only the last equation (2.41d), defining the pulsation Ω_r of the rotor flux density waves, has to be replaced by:

$$\Omega_{r,to} = \nu_r \omega_r - \nu_s \omega_r - \frac{d}{dt} \left(\nu_r \frac{\Gamma_c}{J \omega_c^2} \cos(\omega_c t) \right) \pm |\mu_s \mu_s \omega_s \pm n_{rt} N_r \omega_r \pm 2n_{sa} \omega_s| \quad (2.66)$$

where the index in $\Omega_{r,to}$ denotes the case with load torque oscillations.

2.4.4 Stator Current

The phase modulation of the flux density $B(\theta, t)$ exists for the coil flux $\Phi_i(t)$ itself, as $\Phi_i(t)$ is obtained by simple integration of $B(\theta, t)$ (see 2.3.4). The existence of an additional time-varying term in the phase of a flux density wave does not change the result of the integration of $B(\theta, t)$ with respect to the circumference angle θ .

Therefore, considering only the fundamental flux density waves according to (2.65), the flux $\Phi(t)$ in an arbitrary coil can be expressed in a general form:

$$\Phi(t) = \Phi_s \cos(\omega_s t - \varphi_{\Phi,s}) + \Phi_r \cos(\omega_s t + \beta' \cos(\omega_c t) - \varphi_{\Phi,r}) \quad (2.67)$$

The induced voltage $V_i(t)$ corresponding to this flux is:

$$\begin{aligned} V_i(t) &= \frac{d}{dt} \Phi(t) = -\omega_s \Phi_s \sin(\omega_s t - \varphi_{\Phi,s}) - \omega_s \Phi_r \sin(\omega_s t + \beta' \cos(\omega_c t) - \varphi_{\Phi,r}) \\ &\quad + \omega_c \beta' \sin(\omega_c t) \Phi_r \sin(\omega_s t + \beta' \cos(\omega_c t) - \varphi_{\Phi,r}) \end{aligned} \quad (2.68)$$

Since relatively small torque oscillation are studied, $\beta' \ll 1$. The last term can thus be neglected in the following considerations. The total induced voltage is the sum of the induced voltages in all coils of the winding. The resulting signal is also a PM signal with the same modulation index as demonstrated in appendix A.1.

With the stator voltage imposed by the voltage source, the resulting stator current is linearly related to the induced voltage $V_i(t)$ and has the same frequency

content. As a consequence, the phase-modulated stator current $i_{to}(t)$ for an arbitrary phase in presence of a load torque oscillation expresses as :

$$\begin{aligned} i_{to}(t) &= i_{st}(t) + i_{rt}(t) \\ &= I_{st} \sin(\omega_s t) + I_{rt} \sin(\omega_s t + \beta \cos(\omega_c t - \varphi_\beta) - \varphi_r) \end{aligned} \quad (2.69)$$

where φ_β denotes the phase angle of the modulation. The modulation index β is proportional to β' :

$$\beta \propto \beta' = p \frac{\Gamma_c}{J\omega_c^2} \quad (2.70)$$

The fundamental stator current $i_{to}(t)$ can be considered as the sum of two components: the term $i_{st}(t)$ results from the stator MMF and it is not modulated. The term $i_{rt}(t)$, which is a direct consequence of the rotor MMF, shows the phase modulation due to the considered load torque and speed oscillations.

According to the preceding calculations the PM modulation index of the rotor-related stator current component could be assumed equal to the modulation index of the rotor MMF. However, considering the simplifying assumptions of the modelling approach such as linearity of the magnetic circuit, neglect of higher order armature reactions etc., a proportional relationship is a more cautious modeling hypothesis. The healthy operation state without a load torque oscillation is obtained for $\beta=0$.

The generalized expression of the stator current including time harmonics, rotor slot effects and the phase modulation due to torque oscillations has the following form:

$$\begin{aligned} i_{to}(t) &= \sum_{\mu_s, n_{rt}, i} I_{st, \mu_s, n_{rt}, i} \sin[\mu_s \omega_s t \pm n_{rt} N_r \omega_r t] \\ &\quad + \sum_{\mu_s, n_{rt}, i} I_{rt, \mu_s, n_{rt}, i} \sin[\mu_s \omega_s t \pm n_{rt} N_r \omega_r t + \beta_i \cos(\omega_c t - \varphi_{\beta, i}) - \varphi_{r, i}] \end{aligned} \quad (2.71)$$

with

$$\beta_i \propto \frac{\Gamma_c}{J\omega_c^2} \quad (2.72)$$

This expression shows that the phase modulation affects not only the fundamental component but also stator current components at other frequencies such as time harmonics and rotor slot harmonics.

2.5 Airgap Eccentricity

The preceding section has considered periodic load torque variations and speed oscillations as a consequence of mechanical faults. In addition, mechanical faults may also lead to a displacement of the rotor center with respect to the stator i.e. rotor eccentricity. The consequence is a non-uniform airgap and therefore a change in the normal airgap flux density distribution. Consequently, quantities which are functions of the airgap flux density also change:

- Unbalanced magnetic pull is created i.e. a radial force that tends to further increase the rotor eccentricity. In fact, the unbalanced magnetic pull is in the direction of the smallest airgap because the flux density is highest in these regions.
- The altered airgap flux density distribution and the unbalanced magnetic pull intensify stator frame vibrations and noise.
- Particular frequencies in the stator current spectrum appear or show an increase.
- The average and oscillating components of the electromagnetic output torque change.

Airgap eccentricity and unbalanced magnetic pull in induction machines have been studied since the beginning of the 20th century. Hence, numerous publications deal with this topic and they cannot all be cited or reviewed in this work. Literature reviews can be found e.g. in [Cam86] [Dor93].

Heller and Hamata [Hel77] calculate the airgap magnetic field with an eccentric rotor. Dorrell [Dor93] models unbalanced magnetic pull in cage induction machines using two approaches, conformal transformations and the permeance wave approach. The resulting numerical model is validated with different machines. Ellison and Yang [Ell71] [Yan81], Cameron et al. [Cam86] and Timár [Tim89] study the effects of eccentricity on the airgap flux density, stator frame vibrations and acoustic noise. The detection of eccentricity by stator current spectrum analysis is considered in numerous publications, amongst others [Cam86] [Dor97] [Nan01] [Gul03]. The stator current components showing an increase with eccentricity are often written in a compact form as:

$$f_{ecc} = (n_{rt}N_r \pm i_{ecc,dy}) f_r \pm \mu_s f_s \quad (2.73)$$

This formula shows that dynamic eccentricity ($i_{ecc,dy} \geq 1$) should lead to sidebands of the stator current fundamental frequency, but also of its harmonics and the rotor slot harmonics ($n_{rt} \geq 1$). Static eccentricity does theoretically not produce additional frequencies but experimental investigations have shown an increase of slot harmonic amplitudes [Cam86]. Different degrees of static and dynamic eccentricity and their influence on stator current sidebands are investigated in [Dor97] [Kni05]. Industrial case histories investigating machines with eccentricity are reported by Thomson et al. in [Tho88] [Tho99c] [Tho99a] [Tho99b].

Relatively few works study the influence of eccentricity on the output torque of the motor. Kučera [Kuč70] calculated the changed mutual reactances with an eccentric rotor and derived a higher average torque in this case. Abdel-Kader [AK84] notices through simulations that an increasing level of eccentricity causes a slight rise in the average torque and a decrease in cogging torques. However, Dorrell [Dor94] found that the steady torque decreases with a rising level of eccentricity. He also stated that pulsating torques increase considerably. Rusek [Rus96] simulated induction motors with static and dynamic eccentricity and remarked increasing pulsating torques at the rotor rotational frequency compared to the healthy state.

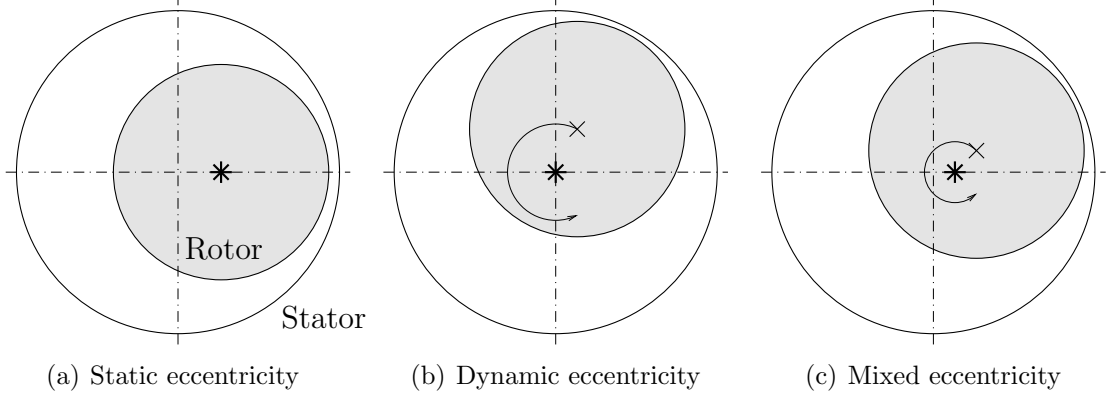


Figure 2.12: Schematic representation of static, dynamic and mixed eccentricity. \times denotes the rotor geometrical center, $*$ the rotor rotational center.

In all the cited works, the pulsating torques are only observed on simulation results and no analytical explanation or demonstration is given.

Generally, three different types of eccentricity can be distinguished (see Fig. 2.12):

Static eccentricity: The rotor geometrical center is identical with the rotational center, but it is displaced with respect to the stator geometrical center. The point of minimal airgap length is stationary with respect to the stator.

Dynamic eccentricity: The rotor geometrical center is different from the rotational center. The rotational center is identical with the stator geometrical center. The point of minimal airgap length is moving with respect to the stator.

Mixed eccentricity: The two effects are combined. The rotor geometrical center, rotor rotational center and stator geometrical center are different. The point of minimal airgap length is also moving with respect to the stator.

Static eccentricity is caused when the rotor axis is not aligned within the stator. Reasons can be manufacturing tolerances, an oval stator core, incorrect bearing positioning or bearing wear. Dynamic eccentricity can also be caused by manufacturing tolerances and bearing wear or furthermore by a bent or flexible shaft. It is also possible that high levels of static eccentricity produce high unbalanced magnetic pull which consequently increases the dynamic eccentricity. The risk of high levels of static or dynamic eccentricity is a mechanical contact between the rotor and the stator resulting in considerable damage for the machine [Ver82] [Cam86] [Dor93].

2.5.1 Airgap Length

The following calculations derive the expression of the airgap length $g(\theta)$ in case of an eccentric rotor [Gul03] [Dor93]. The geometric configuration for a general rotor displacement and the corresponding nomenclature are displayed in Fig. 2.13.

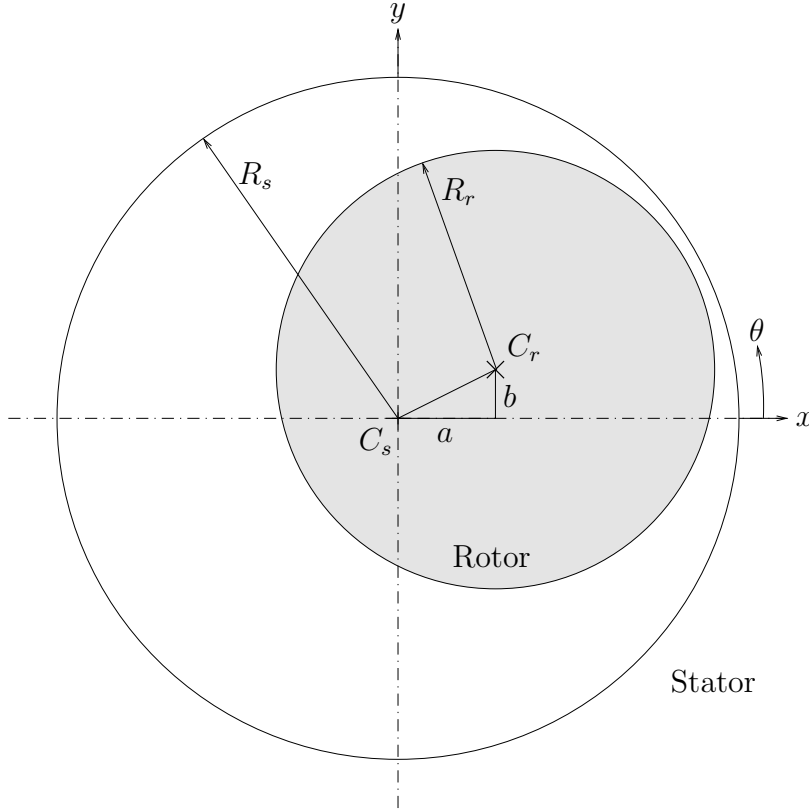


Figure 2.13: General case of rotor displacement and nomenclature.

Note that the following considerations suppose a uniform airgap length in axial direction which allows a two-dimensional problem description analogous to the preceding calculations of the airgap field. However, this simplifying assumption is probably not verified in most practical cases.

The stator inner surface $r_s(\theta)$ with radius R_s is given by the following equation in polar coordinates (r, θ) :

$$r_s(\theta) = R_s \quad (2.74)$$

If the rotor center C_r is at (a, b) in cartesian coordinates, the rotor outer surface is given in cartesian coordinates (x, y) by the circle equation:

$$(x - a)^2 + (y - b)^2 = R_r^2 \quad (2.75)$$

With $x = r_r \cos \theta$ and $y = r_r \sin \theta$, equation (2.75) is transformed into polar coordinates (r_r, θ) . A quadratic equation is obtained for the radius $r_r(\theta)$ of the rotor outer surface. The solution of this equation is:

$$r_r(\theta) = a \cos \theta + b \sin \theta + \sqrt{R_r^2 - (a \sin \theta + b \cos \theta)^2} \quad (2.76)$$

The exact expression of the airgap length $g(\theta)$ is:

$$\begin{aligned} g(\theta) &= r_s(\theta) - r_r(\theta) \\ &= R_s - a \cos \theta - b \sin \theta - R_r \sqrt{1 - \frac{1}{R_r^2} (a \sin \theta + b \cos \theta)^2} \end{aligned} \quad (2.77)$$

In induction machines, the airgap is in general relatively small compared to the rotor radius R_r . Therefore, the rotor displacement described by a and b is also small compared to R_r , and $g(\theta)$ is commonly approximated by:

$$g(\theta) = g_0 - a \cos \theta - b \sin \theta \quad (2.78)$$

where $g_0 = R_s - R_r$ is the mean airgap length without eccentricity.

The parameters a and b in the expression of the airgap length take different expressions with respect to the type of eccentricity. δ_s and δ_d denote respectively the degree of static and dynamic eccentricity with respect to the mean airgap length g_0 . Note that $\delta_s + \delta_d < 1$ in order to avoid a rotor-stator rub.

Static eccentricity: a and b do not depend on the rotor angle θ_r . Without loss of generality, $b = 0$ can be supposed.

$$a = g_0 \delta_s, \quad b = 0 \quad (2.79)$$

Dynamic eccentricity: a and b depend both on the rotor angle θ_r , no constant term is present.

$$a = g_0 \delta_d \cos \theta_r, \quad b = g_0 \delta_d \sin \theta_r \quad (2.80)$$

Mixed eccentricity: a and b depend both on the rotor angle θ_r and a constant term is present. Without loss of generality, the constant term in b can be supposed zero.

$$a = g_0 (\delta_s + \delta_d \cos \theta_r), \quad b = g_0 \delta_d \sin \theta_r \quad (2.81)$$

The exact and approximated expression of the airgap length in case of mixed eccentricity are:

$$\begin{aligned} g(\theta) &= R_s - g_0 (\delta_s \cos \theta - \delta_d \cos (\theta - \theta_r)) \\ &\quad - R_r \sqrt{1 - \frac{g_0^2}{R_r^2} (\delta_s \sin \theta + \delta_d \sin (\theta + \theta_r))^2} \quad (2.82) \\ g(\theta) &\approx g_0 (1 - \delta_s \cos \theta - \delta_d \cos (\theta - \theta_r)) \quad \text{for } g_0 \ll R_r \end{aligned}$$

Note that static and dynamic eccentricity are special cases with $\delta_d = 0$ or $\delta_s = 0$ respectively.

2.5.2 Airgap Permeance

Similar to the reflections in 2.3.2, the airgap permeance accounting for rotor eccentricity is expressed as a Fourier series. Considering in a first time only static eccentricity, the approximated airgap length according to (2.82) is :

$$g(\theta) = g_0 (1 - \delta_s \cos \theta) \quad (2.83)$$

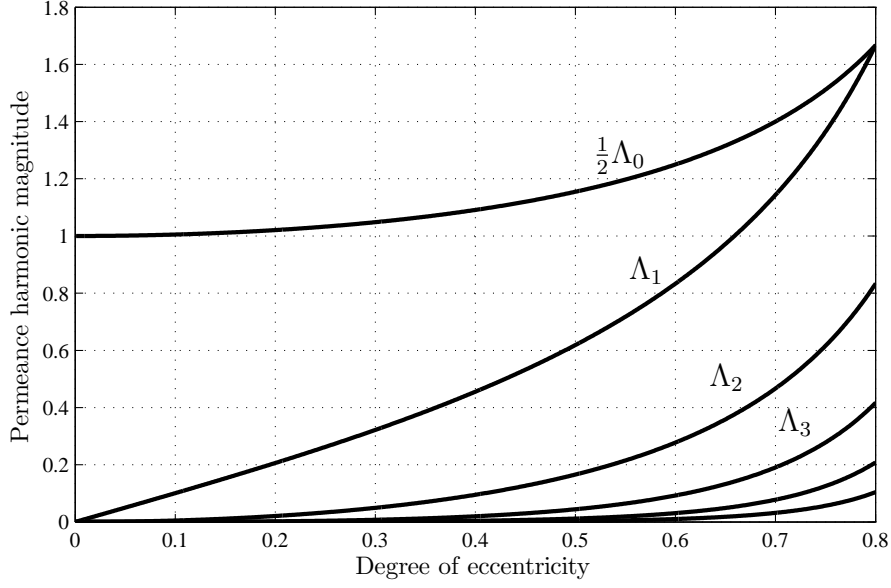


Figure 2.14: Normalized permeance harmonic magnitudes with respect to degree of eccentricity.

The corresponding airgap permeance is proportional to the inverse of this expression and it can be developed into a Fourier series [Dor93]:

$$\Lambda_{ecc,st}(\theta) = \frac{\mu_0}{g_0(1 - \delta_s \cos \theta)} = \frac{1}{2}\Lambda_0 + \sum_{i_{ecc,st}=1}^{\infty} \Lambda_{i_{ecc,st}} \cos(i_{ecc,st}\theta) \quad (2.84)$$

with

$$\Lambda_{i_{ecc,st}} = \frac{2\mu_0}{g_0\sqrt{1 - \delta_s^2}} \left[\frac{1 - \sqrt{1 - \delta_s^2}}{\delta_s} \right]^{i_{ecc,st}} \quad (2.85)$$

The magnitudes of the Fourier series coefficients are shown in Fig. 2.14 with respect to the degree of eccentricity δ_s . It can be noticed that for small levels of eccentricity ($\delta_s < 40\%$), the coefficients Λ_k with $k \geq 2$ are relatively small. Therefore, they will be neglected in some of the following considerations.

When only dynamic eccentricity is present, the permeance varies also with respect to time. The angle θ in equation (2.84) is simply replaced by $(\theta - \omega_r t)$ and the following expression is obtained:

$$\Lambda_{ecc,dy}(\theta, t) = \frac{1}{2}\Lambda_0 + \sum_{i_{ecc,dy}=1}^{\infty} \Lambda_{i_{ecc,dy}} \cos(i_{ecc,dy}\theta - i_{ecc,dy}\omega_r t) \quad (2.86)$$

In case of mixed eccentricity, the permeance expressions with static and dynamic eccentricity are combined and yield [Yan81]:

$$\Lambda(\theta, t) = \sum_{i_{ecc,st}=0}^{\infty} \sum_{i_{ecc,dy}=0}^{\infty} \Lambda_{i_{ecc,st}, i_{ecc,dy}} \cos((i_{ecc,st} + i_{ecc,dy})\theta - i_{ecc,dy}\omega_r t) \quad (2.87)$$

2.5.3 Airgap Flux Density

For the calculation of the magnetic flux density, only the fundamental rotor and stator MMF waves will be considered at first. Supposing relatively small levels of eccentricity, the airgap permeance is approximated by the constant component and the first harmonic of the Fourier series expansion. With these assumptions, the fundamental airgap flux density in presence of static eccentricity is:

$$\begin{aligned}
 B(\theta, t) &= [F_s(\theta, t) + F_r(\theta, t)] \left[\frac{1}{2} \Lambda_0 + \Lambda_1 \cos \theta \right] \\
 &= B_s \left[1 + 2 \frac{\Lambda_1}{\Lambda_0} \cos \theta \right] \cos(p\theta - \omega_s t) \\
 &\quad + B_r \left[1 + 2 \frac{\Lambda_1}{\Lambda_0} \cos \theta \right] \cos(p\theta - \omega_s t - \varphi_r) \\
 &= B_s \cos(p\theta - \omega_s t) + 2B_s \frac{\Lambda_1}{\Lambda_0} \cos((p \pm 1)\theta - \omega_s t) \\
 &\quad + B_r \cos(p\theta - \omega_s t - \varphi_r) + 2B_r \frac{\Lambda_1}{\Lambda_0} \cos((p \pm 1)\theta - \omega_s t - \varphi_r)
 \end{aligned} \tag{2.88}$$

The multiplication of the MMF waves with the modified airgap permeance modulates the amplitude of the flux density waves with respect to θ and leads to new waves having $p \pm 1$ pole pairs. However, these waves have the same pulsation as the fundamental wave which means that no additional pulsations appear.

The relative amplitude of the additional waves with respect to the fundamental flux density is $2\Lambda_1/\Lambda_0$. Using expression (2.85) and a limited series development of $\sqrt{1 - \delta_s^2}$ [Bro99], the following approximation is obtained for small δ_s :

$$2 \frac{\Lambda_1}{\Lambda_0} = 2 \frac{1 - \sqrt{1 - \delta_s^2}}{\delta_s} = \frac{2}{\delta_s} \left[1 - \left(1 - \frac{1}{2} \delta_s^2 - \frac{1}{8} \delta_s^4 - \dots \right) \right] \approx \delta_s \tag{2.89}$$

The relative amplitude of the additional flux density waves is therefore directly the degree of eccentricity.

The calculation of the fundamental flux density waves in presence of dynamic eccentricity yields:

$$\begin{aligned}
 B(\theta, t) &= [F_s(\theta, t) + F_r(\theta, t)] \left[\frac{1}{2} \Lambda_0 + \Lambda_1 \cos(\theta - \omega_r t) \right] \\
 &= B_s [1 + \delta_d \cos(\theta - \omega_r t)] \cos(p\theta - \omega_s t) \\
 &\quad + B_r [1 + \delta_d \cos(\theta - \omega_r t)] \cos(p\theta - \omega_s t - \varphi_r) \\
 &= B_s \cos(p\theta - \omega_s t) + \delta_d B_s \cos((p \pm 1)\theta - (\omega_s \pm \omega_r)t) \\
 &\quad + B_r \cos(p\theta - \omega_s t - \varphi_r) + \delta_d B_r \cos((p \pm 1)\theta - (\omega_s \pm \omega_r)t - \varphi_r)
 \end{aligned} \tag{2.90}$$

In contrast to the case with static eccentricity, the flux density is amplitude modulated with respect to time and θ . The resulting additional flux density waves have pulsations $\omega_s \pm \omega_r$ which means that additional pulsations appear around the fundamental.

If a two-pole motor ($p = 1$) is considered, one of the additional flux density waves has zero pole pairs i.e. it is equivalent to a homopolar flux. The main path of this homopolar flux is from the rotor via the shaft, the bearings and the stator frame back to the stator and the airgap. The permeance corresponding to this path is dependent on the particular machine and its construction [Dor93]. As the detailed analysis of these phenomena goes beyond the scope of this work, a motor with $p > 1$ will be supposed in the following.

The complete expressions for the airgap flux density in the general case are obtained by multiplication of the stator and rotor MMF waves according to (2.38) and (2.39) with the permeance function that includes slotting, saturation and eccentricity (see (2.36) and (2.87)). The following pole pair numbers and pulsations are obtained for the stator and rotor-related flux density waves including the effects of eccentricity [Cam86]:

$$m_s = \nu_s \pm n_{st}N_s \pm n_{rt}N_r \pm 2pn_{sa} \pm i_{ecc,st} \pm i_{ecc,dy} \quad (2.91a)$$

$$\Omega_s = \pm |_{\mu_s} \mu_s \omega_s \pm n_{rt}N_r \omega_r \pm 2n_{sa}\omega_s \pm i_{ecc,dy}\omega_r \quad (2.91b)$$

$$m_r = \nu_r \pm n_{st}N_s \pm n_{rt}N_r \pm 2pn_{sa} \pm i_{ecc,st} \pm i_{ecc,dy} \quad (2.91c)$$

$$\Omega_r = \nu_r \omega_r - \nu_s \omega_r \pm |_{\mu_s} \mu_s \omega_s \pm n_{rt}N_r \omega_r \pm 2n_{sa}\omega_s \pm i_{ecc,dy}\omega_r \quad (2.91d)$$

2.5.4 Stator Current

The stator current in case of an eccentric rotor is calculated similar to the preceding considerations in 2.3.4. First, the time-variable flux in a phase of the stator winding is determined. The flux calculation is different from the development in case of the healthy machine 2.3.4 or with a load torque oscillation, because the amplitude modulation is a function varying with respect to the circumference angle θ and with respect to time in the general case. The flux calculation by integration of the flux density waves yields therefore a different result as it will be demonstrated in the following.

Consider a general amplitude-modulated flux density wave $B_i(\theta, t)$ in case of dynamic eccentricity:

$$B_i(\theta, t) = B_i [1 + \delta_d \cos(\theta - \omega_r t)] \cos(m_i \theta - \Omega_i t - \varphi_i) \quad (2.92)$$

The special case of static eccentricity can be obtained with $\omega_r = 0$ and $\delta_d = \delta_s$. As in 2.3.4, the corresponding flux Φ_i through a stator coil formed by two conductors at angular positions θ_1 and θ_2 is calculated:

$$\begin{aligned} \Phi_i(t) &= l_m R_s \int_{\theta_1}^{\theta_2} B_i(\theta, t) d\theta \\ &= l_m R_s \int_{\theta_1}^{\theta_2} B_i \left\{ \cos(m_i \theta - \Omega_i t - \varphi_i) + \frac{1}{2} \delta_d \cos((m_i - 1)\theta - \Omega_i t + \omega_r t - \varphi_i) \right. \\ &\quad \left. + \frac{1}{2} \delta_d \cos((m_i + 1)\theta - \Omega_i t - \omega_r t - \varphi_i) \right\} d\theta \end{aligned} \quad (2.93)$$

After integration and simplifications using $\sin \alpha - \sin \beta = 2 \cos \frac{\alpha+\beta}{2} \sin \frac{\alpha-\beta}{2}$:

$$\begin{aligned} \Phi_i(t) = l_m R_s B_i & \left\{ \frac{2}{m_i} \sin \left(m_i \frac{\theta_p}{2} \right) \cos \left(m_i \frac{\theta_1 + \theta_2}{2} - \Omega_i t - \varphi_i \right) \right. \\ & + \frac{\delta_d}{m_i - 1} \sin \left((m_i - 1) \frac{\theta_p}{2} \right) \cos \left((m_i - 1) \frac{\theta_1 + \theta_2}{2} - \Omega_i t + \omega_r t - \varphi_i \right) \\ & \left. + \frac{\delta_d}{m_i + 1} \sin \left((m_i + 1) \frac{\theta_p}{2} \right) \cos \left((m_i + 1) \frac{\theta_1 + \theta_2}{2} - \Omega_i t - \omega_r t - \varphi_i \right) \right\} \end{aligned} \quad (2.94)$$

In order to visualize the amplitude modulation of the flux, similar terms are rearranged using $\cos(\alpha + \beta) = \cos \alpha \cos \beta - \sin \alpha \sin \beta$:

$$\begin{aligned} \Phi_i(t) = l_m R_s B_i & \cos \left(m_i \frac{\theta_1 + \theta_2}{2} - \Omega_i t - \varphi_i \right) \\ & \left[\frac{2}{m_i} \sin \left(m_i \frac{\theta_p}{2} \right) + (C_1 + C_2) \cos \left(\omega_r t - \frac{\theta_1 + \theta_2}{2} \right) \right] \\ & + l_m R_s B_i (C_2 - C_1) \sin \left(m_i \frac{\theta_1 + \theta_2}{2} - \Omega_i t - \varphi_i \right) \sin \left(\omega_r t - \frac{\theta_1 + \theta_2}{2} \right) \end{aligned} \quad (2.95)$$

where C_1 and C_2 are constant terms defined as:

$$C_1 = \frac{\delta_d}{m_i - 1} \sin \left((m_i - 1) \frac{\theta_p}{2} \right) \quad (2.96)$$

$$C_2 = \frac{\delta_d}{m_i + 1} \sin \left((m_i + 1) \frac{\theta_p}{2} \right) \quad (2.97)$$

Equation (2.95) shows that the flux is the sum of two amplitude modulated components: The first term is a carrier frequency at Ω_i modulated by a constant component plus a time-varying term at ω_r . This type of amplitude modulation (AM) is denoted double-sideband AM with residual carrier [Tre01]. The second term is a carrier in quadrature to the first carrier, modulated by a component in quadrature to the first modulation term. As the modulation term contains no constant component, the carrier frequency is not present. This type of AM is called double-sideband suppressed-carrier AM. The terms $C_1 + C_2$ and $C_2 - C_1$ are proportional to the modulation indices of the two signals and they depend on the relative degree of eccentricity. Therefore, an increasing eccentricity leads to a higher modulation index. It can also be seen that static eccentricity ($\omega_r = 0$) provokes no modulation of the flux at all because the amplitudes of the two carriers are constant in this case.

The induced voltage $V_i(t)$ in the coil is obtained by differentiating equation

(2.95) with respect to time:

$$\begin{aligned}
 V_i(t) = l_m R_s B_i \sin(\varphi'_i - \Omega_i t) & \left\{ \frac{2}{m_i} \Omega_i \sin\left(m_i \frac{\theta_p}{2}\right) \right. \\
 & \left. + \left[\Omega_i (C_1 + C_2) + \omega_r (C_2 - C_1) \right] \cos\left(\omega_r t - \frac{\theta_1 + \theta_2}{2}\right) \right\} \\
 - l_m R_s B_i \cos(\varphi'_i - \Omega_i t) & \left[\Omega_i (C_2 - C_1) + \omega_r (C_1 + C_2) \right] \sin\left(\omega_r t - \frac{\theta_1 + \theta_2}{2}\right)
 \end{aligned} \tag{2.98}$$

with

$$\varphi'_i = m_i \frac{\theta_1 + \theta_2}{2} - \varphi_i \tag{2.99}$$

Thus, the induced voltage is also the sum of two amplitude modulated signals, similar to the phase flux.

Suitable simplifications for the modulation indices can be found by rewriting $C_1 + C_2$ and $C_2 - C_1$ using $\sin(\alpha + \beta) = \sin \alpha \cos \beta + \sin \beta \cos \alpha$:

$$C_1 + C_2 = \frac{2\delta_d}{m_i^2 - 1} [m_i \sin(m_i \theta_m) \cos \theta_m - \cos(m_i \theta_m) \sin \theta_m] \tag{2.100}$$

$$C_2 - C_1 = \frac{2\delta_d}{m_i^2 - 1} [m_i \cos(m_i \theta_m) \sin \theta_m - \sin(m_i \theta_m) \cos \theta_m] \tag{2.101}$$

where θ_m denotes half the coil pitch: $\theta_m = \theta_p/2$. The pole pair numbers of the flux density waves are $m_i = kp$. The strongest flux density waves are those with $k = 1, 5, 7, 11, \dots$ and $k = N_r/p \pm 1$ for the slot harmonics. In any case, waves with k being even or a multiple of 3 do not exist theoretically. A phase winding, even if it is fractional pitch, can be considered as a sum of full pitch coils with $\theta_p = \pi/p$ [Kos69, p.113]. The angle θ_m is therefore $\theta_m = \pi/2p$. Under these assumptions:

$$\sin(m_i \theta_m) = \sin\left(k \frac{\pi}{2}\right) = \pm 1 \tag{2.102}$$

$$\cos(m_i \theta_m) = \cos\left(k \frac{\pi}{2}\right) = 0 \tag{2.103}$$

and consequently:

$$|C_1 + C_2| = m_i \frac{2\delta_d}{m_i^2 - 1} \cos\left(\frac{\pi}{2p}\right) \tag{2.104}$$

$$|C_2 - C_1| = \frac{2\delta_d}{m_i^2 - 1} \cos\left(\frac{\pi}{2p}\right) \tag{2.105}$$

Since $p > 1$ has been supposed (see 2.5.3), it is true that:

$$|C_1 + C_2| \geq 2 |C_2 - C_1| \tag{2.106}$$

The equality is obtained for $m_i = 2$ i.e. the fundamental flux density wave of a motor with $p = 2$. Hence, the modulation index of the first term in (2.95)

with the residual carrier is always greater than the one of the second term with suppressed carrier, especially if higher order space harmonics or higher pole motors are considered. The same considerations are true for the induced voltage $V_i(t)$ from equation (2.98) because $\Omega_i \geq 2\omega_r$ since $p > 1$. In the following, the term with suppressed carrier is assumed of significantly smaller modulation index compared to the term with residual carrier. Consequently, it will be neglected in some cases for the sake of clarity and simplicity.

The total induced voltage in the phase winding is obtained by superposition of the coil voltages. It can be demonstrated that the sum of several amplitude modulated coil voltages is also an amplitude modulated signal (see appendix A.2).

The resulting stator current $i_{de}(t)$ is a linear function of the induced voltage and is written in a general form as the sum of two amplitude modulated components in quadrature:

$$i_{de}(t) = \sum_i I_i [1 + \alpha_{1,i} \cos(\omega_r t - \varphi_1)] \cos \Omega_i t + \alpha_{2,i} \sin(\omega_r t - \varphi_1) \sin \Omega_i t \quad (2.107)$$

Initial phase angles have been supposed zero. The amplitude modulation indices $\alpha_{1,i}$ and $\alpha_{2,i}$ are directly proportional to the degree of dynamic eccentricity δ_d . The modulation index $\alpha_{2,i}$ of the second term without residual carrier is significantly smaller than $\alpha_{1,i}$.

Naturally, the effect of the amplitude modulation will be most significant on the strongest current components. These are the fundamental supply frequency f_s and in some cases the rotor slot harmonics at $n_{rt}N_r f_r \pm f_s$. A simplified stator current model for an induction motor with eccentricity taking into account only the fundamental current component is therefore given by:

$$i_{de}(t) = I_1 [1 + \alpha_1 \cos(\omega_r t - \varphi_1)] \cos \omega_s t \quad (2.108)$$

where I_1 is the fundamental stator current amplitude. Note that the amplitude modulated component without carrier is neglected in this simplified expression.

2.5.5 Torque

This section attempts to explain theoretically how eccentricity leads to an increase of oscillating components at f_r in the output torque of the induction motor. This has been observed through numerical simulations of induction machines with static eccentricity in [Dor94] and both types of eccentricity in [Rus96]. However, a theoretical demonstration in literature is not known to the author.

According to the considerations in 2.2.4, torque is produced by the interaction of stator and rotor flux density waves with the derivatives of the rotor flux density waves. The interacting waves must have equal pole pair numbers; if not, the resulting torque is zero.

In the following, only the fundamental flux density waves without any higher order armature reactions are considered. Static eccentricity leads to additional flux density waves with $p \pm 1$ pole pairs and pulsation ω_s equal to the fundamental pulsation. Due to their pole pair number, the interaction of these additional waves

with the fundamental does not produce any torque. Torque can be produced if e.g. a stator-related wave with $p \pm 1$ pole pairs (see (2.88)) interacts with the corresponding rotor-related wave with the same pole pair number. However, as both waves have the same pulsation, the resulting torque is independent of time and thus contributes to the average torque. This is identical to the asynchronous torques discussed in 2.3.5. Rusek [Rus96] also observed no significant changes in pulsating torques with static eccentricity.

In the case of dynamic eccentricity, the situation is similar to static eccentricity. The only possible interactions that may produce torque takes place between additional $p \pm 1$ pole pair stator-related waves and the corresponding rotor-related waves (see (2.90)). In contrast to the static eccentricity, these waves have pulsations $\omega_s \pm \omega_r$. However, the waves with equal pole pair numbers have always the same pulsation and the resulting torque is therefore independent of time. Nevertheless, numerical simulations show an increasing oscillating torque at shaft rotational frequency f_r in [Rus96]. Therefore, it can be concluded that the simplified theory developed in the preceding sections cannot provide an explanation.

Oscillating torques coming along with mixed eccentricity can however be explained, in contrast to static or dynamic eccentricity only. Mixed eccentricity leads simultaneously to additional $p \pm 1$ flux density waves with pulsations ω_s and $\omega_s \pm \omega_r$. Having equal pole pair numbers but different pulsations they necessarily produce a time-varying torque. For illustration, consider the following example with stator-related flux density waves resulting from static eccentricity (see (2.88)) which are of the following form:

$$B_s(\theta, t) = \delta_s B_s \cos [(p \pm 1) \theta - \omega_s t] \quad (2.109)$$

These waves interact with rotor-related waves resulting from dynamic eccentricity that can be written as (see (2.90)):

$$B_r(\theta, t) = \delta_d B_r \cos [(p \pm 1) \theta - (\omega_s \pm \omega_r) t - \varphi_r] \quad (2.110)$$

According to equation (2.50), the resulting torque Γ_i from this particular interaction will be:

$$\Gamma_i = -\frac{\pi l_m R_0 g_0}{\mu_0} \delta_s \delta_d B_s B_r' \sin (\mp \omega_r t - \varphi_r) \quad (2.111)$$

The resulting torque is therefore pulsating at ω_r and its amplitude is proportional to the product of the degrees of static and dynamic eccentricity. The torque producing mechanisms correspond to those of synchronous torques. Other possible interactions in the case of mixed eccentricity include:

- Stator-related flux density waves resulting from dynamic eccentricity interact with rotor-related waves resulting from static eccentricity
- Interactions of rotor-related waves with the derivative of other rotor-related waves according to the second term in equation (2.50). One of the interacting waves must result from static eccentricity, the other from dynamic eccentricity.

These interactions also produce pulsating torques at ω_r .

From a practical point of view, every electrical machine has an inherent level of mixed eccentricity due to manufacturing tolerances. Pure static or dynamic eccentricity is not very likely to be found in reality. The considered mechanism for pulsating torque generation can be supposed in nearly all cases. However, it does not explain the pulsating torques that can be found in numerical simulations with dynamic eccentricity only. This requires the consideration of higher order armature reactions in the MMF and permeance wave approach.

Until now, it has been supposed that the fundamental stator and rotor MMFs combined with the modified airgap permeance produce additional flux density waves. These flux density waves may induce currents at non supply frequencies in the stator windings. They may produce oscillating torques in the case of mixed eccentricity. However, these additional currents flowing in the stator windings also give rise to other MMF waves and consequently new corresponding flux density waves. These higher order armature reactions have been neglected up to now, but they can explain the pulsating torques in case of dynamic eccentricity.

The amplitude-modulated stator current in case of dynamic eccentricity (see equation (2.108)) can be rewritten and interpreted as the sum of the fundamental pulsation at ω_s and two sidebands at $\omega_s \pm \omega_r$:

$$\begin{aligned} i_{de}(t) = I_1 \cos \omega_s t \\ + \frac{1}{2} \alpha_1 I_1 \cos [(\omega_s + \omega_r) t - \varphi_1] + \frac{1}{2} \alpha_1 I_1 \cos [(\omega_s - \omega_r) t + \varphi_1] \end{aligned} \quad (2.112)$$

The additional stator current components at $\omega_s \pm \omega_r$ are flowing in the phase windings and therefore give rise to a series of MMF waves with the corresponding pulsation. The pole pair numbers of these waves will be the same as those of the fundamental MMF wave and its space harmonics i.e. $p(6c \pm 1)$ (see equation (2.15)). Among these, the waves with pole pair number p will have the strongest amplitudes and only they will be considered in the following.

The additional MMF waves $F_{ecc,dy}(\theta, t)$ due to the secondary armature reaction in case of dynamic eccentricity are therefore:

$$F_{ecc,dy}(\theta, t) = F_{ecc,dy} \cos [p\theta - (\omega_s \pm \omega_r) t - \varphi_i] \quad (2.113)$$

with amplitude $F_{ecc,dy}$ proportional to the the relative degree of eccentricity. The corresponding flux waves $B_{ecc,dy}(\theta, t)$ are obtained by multiplication of $F_{ecc,dy}(\theta, t)$ with the airgap permeance $\Lambda(\theta, t)$. If only the constant term in the permeance expression is considered, the flux density waves are:

$$B_{ecc,dy}(\theta, t) = B_{ecc,dy} \cos [p\theta - (\omega_s \pm \omega_r) t - \varphi_i] \quad (2.114)$$

The two flux density waves with p pole pairs and pulsations $\omega_s \pm \omega_r$ can interact with the fundamental rotor-related flux density wave that has also p pole pairs but a different pulsation ω_s . According to expression (2.50), the produced torque Γ_i will be of the following form:

$$\Gamma_i = -\frac{\pi l_m R_0 g_0}{\mu_0} B_{ecc,dy} B'_r \sin (\mp \omega_r t - \varphi_i) \quad (2.115)$$

Similar to the case with mixed eccentricity, the resulting torque is pulsating at the angular shaft frequency ω_r . Hence, it has been shown that oscillating torques in case of a pure dynamic eccentricity can be explained by the MMF waves resulting from additional non-supply frequency currents flowing in the stator winding. These MMF waves with the same pole pair number as the fundamental can interact with the fundamental rotor flux density wave to produce an oscillating torque component. The described mechanism will also contribute to oscillating torques in case of mixed eccentricity.

The preceding theoretical considerations attempt to explain the apparition of oscillating torque components in case of dynamic and mixed eccentricity using the MMF and permeance wave approach. Experimental results obtained with dynamic eccentricity corroborate this fact and will be presented later in this work. An important consequence of these oscillating torques is that they lead to speed oscillations and consequently to a phase modulation of the stator current. The phenomenon is equivalent to the considered load torque oscillations in 2.4, with the only difference that the torque oscillations are contained in the electromagnetic motor output torque instead of the load torque. However, the effect on the drive will be exactly the same through speed and rotor angle oscillations. Hence, dynamic and mixed eccentricity are likely to produce not only amplitude modulation of the induction motor stator current but they may also provoke phase modulation through the oscillating motor output torque.

2.6 Summary

This chapter presented an analytical approach for the modeling of mechanical fault related phenomena in induction motor drives. The mechanical faults are supposed to have two possible major effects on the drive: First, a small additional load torque oscillation that leads to oscillations of the mechanical speed. Secondly, mechanical faults may lead to higher levels of static, dynamic or mixed rotor eccentricity.

The chosen modeling method was the classical MMF and permeance wave approach. The main reasons for this choice are the generality of the approach without limitations to a particular machine, the physical comprehension of causes and effects and, above all, the need to obtain analytical expressions for the airgap flux density and the stator current. Actually, only these analytical expressions can provide knowledge about the type of modulation occurring as a consequence of the fault. The emphasis of these considerations was on the determination of the current frequency content and the modulation types, not on the calculation of exact amplitudes of flux density waves and stator current components. This would have required exact knowledge of the machine construction and would have led to a loss of generality.

One purpose of this chapter is the presentation of the different stator current frequency components and their origin without a fault. A healthy induction motor already contains a great number of spectral components due to its supply voltage, rotor slotting and possible iron saturation. Their frequencies as well as their possible variations under different operating conditions must be taken into account.

Table 2.1: Synopsis of stator current frequency components

Name of the Stator Current Component	Frequency	Origin	Modulation
Fundamental	f_s	Supply Voltage	-
Harmonics of supply frequency	nf_s	Harmonics in supply voltage	-
Rotor slot harmonics	$kN_r f_r \pm nf_s$	Modified airgap	AM
Saturation harmonics	$f_s \pm 2kf_s$	Deformation of flux density \rightarrow Modified airgap	AM
Torque/speed oscillation	$nf_s \pm f_c$	Modified rotor MMF	PM
Dynamic eccentricity	$nf_s \pm f_r$	Modified airgap	AM
	$nf_s \pm f_r$	Torque oscillation	PM

This is of great importance for the choice of an appropriate stator current based condition monitoring approach. The results are resumed in the first part of Table 2.1.

Although the MMF and permeance wave approach is used since the beginning of the 20th century, the following new results were obtained for an induction motor analysis under a mechanical fault: It was shown that torque and speed oscillations of the induction motor result in a phase-modulated stator current. In contrast, airgap eccentricity provokes amplitude modulation of the stator current in the particular case of dynamic or mixed eccentricity. These different types of modulations can be distinguished using adequate signal processing methods that will be discussed in further parts of this work. It should therefore be possible to obtain valuable information about the type and origin of a mechanical fault by stator current analysis. This is especially important if a torque oscillation at shaft rotational frequency occurs, because its spectral current signature is identical to the one with dynamic eccentricity. The additional stator current frequencies related to torque oscillations and airgap eccentricity as well as the modulation type are also shown in Table 2.1.

Furthermore, the reasons for the existence of pulsating torques in case of eccentricity have been discussed. So far, only simulation results have been found in literature and no theoretical explanation was given. Using again the MMF and permeance wave approach, interactions between stator and rotor flux density waves were identified that explain the increase in oscillating torques at the rotational frequency in case of dynamic and mixed eccentricity. These oscillating torques and the associated speed ripple will theoretically provoke an additional phase modulation of the stator current of an eccentric motor.

In the following parts of this work, different signal processing methods suitable for stator current analysis will be presented. Since the mechanical fault may provoke both amplitude and phase modulations, methods capable of distinguishing these two modulations will be of particular interest. In addition, given that variable speed drives are considered, transient signals with varying frequencies are encountered requiring non-stationary signal analysis tools.

Chapter 3

Introduction to the Employed Signal Processing Methods

Contents

3.1	Introduction	50
3.2	Basic Concepts	51
3.2.1	Classes of Signals	51
3.2.1.1	Deterministic Signals	51
3.2.1.2	Random Signals	52
3.2.2	Correlation	53
3.2.2.1	Deterministic Signals	53
3.2.2.2	Random Signals	54
3.2.3	Stationarity of Stochastic Processes	54
3.2.4	Fourier Transform	56
3.2.5	Sampling	56
3.2.6	Analytical Signal	57
3.2.6.1	Properties	57
3.2.6.2	Hilbert Transform	59
3.2.6.3	Hilbert Transform of Modulated Signals	60
3.3	Spectral Estimation	61
3.3.1	Definitions	62
3.3.2	Periodogram	63
3.3.3	Averaged Periodogram	64
3.3.4	Window Functions	65
3.4	Time-Frequency Analysis	66
3.4.1	Heisenberg-Gabor Uncertainty Relation	69
3.4.2	Instantaneous Frequency	70

3.4.3	Spectrogram	71
3.4.3.1	Definition	71
3.4.3.2	Properties	72
3.4.3.3	Examples	73
3.4.4	Wigner Distribution	74
3.4.4.1	Definition	74
3.4.4.2	Properties	75
3.4.4.3	Examples	76
3.4.5	Smoothed Wigner Distributions	78
3.4.5.1	Definitions	78
3.4.5.2	Examples	79
3.4.6	Discrete Wigner Distribution	81
3.4.7	Time-Frequency vs. Time-Scale Analysis	82
3.5	Parameter Estimation	83
3.5.1	Basic concepts	84
3.5.2	Estimator Performance and Cramer-Rao Lower Bound .	85
3.5.3	Maximum Likelihood Estimation	87
3.5.4	Detection	89
3.6	Summary	91

3.1 Introduction

This chapter introduces the signal processing methods used for induction motor drive monitoring in the following chapters. The signals correspond to measured physical quantities of the drive. In the context of this work, two types of signals can be distinguished depending on their origin: mechanical signals such as torque, shaft speed, shaft angle, stator frame vibrations, and electrical signals e.g. terminal voltages and particularly the line currents. As the origin of these signals is a rotating machine, they are generally periodic signals.

The basic analysis method for time-periodic signals is the estimation of the signal power spectral density with Fourier transform based methods. This will be referred to as classical spectral analysis in the following. The considered mechanical faults often lead to additional periodic phenomena as demonstrated in the previous chapter. Thus, the fault mechanisms produce additional frequencies or a rise of existing ones in the stator current, torque, shaft speed or vibration. Spectral analysis for condition monitoring and fault detection is therefore an obvious approach, used in most existing works.

However, if an induction motor drive operates under variable speed conditions, the most frequency components are time-varying since they depend almost always

on shaft speed or supply frequency. If these variations are slow during the observation interval, quasi-stationarity can be supposed and the classical spectral analysis techniques may still be applied. However, when variations are faster, more advanced signal processing methods for non-stationary signal analysis are required.

Two popular approaches to non-stationary signal analysis exist: Time-frequency and time-scale or wavelet analysis. The principles of both methods will be shortly presented. However, only time-frequency analysis is used in the following and the reasons for this will be discussed as well.

In the further course of this work, another original approach to current based fault detection is studied: signal parameter estimation. This method does not rely on frequency analysis but identifies model parameters which provide knowledge about possible faults. This method relies on the stator current models derived in chapter 2.

The outline of the chapter is the following: First, some basic concepts of signal processing are reviewed including correlations, the Fourier transform, sampling and the concept of the analytical signal. Then, classical spectral analysis methods based on the Fourier transform will be discussed. In the following, the basic concepts of time-frequency analysis are set forth together with the most important representations. The last part of this chapter deals with signal parameter estimation.

3.2 Basic Concepts

3.2.1 Classes of Signals

Various types of signals may be encountered and it can be useful to classify these signals according to certain properties. The type of signal and its properties are important for the choice of an appropriate method to analyze and process the signal. The reason is that certain signal processing methods will only be effective for a certain class of signals.

In the following, most definitions will be given for continuous-time and discrete-time signals. They will be noted $x(t)$ and $x[k]$ respectively, distinguished by round or square brackets.

3.2.1.1 Deterministic Signals

Signals can first be classified according to their deterministic or random nature. Deterministic signals are mathematically reproducible. Therefore, deterministic signals can be described by a mathematical expression. This implies that future values of the signal can be predicted from past values [Cas03].

Usually, deterministic signals are divided into subclasses: finite energy signals and finite power signals. The energy E of finite energy signals verifies the following

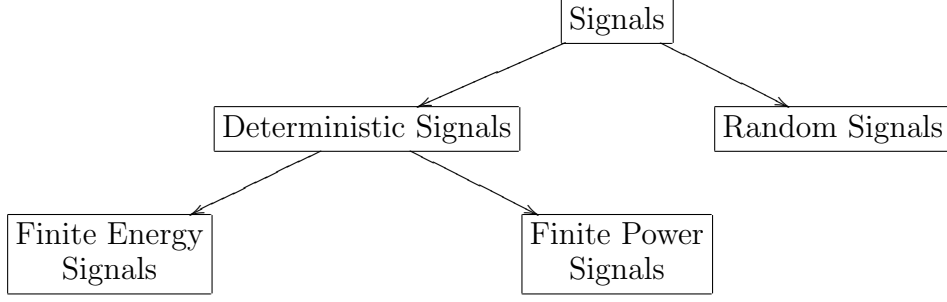


Figure 3.1: Classification of signals.

condition:

$$E = \int_{-\infty}^{+\infty} |x(t)|^2 dt < \infty \quad (3.1a)$$

$$E = \sum_{k=-\infty}^{+\infty} |x[k]|^2 < \infty \quad (3.1b)$$

Finite energy signals generally have a transient or impulse character. They often verify $|x(t)| \rightarrow 0$ for $|t| \rightarrow \infty$.

The power P of finite power signals is:

$$P = \lim_{T \rightarrow \infty} \frac{1}{T} \int_{-\frac{T}{2}}^{+\frac{T}{2}} |x(t)|^2 dt < \infty \quad (3.2a)$$

$$P = \lim_{N \rightarrow \infty} \frac{1}{2N+1} \sum_{k=-N}^{+N} |x[k]|^2 < \infty \quad (3.2b)$$

A typical example of power signals are periodic signals such as sinusoidal signals. The classification scheme is shown in Fig. 3.1.

3.2.1.2 Random Signals

In contrary to deterministic signals, random or stochastic signals cannot be described by a deterministic mathematical expression. They can be considered as realizations of stochastic processes. A stochastic process $x(t)$ is statistically determined by its probability density function $p(x, t)$ [Pap65]. However, since this function is not always known, other quantities can be used to describe the process e.g. the moments or the autocorrelation function.

Consider for example a random signal $n(t)$ which is a Gaussian noise. Gaussian noise is a stochastic process commonly used to model measurement noise. The signal amplitude $n(t)$ is distributed according to a normal distribution and the corresponding probability density function $p(n)$ is:

$$p(n) = \frac{1}{\sqrt{2\pi\sigma^2}} e^{-(n-\mu)^2/2\sigma^2} \quad (3.3)$$

where μ denotes the mean and σ^2 the variance.

After this introductory example, some fundamentals and definitions about random variables and stochastic processes are considered. The moments m_k of a random variable X are defined as follows [Pap65]:

$$m_k = E\{X^k\} = \int_{-\infty}^{+\infty} x^k p(x) dx \quad (3.4)$$

The first moment $E\{X\} = \mu$ defined for $k = 1$ is of particular importance; it is also called mean or expected value. Another important parameter of a random variable is its variance or dispersion σ^2 , defined as the second central moment:

$$\text{var}\{x\} = \sigma^2 = E\{(X - \mu)^2\} = \int_{-\infty}^{+\infty} (x - \mu)^2 p(x) dx \quad (3.5)$$

The positive square root σ of the variance σ^2 is called the standard deviation.

For stochastic processes, the mean $\mu(t)$ is defined in a similar way as the expected value of the random variable $x(t)$:

$$\mu(t) = E\{x(t)\} = \int_{-\infty}^{+\infty} x p(x, t) dx \quad (3.6)$$

Note that the mean is in general a function of time.

3.2.2 Correlation

The following sections review the definitions of correlation functions for deterministic and random signals. In the general case, a correlation function measures the similarity between two signals with respect to their mutual time-delay.

3.2.2.1 Deterministic Signals

The cross-correlation of two complex finite energy signals $x(t)$ and $y(t)$ is defined as [Max00]:

$$R_{xy}(\tau) = \int_{-\infty}^{+\infty} x(t) y^*(t - \tau) dt \quad (3.7)$$

where y^* denotes the complex conjugate of y . For finite power signals:

$$R_{xy}(\tau) = \lim_{T \rightarrow \infty} \frac{1}{T} \int_{-\frac{T}{2}}^{+\frac{T}{2}} x(t) y^*(t - \tau) dt \quad (3.8)$$

The autocorrelation function $R_{xx}(\tau)$ is obtained for $y(t) = x(t)$. According to (3.1a), (3.2a) and (3.8), $R_{xx}(0)$ is the energy or power of a finite energy or finite power signal.

3.2.2.2 Random Signals

The cross-correlation function $R_{xy}(t_1, t_2)$ of two complex stochastic processes $x(t)$ and $y(t)$ is defined as the joint first moment of the random variables $x(t_1)$ and $y^*(t_2)$ [Pap65]:

$$R_{xy}(t_1, t_2) = E\{x(t_1)y^*(t_2)\} = \int_{-\infty}^{+\infty} x(t) y^*(t) p(x, y, t_1, t_2) dx dy \quad (3.9)$$

3.2.3 Stationarity of Stochastic Processes

Different types of stationarity of stochastic processes are distinguished [Pap65]:

Stationarity in the strict sense: A stochastic process $x(t)$ is stationary in the strict sense if its statistics are not affected by a time shift. This means that the two processes $x(t)$ and $x(t + \tau)$ have the same statistics. It follows that the probability density function $p(x, t)$ of the stochastic process is identical for all t and therefore independent of time: $p(x, t) = p(x)$.

Stationarity in the wide sense: A stochastic process $x(t)$ is stationary in the wide sense (or weakly stationary) if its mean $E\{x(t)\}$ is a constant independent of time and if its autocorrelation function $R_{xx}(t_1, t_2)$ depends only on $\tau = t_1 - t_2$ (see 3.2.2)

$$\mu(t) = E\{x(t)\} = \mu \quad , \quad R_{xx}(t_1, t_2) = R_{xx}(\tau) \quad (3.10)$$

All processes that are stationary in the strict sense are also stationary in the wide sense.

Periodical stationarity (or cyclostationarity): The process $x(t)$ is periodically stationary with period T in the strict sense if the statistics are periodic with T . The random variables $x(t), x(t + T), \dots, x(t + nT), \dots$ then have the same probability density function. The wide sense cyclostationarity is verified if only the mean and the autocorrelation are periodic:

$$\mu(t) = \mu(t + nT) \quad , \quad R_{xx}(t_1 + kT, t_2 + mT) = R_{xx}(t_1, t_2) \quad (3.11)$$

For illustration and better understanding, consider the following three examples:

1. The previously mentioned Gaussian noise $n(t)$ in (3.3) could be described by a normal probability density. The density is independent of time which means that all the moments are independent of time. This process is stationary in the strict sense.
2. If a sinusoidal signal with constant and known amplitude A and frequency f is measured from a source at an arbitrary time instant, its phase φ is

generally unknown. The measured signal can be considered as a stochastic process $x(t)$ according to:

$$x(t) = A \sin(2\pi ft + \varphi) \quad (3.12)$$

where φ is a random variable with a uniform density $p(\varphi)$ over the interval $[0, 2\pi[$:

$$p(\varphi) = \begin{cases} 1/2\pi & \text{for } \varphi \in [0, 2\pi[\\ 0 & \text{else} \end{cases} \quad (3.13)$$

This process is not stationary in the strict sense because its probability density depends on time. The mean of this process is:

$$E\{x(t)\} = A E\{\sin(2\pi ft + \varphi)\} = 0 \quad (3.14)$$

because the expected value of $\sin(c + \varphi)$ is zero for an arbitrary constant c with the considered density $p(\varphi)$. The autocorrelation is calculated as follows with $\omega = 2\pi f$:

$$\begin{aligned} R_{xx}(t_1, t_2) &= E\{A \sin(\omega t_1 + \varphi) A \sin(\omega t_2 + \varphi)\} \\ &= \frac{1}{2} A^2 E\{\cos(\omega t_1 - \omega t_2) - \cos(\omega t_1 + \omega t_2 + 2\varphi)\} \\ &= \frac{1}{2} A^2 \cos(\omega t_1 - \omega t_2) = \frac{1}{2} A^2 \cos(\omega \tau) = R_{xx}(\tau) \end{aligned} \quad (3.15)$$

Thus, it becomes clear that this process is weakly stationary due to the constant mean and the autocorrelation R_{xx} depending only on the time delay $\tau = t_1 - t_2$.

3. Consider as last example a stochastic process where the amplitude of a sine is a random variable:

$$x(t) = A \sin(\omega t) \quad (3.16)$$

where ω is a constant and A a normal random variable with zero mean and variance σ^2 . This process can already be classified as periodically stationary in the strict sense because its probability density function is periodic. The mean of this process is zero because:

$$E\{x(t)\} = E\{A\} \sin(2\pi ft) = 0 \quad (3.17)$$

The second moment of A is the variance: $E\{A^2\} = \sigma^2$ because A is centred with $\mu = 0$. The autocorrelation function is then given by:

$$\begin{aligned} R_{xx}(t_1, t_2) &= E\{A^2 \sin(\omega t_1) \sin(\omega t_2)\} = \sigma^2 \sin(\omega t_1) \sin(\omega t_2) \\ &= \frac{1}{2} \sigma^2 [\cos(\omega t_1 - \omega t_2) - \cos(\omega t_1 + \omega t_2)] \neq R_{xx}(\tau) \end{aligned} \quad (3.18)$$

It becomes evident that equation (3.11) is verified i.e. the condition for periodic stationarity in the wide sense. This was already included in the periodic stationarity in the strict sense. However, the process is not stationary in the wide sense according to (3.10) because its autocorrelation function also depends on $t_1 + t_2$.

In the considered application, most signals are cyclostationary when the drive is operating in steady state i.e at constant speed. However, during speed transients, signals will be non-stationary due to the variable fundamental supply frequency.

3.2.4 Fourier Transform

In signal processing, the Fourier transform $X(f)$ of a time continuous signal $x(t)$ is commonly defined as:

$$X(f) = \mathfrak{F}\{x(t)\} = \int_{-\infty}^{+\infty} x(t) e^{-j2\pi ft} dt \quad (3.19)$$

Comparing the Fourier transform to a cross-correlation, it becomes clear that $X(f)$ is a measure of similarity between the signal $x(t)$ and a family of complex monochromatic exponential signals (cisoids) of frequency f . Recall that $X(f)$ is a complex containing information about the similarity in amplitude and the phase, often omitted in spectral analysis. The inverse Fourier transform is then given by:

$$x(t) = \mathfrak{F}^{-1}\{X(f)\} = \int_{-\infty}^{+\infty} X(f) e^{j2\pi ft} df \quad (3.20)$$

The discrete Fourier transform $X[m]$ of a discrete-time signal $x[k]$ of length N samples is defined as [Max00]:

$$X[m] = \sum_{k=0}^{N-1} x[k] e^{-j2\pi mk/N} \quad m = 0, 1, \dots, N-1 \quad (3.21)$$

where m/N is the discrete normalized frequency with respect to the sampling frequency f_s . The physical frequency f is obtained as:

$$f = \frac{m}{N} f_s \quad (3.22)$$

The inverse of the discrete Fourier transform is:

$$x[k] = \frac{1}{N} \sum_{m=0}^{N-1} X[m] e^{j2\pi mk/N} \quad k = 0, 1, \dots, N-1 \quad (3.23)$$

If the signal length is 2^n , the discrete Fourier transform can be efficiently calculated using so-called fast Fourier transform (FFT) algorithms.

3.2.5 Sampling

The continuous-time signal is converted into a discrete-time signal by sampling. In general, sampling consists of taking uniformly spaced samples from the continuous-time signal $x(t)$. These samples then constitute the discrete-time signal $x_d[k]$. The sampling period is defined by $T_s = 1/f_s$ where f_s denotes the sampling frequency.

Mathematically, the discrete-time signal $x_d[k]$ can be described by the multiplication of the continuous-time signal $x(t)$ with a series of equally spaced Dirac delta functions:

$$x_d[k] = x(t) \sum_{k=-\infty}^{\infty} \delta(t - kT_s) \quad (3.24)$$

The Fourier transform $X_d(f)$ of $x_d[k]$ is then obtained by the convolution product of $X(f)$ and the Fourier transforms of the series of Dirac delta functions. The latter is derived using the Poisson formula [Cas03]:

$$\mathfrak{F} \left\{ \sum_{n=-\infty}^{+\infty} \delta(t - nT_s) \right\} = \mathfrak{F} \left\{ \frac{1}{T_s} \sum_{k=-\infty}^{+\infty} e^{j2\pi kt/T_s} \right\} = \frac{1}{T_s} \sum_{k=-\infty}^{+\infty} \delta(f - kf_s) \quad (3.25)$$

Hence, $X_d(f)$ expresses as:

$$X_d(f) = X(f) * \frac{1}{T_s} \sum_{k=-\infty}^{+\infty} \delta(f - kf_s) = \frac{1}{T_s} \sum_{k=-\infty}^{+\infty} X(f - kf_s) \quad (3.26)$$

It can be seen that the Fourier transform of the discrete signal is the f_s -periodic repetition of the original Fourier transform $X(f)$. This is illustrated in Fig. 3.2: The Fourier transform $X(f)$ of the continuous-time signal is shown in Fig. 3.2(a) where $x(t)$ is supposed limited in bandwidth B . The Fourier transforms of the corresponding discrete-time signals are depicted in Fig. 3.2(b) and 3.2(c) for two different sampling frequencies. When $f_s > 2B$ the adjacent spectra do not overlap. On the other hand, if $f_s < 2B$, overlap exists which is called spectral aliasing.

Hence, the *Nyquist-Shannon sampling theorem* can be deduced. It states that a continuous bandwidth-limited signal with bandwidth B can be fully reconstructed after sampling if the condition $f_s > 2B$ is verified. The frequency $f_s/2$ is called the Nyquist frequency. The reconstruction of the continuous-time signal is possible because no aliasing occurs if $f_s > 2B$ is respected. Note that this is true for real signals where the effective bandwidth is $2B$. The situation is slightly different with complex signals (analytical signals).

The signals in this application are not bandlimited due to high frequency inverter switching harmonics. However, all signals are lowpass filtered with adapted anti-aliasing filters before analog to digital conversion.

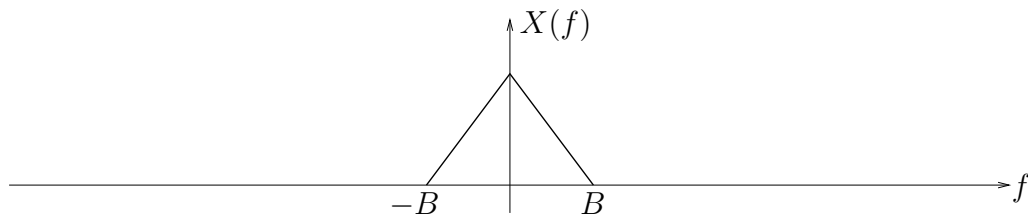
3.2.6 Analytical Signal

3.2.6.1 Properties

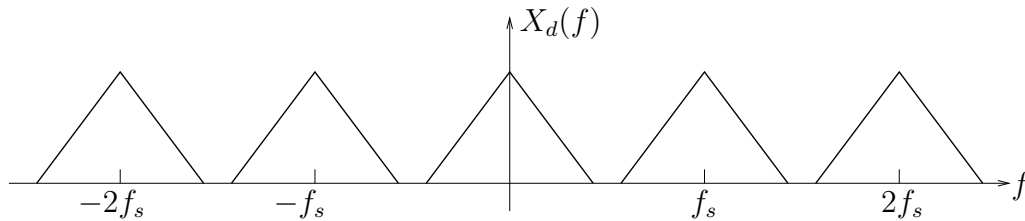
The real and imaginary parts of $X(f)$, the Fourier transform of a real signal $x(t)$, can be written as:

$$\Re \{X(f)\} = \int_{-\infty}^{+\infty} x(t) \cos(2\pi ft) dt \quad (3.27a)$$

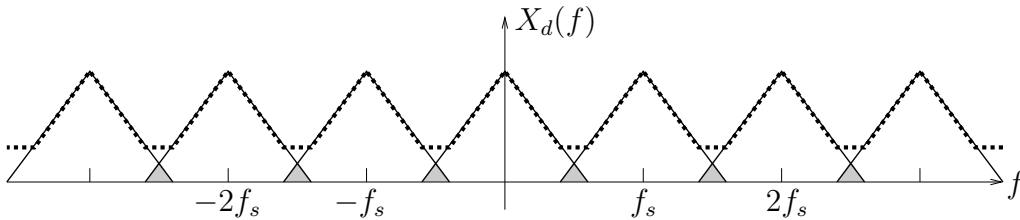
$$\Im \{X(f)\} = - \int_{-\infty}^{+\infty} x(t) \sin(2\pi ft) dt \quad (3.27b)$$



(a) Fourier transform $X(f)$ of the continuous-time signal



(b) Fourier transform $X_d(f)$ of the discrete-time signal with $f_s > 2f_{max}$: no spectral aliasing.



(c) Fourier transform $X_d(f)$ of the discrete-time signal with $f_s < 2f_{max}$: spectral aliasing.

Figure 3.2: Illustration of the effect of sampling on the Fourier transform with different sampling frequencies.

This implies the following symmetry of $X(f)$ [Max00]:

$$\Re\{X(-f)\} = \Re\{X(f)\} \quad (3.28a)$$

$$\Im\{X(-f)\} = -\Im\{X(f)\} \quad (3.28b)$$

These relations show that the values of the Fourier transform with respect to the negative frequencies can be entirely deduced from the values of the positive frequencies. The negative frequencies of $X(f)$ contain no additional information if the values for positive frequencies are known. Therefore, a disadvantage of real valued signals is the large bandwidth that could theoretically be divided by two if the negative frequencies would be omitted.

This is realized considering *analytical signals*. A signal $z(t)$ is called an analytical signal if its Fourier transform is zero for negative frequencies [Boa03]:

$$Z(f) = 0 \quad \text{for } f < 0 \quad (3.29)$$

In general, $z(t)$ will be a complex-valued signal. Analytical signals are useful to avoid additional interferences in quadratic time-frequency distributions and they are important for a univocal phase definition.

3.2.6.2 Hilbert Transform

Consider now how a real signal $x(t)$ is transformed into the corresponding analytical signal $z(t)$. The Fourier transform $Z(f)$ is zero for negative frequencies which leads to the following definition of $Z(f)$ in the frequency domain [Max00]:

$$Z(f) = X(f) + \text{sign}(f)X(f) = X(f) + j(-j)\text{sign}(f)X(f) = X(f) + jY(f) \quad (3.30)$$

where $Y(f)$ is the imaginary part of $Z(f)$ and

$$\text{sign}(f) = \begin{cases} 1 & \text{if } f > 0 \\ 0 & \text{if } f = 0 \\ -1 & \text{if } f < 0 \end{cases} \quad (3.31)$$

which leads to the following relation between $Z(f)$ and $X(f)$:

$$Z(f) = \begin{cases} 2X(f) & \text{if } f > 0 \\ X(0) & \text{if } f = 0 \\ 0 & \text{if } f < 0 \end{cases} \quad (3.32)$$

It can be seen that the energies of $x(t)$ and $z(t)$ are identical since the amplitudes of the positive frequencies double. Expression (3.30) also shows that the analytical signal can be obtained by taking $x(t)$ as its real part and a second signal $y(t)$ as imaginary part. The signal $y(t)$ is obtained from $x(t)$ using a linear filter $h(t)$ of complex gain $H(f) = (-j)\text{sign}(f)$. The gain of this filter is $-j$ for the positive frequencies (i.e. a phase shift of $-\pi/2$) and j for the negative frequencies corresponding to a phase shift of $+\pi/2$. The filter is also called a quadrature filter.

This filter realizes the so-called *Hilbert transform*, denoted $\mathcal{H}\{\}$, and $y(t)$ is called the Hilbert transform of $x(t)$. Therefore, the analytical signal $z(t)$ can be written as:

$$z(t) = x(t) + jy(t) = x(t) + j\mathcal{H}\{x(t)\} \quad (3.33)$$

The impulse response of the filter is $h(t) = 1/(\pi t)$ which leads to the following time-domain expression of the Hilbert transform:

$$y(t) = \mathcal{H}\{x(t)\} = \frac{1}{\pi} \text{p.v.} \int_{-\infty}^{+\infty} \frac{x(\tau)}{t - \tau} d\tau \quad (3.34)$$

where p.v. denotes the Cauchy principal value of the improper integral.

Consider the following simple example for illustration: If the real signal is supposed to be $x(t) = \cos(2\pi f_0 t)$, its Hilbert transform is the corresponding sine. The analytical signal is therefore:

$$z(t) = \cos(2\pi f_0 t) + j\mathcal{H}\{\cos(2\pi f_0 t)\} = \cos(2\pi f_0 t) + j\sin(2\pi f_0 t) = e^{j2\pi f_0 t} \quad (3.35)$$

The Fourier transform of the real signal is $(\delta(f - f_0) + \delta(f + f_0))/2$ i.e. two Dirac delta functions at $\pm f_0$ whereas the Fourier transform of the cisoid $z(t)$ is $\delta(f - f_0)$. This demonstrates the reduction in bandwidth of the analytical signal compared to the corresponding real signal. Theoretically, the sampling rate of an analytical signal could be reduced by the factor two compared to a real signal. However, this would also induce a complex representation of the signal and therefore an equal amount of memory for storage.

3.2.6.3 Hilbert Transform of Modulated Signals

An important application of the Hilbert transform is the demodulation of amplitude and phase modulated signals. Consider the following real-valued modulated signal:

$$x(t) = a(t) \cos \phi(t) \quad (3.36)$$

where $a(t)$ and $\phi(t)$ are the time variable amplitude and phase. It is desirable to obtain through the Hilbert transform an analytical signal $z(t)$ of the form:

$$z(t) = a(t)e^{j\phi(t)} \quad (3.37)$$

where $a(t)$ is the *instantaneous amplitude* and $\phi(t)$ the *instantaneous phase*. The real signal $x(t)$ can be deduced from $z(t)$ without ambiguity by considering $x(t) = \Re\{z(t)\}$. However, the inverse operation i.e. finding the analytical signal $z(t)$ corresponding to a real signal $x(t)$ is not well-defined. Actually, the signal $x(t)$ can be written with an infinite number of pairs $[a(t), \phi(t)]$ so that the definition of instantaneous amplitude and phase of a real signal is ambiguous [Pic97] [Fla98].

The following relation must be true for an unambiguous definition of the analytical signal of $x(t)$:

$$\mathcal{H}\{a(t) \cos \phi(t)\} = a(t) \sin \phi(t) \quad (3.38)$$

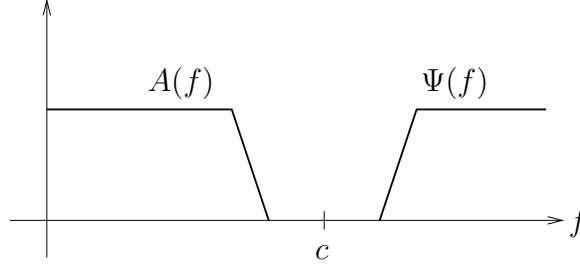


Figure 3.3: Illustration relative to the Bedrosian theorem.

This implies the following two conditions [Fla98]:

$$\mathcal{H}\{a(t) \cos \phi(t)\} = a(t) \mathcal{H}\{\cos \phi(t)\} \quad (3.39)$$

$$\mathcal{H}\{\cos \phi(t)\} = \sin \phi(t) \quad (3.40)$$

The first equation (3.39) is true if the Fourier transforms of $a(t)$ and $\cos \phi(t)$ verify:

$$A(f) = \mathfrak{F}\{a(t)\} = 0 \quad \text{for } |f| > c \quad (3.41)$$

$$\Psi(f) = \mathfrak{F}\{\cos \phi(t)\} = 0 \quad \text{for } |f| < c \quad (3.42)$$

where c is an arbitrary positive constant. According to equations (3.41) and (3.42), the two Fourier transforms do not overlap and $a(t)$ has the characteristics of a low-pass signal whereas $\cos \phi(t)$ is a high-pass signal (see illustration in Fig. 3.3). This is the product theorem for Hilbert transforms, also called the *Bedrosian theorem* [Bed63].

The second equation (3.40) is verified when the bandwidth of $\cos \phi(t)$ is relatively small. The error between the theoretical quadrature component and the one obtained with the Hilbert filter was calculated by Lerner in [Ler60] and found to be of the order of the percentage bandwidth. Further discussions on this topic can be found in contributions from Rihaczek, Nuttall and the corresponding replies from Bedrosian [Rih66] [Nut66].

It can be concluded that a real-valued modulated signal $x(t) = a(t) \cos \phi(t)$ has a corresponding unique analytical signal $z(t) = a(t)e^{j\phi(t)}$ if the Fourier transforms of $a(t)$ and $\cos \phi(t)$ do not overlap and if the bandwidth of $\cos \phi(t)$ is relatively small. Then, the analytical signal can be represented as a vector in a complex plane as depicted in Fig. 3.4. The amplitude of the vector is the instantaneous amplitude $a(t)$, its phase the instantaneous phase $\phi(t)$. It becomes clear that the amplitude and phase information can now easily be extracted from $z(t)$ by simply considering the absolute value and the phase of a complex. Applications are for example amplitude and phase demodulation in communication systems.

3.3 Spectral Estimation

Spectral estimation is widely used for the analysis of stationary signals. The aim is the estimation of the *power spectral density* (PSD) of a signal i.e. the distribution of signal power with respect to frequency. Information about the signal is available

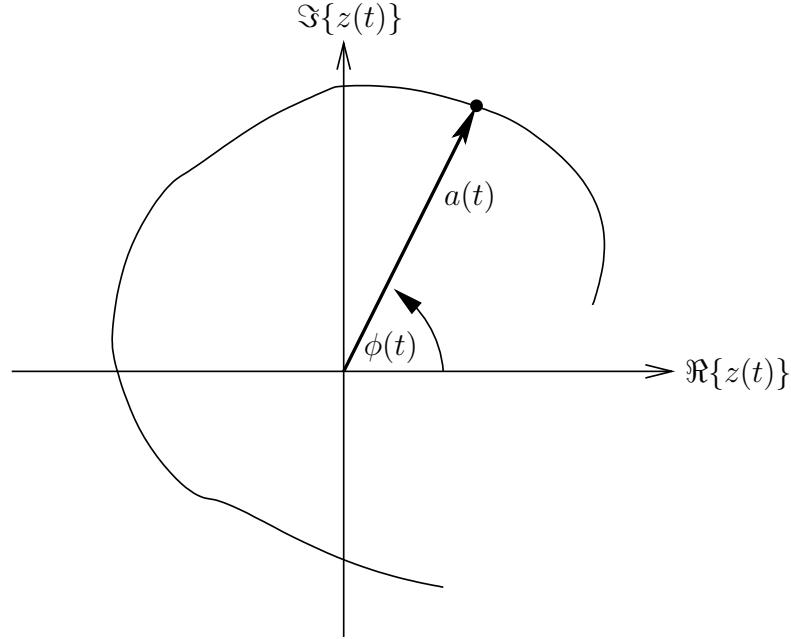


Figure 3.4: Vector representation of an analytical signal $z(t)$ in the complex plane.

through a data record of finite length. Two main approaches exist: parametric and non-parametric spectral estimation.

Parametric methods first suppose a particular signal model. Then, the model parameters are identified from the available data record. Finally, the corresponding signal spectrum is derived as a function of the model parameters. Advantages of this approach are high accuracy and good spectral resolution, especially in case of short data records. However, these methods only perform well for an appropriate signal model. This means that a priori knowledge of the signal is necessary.

Non-parametric methods are sometimes referred to as classical spectral estimation. They do not require any a priori knowledge of the signal to be analyzed. Their performance is satisfactory if long data records are available. In contrast to the parametric approach, these methods rely on the Fourier transform of the signal or its estimated autocorrelation function. In the following, non-parametric spectral estimation will be used for signal analysis since long data records are available. In addition, no a priori assumptions about the signals have to be made that may significantly influence the estimated spectrum. Furthermore, these methods are also more simple to use and can be efficiently computed using Fast Fourier Transform (FFT) algorithms.

3.3.1 Definitions

The power spectral density $P_{xx}(f)$ of a complex discrete-time wide sense stationary random process $x[n]$ is defined as the Fourier transform of its autocorrelation function $R_{xx}[k]$ [Kay88]:

$$P_{xx}(f) = \sum_{k=-\infty}^{\infty} R_{xx}[k] e^{-j2\pi f k} \quad (3.43)$$

where the discrete autocorrelation function $R_{xx}[k]$ is:

$$R_{xx}[k] = E\{x[n]x^*[n+k]\} \quad (3.44)$$

Equation (3.43) is sometimes referred to as the *Wiener-Khintchine theorem*.

Another alternative definition of the PSD is the following:

$$P_{xx}(f) = \lim_{M \rightarrow \infty} E \left\{ \frac{1}{2M+1} \left| \sum_{n=-M}^M x[n]e^{-j2\pi fn} \right|^2 \right\} \quad (3.45)$$

The PSD is the mathematical expectation of the squared magnitude of the Fourier transform divided by the data record length. These two definitions of the PSD are shown to be equal e.g. in [Kay88] [Cas03].

3.3.2 Periodogram

The periodogram spectral estimator $\hat{P}_{per}(f)$ is based on the definition of the PSD given in equation (3.45). The expectation operator is neglected and the estimator expresses as:

$$\hat{P}_{per}(f) = \frac{1}{N} \left| \sum_{n=0}^{N-1} x[n]e^{-j2\pi fn} \right|^2 \quad (3.46)$$

Therefore, the periodogram is simply the squared discrete Fourier transform of the data record divided by the number of samples N . It can be rapidly calculated even for long samples using FFT algorithms.

The performance of the periodogram as estimator for the signal PSD can be studied through the bias and the variance (see section 3.5.2). First, consider the estimation bias: It can be shown that the periodogram is the convolution of the true PSD with the Fourier transform of a triangular Bartlett window [Kay88] [Cas03]. The Bartlett window $w_B[n]$ is given by:

$$w_B[n] = \begin{cases} 1 - \frac{|k|}{N} & |k| \leq N \\ 0 & |k| > N \end{cases} \quad (3.47)$$

and its Fourier transform is:

$$W_B(f) = \frac{1}{N} \left(\frac{\sin \pi f N}{\sin \pi f} \right)^2 \quad (3.48)$$

Therefore, the periodogram is a biased estimator. However, for long data records with $N \rightarrow \infty$, the limit of the Fourier transform of the Bartlett window is the Dirac delta function $\delta(f)$. Thus, the convolution of the true PSD with $\delta(f)$ yields the true PSD. This signifies that the bias tends to zero for long data records:

$$\lim_{N \rightarrow \infty} E \left\{ \hat{P}_{per}(f) \right\} = P_{xx}(f) \quad (3.49)$$

The variance of the periodogram estimator is difficult to calculate for the general case but consider for illustration the signal $x[n]$ which is zero-mean white Gaussian

noise with variance σ_x^2 . The autocorrelation function is $R_{xx}[k] = \sigma_x^2 \delta[k]$ which leads to the true PSD being $P_{xx}(f) = \sigma_x^2$. It is demonstrated in [Kay88] for this special case that the variance of the periodogram with respect to frequency is:

$$\begin{aligned} \text{var} \left\{ \hat{P}_{per}(f) \right\} &= P_{xx}^2(f) \left[1 + \left(\frac{\sin 2\pi N f}{N \sin 2\pi f} \right)^2 \right] \\ &\approx P_{xx}^2(f) \quad \text{if } f \neq 0, \pm \frac{1}{2} \text{ (normalized frequency)} \end{aligned} \quad (3.50)$$

First, it can be observed that the variance is approximately independent of the number of samples N i.e. it does not decrease with growing N . Furthermore, the variance of the periodogram in this case is approximately as great as the square of the quantity to be estimated. The standard deviation, thus, is as large as the mean of the estimated quantity. This demonstrates that the periodogram is an unreliable estimator in these cases: Although the bias tends to zero for long data records, the variance does not decrease.

3.3.3 Averaged Periodogram

The fact that the variance of the periodogram does not decrease with increased data record length is due to the lack of an expectation operator in (3.46) [Kay88]. The latter would be necessary according to the definition of the PSD in (3.45). This can be overcome if several realizations $x_m[n]$ of the same random process $x[n]$ are available. First, the periodogram of each realization is calculated, followed by averaging the periodograms. If K realizations are considered, the averaged periodogram is defined as:

$$\hat{P}_{av,per}(f) = \frac{1}{K} \sum_{m=0}^{K-1} \hat{P}_{per,m}(f) \quad (3.51)$$

where $\hat{P}_{per,m}(f)$ is the periodogram of the m -th realization $x_m[n]$ of $x[n]$.

If the data records $x_m[n]$ can be considered independent, the variance of $\hat{P}_{av,per}(f)$ decreases by a factor K compared to the variance of $\hat{P}_{per,m}(f)$:

$$\text{var} \left\{ \hat{P}_{av,per}(f) \right\} = \frac{1}{K} \text{var} \left\{ \hat{P}_{per,m}(f) \right\} \quad (3.52)$$

In many applications, several independent data records are not available but only one data record of length N . In this case, the data can be segmented into K non-overlapping blocks of length L each where $N = KL$ (see illustration in Fig. 3.5). However, since the blocks are no more uncorrelated the decrease in variance is less than $1/K$ [Kay88]. Furthermore, the segmentation reduces the length of the data records for the calculation of the periodograms to L instead of K . This results in a decrease in length for the previously mentioned Bartlett window and thus increases the estimation bias. This is known as the classical bias-variance tradeoff which states that a reduction in variance goes along with an increase in bias and vice versa. The shorter data record length also induces a greater distance between

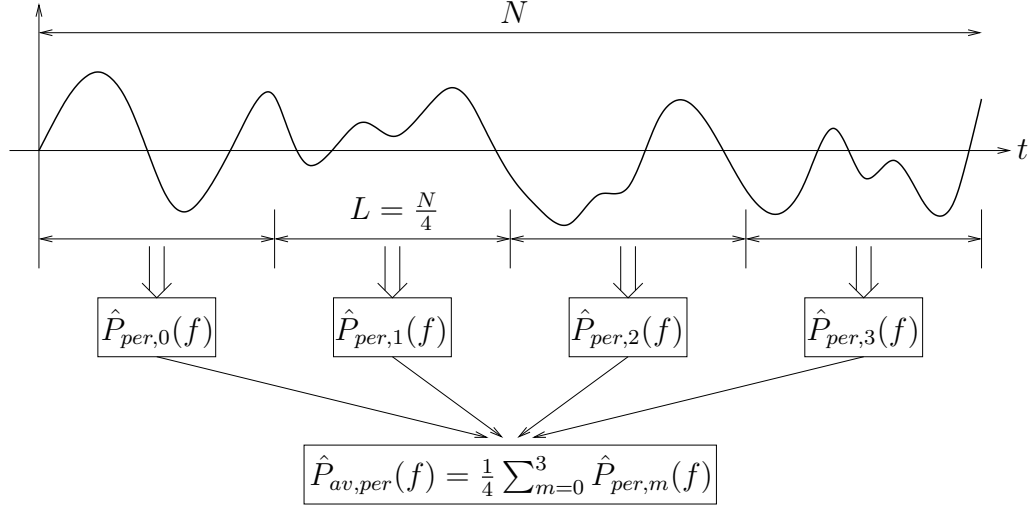


Figure 3.5: Illustration of signal segmentation and calculation of the averaged periodogram with $K = 4$.

two points in the frequency domain i.e. a decrease in spectral resolution. Note that the blocks for calculation of the averaged periodogram can also overlap, but at the expense of smaller reduction in variance.

For illustration purposes, the periodogram and averaged periodogram of a sinusoid of unit amplitude with additive zero-mean white Gaussian noise ($\sigma^2 = 1$) are displayed in Fig. 3.6. The data record length is 256 samples and the frequency of the sinusoid is 0.2 normalized frequency. Fig. 3.6(a) shows the periodogram of the data record without segmentation whereas Fig. 3.6(b) is the averaged periodogram with four segments of length 64 samples. The amplitudes are plotted in a logarithmic scale. The periodogram has a constant average over all frequencies except 0.2, but the variance is high. The variance of the noise floor shows a significant decrease with the averaged periodogram but the spectral resolution is lower and the bias increased. This is visible considering the peak due to the sinusoidal component which increased in width with the averaged periodogram as a consequence of the shorter Bartlett window.

3.3.4 Window Functions

When the spectrum of sinusoidal or narrowband signals is estimated, it is often advantageous to multiply the data with a window function. The use of no particular analysis window is equivalent to the use of a rectangular window of data record length. This leads to relatively high sidelobes of the spectral peaks. The sidelobes can mask smaller components close in frequency and lead to false conclusions [Max00] [Kay88].

The multiplication of the data with a particular window function can reduce the sidelobe amplitudes but increases the width of the mainlobe. Again, a trade-off exists between the sidelobe amplitudes and the bandwidth of the mainlobe. A multitude of analysis windows are possible and extensive information on them can be found in a work of Harris [Har78]. Common window functions are: the rec-

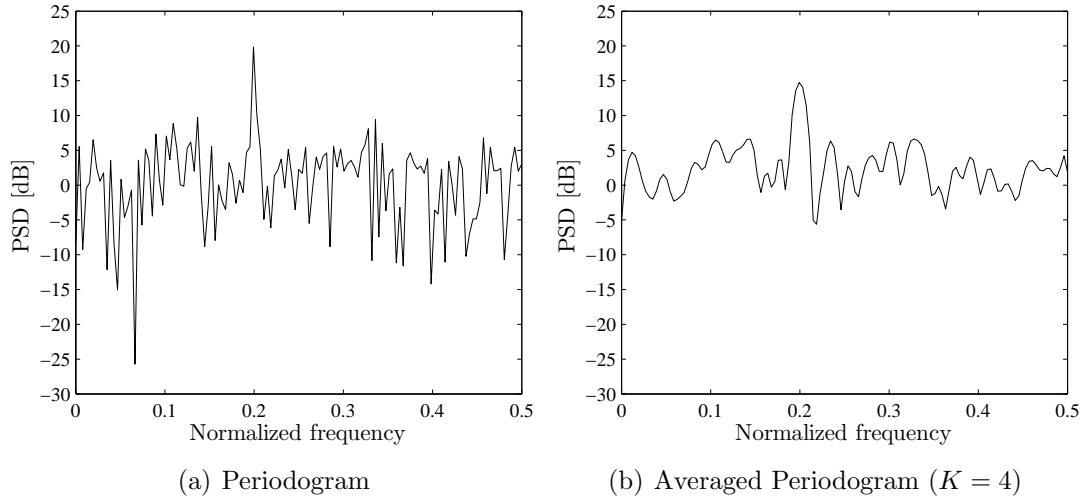


Figure 3.6: Periodogram and averaged periodogram ($K = 4$) of 256 samples of a sinusoid ($f = 0.2$) with additive zero-mean white Gaussian noise.

tangular window or natural window, the triangular or Bartlett window, Hamming window, Hanning window (note that the correct name would be Hann window) or the Blackman window.

The effect of window functions in spectral estimation is shown in Fig. 3.7 where the periodograms of a sinusoidal signal have been calculated with the previously mentioned windows. The rectangular window leads to a narrow mainlobe but the highest sidelobes whereas the Blackman window reduces strongly the sidelobe amplitudes but leads to the largest mainlobe. The other windows are situated between these two cases.

3.4 Time-Frequency Analysis

The Fourier transform and classical spectral estimation are well adapted to signals with a stationary frequency content, i.e. frequencies that are not varying with respect to time. However, this work considers variable speed drives. The supply voltage and the stator current are consequently signals with time-varying frequencies.

The Fourier transform of a signal (see (3.19)) is a measure of similarity between the signal and complex exponentials of constant frequency and infinite support. Moreover, the Fourier transform involves a time integration which means that all information concerning time is lost in the absolute value of the Fourier transform or the spectrum. As a matter of fact, the Fourier transform supposes that the signal can be represented as a sum of signals with constant frequency and infinite length which is simply false in some situations.

Consider for example a transient signal which is zero outside a given interval. The Fourier transform of this signal suggests however that for any time instant the signal is the sum of cisoids with different frequency and infinite length. For

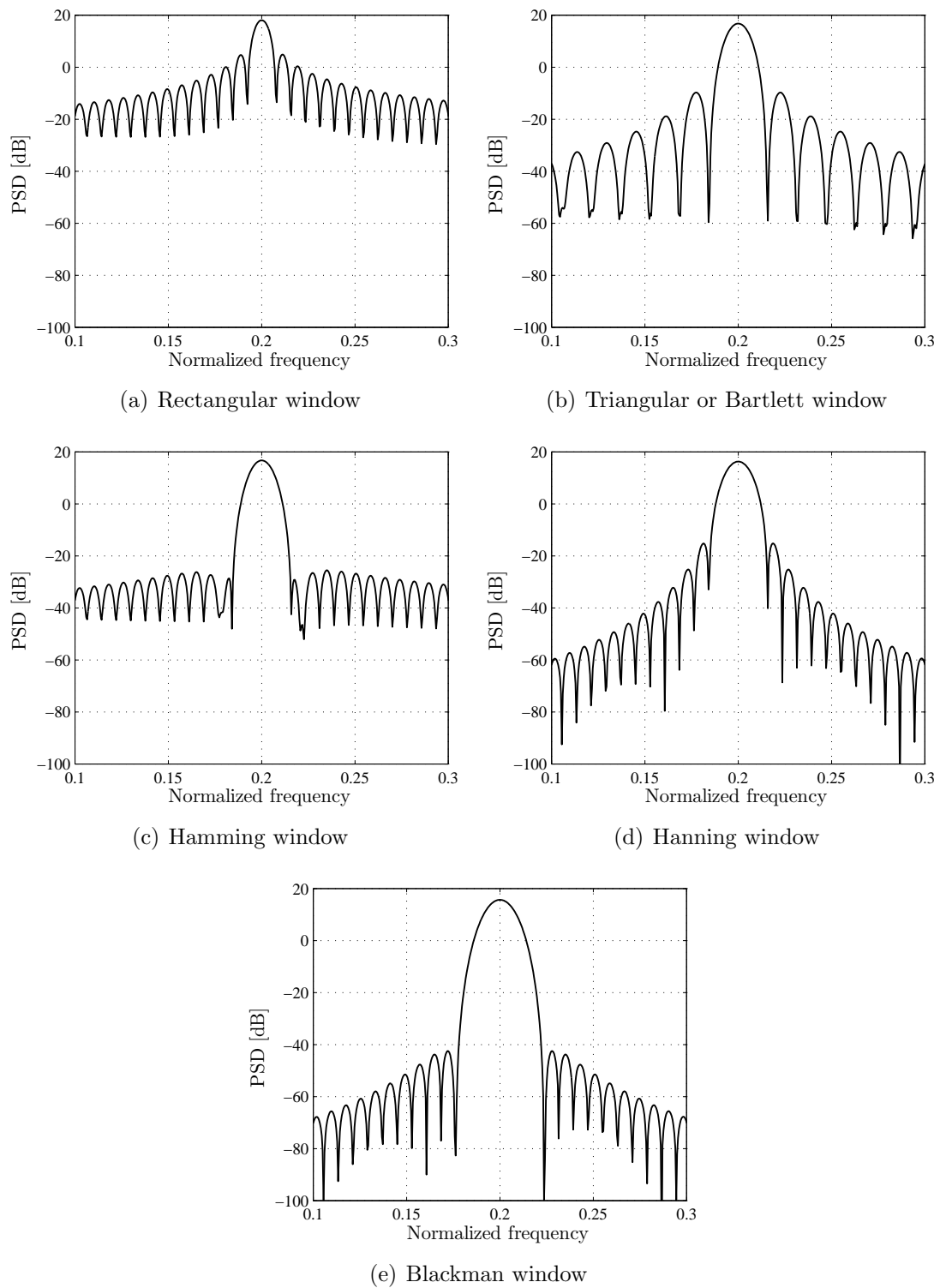


Figure 3.7: Power Spectral Densities of a 128-point sinusoidal signal ($f = 0.2$) analyzed with common window functions.

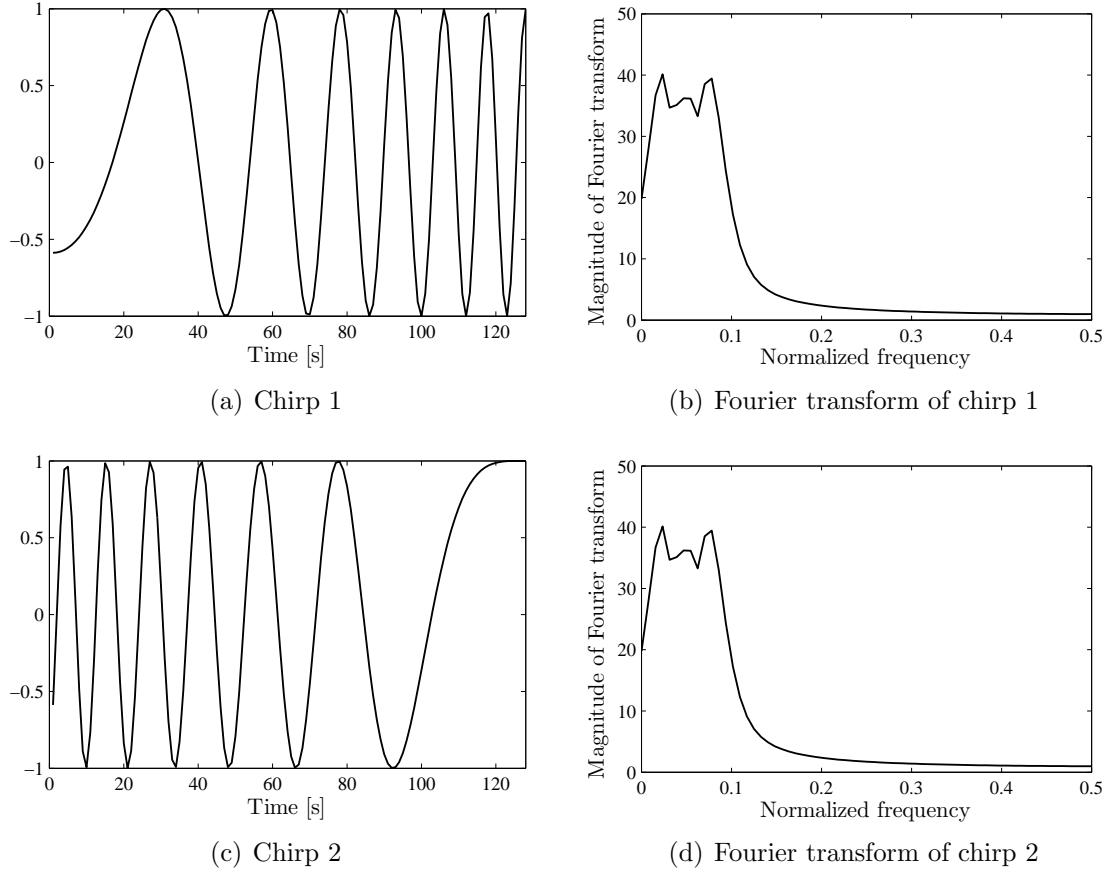


Figure 3.8: Two different chirp signals and the magnitudes of their Fourier transform.

the time instants when the signal is zero, these cisoids interfere and yield zero amplitude i.e. a correct mathematical representation. Nevertheless, in reality, the signal is not a sum of cisoids at these time instants but it is simply zero [Fla98]. Therefore, signal representations based on the Fourier transform are not suitable for such signals.

Another class of signals are those with a time-varying frequency content. Consider for example a signal with a linear frequency modulation. These signals are also called chirp signals and they can be written in complex form as:

$$z(t) = A \exp j2\pi (\alpha_z t + \beta_z t^2/2) \quad (3.53)$$

where A is the amplitude, α_z the initial frequency and β_z the sweep rate. Two different chirp signals are displayed in Figs. 3.8(a) and 3.8(c). The signal *chirp 1* has a normalized frequency evolving from 0 to 0.1 whereas the normalized frequency varies from 0.1 to 0 for *chirp 2*. The Fourier transform magnitude of both signals is shown in Figs. 3.8(b) and 3.8(d). It can be seen that the two Fourier transform magnitudes are identical because the frequency content of the two signals is globally the same. This examples demonstrates that the Fourier transform does not yield a suitable representation of time-variable frequency content.

A desirable signal representation would show frequency information with respect to time. This can be realized using time-frequency analysis or time-scale analysis. Time-frequency analysis is known since the middle of the 20th century but applications emerged only since the 1980s due to the available computational power. Time-scale analysis is more recent (about 1983) but since, it has been of great and increasing popularity in various applications. In the following sections, basic concepts of time-frequency signal analysis are introduced. Various time-frequency methods will be presented and illustrated, followed by a comparison between time-frequency and time-scale analysis. Examples for introductory literature dealing with time-frequency analysis are [Fla98] [Fla99] [Boa03].

3.4.1 Heisenberg-Gabor Uncertainty Relation

The Heisenberg-Gabor uncertainty principle or time-frequency inequality relates the minimum bandwidth of a signal to its duration and vice versa. It states that a signal cannot be perfectly located in time and frequency simultaneously.

First, recall measures for signal duration and the bandwidth. Consider the finite-energy signal $x(t)$ which is supposed to be centred in time and frequency around zero. Gabor [Gab46] defined the effective duration T_e and the effective bandwidth B_e as follows (apart from a different numerical factor):

$$T_e = \frac{1}{E_x} \int_{-\infty}^{+\infty} t^2 |x(t)|^2 dt \quad (3.54)$$

$$B_e = \frac{1}{E_x} \int_{-\infty}^{+\infty} f^2 |X(f)|^2 df \quad (3.55)$$

where E_x is the signal energy given by:

$$E_x = \int_{-\infty}^{+\infty} |x(t)|^2 dt = \int_{-\infty}^{+\infty} |X(f)|^2 df \quad (3.56)$$

These definitions can be interpreted as the second moments of random variables $|x(t)|^2$ and $|X(f)|^2$ with zero mean.

It can be shown that a minimum bound exists in signal processing for the product of effective duration with effective bandwidth of a signal (see [Fla98] for details):

$$T_e B_e \geq \frac{1}{4\pi} \quad (3.57)$$

This inequality is called the *Heisenberg-Gabor uncertainty relation* and it is similar to the Heisenberg uncertainty principle in quantum mechanics. Gaussian signals are special cases because they are the only signals with $T_e B_e = 1/4\pi$.

Consider some examples that illustrate the Heisenberg-Gabor uncertainty relation: A signal with a perfect localization in time is the Dirac delta function $\delta(t)$. In the frequency domain, it cannot be localized at all because $\mathfrak{F}\{\delta(t)\} = 1 \forall f$. The

inverse case is given by a cisoid at frequency f_0 . The perfect localization in frequency is only obtained if the cisoid is of infinite duration. Limiting its duration is equivalent to applying a rectangular window function of finite length. This window function leads to a broader peak in the Fourier transform i.e. a decrease in frequency localization with decreasing window length. This has also been mentioned in the previous section on spectral estimation where the estimation bias decreases with longer samples.

3.4.2 Instantaneous Frequency

Consider a monocomponent analytical signal $z(t)$ with instantaneous amplitude $a(t)$ and instantaneous phase $\phi(t)$:

$$z(t) = a(t)e^{j\phi(t)} \quad (3.58)$$

The instantaneous frequency (IF) of $z(t)$ is defined as [Vil48] [Boa92a]:

$$\text{IF}_z(t) = \frac{1}{2\pi} \frac{d}{dt} \phi(t) \quad (3.59)$$

The IF of a real signal $x(t)$ is unequivocally defined under the following conditions:

- The signal must be a monocomponent signal that can be described by a single IF law. For example, the chirp signal defined in equation (3.53) is a monocomponent signal with a single IF law. The sum of two chirp signals with different sweep rates β would yield a multicomponent signal whose IF law is not correctly described by (3.59).
- The Bedrosian theorem must hold (see section 3.2.6.3).

Consider some examples for illustration: The IF of a real-valued sinusoidal signal $x(t) = \cos(2\pi f_0 t)$ is of course $\text{IF}_x(t) = f_0$ because the corresponding analytical signal is $z(t) = \exp(j2\pi f_0 t)$. The IF of the complex chirp signal $z(t)$ from (3.53) is given by the linear relation $\text{IF}_z(t) = \alpha_z + \beta_z t$. This is illustrated in Fig. 3.9 for a chirp signal with a frequency varying from 0 to 0.5 normalized frequency. The estimated instantaneous frequency is perfectly linear.

Different methods can be used to estimate the IF of a discrete-time analytical signal $z[n] = a[n] \exp j\phi[n]$ [Boa92b]. The most simple and computationally efficient solution is the phase derivation of $z[n]$. The discrete phase derivation can be implemented using a phase difference estimator. The most advantageous is obtained using the central finite difference between two phases $\phi[n+1]$ and $\phi[n-1]$. Consequently, the estimated instantaneous frequency $\hat{\text{IF}}[n]$ is:

$$\hat{\text{IF}}[n] = \frac{1}{4\pi} (\phi[n+1] - \phi[n-1]) \quad (3.60)$$

Other proposed methods use adaptive filtering or the moments of time-frequency distributions but they lead to time-intensive calculations.

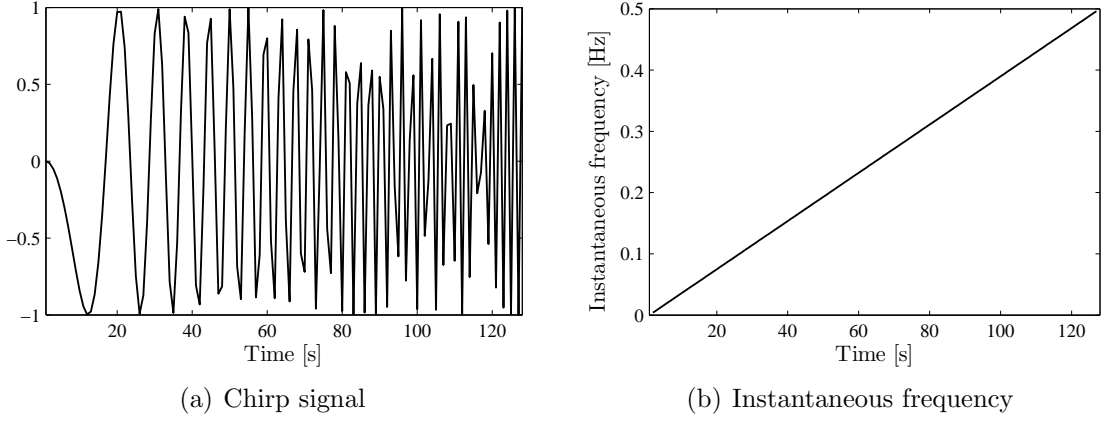


Figure 3.9: Illustration of the instantaneous frequency of a chirp signal.

3.4.3 Spectrogram

The preceding section introduced the IF as a time-frequency representation of a monocomponent signal. However, this is a very particular class of signals and the method cannot be applied to multicomponent signals. This strong limitation is overcome using time-frequency energy distributions. They represent the signal energy with respect to time and frequency and can be interpreted as a time-varying power spectral density under some restrictions.

3.4.3.1 Definition

A first obvious approach is the use of the *short-time Fourier transform*. Instead of using the total signal length for the calculation of the Fourier transform, a sliding observation window is employed (see Fig. 3.10). The window position with respect to the signal depends on time and leads therefore to a time-dependent Fourier transform. The short-time Fourier transform $F_x^w(t, f)$ of a signal $x(t)$ is defined as [Boa03]:

$$F_x^w(t, f) = \mathfrak{F}_{\tau \rightarrow f} \{x(\tau)w(\tau - t)\} = \int_{-\infty}^{\infty} x(\tau)w(\tau - t) e^{-j2\pi f\tau} d\tau \quad (3.61)$$

where $w(\tau)$ is the observation window.

The squared modulus of the short-time Fourier transform is an energy distribution. This energy distribution $S_x^w(t, f)$ is called the *spectrogram* and it was one of the first attempts to obtain the equivalent of a time-dependent spectrum. The definition of the spectrogram is [Fla98]:

$$S_x^w(t, f) = |F_x^w(t, f)|^2 = \left| \int_{-\infty}^{\infty} x(\tau)w(\tau - t) e^{-j2\pi f\tau} d\tau \right|^2 \quad (3.62)$$

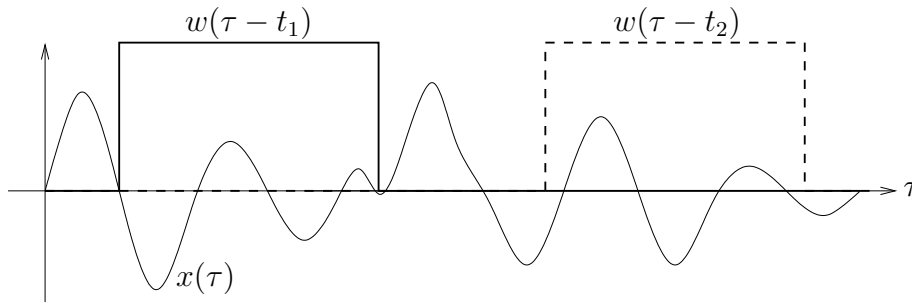


Figure 3.10: Illustration relative to the calculation of the short-time Fourier transform: signal $x(\tau)$ and sliding window $w(\tau - t)$ at two time instants t_1 and t_2 .

3.4.3.2 Properties

An important parameter of the spectrogram is the observation window $w(t)$. The type of window function can be chosen among common windows used in classical spectral estimation (see 3.3.4) in order to obtain the desired tradeoff between sidelobe attenuation and bandwidth of the mainlobe. The capability of the spectrogram to locate certain phenomena in time and frequency is strongly related to the chosen window length. A short observation window leads to a good time localization but at the expense of frequency resolution. On the contrary, a long observation window provides a high frequency resolution but an accurate time localization is no more possible. The windowed signal cannot be perfectly located in time and frequency simultaneously as a consequence of the Heisenberg-Gabor uncertainty principle.

In contrast to time-scale analysis, the spectrogram uses an observation window of constant length for all frequencies. This leads to a constant time and frequency resolution depending only on the window length. An illustration is shown in Fig. 3.11 for two cases with a short and long observation window. The figure shows that the spectrogram leads to a uniform rectangular mapping of the time-frequency plane. Note that the chosen representation is not accurate because the sliding windows normally overlap.

An important consequence is the fact that the spectrogram is not well adapted to the analysis of rapidly changing phenomena. The short-time Fourier transform supposes signal stationarity during the observation window. If this is not guaranteed the non-stationarity will not correctly be represented and information can be lost. Depending on the rate of change of the IF, an optimal window length $N_{w,opt}$ can be deduced for the spectrogram [Boa03], given by:

$$N_{w,opt} = \sqrt{2} \left| \frac{d}{dt} \text{IF}(t) \right|^{-1/2} \quad (3.63)$$

Another important property of the spectrogram concerns interferences in case of multicomponent signals. A multicomponent signal is the sum of several monocomponent signals e.g two sinusoidal signals at different frequencies. Due to their quadratic kernel, most quadratic time-frequency distributions show interference terms when multicomponent signals are analyzed (see further sections). The spectrogram is also a nonlinear distribution but the nonlinearity is only introduced

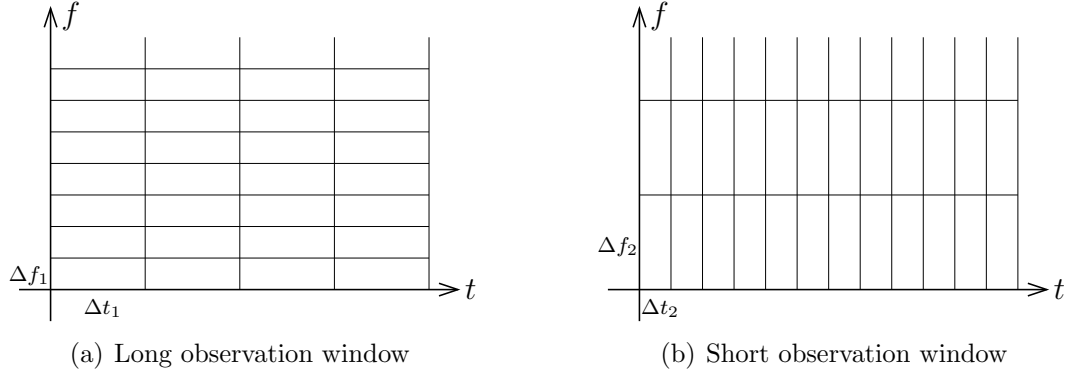


Figure 3.11: Illustration of time and frequency resolution of the spectrogram with respect to window length: The long window leads to good frequency resolution and bad time localization whereas the short window provokes bad frequency resolution but good localization in time ($\Delta f_1 < \Delta f_2$, $\Delta t_1 > \Delta t_2$).

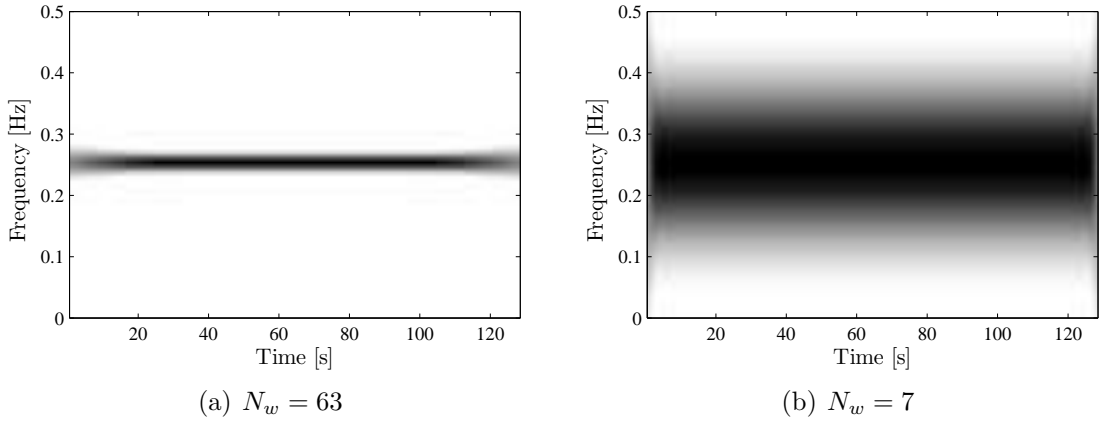


Figure 3.12: Spectrogram of 128 point sinusoidal signal with two different observation windows of length $N_w = 63$ and $N_w = 7$.

in the last step by squaring the short-time Fourier transform. Hence, the spectrogram does not lead to interferences at frequencies or time instants where normally no signal energy is present. Finally, the spectrogram resembles to the periodogram which also introduces a squaring operation in the last step.

3.4.3.3 Examples

Some examples are presented in the following section for illustration of the spectrogram and some of its properties. All the time-frequency distributions are calculated with the time-frequency toolbox for MATLAB [Aug96]. First, consider the spectrogram of a simple complex exponential at constant frequency, displayed in Fig. 3.12. The signal of length 128 samples is analyzed with a Hamming window of length N_w . The amplitudes of the spectrogram corresponding to energy density are coded in grayscale where a darker shade of grey represents a stronger amplitude. The spectrogram with $N_w = 63$ is constituted of a relatively thin line at the frequency

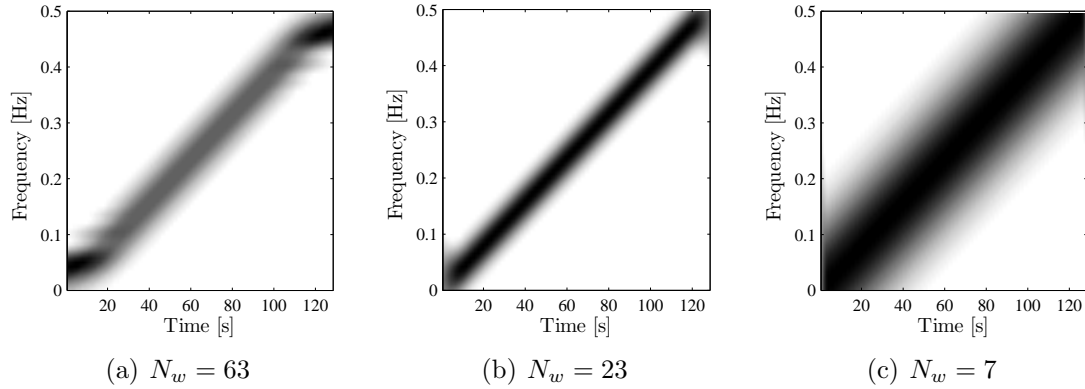


Figure 3.13: Spectrogram of 128 point chirp signal with observation windows of different length N_w where $N_w = 23$ is the optimal window length.

of the sinusoidal signal. Border effects due to the sliding window can be observed at the beginning and the end of the signal where only a part of the signal is analyzed by the window. With $N_w = 7$, the line representing the frequency of the sinusoid is large due to the short window. At the same time, border effects are reduced. These two cases demonstrate the tradeoff between time and frequency resolution. However, in case of signals with constant frequency, the optimal window length would be infinite (see equation (3.63)), i.e. equal to the total signal length in case of finite duration signals. Actually, this corresponds to the calculation of the periodogram.

A linear chirp signal with a normalized frequency varying from 0 to 0.5 is analyzed in Fig. 3.13. The signal length is 128 samples. Three different window lengths are used. Again, a tradeoff between time and frequency resolution must be found through the choice of the window length. As it can be seen in Fig. 3.13(a), the long window $N_w = 63$ leads to bad localization at the borders and a relatively broad linear component. The short window $N_w = 7$ with its poor frequency resolution leads also to a poor energy localization. The optimal window length for a chirp signal is $N_{w,opt} = \sqrt{2T/B}$ according to (3.63) with T the signal duration and B the bandwidth. $N_{w,opt} = 23$ is obtained in this case. The corresponding spectrogram is displayed in Fig. 3.13(b) and demonstrates a good compromise between time and frequency resolution.

3.4.4 Wigner Distribution

3.4.4.1 Definition

In 1948, J. Ville proposed a different approach to obtain the instantaneous spectrum of a signal [Vil48]. He defined a time-frequency energy distribution which is nowadays commonly called the *Wigner Distribution* (WD) or *Wigner-Ville Distribution*. This refers to the physician E. P. Wigner who mentioned the distribution in the context of quantum mechanics [Wig32]. The Wigner Distribution $W_x(t, f)$

of a signal $x(t)$ is defined as:

$$W_x(t, f) = \int_{-\infty}^{+\infty} x\left(t + \frac{\tau}{2}\right) x^*\left(t - \frac{\tau}{2}\right) e^{-j2\pi f\tau} d\tau \quad (3.64)$$

The WD can be seen as the Fourier transform of a kernel $K_x(t, \tau)$ with respect to the delay variable τ :

$$W_x(t, f) = \mathfrak{F}_{\tau \rightarrow f} \{K_x(t, \tau)\} \quad \text{with} \quad K_x(t, \tau) = x\left(t + \frac{\tau}{2}\right) x^*\left(t - \frac{\tau}{2}\right) \quad (3.65)$$

The kernel can be interpreted as the instantaneous autocorrelation function of $x(t)$. Comparing the WD definition to the spectrogram, it becomes clear that the WD does not depend on any parameter whereas the spectrogram depends on the shape and length of the observation window. This is an advantage because no a priori knowledge is necessary to choose this parameter.

3.4.4.2 Properties

Some important properties of the WD are mentioned in the following. More details can be found in [Mec97] [Fla98] [Boa03].

- The WD is real valued: $W_x(t, f) \in \mathbb{R} \quad \forall t, f$
- The WD was interpreted by Ville as an instantaneous spectrum because it satisfies the so-called time and frequency marginals: the integration of $W_x(t, f)$ with respect to frequency yields the instantaneous power, integration with respect to time gives the energy spectrum [Fla98].

$$\text{Time marginal:} \quad \int_{-\infty}^{+\infty} W_x(t, f) df = |x(t)|^2 \quad (3.66)$$

$$\text{Frequency marginal:} \quad \int_{-\infty}^{+\infty} W_x(t, f) dt = |X(f)|^2 \quad (3.67)$$

Consequently, the integration over time and frequency yields the signal energy.

- If the WD is interpreted as a probability density, the first moment of the WD with respect to frequency gives the instantaneous frequency [Fla98]:

$$\frac{\int_{-\infty}^{+\infty} f W_z(t, f) df}{\int_{-\infty}^{+\infty} W_z(t, f) df} = \frac{1}{2\pi} \frac{d}{dt} \arg[z(t)] = \text{IF}_z(t) \quad (3.68)$$

where $z(t)$ is an analytical signal.

- The WD is time and frequency covariant i.e. a time or frequency shift in the signal causes the same shift in the WD:

$$y(t) = x(t - t_0) \Rightarrow W_y(t, f) = W_x(t - t_0, f) \quad (3.69)$$

$$y(t) = x(t)e^{j2\pi f_0 t} \Rightarrow W_y(t, f) = W_x(t, f - f_0) \quad (3.70)$$

- The WD of a linear complex chirp signal is perfectly concentrated on the IF law. Consider a linear chirp $x(t)$ according to (3.53) with:

$$z(t) = A \exp j2\pi (\alpha_z t + \beta_z t^2/2) \quad (3.71)$$

Its WD is:

$$W_z(t, f) = \delta[f - (\alpha_z + \beta_z t)] = \delta[f - \text{IF}_z(t)] \quad (3.72)$$

This illustrates that the previously mentioned Heisenberg-Gabor uncertainty principle does not apply to the WD.

- The WD of the sum of two signals $x(t) + y(t)$ is obtained by the following quadratic superposition:

$$W_{x+y}(t, f) = W_x(t, f) + W_y(t, f) + 2\Re\{W_{xy}(t, f)\} \quad (3.73)$$

where $W_{xy}(t, f)$ is the cross Wigner Distribution of x and y :

$$W_{xy}(t, f) = \int_{-\infty}^{+\infty} x\left(t + \frac{\tau}{2}\right) y^*\left(t - \frac{\tau}{2}\right) e^{-j2\pi f\tau} d\tau \quad (3.74)$$

This last property has the important consequence that the WD of a multicomponent signal is different from the sum of the WDs of the single signals. Actually, the WD of a multicomponent signal contains interference terms that appear at time instants and frequencies where there should not be any signal energy. These interferences are the result of the quadratic kernel. They considerably complicate the lecture and interpretation of the WD. Interferences resulting from interactions between two distinct components are also called *outer interferences*.

Other interferences, the so-called *inner interferences*, appear when signals with a nonlinear frequency modulation (FM) are analyzed. Linear FM signals are perfectly located in the WD but nonlinear FM such as quadratic IF laws or sinusoidal frequency modulations also lead to interference terms.

3.4.4.3 Examples

Some examples illustrating the properties of the WD are presented in the following section. Since the distribution may take negative values in particular cases, only the positive values are displayed for visualization. First, the WD of a sinusoidal signal with constant normalized frequency 0.25 is displayed in Fig. 3.14(a). The signal energy is perfectly concentrated at 0.25 normalized frequency. The WD

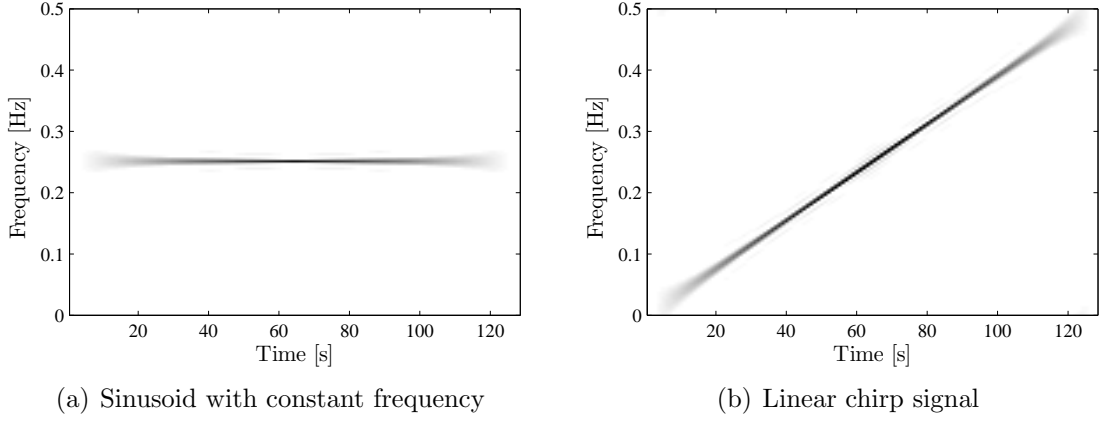


Figure 3.14: Wigner Distribution of sinusoidal signal with constant frequency and WD of linear chirp signal.

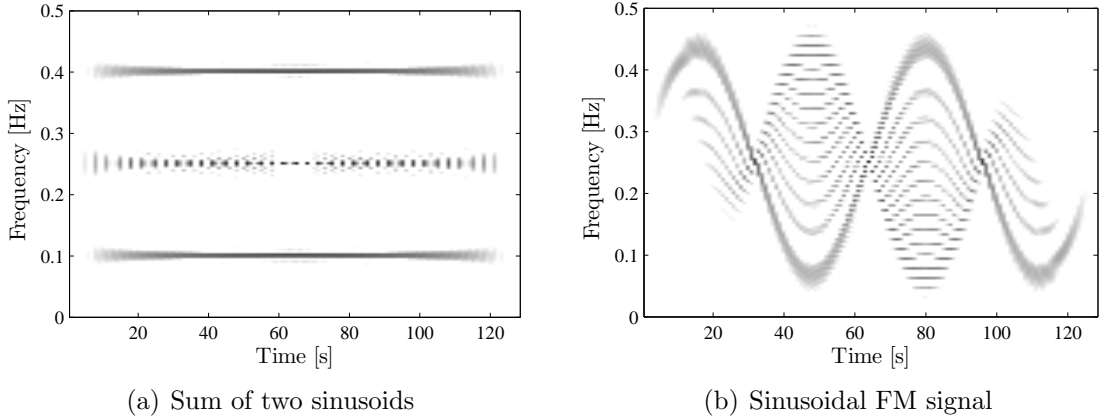


Figure 3.15: Wigner Distribution of sum of two sinusoidal signals with constant frequency and WD of sinusoidal FM signal.

amplitude is smaller at the borders due to the finite signal length. Then, a linear chirp signal is analyzed in Fig. 3.14(b). It can be noticed that the distribution is perfectly concentrated on the IF law of the chirp signal, especially in comparison to the spectrogram (see Fig. 3.13). This corresponds to the previously mentioned properties of the WD.

The apparition of interference is illustrated in two examples. Fig. 3.15(a) shows the WD of the sum of two sinusoidal signals at 0.1 and 0.4 normalized frequency. In addition to the two constant frequencies at 0.1 and 0.4, oscillating terms appear in the distribution at 0.25 normalized frequency. These so-called outer interferences are of relatively strong amplitude and they oscillate i.e. they take negative and positive values. The apparition of negative values in the WD signifies that it cannot be interpreted as an energy distribution in the general case. It has been shown theoretically that the interference terms are generally of oscillating nature and that they are located at the geometrical center of two components [Mec97] [Fla98].

The second type of interference, called inner interference terms, are illustrated

in Fig. 3.15. The signal is a monocomponent FM signal with a sinusoidal frequency modulation. The numerous interferences in the WD demonstrate the fact that they are also produced by nonlinear frequency modulations. Again, their oscillating nature is clearly visible. This example shows that the lecture of the time-frequency distribution can be difficult with these type of signals. A possible solution is smoothing of the WD which will be described in the following.

3.4.5 Smoothed Wigner Distributions

3.4.5.1 Definitions

The previous section has shown that the interference terms in the WD can take strong values which bother the interpretation. Furthermore, the kernel function $K_x(t, \tau)$ exists on an infinite support with respect to τ , leading to problems with the practical implementation. Hence, it can be advantageous to limit the support of $K_x(t, \tau)$ with respect to τ by introducing a window function $p(\tau)$. This leads to the so-called *Pseudo Wigner Distribution* (PWD) $PW_x(t, f)$, defined as:

$$PW_x(t, f) = \int_{-\infty}^{+\infty} p(\tau) x\left(t + \frac{\tau}{2}\right) x^*\left(t - \frac{\tau}{2}\right) e^{-j2\pi f\tau} d\tau \quad (3.75)$$

Some authors also call this distribution the *windowed Wigner Distribution* [Boa03].

The original WD kernel $K_x(t, \tau)$ is therefore multiplied with a window function with respect to the delay variable τ . The PWD is then the Fourier transform of this product with respect to τ . The effect on the WD becomes clear considering that a multiplication in the time domain is equivalent to a convolution product in the frequency domain. Hence, the PWD is the convolution of the window Fourier transform $P(f)$ with the original WD $W_x(t, f)$:

$$PW_x(t, f) = \mathfrak{F}_{\tau \rightarrow f} \{p(\tau) K_x(t, \tau)\} = \int_{-\infty}^{+\infty} P(f - \xi) W_x(t, \xi) d\xi \quad (3.76)$$

This relation clearly illustrates that the PWD is related to the WD by a smoothing only in the frequency direction [Fla98]. The time support and time resolution are therefore not affected, only the frequency resolution decreases. The latter can be controlled by adjusting the window length. A long temporal window $p(\tau)$ has a compact frequency support and leads only to a slight smoothing. A stronger reduction of the interferences is obtained with a shorter window. An infinite window with constant amplitude $p(\tau) = 1$ leads to the original WD.

In addition to frequency smoothing, the WD can also be smoothed in time by introducing a smoothing function which depends on t . It is often advantageous to control time and frequency smoothing separately. This is achieved by a separable smoothing function which is a product of two functions where each function depends on only τ or t . This leads to the definition of the *Smoothed Pseudo Wigner*

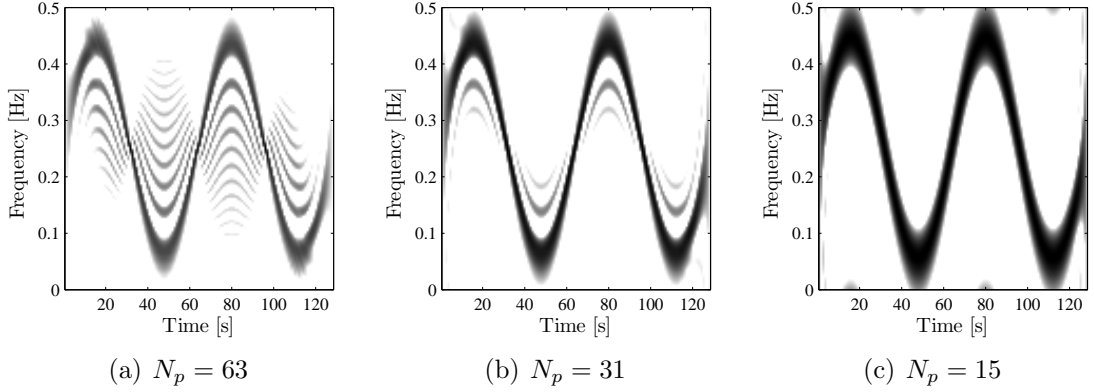


Figure 3.16: Pseudo Wigner Distribution of sinusoidal FM signal with smoothing windows of different length N_p .

Distribution (SPWD) $SPW_x(t, f)$ [Fla98]:

$$SPW_x(t, f) = \int_{-\infty}^{+\infty} p(\tau) \left[\int_{-\infty}^{+\infty} g(s-t) x\left(s + \frac{\tau}{2}\right) x^*\left(s - \frac{\tau}{2}\right) ds \right] e^{-j2\pi f\tau} d\tau \quad (3.77)$$

where $g(t)$ controls the time smoothing. Note that the special case of the PWD is obtained with no time smoothing i.e. $g(t) = \delta(t)$.

3.4.5.2 Examples

The smoothing properties of the PWD are first illustrated with a sinusoidal FM signal. The WD of this signal was shown in Fig. 3.15(b). There exist strong inner interferences due to the nonlinear frequency modulation. The PWD attenuates these interferences by a smoothing operation in the frequency direction. This is illustrated in Fig. 3.16 with different window lengths. The Hamming window of length $N_p = 63$ (see Fig. 3.16(a)) leads already to a noticeable attenuation of the interferences compared to the WD. A further reduction of the window length cancels out nearly all the interferences but leads also to a decrease in frequency resolution. This can be recognized by a loss of energy concentration, particularly in the regions where the frequency evolution is slow i.e. at the minimum and maximum instantaneous frequency.

The different time smoothing properties of the WD, PWD and SPWD can be illustrated with a Dirac delta function which is a signal perfectly located in time. The three calculated distributions are shown in Fig. 3.17. The WD of the Dirac delta function is perfectly located (see Fig. 3.17(a)) with all the energy concentrated at one point in time. Since the PWD smoothes only in the frequency direction, the perfect time localization is preserved as can be seen in Fig. 3.17(b)). Only the SPWD (see Fig. 3.17(c)) provides smoothing in the time direction and the energy of the Dirac delta function is therefore dispersed compared to the two other cases.

In the preceding section, the WD of the sum of two pure sinusoidal signals was calculated and shown in Fig. 3.15(a). The so-called outer interferences were

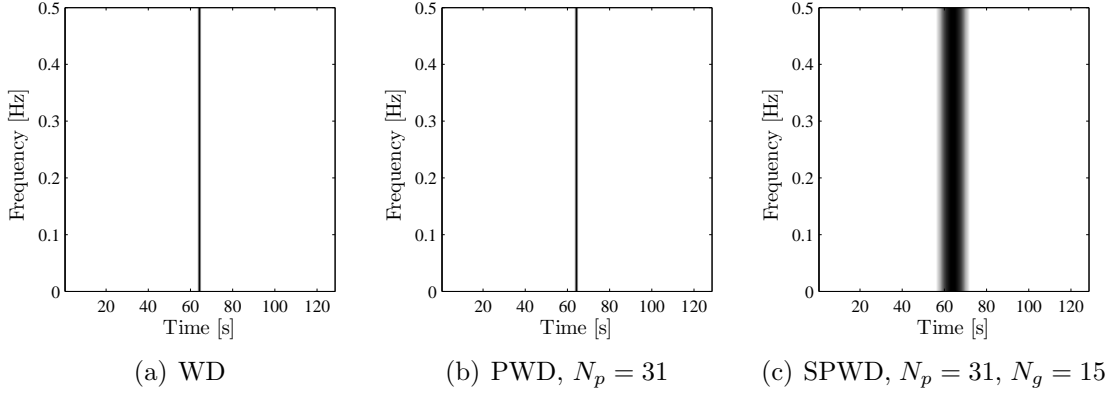


Figure 3.17: Wigner Distribution, Pseudo Wigner Distribution and Smoothed Pseudo Wigner Distribution of Dirac delta function.

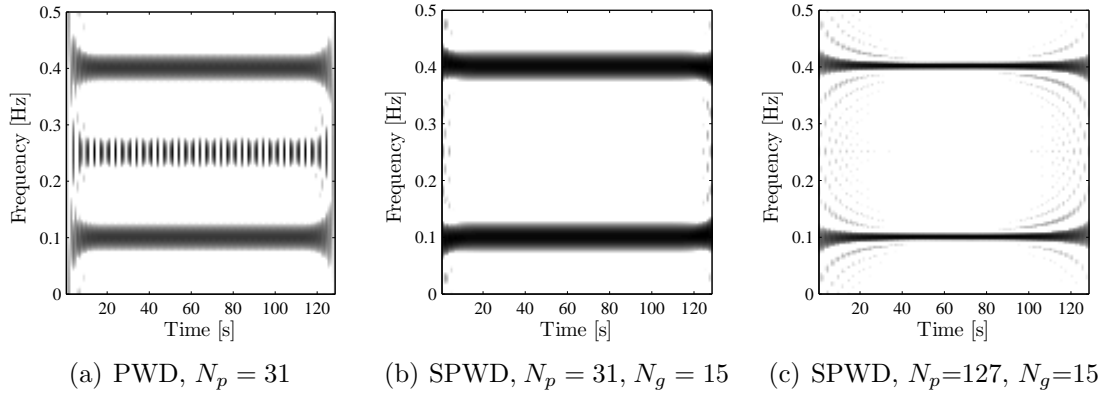


Figure 3.18: Pseudo Wigner Distribution and Smoothed Pseudo Wigner Distribution of sum of two sinusoidal signals with constant frequency.

located at the geometrical centre of the two components. The use of the PWD with the same signal is illustrated in Fig. 3.18(a). Despite the use of a 31 point Hamming window, the interferences are still present. In addition, the frequency resolution is degraded which can be seen by the relatively broad component at 0.1 and 0.4 normalized frequency. This is due to the particular structure of the interferences in this case. Since the interferences oscillate in the time direction, they are not significantly attenuated because the PWD provides only smoothing in the frequency direction. Only the smoothing in the time direction by the SPWD (see Fig. 3.18(b)) improves the readability of the distribution. If a better frequency resolution is desired, the smoothing in the frequency direction can be reduced by a longer window $p(\tau)$. This is realized in Fig. 3.18(c) with $N_p = 127$. A good compromise is achieved by using the time smoothing for the suppression of the interferences between the two components and only a slight frequency smoothing in order to preserve an acceptable frequency resolution.

3.4.6 Discrete Wigner Distribution

For practical implementation, a discrete expression for the WD must be derived. Starting from the definition of the WD in equation (3.64), the delay variable can be substituted by $\tau' = \tau/2$. The following equivalent definition is obtained [Fla98]:

$$W_x(t, f) = 2 \int_{-\infty}^{+\infty} x(t + \tau') x^*(t - \tau') e^{-j4\pi f \tau'} d\tau' \quad (3.78)$$

A discrete version of this expression can then be easily obtained by replacing the integral with a sum. The WD of a discrete-time signal $x[n]$ with $n = t f_s$ is [Fla98]:

$$W_x[n, f] = 2 \sum_{m=-\infty}^{+\infty} x[n + m] x^*[n - m] e^{-j4\pi f m / f_s} \quad (3.79)$$

If the signal is time limited with N samples, the summation index m is limited to $m < |N/2|$ [Boa03].

An important issue when considering the discrete Wigner Distribution (DWD) is the influence of sampling. It has been demonstrated in section 3.2.5 that the Fourier transform of a discrete-time signal is periodic in the frequency domain. In order to avoid overlapping and aliasing, the sampling frequency must be chosen according to the Nyquist-Shannon sampling theorem. The WD is basically the Fourier transform of the product of two signals $x(t)$ with a different time shift. This product, however, has an increased bandwidth compared to the signal $x(t)$. Actually, if $x(t)$ is of bandwidth B , the kernel will be of bandwidth $2B$. When discrete-time signals are considered, the kernel is also a discrete signal. Therefore, the Fourier transform of the kernel i.e. the DWD is also periodic. If the original signal was sampled at the Nyquist frequency, aliasing appears in the DWD due to the increased bandwidth of the kernel [Fla98]. This is illustrated at the top of Fig. 3.19.

Two solutions exist to this problem: First, the real signal can be sampled at twice the Nyquist frequency. The second possibility is the use of the analytical signal. The negative frequencies of the analytical signal are zero and thus, the bandwidth is only half the bandwidth of the real signal. Therefore, the DWD of the analytical signal is free of aliasing as shown at the bottom of Fig. 3.19.

In equation (3.79), the frequencies are not yet discretized. Since the DWD is periodic in f with frequency $f_s/2$ it is convenient to choose [Boa03]:

$$f = \frac{k f_s}{2N} \quad \text{with} \quad k = 0, 1, 2, \dots, N-1 \quad (3.80)$$

Then, equation (3.79) becomes:

$$W_x[n, k] = 2 \sum_{m < |N/2|} x[n + m] x^*[n - m] e^{-j2\pi k m / N} \quad (3.81)$$

This expression is called the *discrete Wigner Distribution*. It can be considered as the discrete Fourier transform of the discrete kernel $x[n + m] x^*[n - m]$. Therefore, if an appropriate signal length is chosen, FFT algorithms can be used for fast computation.

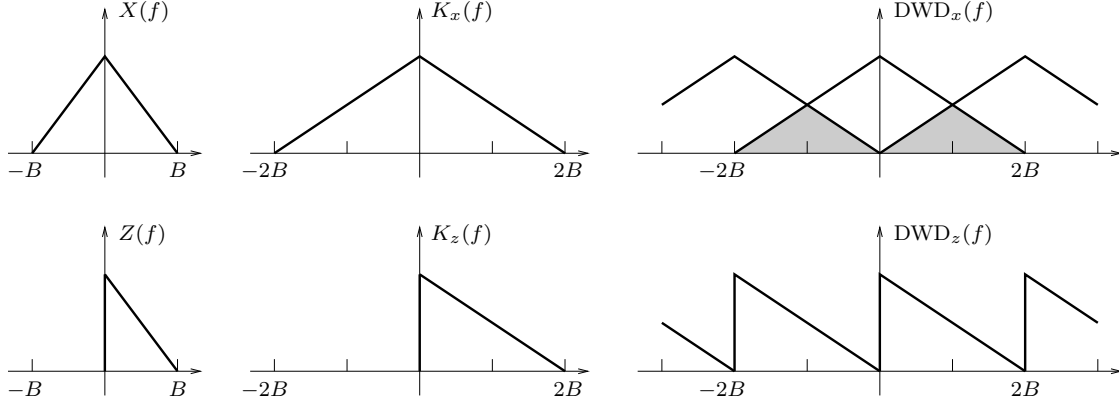


Figure 3.19: Illustration relative to the sampling of the WD: Spectrum $X(f)$ of real signal, kernel spectrum $K_x(f)$ and $DWD_x(f)$ (top) with aliasing; spectrum $Z(f)$ of analytical signal, kernel spectrum $K_z(f)$ and $DWD_z(f)$ (bottom).

3.4.7 Time-Frequency vs. Time-Scale Analysis

Wavelet transforms or time-scale analysis have recently been very popular and they have been successfully applied to condition monitoring and fault diagnosis of rotating machines. Most works employ these methods to mechanical signals. Wavelet analysis compares the signal with a particular reference function called wavelet. The wavelet can be shifted in time and scaled to alter its frequency content. The correlation of the signal to analyze with the shifted and scaled wavelets yields a two dimensional signal representation $T_x(t, a)$ as a function of time t and scale a . The continuous wavelet transform $T_x(t, a)$ of a signal $x(t)$ is defined as:

$$T_x(t, a) = \int_{-\infty}^{+\infty} x(\tau) \frac{1}{\sqrt{a}} \psi^* \left(\frac{\tau - t}{a} \right) d\tau \quad (3.82)$$

where $\psi(t)$ is the mother wavelet. The scale a is the equivalent to the inverse of a frequency: small scale corresponds to high frequencies.

The wavelet transform can be compared to the short-time Fourier transform which is also a so-called *atomic decomposition* of a signal. The spectrogram can be interpreted as a projection of the signal on atoms that are windowed complex exponentials of different frequency, shifted in time through the sliding observation window. The wavelet transform yields a signal projection on scaled and shifted versions of the mother wavelet. Therefore, the wavelet transform is also limited in time-frequency resolution by the Heisenberg-Gabor uncertainty principle since the wavelet localization in time and frequency is limited. However, due to scaling of the mother wavelet, the resolution is not uniform with respect to frequency as it was the case with the spectrogram.

This is illustrated in Fig. 3.20 where the time-frequency resolution of the spectrogram is compared to time-scale analysis. Since the window length of the spectrogram is constant with respect to frequency, the time-frequency resolution is the same in the whole time-frequency plane. On the contrary, the scaling leads to the use of shorter wavelets in the regions of higher frequency. Therefore, when

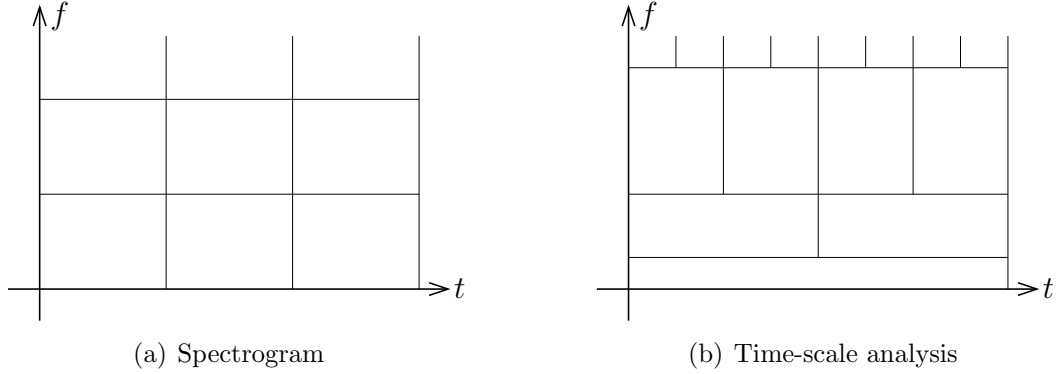


Figure 3.20: Comparison of time and frequency resolution with the spectrogram and time-scale analysis.

the time resolution improves, the frequency resolution is degraded. The product of time and frequency resolution is constant i.e. the surface of the depicted rectangles in Fig. 3.20(b) is always the same. Comprehensive literature on time-scale analysis and the wavelet transform is e.g. [Dau92] [Mal00].

An interesting question is the choice between time-scale or time-frequency analysis in the considered application of motor condition monitoring. In contrast to time-scale analysis, time-frequency analysis provides a signal representation with respect to time and frequency instead of scale. Since the considered mechanical faults lead to phenomena at particular frequencies, the interpretation of the time-frequency representation is easier in the context of this application than the time-scale representation. Moreover, the wavelet transform yields a representation where time and frequency resolution are not constant over all frequencies. The nature of the considered signals in our application implies linear frequency characteristics e.g. harmonics at nf_s and sidebands at $nf_s \pm f_r$ resulting from modulations. Therefore, a constant frequency resolution over the total frequency range is desirable which provides another argument in favor of time-frequency analysis.

3.5 Parameter Estimation

In the further course of this work, a second approach to fault detection is studied: signal parameter estimation. This approach does not rely on frequency analysis but uses knowledge of the temporal signal model to identify its parameters. In chapter 2, models for the stator current signal in presence of a fault have been developed. Two models considering torque oscillations and eccentricity were obtained and each of the models shows a different type of modulation, but with equal modulation frequencies. The idea is to identify the parameters of these two models from a stator current measurement. The values obtained for the modulation indices contain directly information about the fault severity and the type of modulation prevailing in the measured signals. This means that in contrast to the time-frequency approach, postprocessing and feature extraction is not necessary. Furthermore, the information about the modulation type indicates the origin of

the mechanical fault which can be helpful for a more detailed diagnosis.

Another advantage is the shorter required data record length in comparison to classical, non-parametric spectral estimation. The traditional approach assumes that the data outside the observation interval is zero. This leads to the well-known effect of convolution in the frequency domain with the Fourier transform of the observation window. A model based approach does not assume the signal being zero outside the observation and it is well adapted identifying the signal parameters with a limited number of samples [Kay88]. Nevertheless, increasing the number of samples also increases the estimation accuracy. The use of a priori knowledge, i.e. the appropriate signal model, improves the estimation performance. On the contrary, the choice of an incorrect model may lead to completely false results whereas the non-parametric approach does not require a priori knowledge.

The parameter estimation approach is also interesting with regard to the use of discrete-time signals. In general, spectra or time-frequency distributions are theoretically studied using continuous-time signals. In parameter estimation, the theoretical considerations are conducted from the beginning on with discrete-time signals and with a finite number of samples which leads therefore to more coherence between theory and practical implementation.

The following sections describe first some basic concepts related to parameter estimation and the theoretical Cramer-Rao lower bound for the estimation error. Then, the maximum likelihood estimator is explained, followed by some issues about detection.

3.5.1 Basic concepts

Parameter estimation problems can be found in various applications [Kay93]. In the radar application for instance, the problem is to estimate the distance to a target, e.g. from an airport to an aircraft, based on a transmitted and received waveform. In all applications, the measurements correspond to signals embedded in noise.

The first important step in an estimation problem is the choice of the underlying mathematical data model. The model describes the observed data $x[n]$ and contains in general several unknown parameters $\underline{\theta}$ that are to be estimated. The model also includes a stochastic component representing measurement noise. Then, the a priori knowledge can be summarized by the probability density function $p(x; \underline{\theta})$ of the data. The estimator is a function that yields the estimate $\hat{\underline{\theta}}$ with respect to an observation $x[n]$.

Let us consider a simple example: A measured signal $x[n]$ is supposed to be a DC level A plus additive white Gaussian noise $w[n]$. The sample length is N . The data is therefore modelled as:

$$x[n] = A + w[n] \quad n = 0, 1, \dots, N-1 \quad (3.83)$$

A realization of this signal is shown in Fig. 3.21. If the unknown parameter is the DC level, the parameter vector is a scalar $\theta = A$.

Each sample of $w[n]$ is supposed to have the probability density function (PDF) $N(0, \sigma^2)$ i.e. a Gaussian distribution with zero mean and variance σ^2 . The PDF of

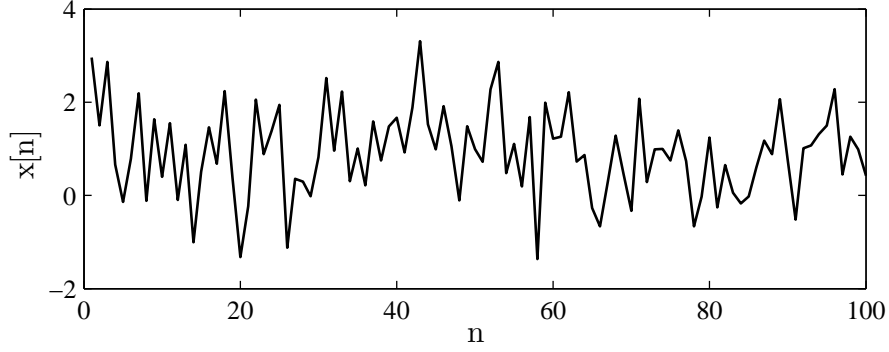


Figure 3.21: Realization of DC level embedded in white Gaussian noise.

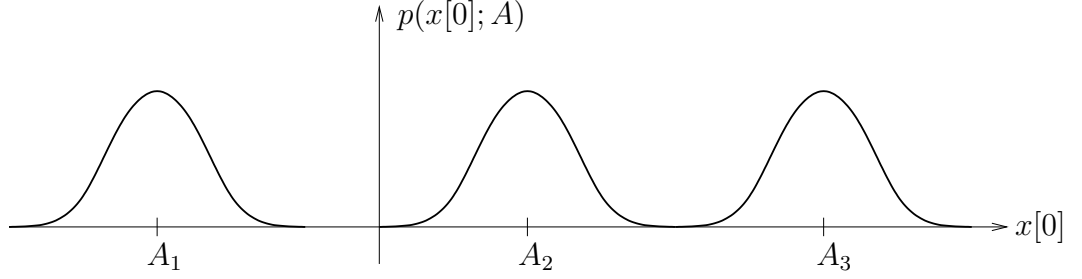


Figure 3.22: Illustration of the probability density function $p(x[0]; A)$ for different parameter values.

the first sample $x[0]$ would therefore be:

$$p(x[0]; A) = \frac{1}{\sqrt{2\pi\sigma^2}} \exp \left[-\frac{1}{2\sigma^2} (x[0] - A)^2 \right] \quad (3.84)$$

where $p(x[0]; A)$ denotes a class of PDFs due to several possible values of A . Several PDFs are illustrated at Fig. 3.22. Considering N samples, the joint PDF is the product of the PDFs for each sample if the noise samples are uncorrelated i.e. if the random variables are independent [Pap65]. Hence, the following PDF is obtained:

$$p(x; A) = \frac{1}{(2\pi\sigma^2)^{\frac{N}{2}}} \exp \left[-\frac{1}{2\sigma^2} \sum_{n=0}^{N-1} (x[n] - A)^2 \right] \quad (3.85)$$

In the preceding example, the parameter A was unknown, but deterministic. Estimation methods based on this assumption are termed *classical estimation* [Kay93]. If the parameters are assumed being random variables, this information can be incorporated through a conditional PDF. This approach is called *Bayesian estimation*.

3.5.2 Estimator Performance and Cramer-Rao Lower Bound

If the estimator performance is evaluated, an optimality criterion has to be fixed. Often, the mean square error (MSE) is used as criterion, measuring the average

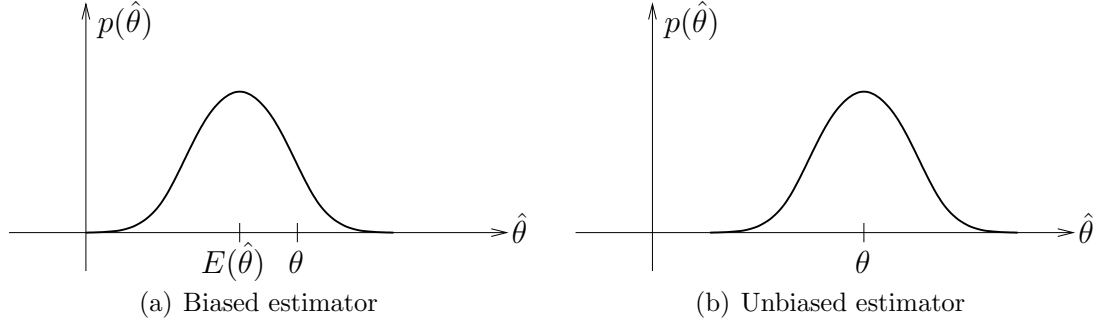


Figure 3.23: Illustration of probability density function of biased and unbiased estimator.

mean squared deviation of the estimator values $\hat{\theta}$ from the true value θ [Kay93]:

$$\text{MSE}(\hat{\theta}) = E \left\{ \left(\hat{\theta} - \theta \right)^2 \right\} \quad (3.86)$$

The MSE can be rewritten:

$$\begin{aligned} \text{MSE}(\hat{\theta}) &= E \left\{ \left[\hat{\theta} - E(\hat{\theta}) + E(\hat{\theta}) - \theta \right]^2 \right\} \\ &= \text{var} \left\{ \hat{\theta} \right\} + \left[E(\hat{\theta}) - \theta \right]^2 = \text{var} \left\{ \hat{\theta} \right\} + b^2(\theta) \end{aligned} \quad (3.87)$$

since the other terms cancel out. This expression demonstrates that the MSE is composed of the variance of the estimator and the squared bias $b(\theta)$.

The estimator bias $b(\theta)$ is defined as the difference between the estimator mean $E(\hat{\theta})$ and the true value θ :

$$b(\theta) = E \left\{ \hat{\theta} \right\} - \theta \quad (3.88)$$

An estimator is unbiased if $b(\theta) = 0$ i.e. $E(\hat{\theta}) = \theta$. This signifies that on the average, the estimator yields the true value of the unknown parameter. Unbiasedness is an important and in general required property of an estimator. The PDFs of an unbiased and biased estimator are displayed in Fig. 3.23 for illustration. Hence, it can be concluded that if an estimator is unbiased, the remaining mean square estimation error is the estimator variance. When the performance of several unbiased estimators is compared, the ideal one would have the minimum variance. Such an estimator is called minimum variance unbiased (MVU) estimator.

For a given estimation problem, a theoretical lower bound, called the *Cramer-Rao lower bound* (CRLB) exists for the estimator variance. It determines the best theoretical performance an estimator may attain. The evaluation of the CRLB thus gives valuable information about the minimum achievable estimation error.

A necessary condition for the calculation of the CRLB is that the PDF $p(x; \theta)$ satisfies the so-called *regularity condition* [Kay93]:

$$E \left\{ \frac{\partial \ln p(x; \theta)}{\partial \theta_i} \right\} = 0 \quad \forall \theta_i \quad (3.89)$$

The Fisher information matrix $I(\underline{\theta})$ is defined as:

$$[I(\underline{\theta})]_{ij} = -E \left\{ \frac{\partial^2 \ln p(x; \underline{\theta})}{\partial \theta_i \partial \theta_j} \right\} \quad (3.90)$$

The CRLB is then obtained as the diagonal elements of the inverse Fisher information matrix:

$$\text{var} \left\{ \hat{\theta}_i \right\} \geq [I^{-1}(\underline{\theta})]_{ii} \quad (3.91)$$

If an estimator can be found that satisfies the equality condition, it is the MVU estimator.

For illustration, consider the preceding example of estimating a DC level A in white Gaussian noise. Straightforward derivations lead to:

$$\text{var} \left\{ \hat{A} \right\} \geq \frac{\sigma^2}{N} \quad (3.92)$$

Let us now examine one possible estimator for A . A reasonable choice could be:

$$\hat{A} = \frac{1}{N} \sum_{n=0}^{N-1} x[n] \quad (3.93)$$

which is the sample mean. This estimator is unbiased because:

$$E(\hat{A}) = E \left\{ \frac{1}{N} \sum_{n=0}^{N-1} x[n] \right\} = \frac{1}{N} \sum_{n=0}^{N-1} E(x[n]) = A \quad (3.94)$$

Its variance can be calculated according to:

$$\text{var} \left\{ \hat{A} \right\} = \text{var} \left\{ \frac{1}{N} \sum_{n=0}^{N-1} x[n] \right\} = \frac{1}{N^2} \text{var} \left\{ \sum_{n=0}^{N-1} x[n] \right\} = \frac{1}{N^2} N \sigma^2 = \frac{\sigma^2}{N} \quad (3.95)$$

The variance of this estimator is N/σ^2 and it equals the CRLB. The estimator is therefore the MVU estimator and thus the best estimator for this problem.

3.5.3 Maximum Likelihood Estimation

In the previous section, it was shown that the optimal estimator for a given problem is the MVU estimator. This estimator is unbiased and its variance is equal to the CRLB. However, there is no general method describing how this estimator can be found. Especially in case of complex problems, it may even not exist. On the contrary, the *maximum likelihood estimator* (MLE) is provided by a systematic method. This estimator is approximately the MVU estimator, i.e. for large data records, it is asymptotically unbiased and its variance approaches the CRLB [Kay93]. Moreover, this estimator can be easily derived and its practical implementation is possible.

When the PDF $p(x; \underline{\theta})$ is considered a function of the unknown parameters with x fixed, it is termed the *likelihood function*. This function indicates which values

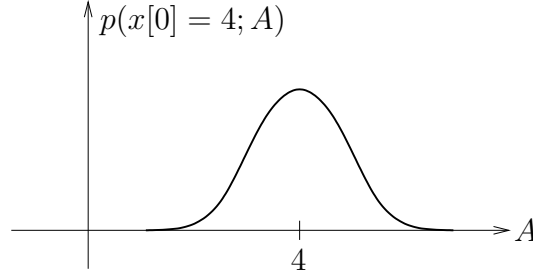


Figure 3.24: Example of likelihood function for parameter A after observation of one single sample $x[0]$.

of θ are likely based on the observation of x . Consider for illustration the previous example of estimating a DC level embedded in white Gaussian noise. If one single sample $x[0]$ is observed and this sample takes e.g. the value 4, the likelihood function takes the shape displayed in Fig. 3.24. According to this function, the parameter A is likely to take values near 4.

This leads to the definition of the MLE: The MLE for a vector parameter $\underline{\theta}$ is found by maximizing the likelihood function $p(x; \underline{\theta})$ over the allowable domain for $\underline{\theta}$. The location of the maximum yields the estimate $\hat{\underline{\theta}}$. In the previous example, this corresponds to the reasonable consideration that $A = 4$ is more likely than e.g. $A = 6$. If A had to be estimated based on this observation, it would be reasonable to choose $\hat{A} = 4$ according to the maximum of the likelihood function.

In case of the previous example of estimating a DC level in white Gaussian noise, the MLE is obtained in the following way. The likelihood function is the PDF of the observed samples with respect to the unknown parameter:

$$p(x; A) = \frac{1}{(2\pi\sigma^2)^{\frac{N}{2}}} \exp \left[-\frac{1}{2\sigma^2} \sum_{n=0}^{N-1} (x[n] - A)^2 \right] \quad (3.96)$$

The value of A that maximizes this function is the maximum likelihood estimate. Maximizing $p(x; A)$ with respect to A is equivalent to maximizing the exponent with respect to A . Derivation of the exponent yields:

$$\frac{\partial}{\partial A} \left[-\frac{1}{2\sigma^2} \sum_{n=0}^{N-1} (x[n] - A)^2 \right] = \frac{1}{\sigma^2} \sum_{n=0}^{N-1} (x[n] - A) \quad (3.97)$$

Setting this expression to zero, the MLE is obtained as:

$$\hat{A} = \frac{1}{N} \sum_{n=0}^{N-1} x[n] \quad (3.98)$$

The MLE is therefore the sample mean. This result is identical to the previous MVU estimator, showing that the MLE results in this particular case in the optimal estimator.

In this example, the maximum of the likelihood function could be calculated as a closed analytical expression. Generally, this is not possible in more complex

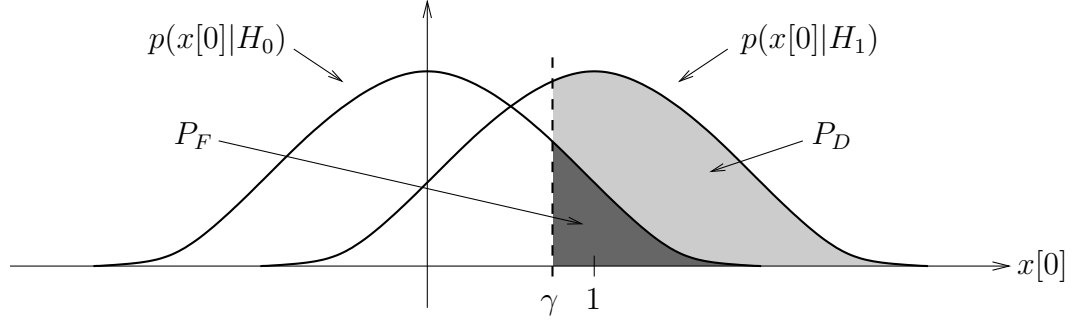


Figure 3.25: Probability density functions of $x[0]$ for hypothesis H_0 and H_1 .

estimation problems. In these cases, the maximum of the likelihood function can be found by numerical optimization techniques that may however be time-intensive to compute.

3.5.4 Detection

When dealing with fault detection in electrical drives, we might want to decide between two situations: The drive is healthy or a fault is present. The decision will be based on a signal observation followed by an adequate processing in order to extract a suitable fault indicator. The indicator calculation can be based on the previously described parametric or non-parametric methods. The problem is therefore equivalent to a binary hypothesis test [Kay98].

A relatively simple and general example is the signal detection problem. Based on an observation $x[n]$, we want to decide between the two hypothesis H_0 (noise only hypothesis) and H_1 (signal + noise hypothesis):

$$\begin{aligned} H_0 : \quad & x[n] = w[n] \\ H_1 : \quad & x[n] = s[n] + w[n] \end{aligned}$$

where $w[n]$ denotes the noise and $s[n]$ the signal to detect. For simplification, consider in the following that only one single sample $x[0]$ is observed and that the signal $s[0] = 1$. The noise $w[n]$ is supposed to be white and Gaussian with variance σ^2 .

The two probability density functions are therefore the following:

$$\begin{aligned} p(x[0]|H_0) &= \frac{1}{\sqrt{2\pi\sigma^2}} \exp \left[-\frac{1}{2\sigma^2} x[0]^2 \right] \\ p(x[0]|H_1) &= \frac{1}{\sqrt{2\pi\sigma^2}} \exp \left[-\frac{1}{2\sigma^2} (x[0] - 1)^2 \right] \end{aligned}$$

where $p(x[0]|H_0)$ denotes a conditional PDF. They are displayed for a given variance σ^2 in Fig. 3.25. For a high variance, the PDFs overlap more which complicates in consequence the detection problem.

In this binary hypothesis test, the decision between H_0 and H_1 will be based on a threshold γ . If $x[0] > \gamma$, H_1 will be decided, otherwise H_0 . Thus, four situations

can be distinguished: two correct decisions i.e. deciding H_0 (H_1) when H_0 (H_1) is true and the two following errors:

- Decide H_1 when H_0 is true. This error is called *Type I error* or *false alarm*.
- Decide H_0 when H_1 is true. This situation is termed *Type II error* or *miss*.

The probabilities for correct or false decisions depend on the choice for the threshold γ . The detector performance is generally characterised by two probabilities:

Probability of detection P_D : It expresses the probability for deciding H_1 when H_1 is true. P_D equals in the preceding example the surface under the PDF $p(x[0]|H_1)$ with $x[0] > \gamma$ (see Fig. 3.25):

$$P_D = p(H_1; H_1) = p(x[0] > \gamma; H_1) = \int_{\gamma}^{+\infty} \frac{1}{\sqrt{2\pi\sigma^2}} \exp \left[-\frac{1}{2\sigma^2}(\tau - 1)^2 \right] d\tau \quad (3.99)$$

Probability of false alarm P_F : The probability for deciding H_1 when H_0 is true. P_F equals in the preceding example the surface under the PDF $p(x[0]|H_0)$ with $x[0] > \gamma$ (see Fig. 3.25):

$$P_F = p(H_1; H_0) = p(x[0] > \gamma; H_0) = \int_{\gamma}^{+\infty} \frac{1}{\sqrt{2\pi\sigma^2}} \exp \left[-\frac{1}{2\sigma^2}\tau^2 \right] d\tau \quad (3.100)$$

The probability of miss and the probability of deciding correctly H_1 are the complementary probabilities of P_D and P_F respectively.

An ideal detector is characterised by $P_D = 1$ and $P_F = 0$ which signifies that the probabilities of the two errors is zero. This is only possible if the two PDFs are completely distinct from each other. In general, this is not the case and P_D and P_F depend on the threshold γ . Considering the previous example in Fig. 3.25, it can be seen that a higher threshold γ reduces the probability of false alarm P_F but leads at the same time to a lower probability of detection P_D . On the contrary, decreasing γ increases P_D but also P_F . It is therefore obvious that a tradeoff exists between P_D and P_F for a given detection problem.

The detector performance can be visualized by plotting P_D versus P_F for different threshold values. The resulting graph is termed *receiver operating characteristic* (ROC) [Tre01]. For a desired probability of false alarm P_F , the value of P_D can be directly read. Several ROC curves are displayed in Fig. 3.26. The ideal ROC curve is $P_D = 1$ for all P_F . The poorest detector performance is a ROC curve where $P_D = P_F$ (dashed line)[Kay98]. Realistic curves are situated between them. When the threshold γ increases, P_F decreases but also P_D and the ROC curve tends versus the point $(0, 0)$.

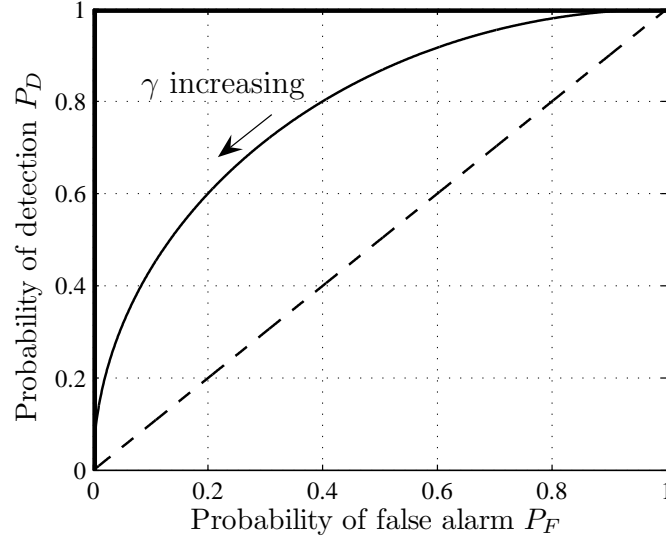


Figure 3.26: Example of receiver operating characteristics (ROC).

3.6 Summary

This chapter provided an introduction to the signal processing methods that will be used in the further course of this work. After some general remarks on classes of signals, basic tools such as correlation and the Fourier transform were recalled followed by a presentation of the concept of analytical signals. The next part dealt with the most widely used method for frequency domain analysis which is classical spectral estimation. The most popular estimator, the periodogram, was discussed together with the influence of certain important parameters such as data record length, windowing and averaging.

After this first part on stationary signal analysis, the concept of time-frequency analysis was introduced. Several methods were discussed together with their performances. An important criterion is the achievable time-frequency resolution. The resolution power of the Wigner Distribution was shown to be superior the spectrogram but at the expense of interferences. Methods for interference reduction by different smoothing operations were then mentioned.

An alternative approach for stationary or quasi-stationary signals is parameter estimation. Advantages include shorter data records and the directly obtained fault indicator. However, a priori knowledge is necessary and the performance of the method depends considerably on the model accuracy. The maximum likelihood estimator provides a practical estimation method with good asymptotical performances. At last, some basic concepts of detection theory in case of binary hypothesis testing were presented.

In the subsequent chapter, these methods will be applied to the signal models derived in chapter 2 with the aim to determine fault signatures and indicators. Steady and transient conditions will be considered.

Chapter 4

Fault Signatures with the Employed Signal Processing Methods

Contents

4.1	Introduction	94
4.2	Spectral Estimation	95
4.2.1	Stationary PM Signal	96
4.2.2	Stationary AM Signal	97
4.2.3	Simulation Results	98
4.2.4	Fault Indicator	99
4.3	Time-Frequency Analysis	103
4.3.1	Instantaneous Frequency	103
4.3.1.1	Stationary PM Signal	103
4.3.1.2	Transient PM Signal	104
4.3.1.3	AM Signal	105
4.3.1.4	Simulation Results	105
4.3.1.5	Fault Indicator	108
4.3.2	Spectrogram	111
4.3.2.1	Stationary PM and AM Signals	111
4.3.2.2	Transient PM and AM Signals	113
4.3.2.3	Simulation Results	113
4.3.3	Wigner Distribution	114
4.3.3.1	Stationary PM Signal	114
4.3.3.2	Transient PM Signal	119
4.3.3.3	Stationary AM Signal	120
4.3.3.4	Transient AM Signal	121

4.3.3.5	Simulation Results	122
4.3.3.6	Fault Indicator	123
4.4	Parameter Estimation	130
4.4.1	Stationary PM Signal	131
4.4.1.1	Choice of Signal Model	131
4.4.1.2	Cramer-Rao Lower Bounds	132
4.4.1.3	Maximum Likelihood Estimation	133
4.4.1.4	Numerical Optimization	135
4.4.1.5	Simulation Results	137
4.4.2	Stationary AM Signal	138
4.4.2.1	Simulation Results	139
4.5	Summary	140

4.1 Introduction

This chapter studies the fault signatures of the phase-modulated (PM) and amplitude-modulated (AM) stator current signals derived in chapter 2. The considered signal processing methods are those presented in chapter 3: classical spectral estimation, time-frequency analysis and signal parameter estimation.

The simplified real stator current signal models with PM and AM, resulting from torque oscillations and dynamic eccentricity, are:

$$i_{pm,r}(t) = i_{to}(t) = I_{st} \cos(\omega_s t) + I_{rt} \cos(\omega_s t + \beta \cos(\omega_c t - \varphi_\beta) - \varphi_r) \quad (4.1)$$

$$i_{am,r}(t) = i_{de}(t) = I_1 [1 + \alpha \cos(\omega_c t - \varphi_\alpha)] \cos \omega_s t \quad (4.2)$$

where the AM signal is written in a more general form than in (2.108) with modulation frequency ω_c . The theoretical calculations are less complex using analytical signals. Therefore, consider these signals in their analytical form:

$$i_{pm}(t) = I_{st} \exp j(\omega_s t) + I_{rt} \exp j(\omega_s t + \beta \cos(\omega_c t - \varphi_\beta) - \varphi_r) \quad (4.3)$$

$$i_{am}(t) = I_1 [1 + \alpha \cos(\omega_c t - \varphi_\alpha)] \exp j\omega_s t \quad (4.4)$$

These signal models only take into account the modulations of the fundamental stator current component and not of higher frequency current harmonics. Since the fundamental exhibits the highest amplitude of all current components, the modulation effects will also be strongest in the baseband around the fundamental. Therefore, the subsequent fault detection schemes will mainly be carried out by analysis of the stator current fundamental.

In this work, speed and frequency transients are also considered. For simplified calculations, the speed and frequencies are supposed to vary linearly with respect to time which is often the case in variable speed drives during acceleration and

braking. Since the fault characteristic frequency f_c is a function of the shaft rotational frequency f_r , it will also be time-varying with similar characteristics. The supply and fault pulsations $\omega_s(t)$ and $\omega_c(t)$ are supposed as follows:

$$\omega_s(t) = 2\pi f_s(t) = 2\pi \left(\alpha_s + \frac{1}{2}\beta_s t \right) \quad (4.5)$$

$$\omega_c(t) = 2\pi f_c(t) = 2\pi \left(\alpha_c + \frac{1}{2}\beta_c t \right) \quad (4.6)$$

where α_s, α_c are the initial frequencies and β_s, β_c the sweep rates. In the study of the transient signals, these expressions simply replace ω_s and ω_c in equations (4.3) and (4.4). The transient signals are denoted $i_{pm,tr}(t)$ and $i_{am,tr}(t)$ in the following.

The fault relevant information in the current signal can be processed in several ways. A first approach is signal analysis with a specific method e.g. spectrum analysis. The decision regarding fault occurrence will then be taken based on the presence of typical *fault signatures*. A human expert can then take a decision based on his acquired experience. If an automated monitoring system is desired, the human expert must be replaced by an appropriate post-processing including the calculation of a *fault indicator* or signature classification. Then, the system can take a decision based on the indicator values or the obtained classification. In the following, the fault signatures obtained with the different methods as well as strategies for an indicator extraction will be presented.

The theoretical modeling approach showed that the fault severity is reflected in the modulation indices of the PM/AM signals i.e. the phase modulation index β and the amplitude modulation index α . Hence, the modulation indices can often be used as fault indicators. Signal processing methods will therefore be used to estimate either these modulation indices or extract proportional quantities. Furthermore, this approach reveals information about the fault origin since PM and AM effects can be distinguished.

The following sections are structured similar to chapter 3. With each signal processing approach, the theoretical fault signatures are first calculated. Then, they are validated using simulated signals with additive noise. Based on the fault signatures, methods for the extraction of fault indicators will be described and tested with simulated signals.

4.2 Spectral Estimation

Stator current based motor condition monitoring is generally based upon spectral analysis with the periodogram. Therefore, this approach will also be discussed for reference and comparison. Since this method requires stationary signals and relatively long data records, speed and frequency transients cannot be analyzed. Hence, the supply frequency will be supposed stationary.

Since the PSD is obtained through the squared magnitude of the Fourier transform, the latter will first be calculated for the two signals.

4.2.1 Stationary PM Signal

The Fourier transform (FT) of a PM current signal according to (4.3) is the sum of the FTs of the two components due to the FT linearity property. The two components are denoted as follows:

$$i_{st}(t) = I_{st} \exp j(\omega_s t) \quad (4.7)$$

$$i_{rt}(t) = I_{rt} \exp j(\omega_s t + \beta \cos(\omega_c t - \varphi_\beta) - \varphi_r) \quad (4.8)$$

The Fourier transform magnitude of the first component is simply:

$$|I_{st}(f)| = I_{st} \delta(f - f_s) \quad (4.9)$$

The Fourier transform of a PM signal is more complex to derive but quite common in communication theory (see e.g. [Cou93]). First, the PM signal has to be developed into a Fourier series.

Consider the following series development [Abr64, p. 361]:

$$e^{\frac{1}{2}\beta(t-1/t)} = \sum_{k=-\infty}^{+\infty} t^k J_k(\beta) \quad t \neq 0 \quad (4.10)$$

where $J_k(\beta)$ denotes the k -th order Bessel function of the first kind. Setting the parameter $t = je^{j\theta}$, the so-called *Jacobi-Anger expansion* is obtained:

$$e^{j\beta \cos \theta} = \sum_{k=-\infty}^{+\infty} j^k J_k(\beta) e^{jk\theta} \quad (4.11)$$

Using this expression, the FT of $i_{rt}(t)$ is written as the following convolution product:

$$\mathfrak{F}\{i_{rt}(t)\} = I_{rt} \mathfrak{F}\{e^{j(\omega_s t - \varphi_r)}\} * \mathfrak{F}\left\{\sum_{k=-\infty}^{+\infty} j^k J_k(\beta) e^{jk(\omega_c t - \varphi_\beta)}\right\} \quad (4.12)$$

Hence, the FT magnitude is:

$$|I_{rt}(f)| = I_{rt} \sum_{k=-\infty}^{+\infty} J_k(\beta) \delta(f - (f_s + kf_c)) \quad (4.13)$$

The FT magnitude of the PM stator current according to (4.3) is then obtained as:

$$|I_{pm}(f)| = I_{st} \delta(f - f_s) + I_{rt} \sum_{k=-\infty}^{+\infty} J_k(\beta) \delta(f - (f_s + kf_c)) \quad (4.14)$$

Since [Abr64]

$$J_{-k}(\beta) = (-1)^k J_k(\beta) \quad (4.15)$$

the lower and upper sidebands of same order have the same FT magnitude. The FT magnitude of such a signal is shown schematically in Fig. 4.1(a). Theoretically,

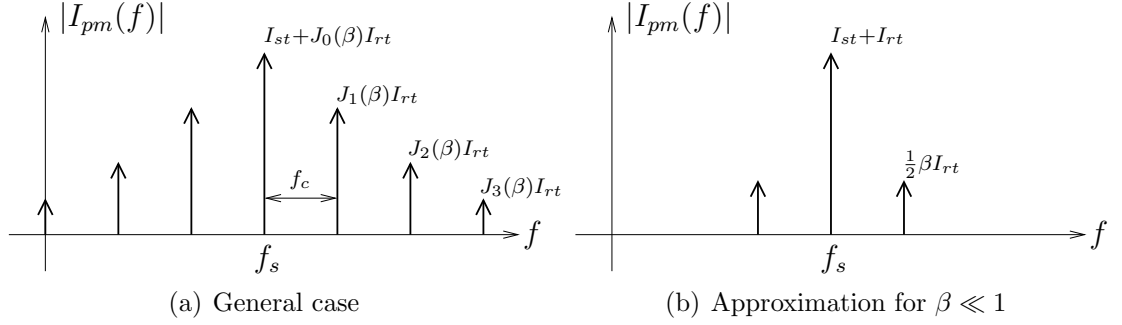


Figure 4.1: Illustration of the Fourier transform magnitude of a PM stator current signal.

an infinite number of sidebands at $f_s \pm k f_c$ arises in consequence of the phase modulation. The sideband amplitudes depend on the phase modulation index β .

Considering reasonable physical values for the machine parameters and small torque oscillations, the phase modulation index β can be supposed relatively small: $\beta \ll 1$ holds in most cases. Then, the Bessel functions of order $|k| \geq 2$ are of small amplitude and can be neglected. This is a common approximation in communication theory [Cou93]. The Bessel functions $J_k(\beta)$ can be approximated for $\beta \rightarrow 0$ by [Abr64]:

$$J_k(\beta) \approx \frac{\left(\frac{1}{2}\beta\right)^k}{\Gamma(k+1)} \quad (k \neq -1, -2, -3, \dots) \quad (4.16)$$

where $\Gamma(k)$ denotes the Gamma or factorial function. The following approximations are consequently obtained for $J_0(\beta)$ and $J_1(\beta)$ with $\beta \rightarrow 0$:

$$J_0(\beta) \approx \frac{1}{\Gamma(1)} = 1$$

$$J_1(\beta) \approx \frac{\frac{1}{2}\beta}{\Gamma(2)} = \frac{1}{2}\beta$$

With these approximations, equation (4.14) becomes:

$$|I_{pm}(f)| = (I_{st} + I_{rt}) \delta(f - f_s) + \frac{1}{2}\beta I_{rt} \delta(f - (f_s \pm f_c)) \quad (4.17)$$

which means that there are only two significant sideband components at $f_s \pm f_c$. This approximation is also termed *narrowband approximation* [Cou93]. The FT magnitude of a PM stator current signal with small modulation index is illustrated schematically in Fig. 4.1(b).

4.2.2 Stationary AM Signal

The AM stator current signal according to (4.4) can be rewritten as:

$$i_{am}(t) = I_1 \exp j\omega_s t + \alpha I_1 \cos(\omega_c t - \varphi_\alpha) \exp j\omega_s t \quad (4.18)$$

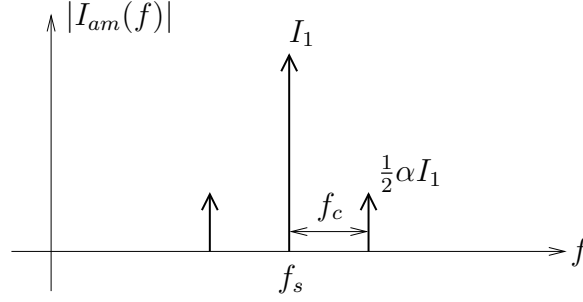


Figure 4.2: Illustration of the Fourier transform magnitude of an AM stator current signal.

The FT of the last term is the convolution product of the FT of each factor. This leads to the following FT magnitude $I_{am}(f)$:

$$|I_{am}(f)| = I_1 \delta(f - f_s) + \frac{1}{2} \alpha I_1 \delta(f - (f_s \pm f_c)) \quad (4.19)$$

The amplitude modulation therefore leads to two sideband components at $f_s \pm f_c$ with equal amplitude $\alpha I_1/2$. This is illustrated schematically in Fig. 4.2.

It is important to note that the AM and PM signal have the same spectral signature if the PM modulation index is small. Moreover, measured signals contain often additive white noise leading to a constant noise floor in the spectrum. Since the PM signal sideband components with $k \geq 2$ are of relatively small amplitude they are often embedded in the noise floor. Hence, spectral estimation is not an appropriate tool to distinguish the two modulation types.

4.2.3 Simulation Results

Tests with simulated signals are carried out in order to verify the previous theoretical considerations. The real-valued, discrete PM and AM signals used for simulation are:

$$i_{pm,r}[n] = I_{st} \cos(2\pi f_s n) + I_{rt} \cos(2\pi f_s n + \beta \cos(2\pi f_c n - \varphi_\beta) - \varphi_r) + w[n] \quad (4.20)$$

$$i_{am,r}[n] = I_1 [1 + \alpha \cos(2\pi f_c n - \varphi_\alpha)] \cos(2\pi f_s n) + w[n] \quad (4.21)$$

where $w[n]$ is a white Gaussian noise of variance σ^2 . The parameters take the following default values, typical of the considered application:

$$\begin{aligned} f_s &= 0.25 & f_c &= 0.125 \\ \alpha &= \beta = 0.01 & \varphi_\beta &= \varphi_\alpha = \frac{\pi}{4} \\ \varphi_r &= \frac{\pi}{8} & I_{st} &= I_{rt} = \frac{\sqrt{2}}{2} \\ I_1 &= \sqrt{2} & \text{SNR} &= 50 \text{ dB} \end{aligned}$$

In this application, the acquired current signals are all downsampled to 200 Hz to preserve only frequencies around the fundamental at $f_s = 50$ Hz. Therefore,

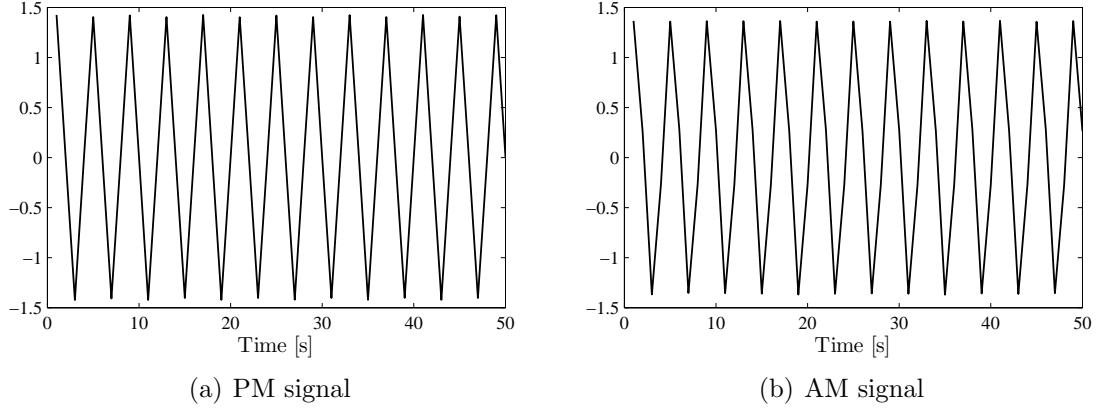


Figure 4.3: Simulated PM and AM test signals.

$f_s = 0.25$ normalized frequency has been chosen for the simulation. The fault characteristic frequency f_c is supposed to be equal to the shaft rotational frequency $f_r \approx f_s/2$. A realization of each PM and AM test signal with these parameters is shown in Fig. 4.3. The different modulation types cannot be distinguished due to the small modulation indices.

For the spectral estimation, the signals of length $N = 512$ are transformed into their analytical form before the periodogram computation. For illustration of the window effects, the periodogram of the stator current PM signal is estimated with the previously mentioned 5 windows and additional zero padding. The results are displayed in Fig. 4.4. The rectangular window is not suitable in this case due to high sidelobe amplitudes that mask the sideband peaks. The Bartlett and Hamming window lead also to relatively high sidelobes around the main peak. Hanning and Blackman windows are adequate for this application.

For comparison between the PM and AM signal, the two periodograms computed using a Hanning window of length N are displayed in Fig. 4.5. First, it can be noted that the two spectral estimates are very similar. The AM or PM modulation cannot be clearly identified since higher order sidebands of the PM signal are buried in the noise. Secondly, the relative amplitude of the sidebands with respect to the fundamental is -52 dB (0.0025) in the PM case which corresponds to $\beta/4$. This is correct since the fundamental amplitude is $I_{st} + I_{rt} = 2I_{rt} = I_1$. With the AM signal, the relative sideband amplitude is -46 dB (0.005) corresponding to $\alpha/2$.

4.2.4 Fault Indicator

With the preceding considerations, a suitable fault indicator based on the stator current spectrum can be derived. It has been demonstrated that the modulation indices are reflected in the relative sideband amplitudes. The modulation indices themselves are theoretically proportional to the fault severity. Therefore, the proposed fault indicator is the sum of the two relative sideband amplitudes.

The proposed fault indicator is obtained as depicted in Fig. 4.6. First, the stator

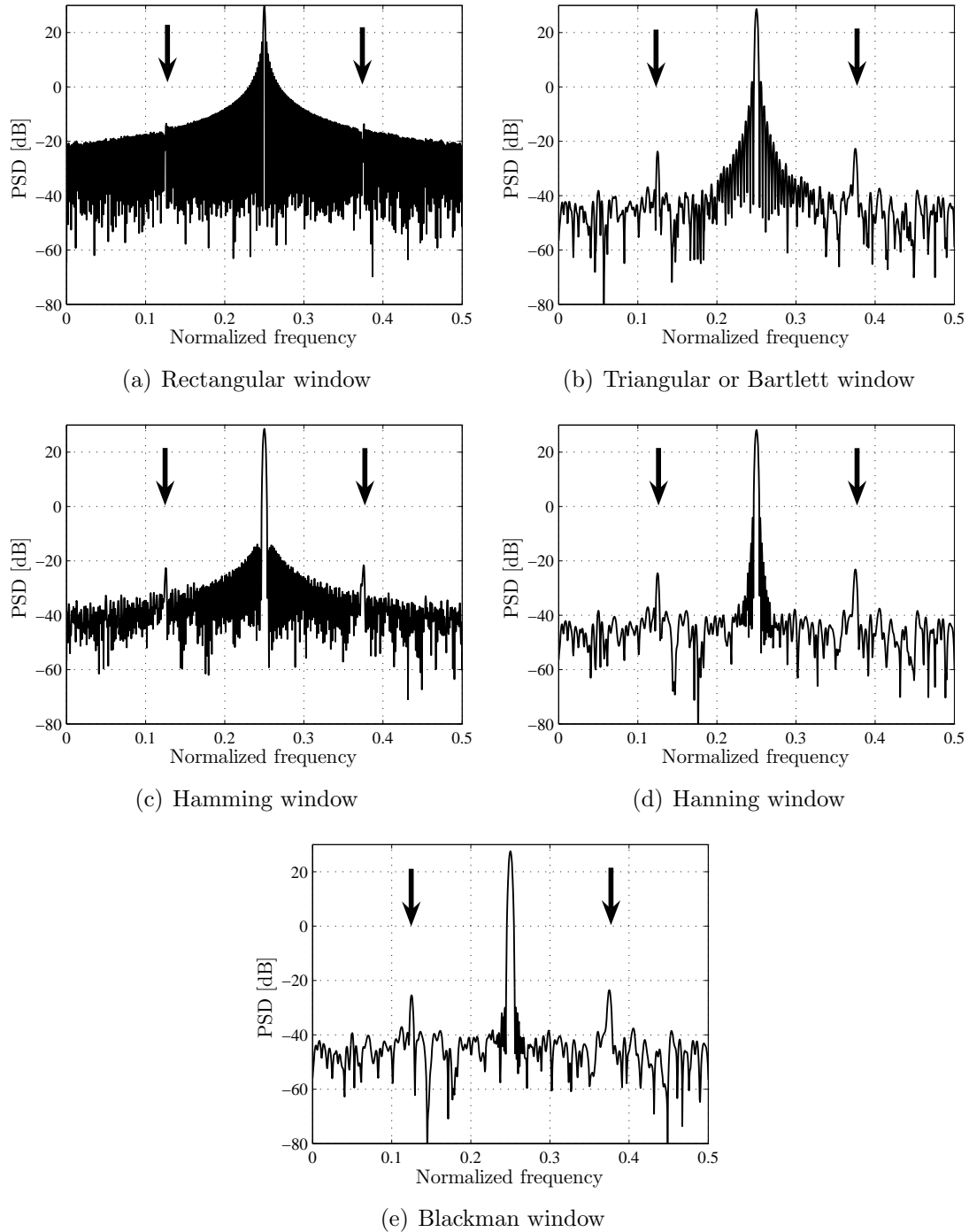


Figure 4.4: Power Spectral Densities of simulated stator current PM signal analyzed with common window functions.

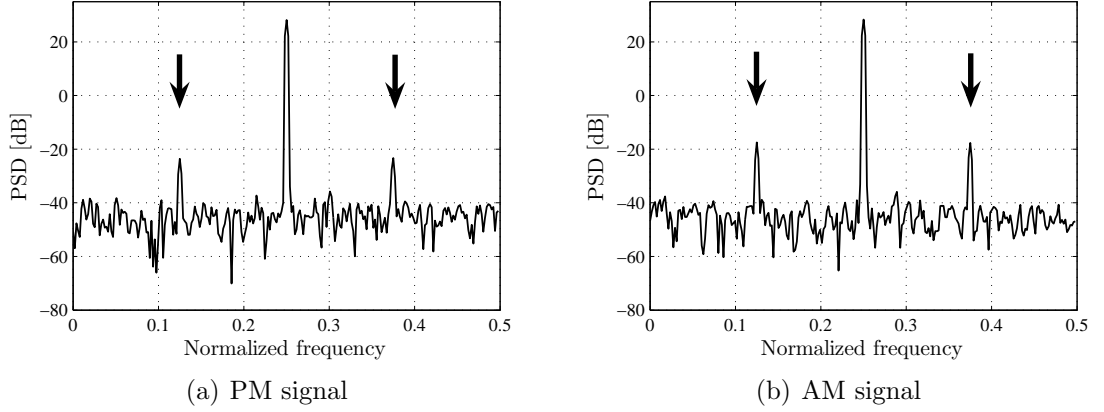


Figure 4.5: Periodogram of PM and AM signal.

current PSD is estimated in the frequency range of interest, usually depending on the fundamental f_s and the characteristic fault frequency f_c . In case of faults such as eccentricity, load unbalance or shaft misalignment, f_c is equal to the shaft rotational frequency f_r . Then, the supply frequency f_s is estimated through the localization of the maximum of the PSD. The amplitude A of the fundamental is also retained. Depending on the possible variations of f_r , minimum and maximum values $f_{c,min}$ and $f_{c,max}$ are determined. As an example, if $f_c = f_r$ and the maximal motor slip is $s_{max} = 5\%$:

$$f_{c,max} = \frac{f_s}{p} \quad f_{c,min} = (1 - s_{max}) \frac{f_s}{p} = 0.95 \frac{f_s}{p} \quad (4.22)$$

These values limit the frequency range for the sideband location. The lower sideband is located in the interval $I_l = [f_s - f_{c,max}, f_s - f_{c,min}]$ whereas the upper sideband is in $I_u = [f_s + f_{c,min}, f_s + f_{c,max}]$. The maximum PSD values from these intervals, A_l and A_u respectively, characterize the sideband amplitudes. In order to obtain the relative sideband amplitude, the sum of A_l and A_u is normalized with respect to the fundamental amplitude A . The resulting spectrum-based fault indicator is simply:

$$\text{IPSD} = \frac{A_l + A_u}{A} \quad (4.23)$$

It should be proportional to the modulation index α or β . The normalization is necessary to provide a load independent indicator. When β is estimated according to the PM stator current model in equation (4.1), the rotor-related current amplitude I_{rt} would be required for correct normalization. However, since this quantity is not available, the current fundamental amplitude $I_{rt} + I_{st}$ is used instead. It should also be noted that the PM model according to (4.1) is rather simple and neglects higher order armature reactions. Actually, the stator-related current component with amplitude I_{st} should also be modulated which would reduce the committed normalization error. If the stator current is amplitude modulated according to (4.2), the correct value for α is obtained.

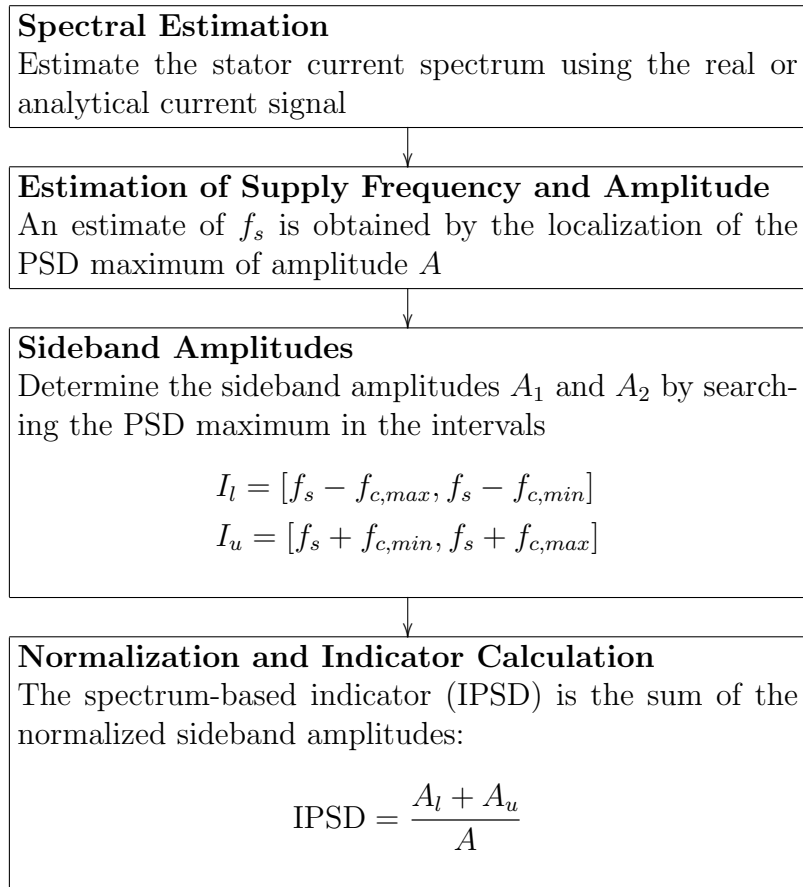


Figure 4.6: Calculation of the spectrum based fault indicator IPSD.

4.3 Time-Frequency Analysis

The following sections study the fault signatures with the previously discussed time-frequency methods. These signal processing methods, suitable for non-stationary signal analysis, are applied to signals with time-varying frequencies.

4.3.1 Instantaneous Frequency

The instantaneous frequency (IF) of the PM and AM stator current must be calculated using the analytical signals for a univocal phase definition.

4.3.1.1 Stationary PM Signal

The IF of an analytical signal was defined in (3.59). For simplification, this definition is first applied to a monocomponent PM signal such as the rotor current component $i_{rt}(t)$ in (4.8):

$$\text{IF}_{i_{rt}}(t) = \frac{1}{2\pi} \frac{d}{dt} \arg\{i_{rt}(t)\} = f_s - \beta f_c \sin(2\pi f_c t - \varphi_\beta) \quad (4.24)$$

It can be seen through this expression that the IF of this sinusoidal PM signal is a constant component at carrier frequency f_s plus an oscillating component. The frequency of the latter is the modulation frequency f_c , its amplitude is βf_c .

The IF calculation of a PM stator current signal according to (4.3) is more complex since it is the sum of a modulated and a non-modulated component. First, $i_{pm}(t)$ can be rewritten as a product:

$$\begin{aligned} i_{pm}(t) &= \exp j(\omega_s t) [I_{st} + I_{rt} \exp j(\beta \cos(\omega_c t - \varphi_\beta) - \varphi_r)] \\ &= b(t) c(t) \end{aligned} \quad (4.25)$$

For the IF of a product, consider two complex functions $z_1(t)$ and $z_2(t)$. The IF of $z(t) = z_1(t)z_2(t)$ is the sum of the two IF laws:

$$\begin{aligned} \text{IF}_z(t) &= \frac{1}{2\pi} \frac{d}{dt} \arg\{z(t)\} = \frac{1}{2\pi} \frac{d}{dt} [\arg\{z_1(t)\} + \arg\{z_2(t)\}] \\ &= \text{IF}_{z_1}(t) + \text{IF}_{z_2}(t) \end{aligned} \quad (4.26)$$

In equation (4.25), $\text{IF}_b(t) = f_s$ and

$$\text{IF}_c(t) = \frac{1}{2\pi} \frac{d}{dt} \arctan \frac{I_{rt} \sin(\beta \cos(\omega_c t - \varphi_\beta) - \varphi_r)}{I_{st} + I_{rt} \cos(\beta \cos(\omega_c t - \varphi_\beta) - \varphi_r)} \quad (4.27)$$

With

$$\left(\arctan \frac{u}{v} \right)' = \frac{1}{1 + \frac{u^2}{v^2}} \frac{u'v - v'u}{v^2} = \frac{u'v - v'u}{u^2 + v^2} \quad (4.28)$$

$\text{IF}_c(t)$ can be calculated as:

$$\text{IF}_c(t) = -\beta f_c \sin(\omega_c t - \varphi_\beta) \frac{I_{rt}^2 + I_{st} I_{rt} \cos(\beta \cos(\omega_c t - \varphi_\beta) - \varphi_r)}{I_{rt}^2 + I_{st}^2 + 2I_{st} I_{rt} \cos(\beta \cos(\omega_c t - \varphi_\beta) - \varphi_r)} \quad (4.29)$$

In order to evaluate the last term of the product, consider the following series development [Abr64]:

$$\cos(\beta \cos \theta) = J_0(\beta) + 2 \sum_{k=1}^{\infty} (-1)^k J_{2k}(\beta) \cos(2k\theta) \quad (4.30)$$

If β is small enough, the higher order Bessel functions with $k \geq 2$ are neglected as in the previous narrowband approximation and only the constant term $J_0(\beta) \approx 1$ remains. This leads to the following approximation for the time-variable terms in the fraction of (4.29):

$$\cos(\beta \cos(\omega_c t - \varphi_\beta) - \varphi_r) \approx 1 \quad \text{if} \quad \beta \ll 1 \quad (4.31)$$

Therefore, using this approximation for $\text{IF}_c(t)$, the IF of the PM stator current $\text{IF}_{i_{pm}}(t)$ becomes:

$$\begin{aligned} \text{IF}_{i_{pm}}(t) &\approx f_s - \beta f_c \sin(\omega_c t - \varphi_\beta) \frac{I_{rt}^2 + I_{st} I_{rt}}{I_{rt}^2 + I_{st}^2 + 2I_{st} I_{rt}} \\ &= f_s - \beta f_c \sin(\omega_c t - \varphi_\beta) \frac{I_{rt}}{I_{st} + I_{rt}} \\ &= f_s - \beta f_c C(I_{st}, I_{rt}) \sin(\omega_c t - \varphi_\beta) \end{aligned} \quad (4.32)$$

where $C(I_{st}, I_{rt})$ is a time independent function of the current component amplitudes I_{st} and I_{rt} . Furthermore, $0 < C(I_{st}, I_{rt}) < 1$ and $C(I_{st}, I_{rt}) \rightarrow 1$ for $I_{rt} \gg I_{st}$.

It can be concluded that the PM stator current IF shows oscillations at f_c with amplitude proportional to βf_c . Thus, the IF can be used to detect phase modulations. However, the amplitude of the oscillating IF component also varies with changing load conditions since it depends on I_{st} and I_{rt} .

4.3.1.2 Transient PM Signal

The transient PM stator current signal in a product form is:

$$\begin{aligned} i_{pm,tr}(t) &= \exp j(\omega_s(t)t) [I_{st} + I_{rt} \exp j(\beta \cos(\omega_c(t)t - \varphi_\beta) - \varphi_r)] \\ &= b_{tr}(t) b_{tr}(t) \end{aligned} \quad (4.33)$$

The IF of the first term is with $\omega_s(t) = 2\pi(\alpha_s + \beta_s t/2)$:

$$\text{IF}_{b,tr}(t) = \alpha_s + \beta_s t \quad (4.34)$$

The IF of the transient PM signal $i_{pm}(t)$ is calculated similar to the stationary case. It expresses in the approximated form as follows:

$$\text{IF}_{i_{pm,tr}}(t) \approx \alpha_s + \beta_s t - \beta(\alpha_c + \beta_c t) C(I_{st}, I_{rt}) \sin[2\pi(\alpha_c + \beta_c t/2)t - \varphi_\beta] \quad (4.35)$$

This expression is similar to the stationary case. The IF of the PM current signal is the IF of the unmodulated signal $\text{IF}_{b,tr}(t)$ plus oscillations. The oscillations are at the variable fault pulsation $\omega_c(t)$ and their amplitude is proportional to β , $C(I_{st}, I_{rt})$ and $(\alpha_c + \beta_c t)$.

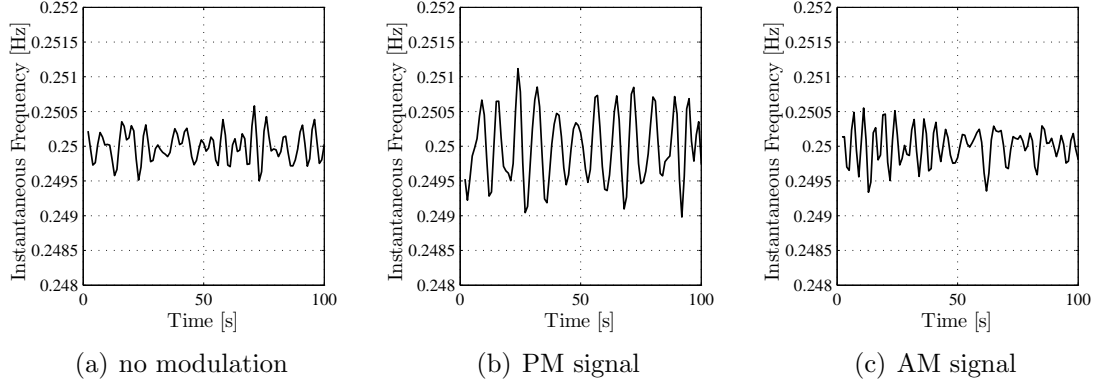


Figure 4.7: Instantaneous frequency of simulated signals: signal without modulation, PM and AM signal.

4.3.1.3 AM Signal

The IF of an AM stator current signal according to (4.4) is simply a constant at f_s :

$$\text{IF}_{i_{am}}(t) = f_s \quad (4.36)$$

In contrast to the PM stator current signal, no time-variable component is present. The AM modulation index α is not reflected in the IF. Consequently, the IF of this signal cannot be used for amplitude modulation detection.

The same is true in the transient case where the AM signal IF is equal to the corresponding unmodulated signal IF:

$$\text{IF}_{i_{am,tr}}(t) = \alpha_s + \beta_s t \quad (4.37)$$

4.3.1.4 Simulation Results

Simulations consider the AM and PM signals with the parameter values given in 4.2.3. The data record length is $N = 512$. First, the analytical signal is calculated using the Hilbert transform. Then, the instantaneous frequency is estimated using the function *instfreq* from the Matlab Time-Frequency Toolbox [Aug96]. This function employs the previously mentioned phase difference estimation.

The obtained IF estimations are displayed in Fig. 4.7. First, the IF of an unmodulated signal is calculated (see Fig. 4.7(a)). The mean IF value is the supply frequency at $f_s = 0.25$ normalized frequency. Since the signal is generated with additive noise, the noise is also present on the IF estimation. In contrast, the IF of the PM signal (displayed in Fig. 4.7(b)) shows a deterministic oscillating component at $f_c = 0.125$ as predicted by equation (4.32). The AM signal IF (see Fig. 4.7(c)) resembles to the unmodulated case where no deterministic oscillation is visible.

The amplitude and frequency of the oscillating IF component are then derived from the estimated IF spectrum. Since the average IF value is relatively high compared to the oscillations, it is removed before the spectral estimation in order to avoid sidelobe effects. Moreover, the average IF does not contain relevant fault

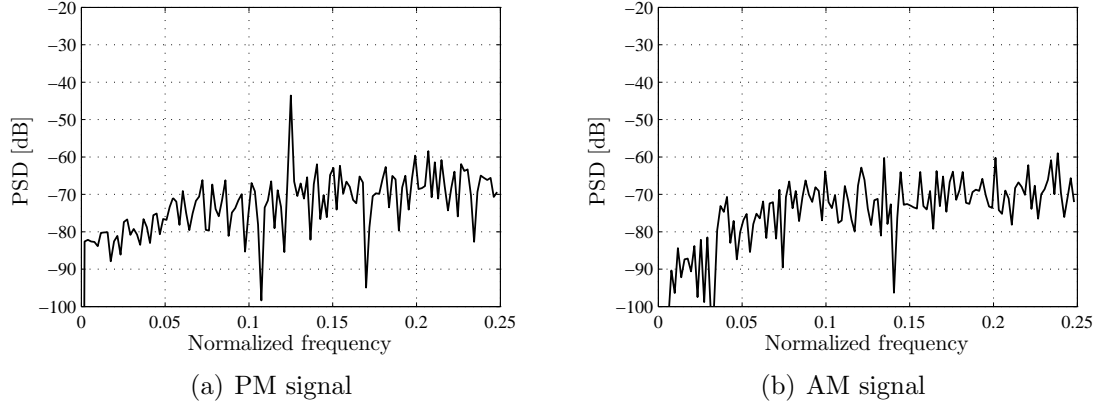


Figure 4.8: Periodogram of instantaneous frequency of simulated PM and AM signals.

information. The PSD is estimated using a standard periodogram with rectangular window function. The PSD estimates for the PM and AM signal are shown in Fig. 4.8. With the PM signal, the IF spectrum clearly shows a peak at $f_c = 0.125$ which is not visible with the AM signal. The peak amplitude corresponds to a sinusoidal component amplitude of $5.875 \cdot 10^{-4} = \beta f_c C(I_{st}, I_{rt})$. With the chosen values for $I_{st} = I_{rt}$, $C(I_{st}, I_{rt}) = 0.5$. Therefore, β is estimated as 0.0094 which is slightly smaller than the chosen value 0.01. The error may result from the spectral estimation or the approximation for the IF oscillating component amplitude. However, simulations showed that the error depends on f_c : a smaller value of f_c decreases this error. Consequently, it can be supposed to be related to the IF estimation procedure through the phase differentiation. A higher sampling frequency is likely to reduce the estimation error of the IF oscillating component amplitude.

The corresponding simulations are carried out with the transient signals. The frequency variation is linear with the following parameters:

$$\begin{aligned} \alpha_s &= 0.05 & \beta_s &= 0.2/N \\ \alpha_c &= \alpha_s/2 & \beta_c &= \beta_s/2 \end{aligned}$$

The supply frequency $f_s(t)$ is therefore varying from 0.05 to 0.25 normalized frequency. The modulation frequency $f_c(t)$ is half the supply frequency. In order to better visualize the modulation effects, the following higher values are chosen for the modulation indices: $\alpha = \beta = 0.1$. The IF of the transient PM and AM stator current signal is shown in Fig. 4.9. The linear evolution of the supply frequency is clearly visible apart from border effects. With the PM signal, oscillations at varying fault frequency $f_c(t)$ can be recognized. In case of the AM signal, no oscillations are present.

In order to extract the fault signature from the IF, information about amplitude and frequency of the oscillating component must be obtained. Since the fault frequency is time-varying, a spectral estimate can no longer be used. Instead, a time-frequency representation of the stator current IF can reveal the fault signature. Since the fault signature is a signal component with a linear frequency mod-

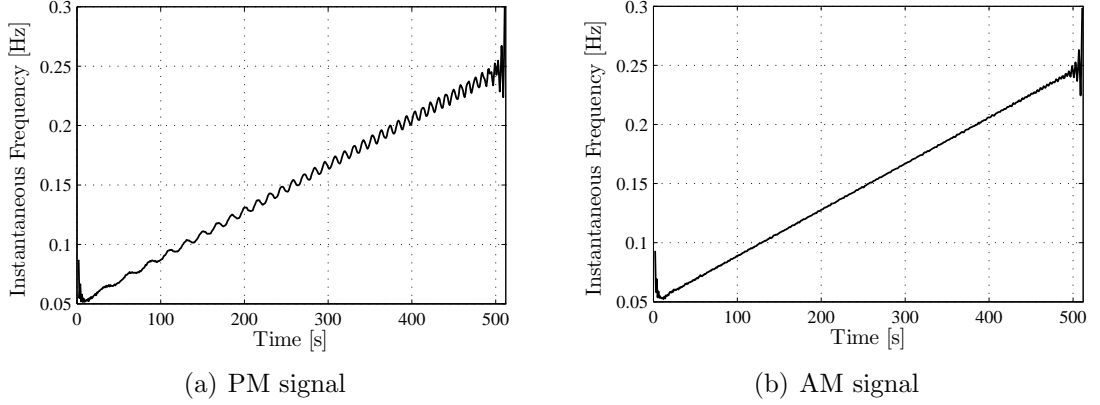


Figure 4.9: Instantaneous frequency of simulated transient PM and AM signals.

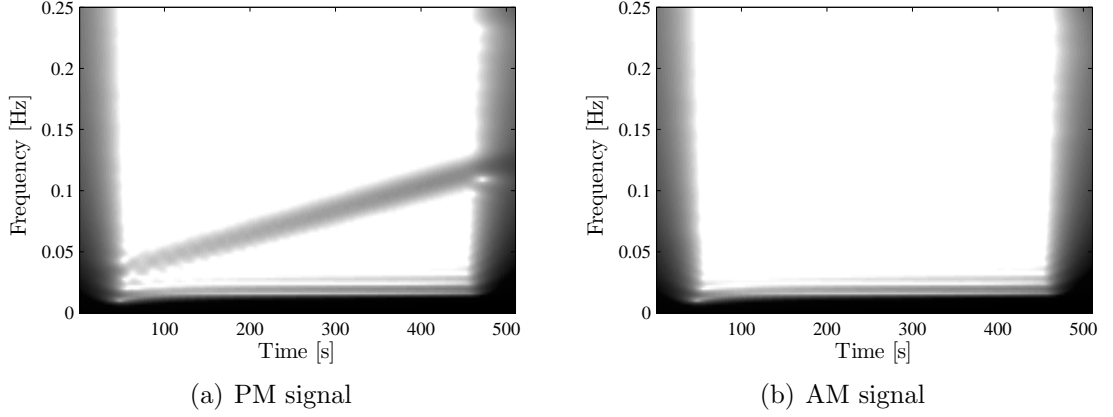


Figure 4.10: Spectrogram of instantaneous frequency of simulated transient PM and AM signals.

ulation and since the sweep rate is relatively slow, the spectrogram can be used. Another advantage with the spectrogram is the absence of interference terms. The DC component in the IF is of high amplitude compared to the oscillating terms which leads to interferences in quadratic time-frequency representations. Moreover, the amplitude of the DC component varies during the considered transient so that it cannot be simply removed. Thus, the spectrogram is a reasonable choice in this case.

The spectrogram of the PM and AM signal IF is displayed in Fig. 4.10. Besides the strong DC component at 0 Hz, the signature of a linear FM signal component is clearly visible with the PM signal. Its frequency varies from 0.025 to 0.125 which corresponds to the IF law of a sinusoidal signal with $f_c(t)$. As f_c increases, the amplitude of the oscillating component also increases according to equation (4.35). In contrast, the spectrogram of the AM signal IF shows no oscillating component. These examples show that the spectrogram is an adapted tool for IF analysis in this application.

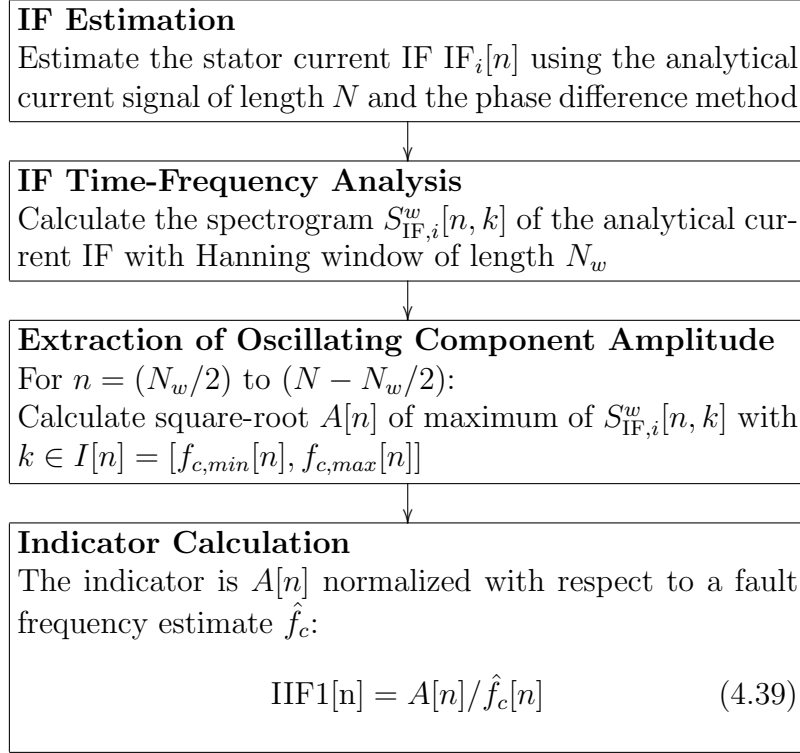


Figure 4.11: Calculation of the IF based fault indicator IIF1.

4.3.1.5 Fault Indicator

Following the preceding considerations, two IF based fault indicators are proposed. If the signals are at constant supply frequency f_s , spectral analysis of the IF followed by peak detection in a suitable frequency range provides a straightforward indicator for the PM modulation index. However, since the IF analysis is adapted for transient signal analysis, only this more general case will be considered.

The calculation of the first IF based fault indicator (IIF1) is schematically shown in Fig. 4.11 [Blö06b]. First, the IF $IF_i[n]$ of the analytical stator current signal is computed, followed by the spectrogram $S_{IF,i}^w[n, k]$ of the analytical stator current IF. The window function is a Hanning window of length N_w . In order to extract the amplitude of the oscillating component from the spectrogram, a frequency interval $I[n] = [f_{c,min}, f_{c,max}]$ is defined for each time bin n . Based on the previously estimated IF value with respect to n , the frequency range can be determined to account for variations of f_r . In this example, $f_{c,min}[n] = 0.95 IF_i[n]/2$ and $f_{c,max}[n] = 1.05 IF_i[n]/2$. The oscillating component amplitude $A[n]$ is the square root of the maximum of $S_{IF,i}^w[n, k]$ with $k \in I[n]$. Note that $A[n]$ is only extracted for $n \in [N_w/2, (N - N_w/2)]$ where N denotes the data record length. This avoids the influence of border effects on the fault indicator.

The oscillating component amplitude $A[n]$ can already be used as a fault indicator (see Fig. 4.12(a)). Several simulations have been carried out with increasing modulation index β . It becomes clear that $A[n]$ is proportional to the modulation index β . However, it still depends on the value of the fault characteristic frequency

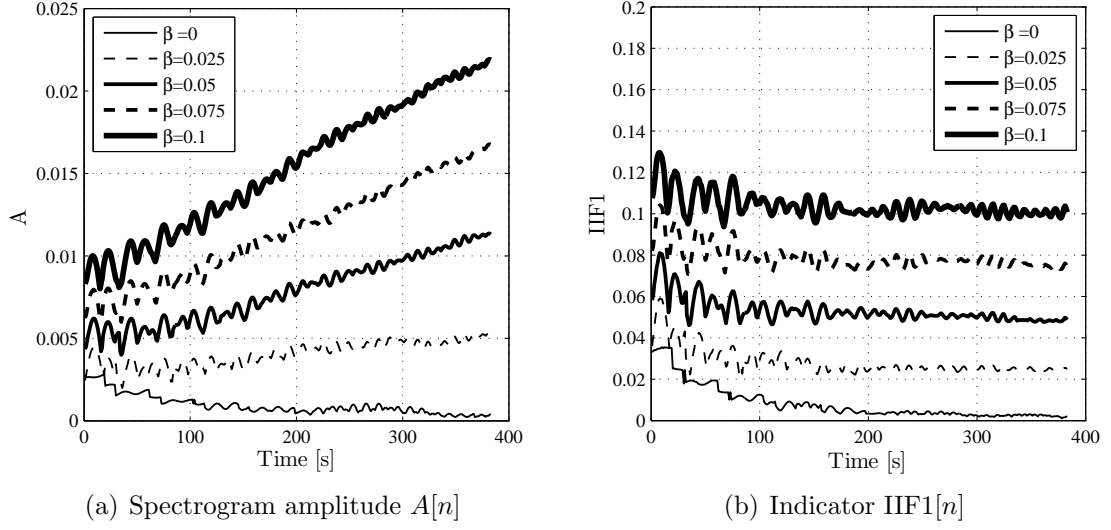


Figure 4.12: Spectrogram amplitude $A[n]$ and fault indicator $IIF1$ with respect to time for different PM modulation indices β .

$f_c(t)$ since A is smaller when f_c is smaller. Therefore, in order to obtain an indicator independent of the varying supply and fault frequency, $A[n]$ must be divided by the fault characteristic frequency f_c (see equation (4.35)). Since the exact value of f_c is not known, it has to be estimated. A first approach might be the localization of the oscillating component in the spectrogram. However, the obtained estimations exhibit a high variance which leads to an unusable fault indicator. A second method is the use of $IF_i[n]$. The fault frequency f_c is approximately f_s/p so that f_c is estimated by $\hat{f}_c[n] = IF_i[n]/p$. The fault indicator $IIF1$ is therefore:

$$IIF1[n] = \frac{A[n]}{\hat{f}_c[n]} \quad \text{with} \quad A[n] = \sqrt{\max \{S_{IF,i}^w[n, k]\}}, \quad k \in [f_{c,min}[n], f_{c,max}[n]] \quad (4.40)$$

The obtained results displayed in Fig. 4.12(b) have a lower variance than with the first method for estimating f_c . Since the value of f_c is smaller at the beginning, the variance of $IIF1$ is higher. For higher n , the average of $IIF1$ is approximately constant. Moreover, the indicator value is proportional to the modulation index β which demonstrates the effectiveness of the indicator.

Indicator $IIF1$ suffers from the dependence of the spectrogram amplitude on the frequency sweep rate of the analyzed signal. Assuming a constant window length N_w , the peak in the spectrogram is larger if the frequency variation is high. Consequently, since the total energy is constant with respect to the sweep rate, the larger peak is of smaller amplitude. Therefore, higher sweep rates lead to smaller peak amplitudes of the linear chirp component. Hence, the fault indicator based on the maximum of the periodogram can only be used if the sweep rates are always constant i.e. during the same speed profiles. Indicator values $IIF1$ with different sweep rates β_s are displayed in Fig. 4.13(a). The indicators drops by approximately 25% if $\beta_s = 0.3/N$ compared to the slow variation $\beta_s = 0.1/N$.

An alternative is the calculation of the total energy in an interval $S_{IF,i}^w[n, k]$ with

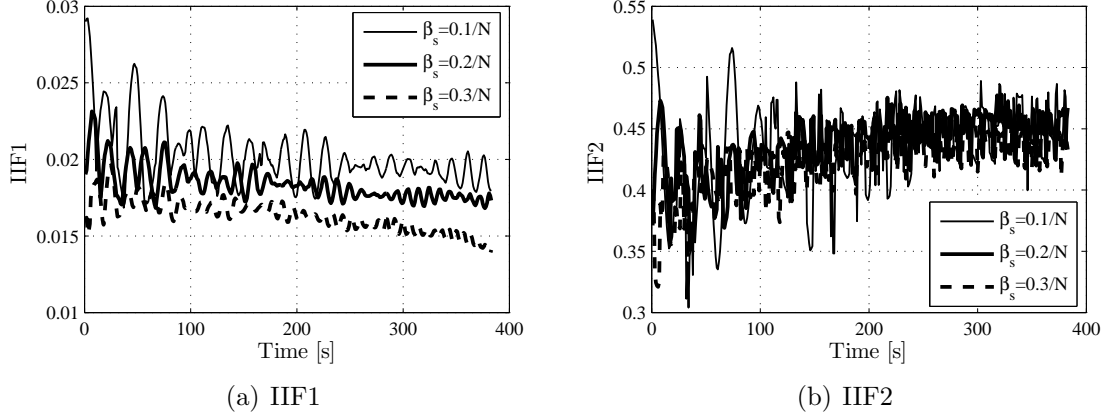


Figure 4.13: Comparison of indicators IIF1 and IIF2 with respect to different frequency sweep rates β_s of the supply frequency, modulation index $\beta = 0.1$.

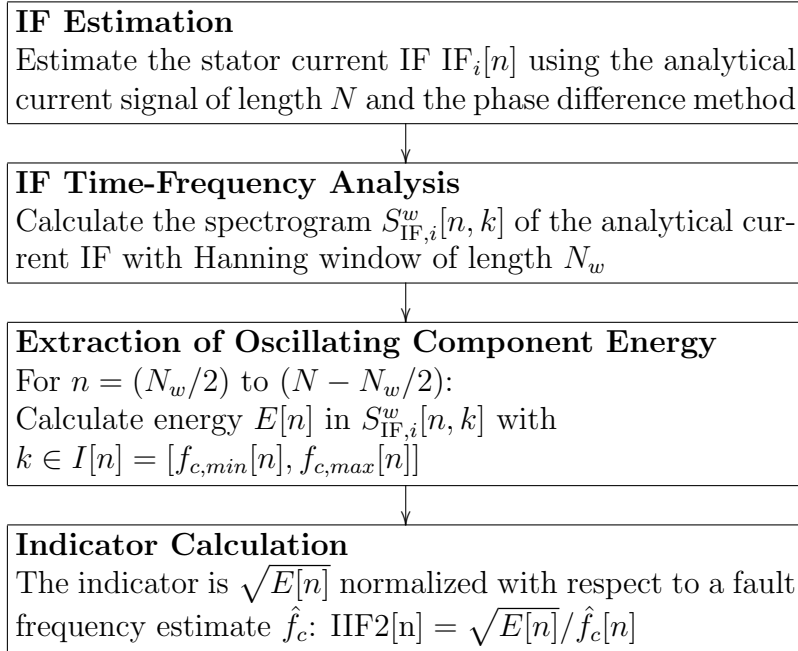


Figure 4.14: Calculation of the IF based fault indicator IIF2.

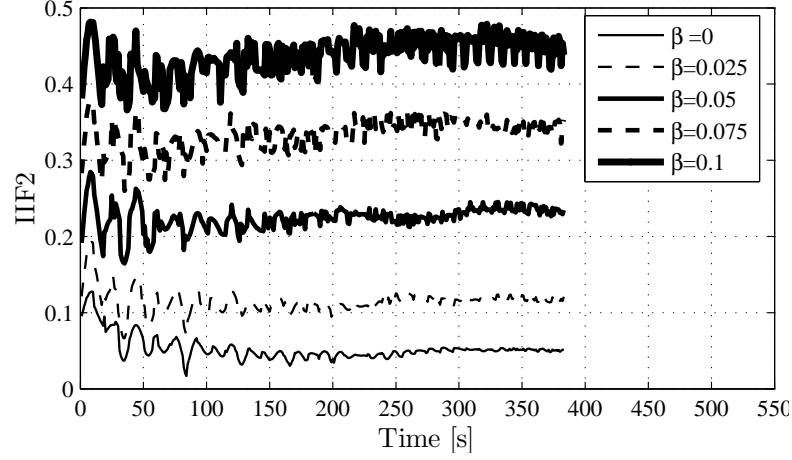


Figure 4.15: Fault indicator IIF2 with respect to time for different PM modulation indices β .

$k \in I[n]$. Considering the energy square root and an appropriate normalization with respect to f_c , the fault indicator IIF2 is obtained as:

$$\text{IIF2}[n] = \frac{\sqrt{E[n]}}{\hat{f}_c[n]} \quad \text{with} \quad E[n] = \sum_{k=f_{c,min}[n]}^{f_{c,max}[n]} S_{\text{IF},i}^w[n, k] \quad (4.41)$$

Its calculation is schematically depicted in Fig. 4.14. Results with simulated signals are displayed in Fig. 4.15. Besides the indicator value, they are similar to IIF1. However, tests with different frequency sweep rates showed less indicator variations compared to IIF1. An example can be seen in Fig. 4.13(b) where the final indicator values are relatively stable with respect to the sweep rate.

4.3.2 Spectrogram

The spectrogram is only shortly discussed because of various disadvantages compared to the other proposed time-frequency methods. Since the spectrogram is the squared short-time Fourier transform, it is limited in resolution by the Heisenberg-Gabor uncertainty principle. The choice of the window length is primordial for the time-frequency resolution and the accuracy of the analysis.

4.3.2.1 Stationary PM and AM Signals

Consider first stationary PM and AM signals. If the analysis window is long compared to the modulation period, the spectrogram becomes similar to the periodogram. The phase or amplitude modulation will lead to sidebands around the fundamental frequency at $f_s \pm f_r$. When the PM modulation index is small or when the SNR is low, the higher order sidebands of the PM signal are small and buried in the noise floor. In these cases, the PM and AM signature will be identical and there is no advantage of the spectrogram over the periodogram.

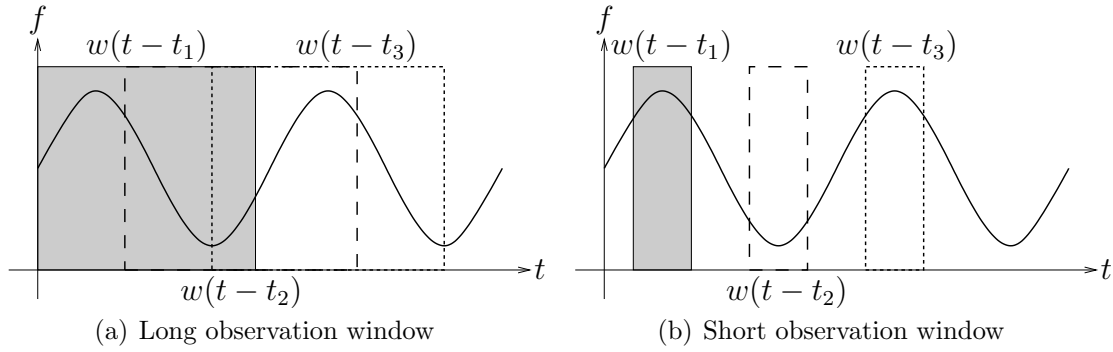


Figure 4.16: Illustration relative to the spectrogram of a sinusoidal PM signal with different window lengths.

Since the phase modulation corresponds to a time-varying instantaneous frequency and the amplitude modulation to a time-varying amplitude, a time-frequency analysis using the spectrogram should reveal the difference. For this purpose, the window length N_w must be chosen adequately with respect to the modulation period T_c . If e.g. the window length is exactly the modulation period $N_w = T_c$, the time-variable frequency or amplitude will not be visible in the spectrogram. Actually, the squared Fourier transform is identical for each window position. This is illustrated graphically in Fig. 4.16(a) with the time-frequency representation of a sinusoidal PM signal and three different window positions. The spectrogram yields the average frequency content of the windowed signal, being the same in each case. Thus, the window length should ideally be chosen smaller or only slightly higher than the modulation period so that the changes in frequency or amplitude will be visible in the spectrogram. Fig. 4.16(b) shows the corresponding case with shorter observation windows. The average frequencies for each window position are different leading to a variable frequency in the spectrogram. Nevertheless, even a window length longer than the modulation period can still be adequate since e.g. with $N_w = 1.5 T_c$ the average frequency of the window changes with respect to the window position.

It should also be recalled that the window length in the preceding considerations strongly influences the frequency resolution. The short observation window, required to analyse the time-varying frequency or amplitude, degrades the frequency resolution according to the Heisenberg-Gabor uncertainty. In case of a small modulation frequency compared to the carrier frequency, the observation window can be chosen long enough for a satisfying frequency resolution. However, when the modulation frequency is relatively high, the required short window length may lead to an unacceptable frequency resolution. In the considered application, the modulation frequency f_c is typically half the carrier frequency f_s with $f_s = 0.25$ normalized frequency. Choosing e.g. a window length N_w which is half the modulation period i.e. $N_w = 4$, it becomes clear that the frequency resolution is too poor for an effective analysis.

It can be concluded that a spectrogram analysis in this application requires relatively short windows for discriminating AM and PM signals. The resulting frequency resolution may be problematic. Long observations windows lead to good

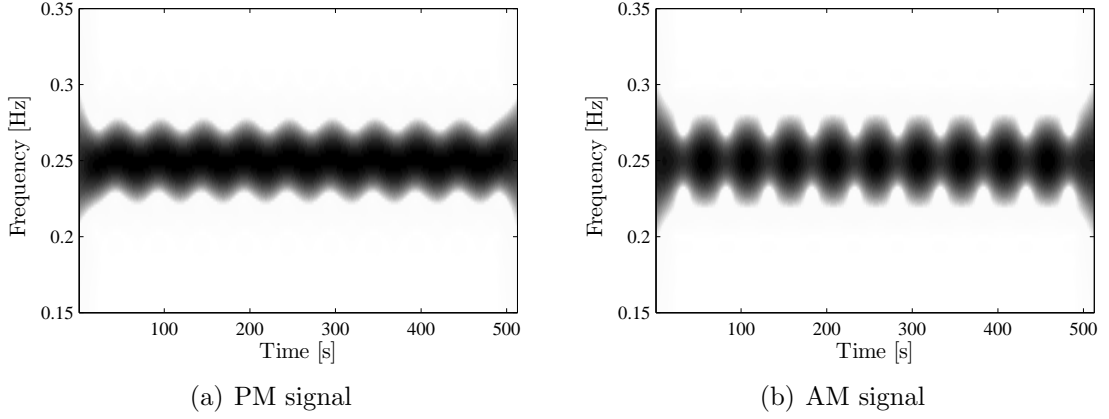


Figure 4.17: Spectrogram of simulated PM and AM signals with low modulation frequency ($f_c = 0.02$) and higher modulation indices ($\alpha = \beta = 0.5$), window length $N_w = 63$.

frequency resolution but the modulation type may be impossible to identify with small modulation indices.

4.3.2.2 Transient PM and AM Signals

With transient PM and AM signals the same previously discussed problems arise. Moreover, increasing the window length for better resolution leads to a higher degree of non-stationarity of the windowed signal. The time-varying frequencies appear as relatively broad peaks that may mask phenomena of smaller amplitude. Examples will be given in the following that illustrate the difficulty to analyze the signals with the spectrogram in our application.

4.3.2.3 Simulation Results

First, stationary signals with relatively low modulation frequencies are considered. In these cases, the spectrogram can be used to distinguish between PM and AM. Compared to the initial parameters of the simulated signals given in section 4.2.3, the modulation frequency f_c and the modulation indices are changed: $f_c = 0.02$ and $\alpha = \beta = 0.5$. The modulation period is therefore $T_c = 50$ samples, allowing an adequate window length for acceptable frequency resolution and the visualization of the time-varying frequency and amplitude. The obtained time-frequency representations are displayed in Fig. 4.17. They have been calculated using a Hanning window of length N_w . In the spectrogram of the sinusoidal PM signal (Fig. 4.17(a)), the sinusoidally varying instantaneous frequency can be recognized through the mean frequency with respect to time. The period of the sinusoidal variations is the modulation period $T_c = 50$ samples. In case of the AM signal (Fig. 4.17(b)), the instantaneous frequency i.e the frequency average of the spectrogram shows no variations since it is always 0.25 for all points in time. The signal AM character becomes visible through the time-varying amplitude of the fundamental frequency.

The previous example illustrated that the PM or AM character of a signal can be distinguished through the spectrogram for a small modulation frequency. If typical values for our application are considered, the modulation frequency is relatively high with $f_c = 0.125 = f_s/2$. For the following simulations, f_c takes this value and the modulation indices are reset to the smaller values with $\alpha = \beta = 0.1$. The obtained spectrograms are displayed for two different window lengths $N_w = 11$ and $N_w = 49$ samples in Fig. 4.18. When a relatively short window length is chosen ($N_w = 11$), a difference between the PM and AM signal can be seen in a zoom on the fundamental frequency (Figs. 4.18(c) and 4.18(d)). The PM signal spectrogram shows a sinusoidally varying instantaneous frequency whereas the time-varying amplitude can be recognized with the AM signal. The modulation period is in each case 8 samples which corresponds to $T_c = 1/f_c$. Increasing the window length yields a spectrogram where the sidebands at $f_s \pm f_c$ become visible (see Figs. 4.18(e) and 4.18(f)). According to the preceding reflections, the PM and AM signatures are identical and cannot be distinguished. The situation resembles to the periodogram.

After simulations with stationary signals, consider now transient AM and PM signals. The chosen parameters correspond to those in section 4.3.1.4. Figure 4.19 displays the time-frequency representations with $N_w = 11$, $N_w = 49$ and $N_w = 149$. In contrast to the stationary signal, the PM/AM modulation is difficult to identify with the short analysis window. With $N_w = 49$, the sidebands are not yet visible due to the time-varying modulation frequencies and their small value at the beginning of the data record. With longer analysis windows, e.g. $N_w = 149$, the sidebands become visible. However, the lack of resolution makes it a difficult task to extract automatically fault indicators, especially at low fundamental frequencies.

4.3.3 Wigner Distribution

4.3.3.1 Stationary PM Signal

First, the WD of a monocomponent PM signal $i_{rt}(t)$ according to equation (4.8) is derived. The WD kernel expresses as:

$$\begin{aligned} K_{i_{rt}}(t, \tau) &= i_{rt}\left(t + \frac{\tau}{2}\right) i_{rt}^*\left(t - \frac{\tau}{2}\right) \\ &= I_{rt}^2 \exp j \{ \omega_s \tau \} \exp j \left\{ -2\beta \sin(\omega_c t - \varphi_\beta) \sin\left(\frac{\omega_c}{2}\tau\right) \right\} \end{aligned} \quad (4.42)$$

The FT of $K_{i_{rt}}(t, \tau)$ with respect to τ yields the WD. The kernel can be considered as a product which leads to a convolution of the FTs of the factors. Hence:

$$\begin{aligned} W_{i_{rt}}(t, f) &= \mathfrak{F}_{\tau \rightarrow f} \{ K_{i_{rt}}(t, \tau) \} \\ &= I_{rt}^2 \mathfrak{F}_{\tau \rightarrow f} \{ \exp j(\omega_s \tau) \} * \mathfrak{F}_{\tau \rightarrow f} \left\{ \exp j \left[-2\beta \sin(\omega_c t - \varphi_\beta) \sin\left(\frac{\omega_c}{2}\tau\right) \right] \right\} \end{aligned} \quad (4.43)$$

For the calculation of the second term, consider (4.10) with $t = \exp j\theta$. The complex notation of the sine function yields:

$$e^{j\gamma \sin \theta} = \sum_{k=-\infty}^{+\infty} J_k(\gamma) e^{jk\theta} \quad (4.44)$$

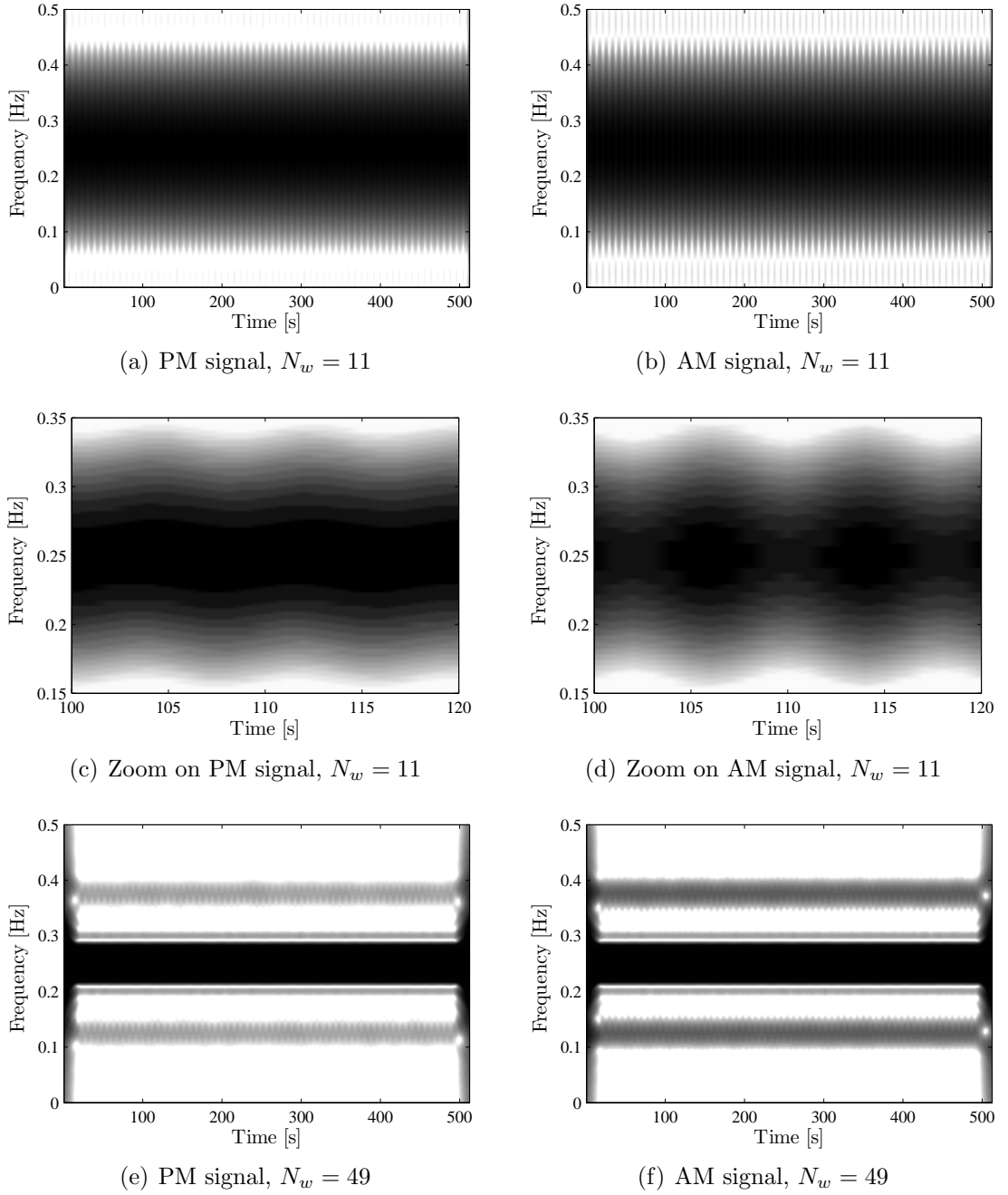


Figure 4.18: Spectrogram of simulated PM and AM stator current signals, $f_c = 0.125$, $\alpha = \beta = 0.1$, different window lengths.

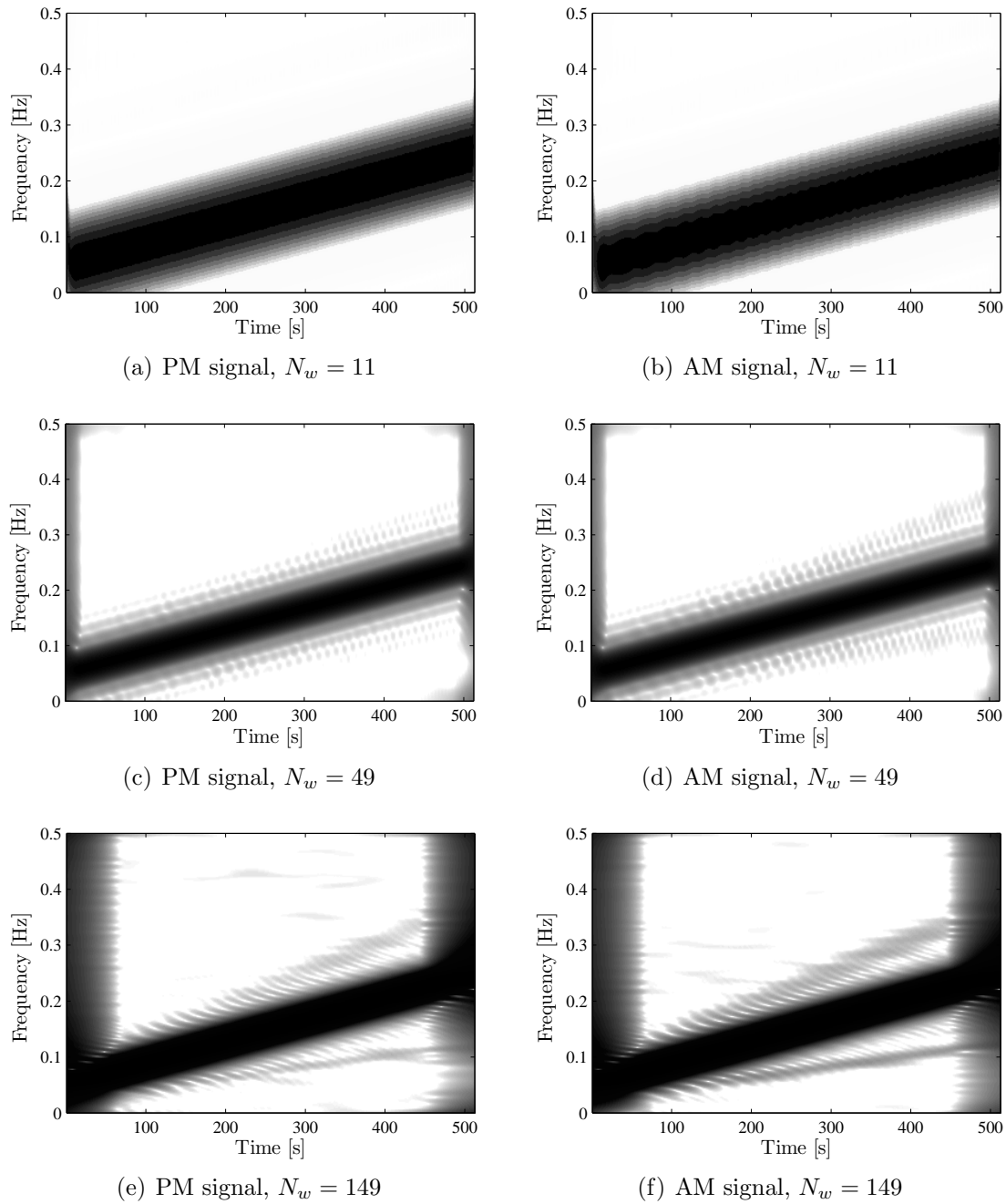


Figure 4.19: Spectrogram of simulated transient PM and AM stator current signals, $\alpha = \beta = 0.1$, different window lengths.

Using this relation and $\gamma = -2\beta \sin(\omega_c t - \varphi_\beta)$, the WD of $i_{rt}(t)$ can be rewritten:

$$\begin{aligned} W_{i_{rt}}(t, f) &= I_{rt}^2 \delta(f - f_s) * \mathfrak{F}_{\tau \rightarrow f} \left\{ \sum_{k=-\infty}^{+\infty} J_k(\gamma) e^{jk\omega_c \tau/2} \right\} \\ &= I_{rt}^2 \delta(f - f_s) * \sum_{k=-\infty}^{+\infty} J_k(\gamma) \delta\left(f - k\frac{f_c}{2}\right) \\ &= I_{rt}^2 \sum_{k=-\infty}^{+\infty} J_k(\gamma) \delta\left(f - f_s - k\frac{f_c}{2}\right) \end{aligned} \quad (4.45)$$

Since only small modulation indices are considered, the higher order Bessel function with $|k| \geq 2$ can be neglected and the following approximation is obtained (see section 4.2.1):

$$\begin{aligned} W_{i_{rt}}(t, f) &\approx J_0(\gamma) I_{rt}^2 \delta(f - f_s) + J_1(\gamma) I_{rt}^2 \delta\left(f - f_s - \frac{f_c}{2}\right) \\ &\quad - J_1(\gamma) I_{rt}^2 \delta\left(f - f_s + \frac{f_c}{2}\right) \\ &\approx I_{rt}^2 \delta(f - f_s) - \beta \sin(\omega_c t - \varphi_\beta) I_{rt}^2 \delta\left(f - f_s - \frac{f_c}{2}\right) \\ &\quad + \beta \sin(\omega_c t - \varphi_\beta) I_{rt}^2 \delta\left(f - f_s + \frac{f_c}{2}\right) \end{aligned} \quad (4.46)$$

This approximation clearly demonstrates the WD signature of a stationary PM signal with small modulation index. A strong component of amplitude I_{rt}^2 is present at the carrier or supply frequency f_s . The phase modulation leads to oscillating sidebands at frequencies $f_s \pm f_c/2$. The amplitudes of the sideband component are proportional to the modulation index β and I_{rt}^2 . The sideband amplitude oscillates at the fault characteristic frequency f_c . The upper and lower sidebands have opposed amplitudes for a given point in time, i.e. the phase shift between them is π . The sidebands can be considered as outer interferences since they result from nonlinear frequency modulation [Mec97].

The WD of the unmodulated stator current component $i_{st}(t)$ (see (4.7)) is simply:

$$W_{i_{st}}(t, f) = I_{st}^2 \delta(f - f_s) \quad (4.47)$$

The WD of the stator current PM signal $i_{pm}(t) = i_{st}(t) + i_{rt}(t)$ must be calculated according to the quadratic addition formula (3.73). For this purpose, the cross WD between $i_{st}(t)$ and $i_{rt}(t)$ is derived:

$$\begin{aligned} W_{i_{st}, i_{rt}}(t, f) &= \int_{-\infty}^{+\infty} i_{st}\left(t + \frac{\tau}{2}\right) i_{rt}^*\left(t - \frac{\tau}{2}\right) e^{-j2\pi f \tau} d\tau \\ &= I_{st} I_{rt} e^{j\varphi_r} \sum_{k=-\infty}^{\infty} \sum_{m=-\infty}^{\infty} j^k J_k(\gamma_1) J_m(\gamma_2) \delta\left(f - f_s - k\frac{f_c}{2} - m\frac{f_c}{2}\right) \end{aligned} \quad (4.48)$$

with

$$\gamma_1 = -\beta \cos(\omega_c t - \varphi_\beta) \quad \gamma_2 = -\beta \sin(\omega_c t - \varphi_\beta) \quad (4.49)$$

As before, Bessel functions $J_k(\gamma_i)$ with order $|k| \geq 2$ are neglected since β is supposed small. Therefore, all products $J_k(\gamma_1)J_m(\gamma_2)$ with $|k| \geq 2$ or $|m| \geq 2$ will be neglected. Furthermore, using $J_0(\gamma_i) \approx 1$ and $J_1(\gamma_i) \approx \beta/2$, the following approximation is obtained:

$$\begin{aligned} W_{i_{st}, i_{rt}}(t, f) &\approx I_{st} I_{rt} e^{j\varphi_r} \delta(f - f_s) \\ &\quad - \frac{1}{2} \beta j e^{-j(\omega_c t - \varphi_\beta - \varphi_r)} I_{st} I_{rt} \delta\left(f - f_s - \frac{f_c}{2}\right) \\ &\quad - \frac{1}{2} \beta j e^{j(\omega_c t - \varphi_\beta + \varphi_r)} I_{st} I_{rt} \delta\left(f - f_s + \frac{f_c}{2}\right) \end{aligned} \quad (4.50)$$

In the quadratic addition formula, twice the real part of the cross WD appears:

$$\begin{aligned} 2\Re\{W_{i_{st}, i_{rt}}(t, f)\} &\approx 2I_{st} I_{rt} \cos \varphi_r \delta(f - f_s) \\ &\quad - \beta \sin(\omega_c t - \varphi_\beta - \varphi_r) I_{st} I_{rt} \delta\left(f - f_s - \frac{f_c}{2}\right) \\ &\quad + \beta \sin(\omega_c t - \varphi_\beta + \varphi_r) I_{st} I_{rt} \delta\left(f - f_s + \frac{f_c}{2}\right) \end{aligned} \quad (4.51)$$

This expression is similar to the WD of the monocomponent PM signal in equation (4.46) with an approximately constant component at f_s and oscillating sidebands at $f_s \pm f_c/2$. However, in contrast to (4.46), the phase shift between the upper and the lower sideband is no longer π but depends on the angle φ_r between rotor and stator MMF. This angle depends on the motor load condition which signifies that the average load directly influences the interference structure of the cross WD. The phase shift in this case is $(\pi - 2\varphi_r)$.

The WD of $i_{pm}(t)$ is then obtained as the sum of equations (4.46), (4.47) and (4.51):

$$\begin{aligned} W_{i_{pm}}(t, f) &\approx (I_{st}^2 + I_{rt}^2 + 2I_{st} I_{rt} \cos \varphi_r) \delta(f - f_s) \\ &\quad - \beta [I_{rt}^2 \sin(\omega_c t - \varphi_\beta) + I_{st} I_{rt} \sin(\omega_c t - \varphi_\beta - \varphi_r)] \delta\left(f - f_s - \frac{f_c}{2}\right) \\ &\quad + \beta [I_{rt}^2 \sin(\omega_c t - \varphi_\beta) + I_{st} I_{rt} \sin(\omega_c t - \varphi_\beta + \varphi_r)] \delta\left(f - f_s + \frac{f_c}{2}\right) \end{aligned} \quad (4.52)$$

As in the previous expression of the cross WD, the phase shift between the upper and lower sideband depends on φ_r and consequently the motor load. However, approximations are possible: First consider the case of small load. Since the output torque depends on φ_r , φ_r is small in this case. The phase shift in the cross WD will then be close to π as well as the phase shift in $W_{i_{pm}}(t, f)$. When the load becomes higher, φ_r increases and the phase shift in the cross WD becomes different from π . However, the rotor current I_{rt} will also be greater than I_{st} in this case. This leads to a greater amplitude of the sideband components with amplitude I_{rt}^2

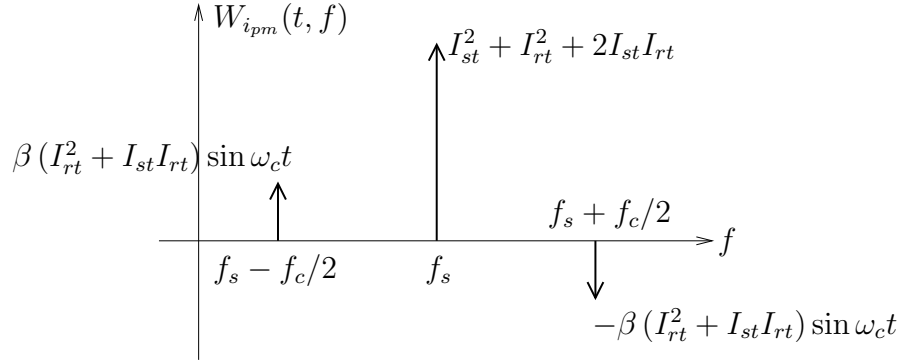


Figure 4.20: Illustration of the Wigner Distribution of a PM stator current signal with $\varphi_r = 0$ and $\varphi_\beta = 0$.

compared to the sidebands of amplitude $I_{st}I_{rt}$ resulting from the cross WD. The influence of the latter on the total phase shift between upper and lower sideband will therefore become smaller with increasing I_{rt} . Consequently, a value close to π can be supposed in most cases.

The WD of a PM stator current signal is illustrated in Fig. 4.20 for a certain point in time. The fundamental and sideband amplitudes are indicated. For simplification, $\varphi_r = 0$ and $\varphi_\beta = 0$ have been supposed. Note that the sideband amplitudes vary sinusoidally with respect to time.

4.3.3.2 Transient PM Signal

The exact analytical determination of the WD of a transient PM signal according to (4.33) is complex and will not be presented here. An approximation is possible when the fault pulsation $\omega_c(t)$ is supposed quasi-stationary: $\omega_c(t) \approx 2\pi f_c$. Then, the transient PM signal can be considered as the product of a stationary PM signal with $\omega_s = 0$ and a linear chirp signal $z_{tr}(t)$:

$$\begin{aligned} i_{pm,tr}(t) &= [I_{st} + I_{rt} \exp j(\beta \cos(\omega_c t - \varphi_\beta) - \varphi_r)] \exp j(2\pi(\alpha_s + \beta_s t/2)t) \\ &= i_{pm}(t)|_{\omega_s=0} z_{tr}(t) \end{aligned} \quad (4.53)$$

The WD of the stationary PM signal has been calculated in the previous section. The WD of $z_{tr}(t)$ is obtained as:

$$W_{z_{tr}}(t, f) = \delta(f - \alpha_s - \beta_s t) \quad (4.54)$$

The modulation invariance property of the WD states [Boa03]:

$$z_3(t) = z_1(t)z_2(t) \quad , \quad W_{z_3}(t, f) = W_{z_1}(t, f) *_f W_{z_2}(t, f) \quad (4.55)$$

where $*_f$ denotes the frequency convolution. This property can be used to obtain

the approximated WD of equation (4.53):

$$\begin{aligned}
W_{i_{pm},tr}(t, f) &= W_{i_{pm}}(t, f)|_{\omega_s=0} *_f W_{ztr}(t, f) \\
&\approx (I_{st}^2 + I_{rt}^2 + 2I_{st}I_{rt}) \delta(f - \alpha_s - \beta_s t) \\
&\quad - \beta [I_{rt}^2 \sin(\omega_c t - \varphi_\beta) + I_{st}I_{rt} \sin(\omega_c t - \varphi_\beta - \varphi_r)] \delta\left(f - \alpha_s - \beta_s t - \frac{f_c}{2}\right) \\
&\quad + \beta [I_{rt}^2 \sin(\omega_c t - \varphi_\beta) + I_{st}I_{rt} \sin(\omega_c t - \varphi_\beta + \varphi_r)] \delta\left(f - \alpha_s - \beta_s t + \frac{f_c}{2}\right)
\end{aligned} \tag{4.56}$$

This expression shows that the fault signature calculated in the stationary case is preserved. The sidebands with opposed amplitudes appear around the time-varying supply frequency.

4.3.3.3 Stationary AM Signal

In the following, the WD of a stationary AM signal according to (4.36) is calculated. The kernel $K_{iam}(t, \tau)$ expresses as:

$$\begin{aligned}
K_{iam}(t, \tau) &= i_{am}\left(t + \frac{\tau}{2}\right) i_{am}^*\left(t - \frac{\tau}{2}\right) \\
&= I_1^2 \exp j\{\omega_s \tau\} \left[1 + \frac{1}{2}\alpha^2 \cos(2\omega_c t - 2\varphi_\alpha) \right. \\
&\quad \left. + 2\alpha \cos(\omega_c t - \varphi_\alpha) \cos\left(\frac{\omega_c}{2}\tau\right) + \frac{1}{2}\alpha^2 \cos(\omega_c \tau) \right]
\end{aligned} \tag{4.57}$$

The Fourier transform of this expression yields the WD:

$$\begin{aligned}
W_{iam}(t, f) &= \mathfrak{F}_{\tau \rightarrow f} \{K_{iam}(t, \tau)\} \\
&= \left[1 + \frac{1}{2}\alpha^2 \cos(2\omega_c t - 2\varphi_\alpha) \right] I_1^2 \delta(f - f_s) \\
&\quad + \alpha \cos(\omega_c t - \varphi_\alpha) I_1^2 \left[\delta\left(f - f_s - \frac{f_c}{2}\right) + \delta\left(f - f_s + \frac{f_c}{2}\right) \right] \\
&\quad + \frac{1}{4}\alpha^2 I_1^2 \left[\delta(f - f_s - f_c) + \delta(f - f_s + f_c) \right]
\end{aligned} \tag{4.58}$$

An approximation for this expression can be obtained considering that the terms containing α^2 can be neglected for small α :

$$\begin{aligned}
W_{iam}(t, f) &\approx I_1^2 \delta(f - f_s) + \alpha \cos(\omega_c t - \varphi_\alpha) I_1^2 \delta\left(f - f_s - \frac{f_c}{2}\right) \\
&\quad + \alpha \cos(\omega_c t - \varphi_\alpha) I_1^2 \delta\left(f - f_s + \frac{f_c}{2}\right)
\end{aligned} \tag{4.59}$$

This equation clearly shows the AM signature on the WD: The amplitude modulation leads to sidebands at $f_s \pm f_c/2$. The sidebands oscillate at fault frequency f_c , their amplitude is αI_1^2 . It should be noted that the signature is similar to the

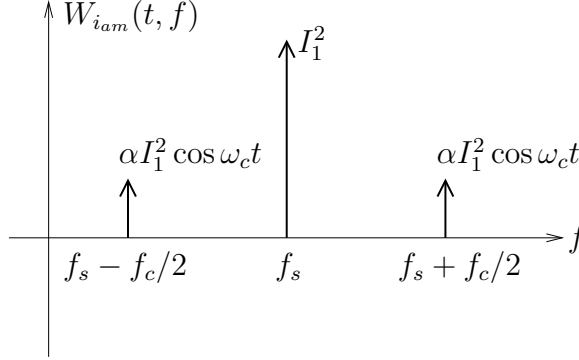


Figure 4.21: Illustration of the Wigner Distribution of an AM stator current signal with $\varphi_\alpha = 0$.

PM signal but with the important difference that the upper and lower sideband oscillations have the same amplitudes for a given point in time i.e. their phase shift is zero.

In Fig. 4.21, the WD of an AM stator current signal is illustrated for a certain point in time including the fundamental and sideband amplitudes. For simplification, $\varphi_\alpha = 0$ has been supposed. Note that the sideband amplitudes vary sinusoidally with respect to time and that the upper and lower sideband are always in phase.

4.3.3.4 Transient AM Signal

As in the case of the transient PM signal, the transient AM signal is only calculated with the quasi-stationary approximation $\omega_c(t) = 2\pi f_c$. The transient AM signal is also considered as a product:

$$\begin{aligned} i_{am,tr}(t) &= I_1 [1 + \alpha \cos(\omega_c t - \varphi_\alpha)] \exp j(2\pi(\alpha_s + \beta_s t/2)t) \\ &= i_{am}(t)|_{\omega_s=0} z_{tr}(t) \end{aligned} \quad (4.60)$$

The WD of $i_{am,tr}(t)$ is then the frequency convolution of $W_{i_{am}}(t, f)$ and $W_{z_{tr}}(t, f)$. It is approximated as:

$$\begin{aligned} W_{i_{am,tr}}(t, f) &= W_{i_{pm}}(t, f)|_{\omega_s=0} *_f W_{z_{tr}}(t, f) \\ &\approx I_1^2 \delta(f - \alpha_s - \beta_s t) \\ &\quad + \alpha \cos(\omega_c t - \varphi_\alpha) I_1^2 \delta\left(f - \alpha_s - \beta_s t - \frac{f_c}{2}\right) \\ &\quad + \alpha \cos(\omega_c t - \varphi_\alpha) I_1^2 \delta\left(f - \alpha_s - \beta_s t + \frac{f_c}{2}\right) \end{aligned} \quad (4.61)$$

This expression shows that the fault signature calculated in the stationary case is preserved. The sideband structure appears now around the varying supply frequency.

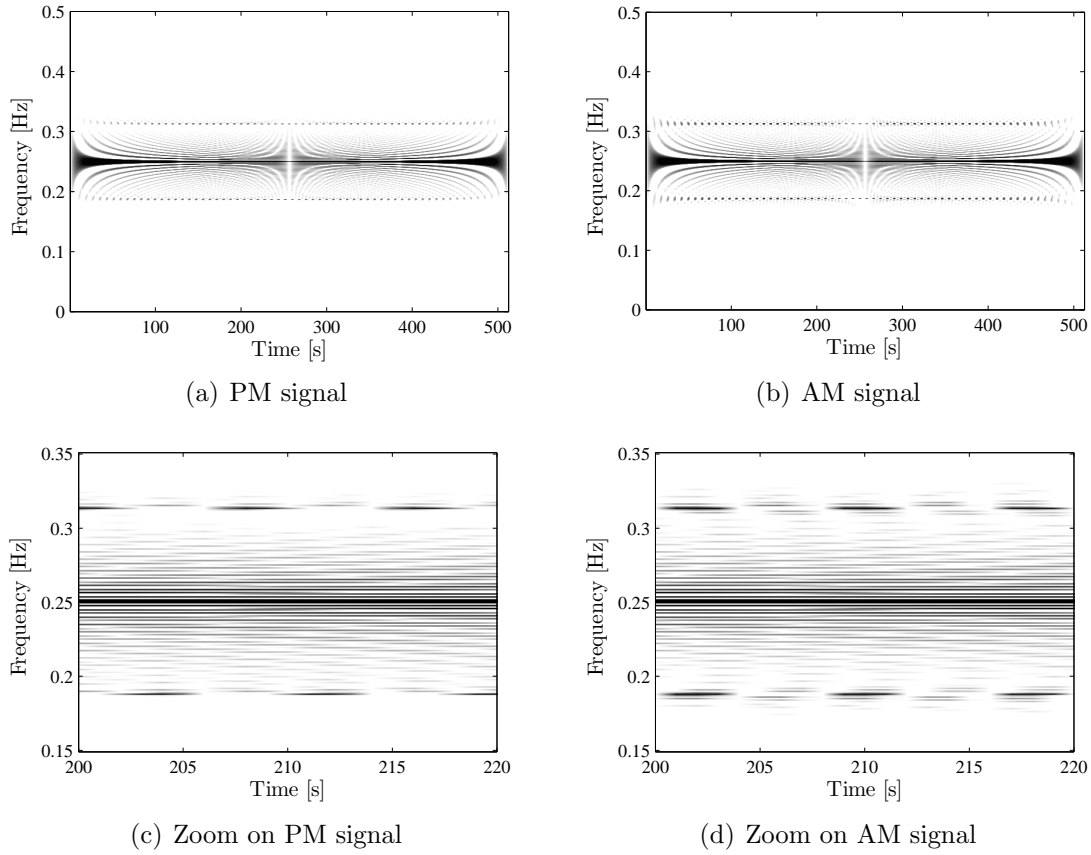


Figure 4.22: Wigner Distribution of simulated PM and AM signals with zoom on interference structure.

4.3.3.5 Simulation Results

First, simulations with stationary signals are presented. The simulated signals are synthesized with parameters according to 4.2.3 and data record length $N = 512$. The modulation indices are $\alpha = \beta = 0.1$. Similar to the instantaneous frequency, the real valued signals are transformed into their corresponding analytical signal before calculation of the time-frequency distributions. Thereto, algorithms from the Matlab Time-Frequency Toolbox [Aug96] are used.

The WD of the stator current PM and AM signals is displayed in Fig. 4.22. The theoretically calculated sidebands reflecting the modulation are clearly visible at $0.25 \pm 0.125/2$ normalized frequency. The zoom on the characteristic interferences in Figs. 4.22(c) and 4.22(d) shows the oscillating nature and the previously mentioned phase shift. The period of the oscillations is 8 samples which corresponds to the fault frequency $f_c = 0.125$. The phase shift between the sidebands is zero in the AM case and approximately π with the PM signal. However, the lecture of the WD is disturbed by various other interferences.

In order to reduce these interferences, the PWD is calculated using the same signals and a Hanning window of length $N_w = 127$. The resulting distributions are displayed in Fig. 4.23. Except for interferences at the beginning and end of the

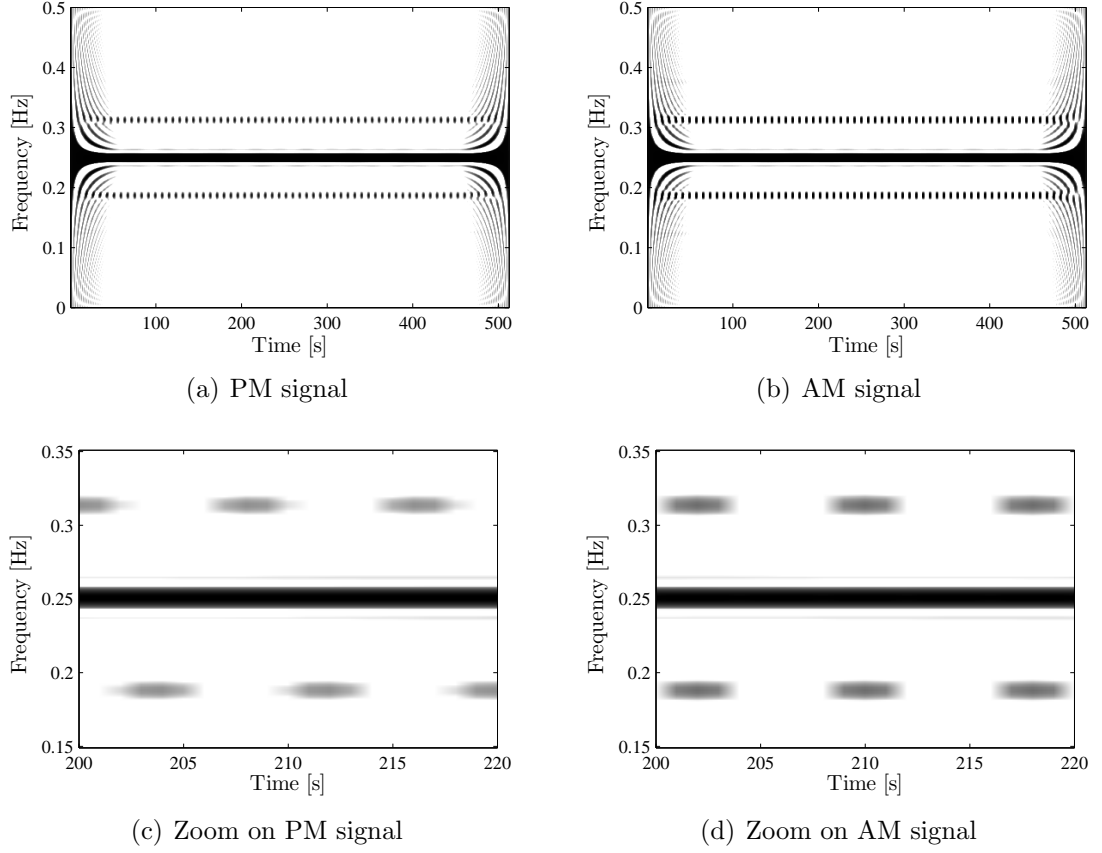


Figure 4.23: Pseudo Wigner Distribution of simulated PM and AM signals with zoom on interference structure.

data record, the distribution is nearly free of them. The fault signatures appear clearly around the fundamental. The zoom on the sidebands illustrates the differences in the phase shift between the PM and AM signal. Since the characteristic interference structure requires a good time resolution, no time smoothing should be used. Hence, the PWD will be preferred in the following to the WD or SPWD.

After the study of stationary signals, results with transient signals are shown. The synthesized signal parameters correspond to those in section 4.3.1.4. The results displayed in Fig. 4.24 demonstrate that the characteristic interference structure due to the modulation is also preserved in the transient case. This justifies the preceding simplifications in the theoretical calculations of the transient signal's WD. The zoom on the signature shows that the sidebands are located at $f_s(t) \pm f_c/2$. Their oscillation frequency corresponds to f_c with $f_c = f_s/2$.

4.3.3.6 Fault Indicator

The calculation of fault indicators based on the WD will be developed in the following for transient signals only since this is the more general case. Bearing in mind the characteristic fault signatures of AM and PM signals, several indicators with different performances can be imagined. The most simple indicator is the

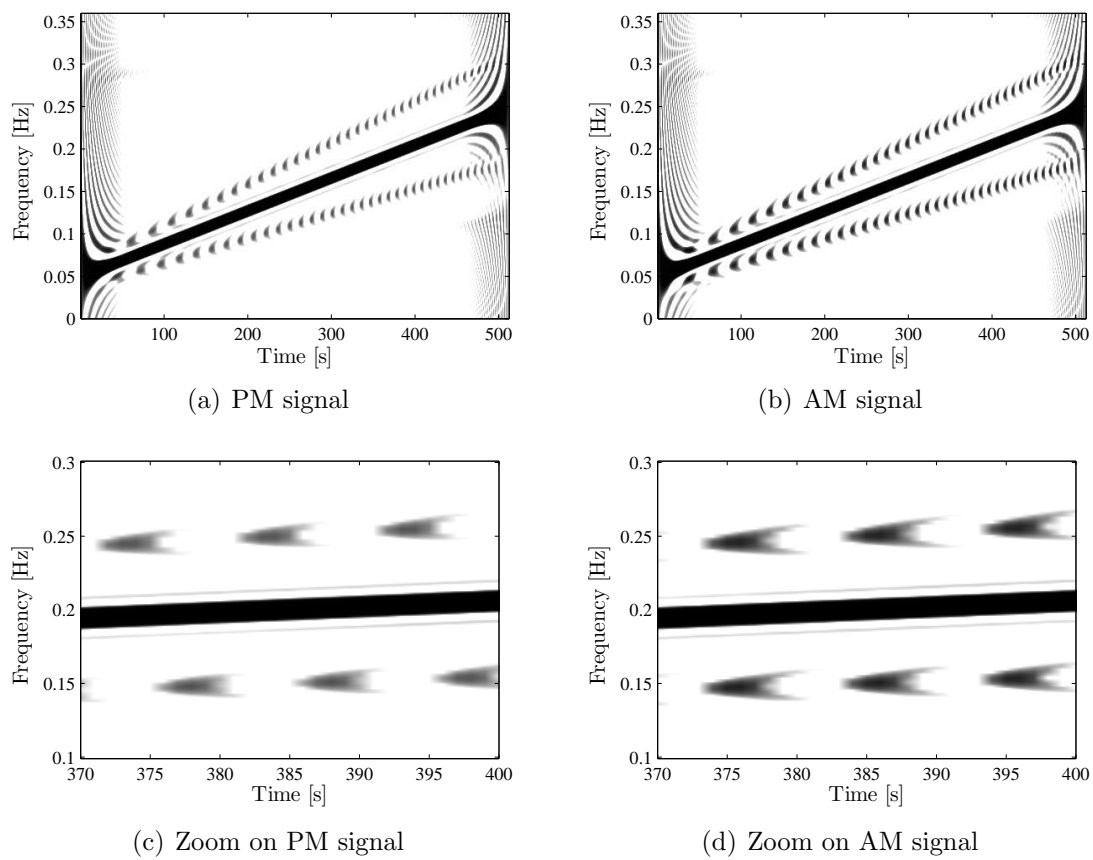


Figure 4.24: Pseudo Wigner Distribution of simulated transient PM and AM signals with zoom on interference structure.

energy of the fault-related sidebands. More advanced indicators could use the phase shift between upper and lower sideband to determine the type of modulation, i.e. if the sidebands result from PM or AM [Blö06b] [Blö06c].

The first fault indicator IWD1 is simply the sideband energy density. It is obtained as depicted in Fig. 4.25. After the calculation of the discrete PWD $PW[n, k]$ of the analytical stator current signal, the time varying supply frequency $f_s[n]$ is estimated. For each time bin n , the maximum value of the PWD yields the supply frequency $f_s[n]$ and its PWD amplitude, denoted $A[n]$. Depending on $f_s[n]$, the frequency intervals $I_l[n]$ and $I_u[n]$ for the sideband locations can be defined, since the sidebands are located at $f_s \pm f_c/2$. The value of $f_c[n]$ depends on $f_s[n]$ and the relation to f_r . In the considered example with $f_c = f_r$ and $p = 2$, $f_{c,min}[n] = 0.93 f_s[n]/2$ and $f_{c,max}[n] = 1.02 f_s[n]/2$ are supposed. The energy in these intervals is simply the sum of the absolute PWD amplitudes. In order to obtain energy densities $E_l[n]$ and $E_u[n]$, the energy is divided by the number of frequency bins N_l or N_u in the corresponding interval. Tests have shown the better performance of energy densities in case of variable supply frequency compared to simply the energy. This can be explained by the fact that the intervals $I_{l,u}$ are larger for higher supply frequencies, leading to higher energy values. This is related to the smoothing in the frequency direction which is at the origin for relatively broad peaks. Simulations showed the superior performance of energy densities compared to the total energy with quasi-constant indicators at variable supply frequency.

The obtained energy densities are added together and normalized with respect to the fundamental supply frequency amplitude $A[n]$. This should provide a certain indicator independence of the average load level. It should be noted that the obtained indicator IWD1[n] is oscillating since the sidebands itself are oscillating. Therefore, an averaging operation is required in a practical implementation. Anyway, the PWD must be calculated on distinct data records of finite length and thus, the average indicator value can be derived for the whole data record. Examples for indicators IWD1 with simulated transient signals are shown in Fig. 4.26. The signal parameters are the same as before but with varying modulation indices to test the indicator values. First, it is clearly visible that higher modulation indices lead to higher indicator values with an approximately linear relationship. The indicator is of oscillating nature and the oscillation frequency increases due to increasing f_s . The maximum indicator values are relatively independent of f_s since the energy density is used. The values of IWD1 in the PM case are approximately half of the indicator magnitude in the AM case. This can be explained by the fact that only the rotor related component of the PM signal is modulated. The normalization with respect to the total fundamental amplitude leads thus to smaller estimated indices. Since $I_{st} = I_{rt}$ in the simulation, the values are approximately half the values with the AM signal which is only composed of one component. These illustrations also show the major disadvantage of this indicator which is the same signature for PM and AM signals. Hence, the modulation type cannot be determined with this approach.

The problem can be overcome using a more sophisticated indicator which takes advantage of the phase shift between the upper and lower sideband of the fault signature. Instead of only calculating the total sideband energy or energy density

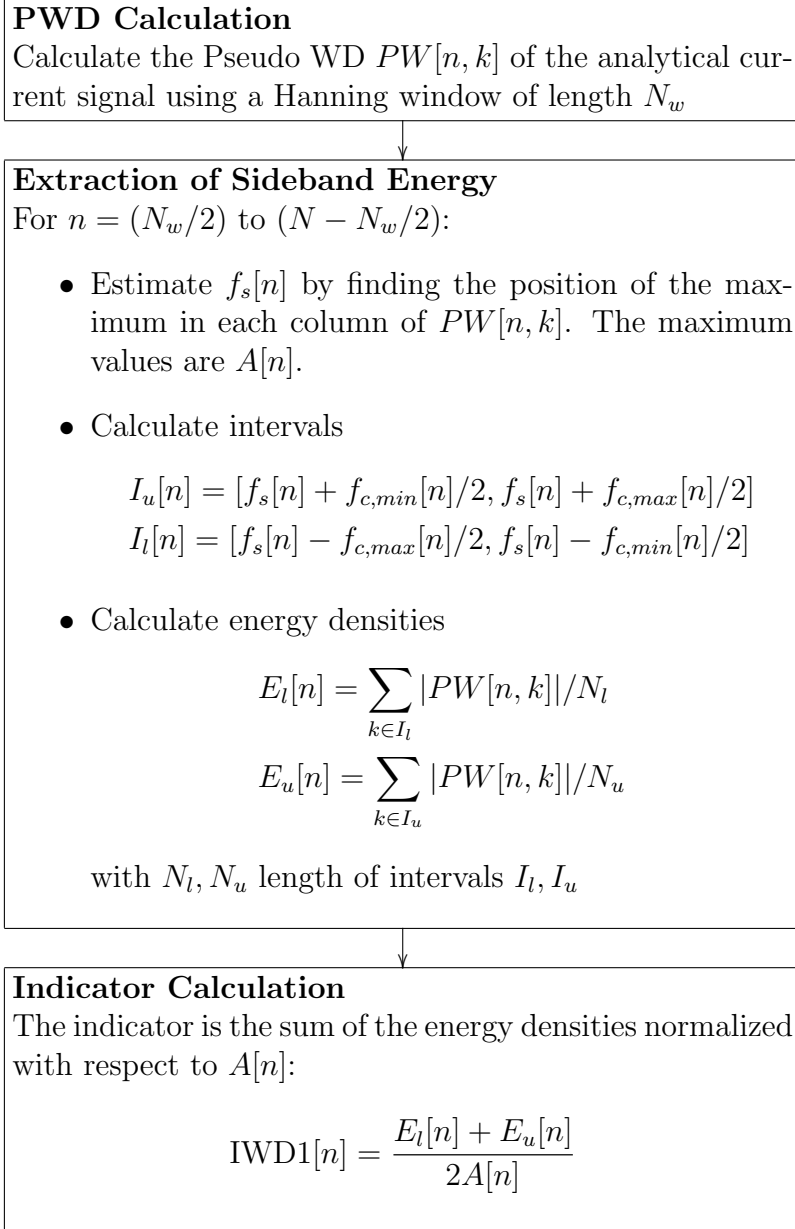


Figure 4.25: Calculation of the WD based fault indicator IWD1.

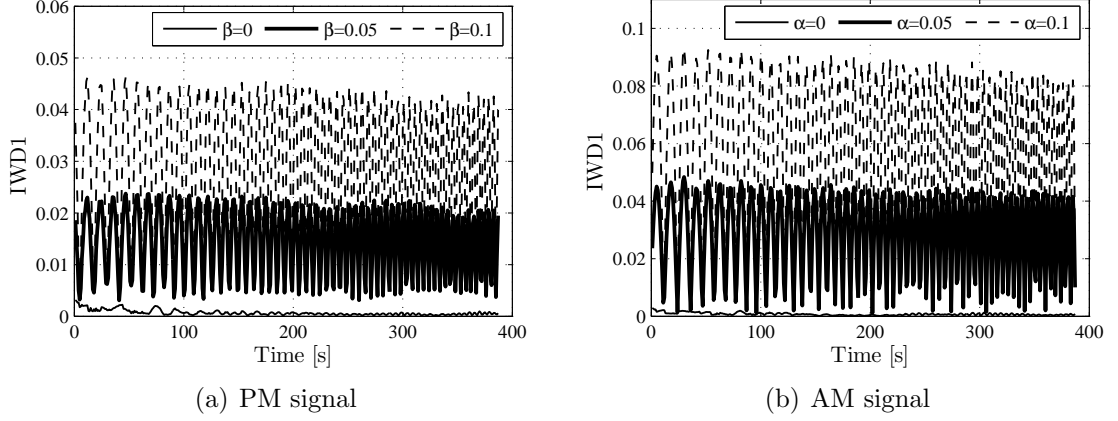


Figure 4.26: Fault indicator IWD1 with respect to time for different PM and AM modulation indices.

in the PWD, two signals containing the upper and lower sideband amplitudes are extracted and then processed. The scheme for obtaining this indicator, termed IWD2, is depicted in Fig. 4.27. As with the indicator IWD1, the stator current PWD is first calculated. After having determined the sideband intervals I_l and I_u , the algorithm searches for the maximum absolute value of the PWD in these intervals. Since the sidebands are oscillating and take negative values, the sign is also determined. The signed values of the maxima in I_l and I_u constitute the sideband signals $s_l[n]$ and $s_u[n]$ after normalization with respect to the fundamental amplitude $A[n]$.

The two sideband signals $s_l[n]$ and $s_u[n]$ contain information on:

- the modulation index through their amplitude which is normally the same for $s_l[n]$ and $s_u[n]$
- the modulation type through the phase shift between $s_l[n]$ and $s_u[n]$

The two sideband signals of transient PM and AM stator current signals are displayed in Fig. 4.28 for illustration. Their amplitude is approximately $\beta/2$ and α . In case of the PM signal, the amplitude is $\beta/2$ due to the multicomponent character with $I_{st} = I_{rt}$ and the normalization. The different phase shift resulting from PM and AM is clearly visible in the zoom with a phase shift close to π with the PM signal and close to zero in the AM case. It should be noted that the sideband signal frequency is variable.

In order to extract the two pieces of information, amplitude and phase shift, from the sideband signals, various methods can be imagined. If the signals are stationary, Fourier transform based techniques perform well. In the general case though, the sideband signals are non-stationary with variable frequency. A possible approach is the use of analytical signals for a simple extraction of the amplitudes and the phase difference. Thereto, the corresponding analytical sideband signals $s_{la}[n]$ and $s_{ua}[n]$ are synthesized. The signal envelopes i.e. their absolute value provides an estimate for their amplitude. The average amplitude $A_s[n]$ of both signals is calculated. The phase difference $\varphi_s[n]$ is obtained through the difference of

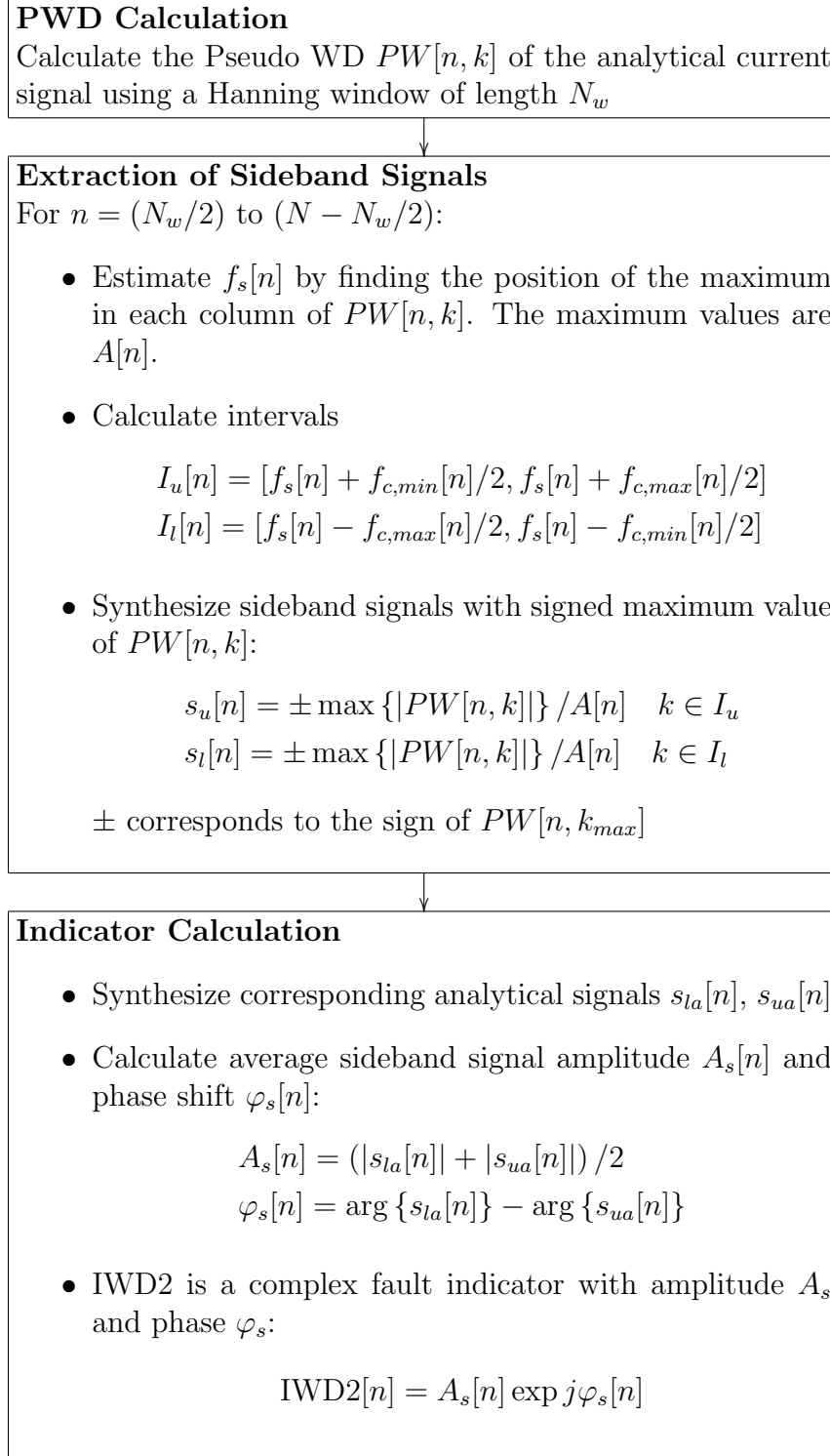
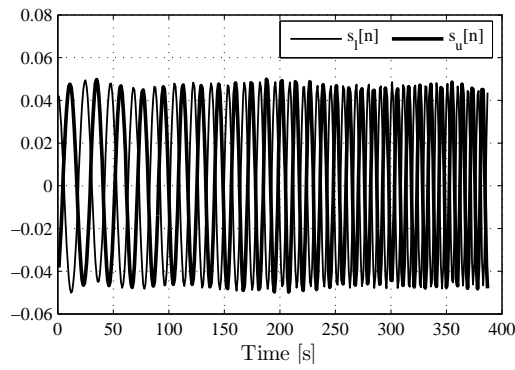
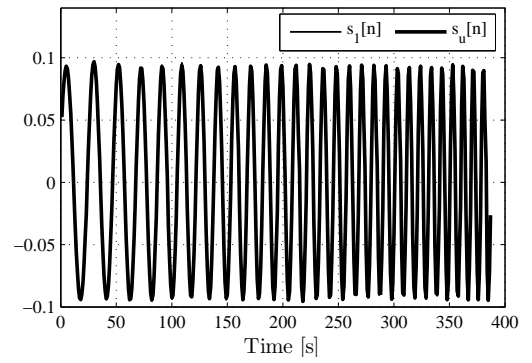


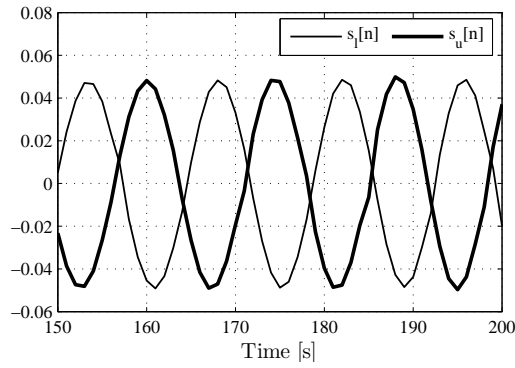
Figure 4.27: Calculation of the WD based fault indicator IWD2.



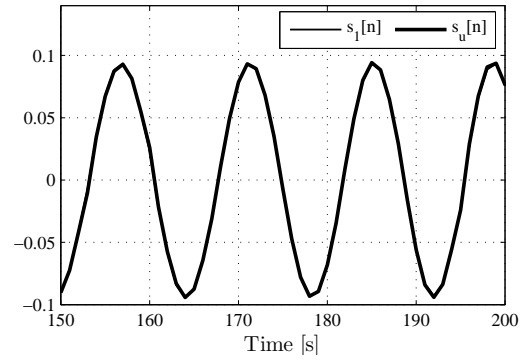
(a) Sidebands of PM signal



(b) Sidebands of AM signal



(c) Zoom on sidebands of PM signal



(d) Zoom on sidebands of AM signal

Figure 4.28: Example of extracted sideband signals from the PWD of simulated transient PM and AM stator current signals.

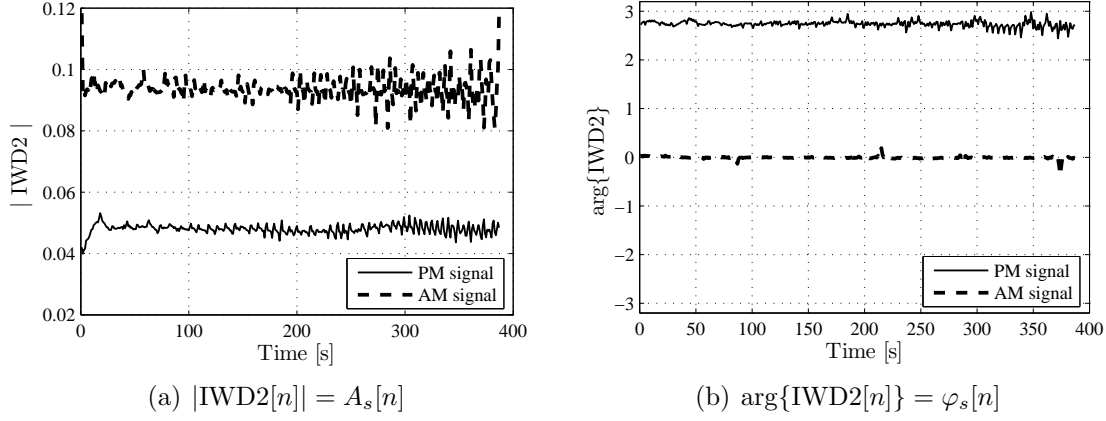


Figure 4.29: Absolute value and phase of complex fault indicator IWD2 for simulated transient PM and AM stator current signals.

the arguments of $s_{la}[n]$ and $s_{ua}[n]$. For simplicity and graphical representation, the fault indicator IWD2 is then considered in a compact form as a complex quantity with amplitude $A_s[n]$ and phase $\varphi_s[n]$:

$$IWD2[n] = A_s[n] \exp j\varphi_s[n] \quad (4.62)$$

For the previous example of the two sideband signals extracted from simulated transient PM and AM stator current signals, the amplitude and phase of IWD2 are displayed in Fig. 4.29. Despite the time varying frequency of the sideband signals, the amplitude $A_s[n] = |IWD2[n]|$ is approximately constant. The phase in Fig. 4.29(b) allows a clear discrimination of the modulation type: $\varphi_s[n]$ close to π for the PM signal whereas $\varphi_s[n] \approx 0$ with the AM signal.

For an easy distinction of the modulation types and for classification purposes, the fault indicator IWD2 is represented in the complex plane as in Fig. 4.30 for different modulation indices $\alpha, \beta = 0.0, 0.025, 0.05, 0.075, 0.1$. The average fault indicator is displayed i.e. the mean amplitude and phase for each data record. The AM and PM signals can be easily discriminated due to the different phase angle in the complex plane. An increase in the modulation index leads to an increasing absolute indicator value. The obtained phase angles are slightly smaller than π in the PM case due to the phase angle $\varphi_r \neq 0$ between rotor and stator current component (see equation (4.52)).

4.4 Parameter Estimation

The previously presented analysis methods were non-parametric methods that do not require a priori information about the signal model. An alternative approach is signal parameter estimation based on the signal models derived in chapter 2.

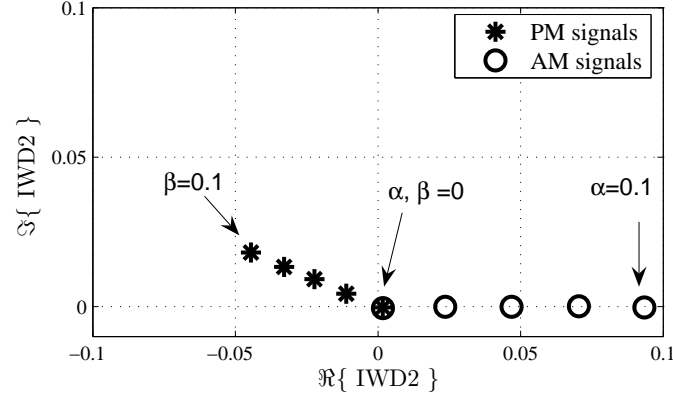


Figure 4.30: Complex representation of fault indicator IWD2 for simulated transient PM and AM stator current signals with different modulation indices.

4.4.1 Stationary PM Signal

4.4.1.1 Choice of Signal Model

The analytical stator current signal representing the effect of load torque oscillations takes the following expression according to (4.3):

$$i_{pm}(t) = I_{st} \exp j(\omega_s t) + I_{rt} \exp j(\omega_s t + \beta \cos(\omega_c t - \varphi_\beta) - \varphi_r) \quad (4.63)$$

An estimation of the model parameters is not directly possible since there are too much degrees of freedom. Consider for illustration the case with $\beta = 0$, i.e. without any oscillating torque. The observed signal is composed of two sinusoidal components with the same frequency, but unknown phase angle and amplitudes. An infinite number of solutions exists to this problem. Therefore, the use of this model for parameter estimation is not a reasonable choice.

A univocal solution can be determined by supposing a monocomponent sinusoidal PM signal. This approximation holds under medium to heavy load conditions since I_{rt} is strong compared to I_{st} . Moreover, recall that the developed PM stator current model neglects higher order armature reactions that should also lead to a phase modulation of the stator field related component with amplitude I_{st} . Furthermore, the PM modulation index β is the only parameter of interest for fault detection. Consequently, the estimation accuracy for other parameters is nonsignificant if it does not influence the estimation of β . The monocomponent analytical sinusoidal PM signal model expresses in discrete form as:

$$i_{pm,a}[n, \underline{\theta}] = \theta_1 \exp j[\theta_2 + \theta_3 \cos(2\pi\theta_4 n + \theta_5) + 2\pi\theta_6 n] \quad (4.64)$$

with $\underline{\theta} = [\theta_1 \ \theta_2 \ \theta_3 \ \theta_4 \ \theta_5 \ \theta_6]$ the parameter vector. The parameters have the following signification:

θ_1 : signal amplitude

θ_2 : initial phase of carrier frequency

θ_3 : PM modulation index which is the parameter of interest for fault detection

θ_4 : modulation frequency

θ_5 : initial phase of modulation

θ_6 : carrier frequency, supposed zero if signal is previously demodulated

By identification, the monocomponent model parameters can be related to the physical parameters in (4.63):

$$\begin{aligned}
 \theta_1 &= \sqrt{I_{st}^2 + I_{rt}^2 + 2I_{st}I_{rt} \cos(\beta \cos(\omega_c t - \varphi_\beta) - \varphi_r)} \\
 &\approx \sqrt{I_{st}^2 + I_{rt}^2 + 2I_{st}I_{rt} \cos(\varphi_r)} \quad \text{for } \beta \ll 1 \\
 \theta_2 &\approx \frac{-I_{rt} \sin \varphi_r}{I_{st} + I_{rt} \cos \varphi_r} \quad (*) \\
 \theta_3 &\approx \beta \frac{I_{rt} \cos \varphi_r}{I_{st} + I_{rt} \cos \varphi_r} \quad (*) \\
 \theta_4 &= f_c \\
 \theta_5 &= \varphi_\beta \\
 \theta_6 &= f_s
 \end{aligned}$$

Note that the approximations (*) are only valid for $\beta \ll 1$ and $\sin \varphi_r \ll 1$, i.e. φ_r small. It is important to note that the parameter θ_3 is directly proportional to the modulation index β . Therefore, an estimate of θ_3 can be used as a fault indicator.

The observed real signal is denoted $z[n]$ and it is supposed being the real part of $i_{pm,a}[n]$ plus additive zero-mean white Gaussian noise $w[n]$ of variance σ^2 :

$$z[n] = \Re\{i_{pm,a}[n]\} + w[n] = i_{pm}[n] + w[n] \quad (4.65)$$

The analytical signal is obtained through the Hilbert transform as follows:

$$z_a[n] = i_{pm,a}[n] + w_a[n] = i_{pm}[n] + j\mathcal{H}\{i_{pm}[n]\} + w[n] + j\mathcal{H}\{w[n]\} \quad (4.66)$$

Then, the joint PDF of the observed N samples is:

$$\begin{aligned}
 p(z_a, \underline{\theta}) &= \frac{1}{(2\pi\sigma^2)^N} \exp \left[-\frac{1}{2\sigma^2} \sum_{n=0}^{N-1} |z_a[n] - i_{pm,a}[n]|^2 \right] \\
 &= \frac{1}{(2\pi\sigma^2)^N} \exp \left[-\frac{1}{2\sigma^2} \sum_{n=0}^{N-1} (z[n] - i_{pm}[n])^2 + (\mathcal{H}\{z[n]\} - \mathcal{H}\{i_{pm}[n]\})^2 \right]
 \end{aligned} \quad (4.67)$$

4.4.1.2 Cramer-Rao Lower Bounds

The Cramer-Rao Lower Bounds (CRLB) for the parameter estimation of the monocomponent PM signal are calculated. First, the regularity condition (equation (3.89)) has been verified. The next step is the calculation of the Fisher information matrix $[I(\underline{\theta})]$. The elements can be calculated according to expression (3.90).

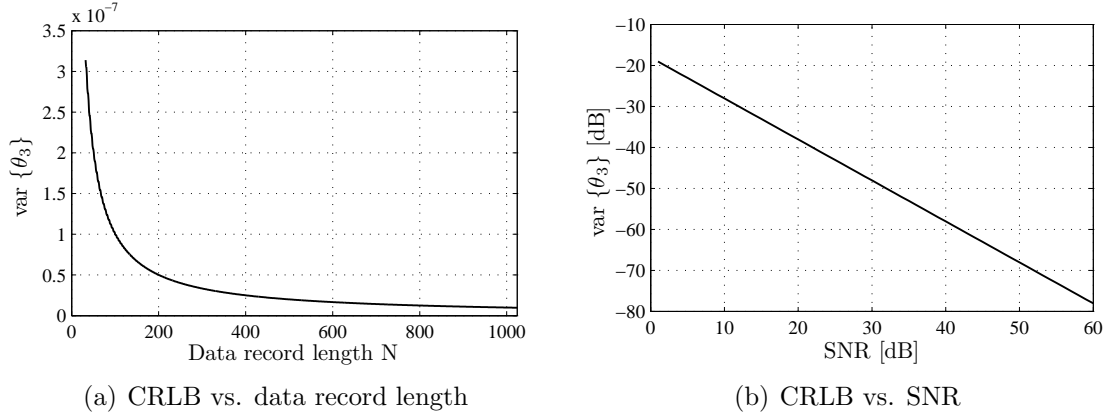


Figure 4.31: Theoretical Cramer-Rao lower bounds for $\text{var}\{\theta_3\}$ with respect to data record length N and SNR.

In the special case of the considered Gaussian PDF, the following formula can also be used (see [Rif74]):

$$[I(\underline{\theta})]_{ij} = \frac{1}{\sigma^2} \sum_{n=0}^{N-1} \left[\frac{\partial i_{pm}[n]}{\partial \theta_i} \frac{\partial i_{pm}[n]}{\partial \theta_j} + \frac{\partial \mathcal{H}\{i_{pm}[n]\}}{\partial \theta_i} \frac{\partial \mathcal{H}\{i_{pm}[n]\}}{\partial \theta_j} \right] \quad (4.68)$$

For the considered estimation problem, $[I(\underline{\theta})]$ is symmetric and takes the following form:

$$[I(\underline{\theta})] = \begin{bmatrix} f_{11} & 0 & 0 & 0 & 0 & 0 \\ 0 & f_{22} & f_{23} & f_{24} & f_{25} & f_{26} \\ 0 & f_{23} & f_{33} & f_{34} & f_{35} & f_{36} \\ 0 & f_{24} & f_{34} & f_{44} & f_{45} & f_{46} \\ 0 & f_{25} & f_{35} & f_{45} & f_{55} & f_{56} \\ 0 & f_{26} & f_{36} & f_{46} & f_{56} & f_{66} \end{bmatrix} \quad (4.69)$$

The expressions of the matrix elements are given in appendix B.1 [Blö06a]. They are in accordance with the more general results in [Gho99].

Due to the complexity of these expressions, their calculation and the following matrix inversion is realized numerically. The CRLB for the modulation index θ_3 is displayed in Fig. 4.31 with respect to the data record length N and the SNR. The fixed parameters take the following default values: $N = 64$, $\text{SNR} = 50$ dB, $\underline{\theta} = [1, \pi, 0.01, 0.125, \pi/4, 0.25]$. Fig. 4.31(a) shows that the CRLB decreases proportionally to the inverse of the data record length N . The bound is also inversely proportional to the SNR as can be seen on Fig. 4.31(b).

4.4.1.3 Maximum Likelihood Estimation

The MLE is obtained by maximizing the PDF $p(z_a, \underline{\theta})$ of the observed samples with respect to the parameters $\underline{\theta}$. Since the noise variance is not to be estimated, the argument of the exponential function has to be maximized. Note that since the noise is Gaussian, the MLE is equivalent to least squares estimation. The following

development (see [Blö06a]) has been inspired by the the single-tone parameter estimation procedure, described by Rife and Boorstyn in [Rif74].

Maximizing the PDF is equivalent to maximizing the function $L_0(z_a, \underline{\theta})$ with:

$$\begin{aligned} L_0(z_a, \underline{\theta}) &= -\frac{1}{N} \sum_{n=0}^{N-1} (z[n] - i_{pm}[n])^2 + (\mathcal{H}\{z[n]\} - \mathcal{H}\{i_{pm}[n]\})^2 \\ &= -\frac{1}{N} \sum_{n=0}^{N-1} z^2[n] + \mathcal{H}\{z[n]\}^2 - 2z[n]i_{pm}[n] - 2\mathcal{H}\{z[n]\}\mathcal{H}\{i_{pm}[n]\} \\ &\quad + i_{pm}^2[n] + \mathcal{H}\{i_{pm}[n]\}^2 \end{aligned} \quad (4.70)$$

Since the terms $z^2[n]$ and $\mathcal{H}\{z[n]\}^2$ are independent of the parameters, they are not considered in the following. Moreover:

$$i_{pm}^2[n] + \mathcal{H}\{i_{pm}[n]\}^2 = |i_{pm,a}[n]|^2 = \theta_1^2 \quad (4.71)$$

This leads to the equivalent problem of maximizing the function $L(z_a, \underline{\theta})$:

$$L(z_a, \underline{\theta}) = -\theta_1^2 + \frac{2}{N} \sum_{n=0}^{N-1} z[n]i_{pm}[n] + \mathcal{H}\{z[n]\}\mathcal{H}\{i_{pm}[n]\} \quad (4.72)$$

In the following, the phase of the PM model is supposed of a general form:

$$i_{pm,a}[n, \underline{\theta}] = \theta_1 \exp j[\theta_2 + \phi[n]] \quad (4.73)$$

where $\phi[n]$ contains only terms depending on n . Then, $L(z_a, \underline{\theta})$ expresses as:

$$L(z_a, \underline{\theta}) = -\theta_1^2 + \frac{2}{N} \theta_1 \sum_{n=0}^{N-1} z[n] \cos(\theta_2 + \phi[n]) + \mathcal{H}\{z[n]\} \sin(\theta_2 + \phi[n]) \quad (4.74)$$

This equation can be simplified since $z[n]$ and $\mathcal{H}\{z[n]\}$ are the real and imaginary part of $z_a[n]$. Consider an arbitrary complex number $z_1 = x_1 + jy_1$. With a real-valued angle φ , it can be derived that:

$$\Re\{z_1 e^{-j\varphi}\} = \Re\{(x_1 + jy_1) \cos \varphi - j(x_1 + jy_1) \sin \varphi\} = x_1 \cos \varphi + y_1 \sin \varphi \quad (4.75)$$

Hence:

$$L(z_a, \underline{\theta}) = -\theta_1^2 + \frac{2}{N} \theta_1 \sum_{n=0}^{N-1} \Re\{z_a[n] e^{-j(\theta_2 + \phi[n])}\} \quad (4.76)$$

Let define the complex function $B(z_a, \underline{\theta}')$, independent of θ_1, θ_2 and depending on $\underline{\theta}' = [\theta_3 \ \theta_4 \dots]$:

$$B(z_a, \underline{\theta}') = \frac{1}{N} \sum_{n=0}^{N-1} z_a[n] e^{-j\phi[n]} \quad (4.77)$$

Subsequently, $L(z_a, \underline{\theta})$ is:

$$L(z_a, \underline{\theta}) = -\theta_1^2 + 2\theta_1 \Re\{e^{-j\theta_2} B(z_a, \underline{\theta}')\} \quad (4.78)$$

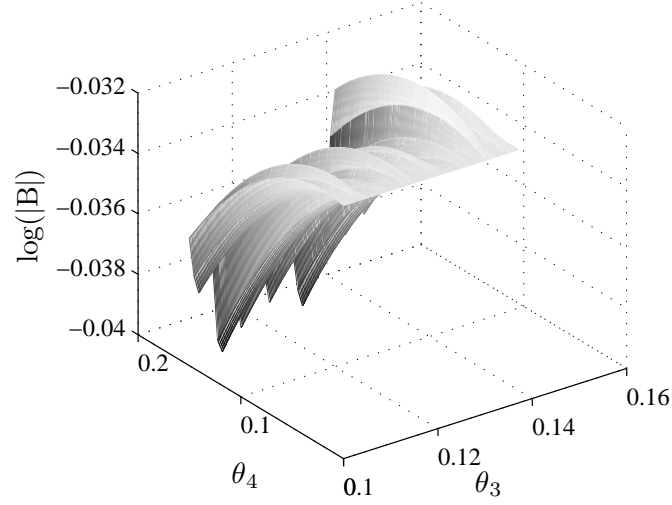


Figure 4.32: Example of function $|B(z_a, \underline{\theta}')|$ in logarithmic scale with $\theta_5, \theta_6 = \text{const.}$ and typical data record $z_a[n]$.

First, the maximum of this expression with respect to θ_2 is considered. The real part of any complex is maximized at constant absolute value when the complex is purely real. This means that equation (4.78) is maximized over θ_2 for fixed θ_1 and $B(z_a, \underline{\theta}')$ if:

$$\theta_2 = \arg \{B(z_a, \underline{\theta}')\} \quad (4.79)$$

Under this condition, the maximum of $L(z_a, \underline{\theta})$ is:

$$\max_{\theta_2} \{L(z_a, \underline{\theta})\} = -\theta_1^2 + 2\theta_1 |B(z_a, \underline{\theta}')| \quad (4.80)$$

For a given value of $|B(z_a, \underline{\theta}')|$, this expression is maximal with respect to θ_1 for:

$$\theta_1 = |B(z_a, \underline{\theta}')| \quad (4.81)$$

Then, the maximum of $L(z_a, \underline{\theta})$ is:

$$\max_{\theta_1, \theta_2} \{L(z_a, \underline{\theta})\} = |B(z_a, \underline{\theta}')|^2 \quad (4.82)$$

The MLE can therefore be resumed as follows: First, the function $|B(z_a, \underline{\theta}')|$ is maximized over $\underline{\theta}'$ to determine an estimate of these parameters. The remaining parameters θ_1 and θ_2 are then obtained by the analytical expressions (4.81) and (4.79).

4.4.1.4 Numerical Optimization

The maximum of $|B(z_a, \underline{\theta}')|$ cannot be found analytically. Moreover, it is a highly multimodal function as can be seen in Fig. 4.32 for an example with fixed θ_5, θ_6 . Numerical optimization techniques adapted to multimodal functions with various local minima and maxima are required.

The number of optimization parameters has been reduced from 6 to 4 by the preceding theoretical development. It can further be reduced by demodulation of

the complex stator current samples with an estimate of the supply frequency f_s . The latter can be rapidly obtained by the maximum of the periodogram using additional zero-padding. The PM parameter estimation is then carried out on the complex envelope, obtained by setting the parameter $\theta_6 = 0$ in the model.

Since the search space is relatively limited, a fixed grid search has first been implemented. This method has the advantage of delivering the global maximum in the search space with respect to the chosen grid. However, its computation is time-intensive and the discretization of the search space may lead to inaccurate results.

A popular stochastic algorithm is simulated annealing [Kir83] [Sch95c] that has been implemented and tested. However, the results could not be exploited due the poor algorithm convergence in our context.

A fast class of optimization algorithms are evolutionary algorithms. They imitate mechanisms found in natural evolution. Examples are genetic algorithms, evolutionary programming and evolution strategies [Bäc96] [Sch95c]. The latter have been chosen for our application. They appeared first in the 1960s at the Technical University of Berlin and were mainly used for design purposes by Rechenberg and Schwefel. In our case, a $(\mu + \lambda)$ -evolution strategy with auto-adaptive mutation is used [Bey02].

The general principle of the algorithm is displayed in Fig. 4.33. Each individual is represented by the object parameters $\underline{\theta}$ describing its location in the search space and the strategy parameters $\underline{\sigma}$. The number of object parameters N_θ is equivalent to the dimension of the search space and the same number of strategy parameters is used. The algorithm is initialized by generating a population of μ parents, uniformly distributed in the search space. Then, λ children are created by mutation, i.e. each parent creates λ/μ children by mutation of its object parameters according to:

$$\tilde{\theta}_i = \theta_i + \sigma_i N(0, 1) \quad (4.83)$$

where $\tilde{\theta}_i$ is the i -th object parameter of the child and $N(0, 1)$ a random number from a normal distribution with zero mean and variance $\sigma^2 = 1$. Before this step, the strategy parameters $\underline{\sigma}$ are also subject to mutation according to:

$$\tilde{\underline{\sigma}} = \exp(\tau_0 N(0, 1)) \cdot \begin{bmatrix} \sigma_1 \exp(\tau N(0, 1)) \\ \sigma_2 \exp(\tau N(0, 1)) \\ \dots \\ \sigma_{N_\theta} \exp(\tau N(0, 1)) \end{bmatrix} \quad (4.84)$$

with the following learning parameters:

$$\tau_0 = \frac{c}{\sqrt{2N_\theta}} \quad , \quad \tau = \frac{c}{\sqrt{2\sqrt{N_\theta}}} \quad (4.85)$$

In [Bey02], $c = 1$ is mentioned as a reasonable choice for a (10,100) evolution strategy. Each strategy parameter σ_i is initialized at the beginning as the width of the corresponding dimension of the search space divided by 10.

The mutation is followed by an evaluation and selection process. The cost function is calculated for each new individual. Depending on its value, the best μ

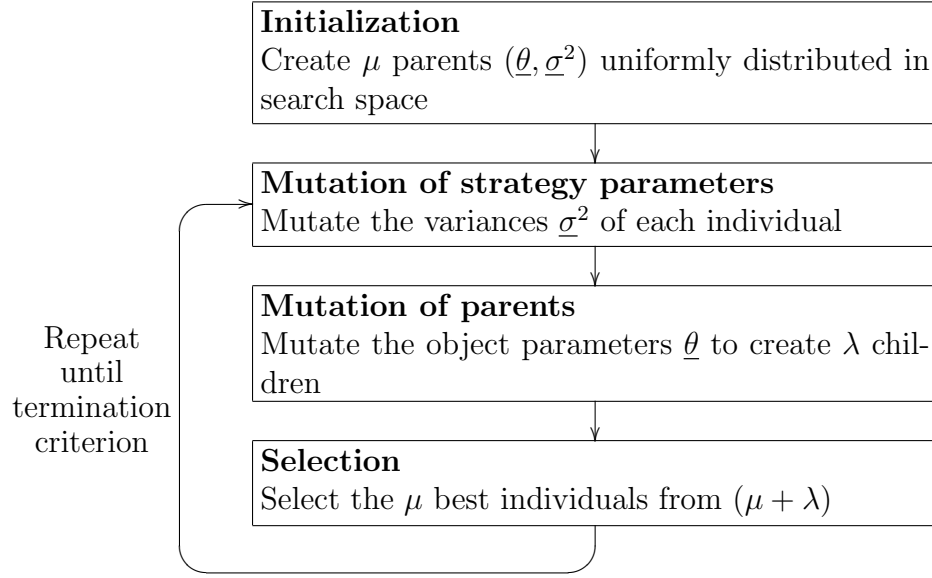


Figure 4.33: Scheme of the evolutionary optimization algorithm: $(\mu+\lambda)$ -evolution strategy.

individuals with respect to the optimization criterion are selected to form the next parent generation. The loop including mutation and selection is executed until the termination criterion is reached. This can be e.g. a maximum number of generations or an optimum that did not change during a certain number of generations. In the present case, a constant optimum during 30 generations or a maximum of 1000 generations is used as stop condition.

4.4.1.5 Simulation Results

The PM estimation procedure is tested through simulations for different data record lengths N . A monocomponent real PM signal $z[n]$ is generated according to:

$$z[n, \underline{\theta}] = \theta_1 \cos [\theta_2 + \theta_3 \cos (2\pi\theta_4 n + \theta_5) + 2\pi\theta_6 n] + w[n] \quad (4.86)$$

where $w[n]$ is zero-mean white Gaussian noise of variance σ^2 . The chosen SNR is 50 dB and the parameter vector $\underline{\theta} = [\sqrt{2} \quad -\pi/8 \quad 0.01 \quad 0.125 \quad \pi/4 \quad 0.25]$.

Prior to the estimation procedure, the corresponding analytical signal $z_a[n]$ is calculated and then demodulated for a faster estimation procedure. The demodulation frequency is obtained through a periodogram estimate of $z_a[n]$ with zero-padding. The estimation is then carried out using a model with $\theta_6 = 0$. The following optimization problem depends on only 3 parameters.

First, a $(40+200)$ evolution strategy is used. The termination criterion is a constant optimum during 30 generations or a maximum of 1000 generations. The estimator performance is studied for different data record lengths from $N = 64$ to 512 samples. For each data record length, 1000 independent simulations are carried out.

The results obtained with the evolution strategy are displayed in Fig. 4.34.

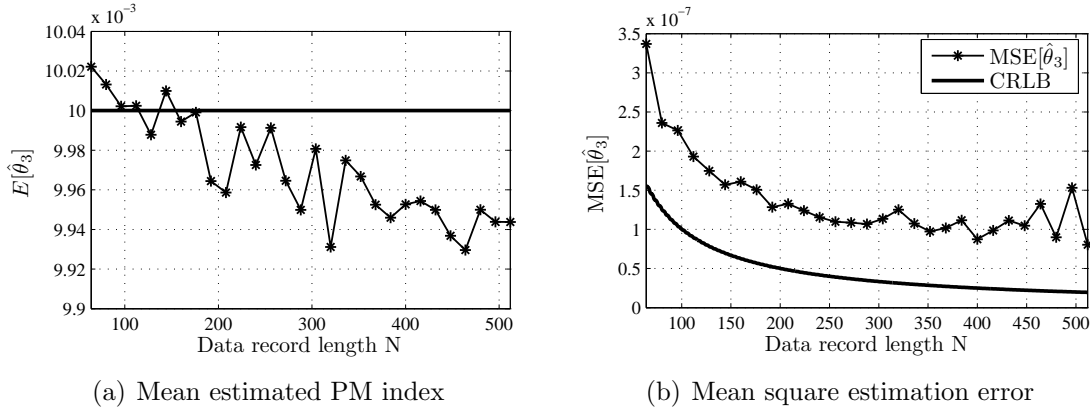


Figure 4.34: Simulation results: mean estimated PM index vs. N and mean square estimation error together with CRLB vs. N , optimization with (40+200)-evolution strategy.

Fig. 4.34(a) shows the mean estimated modulation index vs. the data record length. The estimation bias seems to increase with the data record length. This could be related to convergence problems due to an increasing number of local maxima when N increases. However, the relative bias is always inferior to 0.8%. The MSE is displayed in Fig. 4.34(b) vs. the theoretical CRLB. The MSE decreases with increasing data record length similar to the CRLB. However, the difference between the MSE and the CRLB seems to be relatively constant and could be due to the bias.

The same simulations have been carried out using the fixed grid search for optimization. The chosen step sizes for the three parameters are:

$$\Delta\theta_3 = 0.001 \quad \Delta\theta_4 = 0.001 \quad \Delta\theta_5 = 0.25 \quad (4.87)$$

The results in Fig. 4.35 show a decreasing bias with increasing data record length and the MSE approaching the CRLB. The improved performance of the fixed grid search is at the expense of computation time since the estimation procedure is about 4 times faster using the evolution strategy.

4.4.2 Stationary AM Signal

The equivalent estimation procedure as in the PM case can be used for parameter estimation of the AM signal. The model for the discrete analytical AM signal corresponding to (4.4) is:

$$i_{am,a}[n, \underline{\kappa}] = \kappa_1 [1 + \kappa_2 \cos(2\pi\kappa_3 n - \kappa_4)] \exp j(2\pi\kappa_5 n - \kappa_6) \quad (4.88)$$

with $\underline{\kappa} = [\kappa_1, \dots, \kappa_6]$ the parameter vector. The parameter of interest for fault detection is the AM modulation index κ_2 .

However, the simplifications for reduction of the number of parameters with the PM signal cannot be applied in this case. Hence, a time-consuming optimization

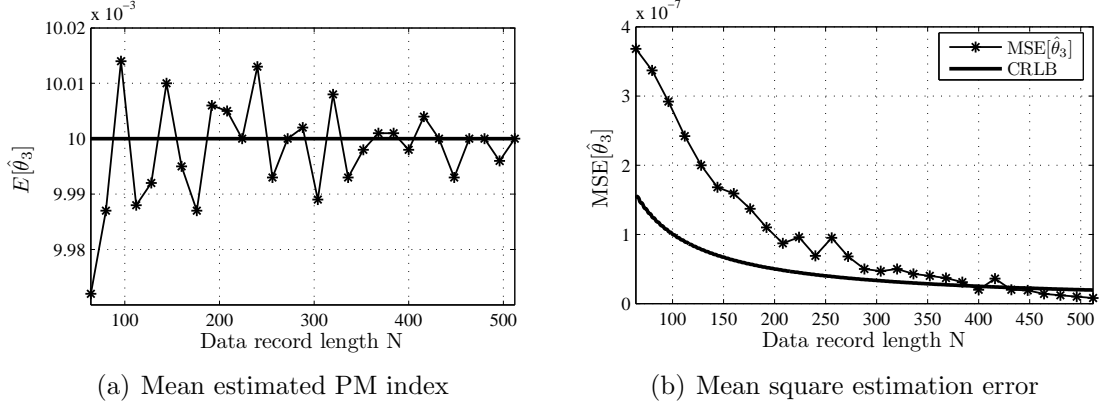


Figure 4.35: Simulation results: mean estimated PM index vs. N and mean square estimation error together with CRLB vs. N , optimization with fixed grid search.

must be carried out with respect to 6 parameters or 5 with previous demodulation. An alternative is the use of the instantaneous amplitude $a_{i_{am,a}}[n, \underline{\kappa}']$ i.e. the absolute value of the analytical signal which is given by the following expression in our case:

$$a_{i_{am,a}}[n, \underline{\kappa}'] = |i_{am,a}[n, \underline{\kappa}]| = \kappa_1 [1 + \kappa_2 \cos(2\pi\kappa_3n - \kappa_4)] \quad (4.89)$$

with $\underline{\kappa}' = [\kappa_1 \kappa_2 \kappa_3 \kappa_4]$.

Using the instantaneous amplitude, the problem of estimating κ_2 is now equivalent to estimating the amplitude of a sinusoid with an additional DC component. κ_2 is the relative amplitude of the sinusoidal component with respect to the DC level κ_1 . It is well known that the MLE for this problem is the maximum of the periodogram (see [Kay88]). The estimation procedure is therefore the following:

- Estimation of the DC level $\hat{\kappa}_1 = \frac{1}{N} \sum_{n=0}^{N-1} a_{i_{am,a}}[n, \underline{\kappa}']$
- $\hat{\kappa}_2$ is the maximum of the periodogram of $(a_{i_{am,a}}[n, \underline{\kappa}'] - \hat{\kappa}_1)$, normalized with respect to $\hat{\kappa}_1$. Zero-padding can be used for greater accuracy and the search of the maximum can be limited to an interval $[f_{c,min}, f_{c,max}]$.

4.4.2.1 Simulation Results

In order to test the AM modulation index estimator, numerical simulations are carried out. The generated real AM signals are of the following form (see (4.88)):

$$i_{am}[n, \underline{\kappa}] = \kappa_1 [1 + \kappa_2 \cos(2\pi\kappa_3n - \kappa_4)] \cos(2\pi\kappa_5n - \kappa_6) + w[n] \quad (4.90)$$

where $w[n]$ is zero-mean white Gaussian noise of variance σ^2 . The chosen SNR is 50 dB and the parameters are $\underline{\kappa} = [\sqrt{2} \ 0.01 \ 0.125 \ \pi/4 \ 0.25 \ 0]$.

The estimator is tested for different values of the data record length N . For each value of N , 1000 independent realizations of $i_{am}[n]$ are generated and $\hat{\kappa}_2$ is calculated. The results are displayed in Fig. 4.36. Fig. 4.36(a) shows the mean

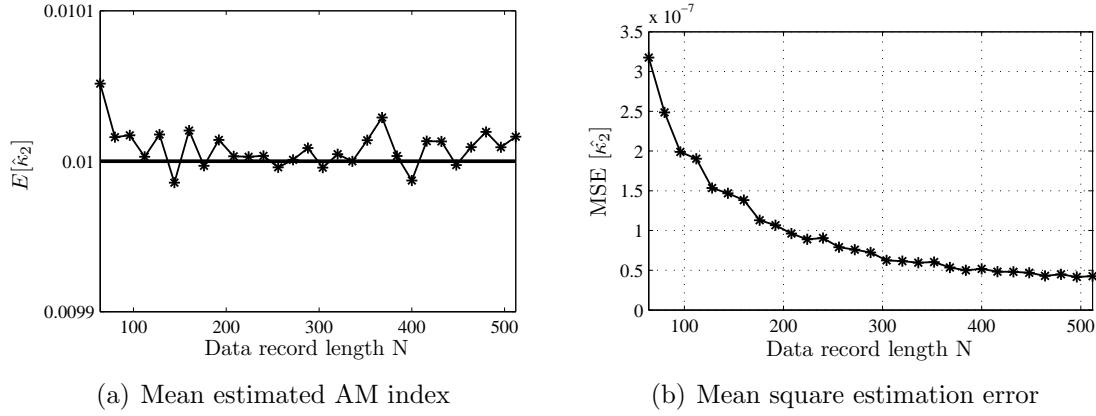


Figure 4.36: Simulation results: mean estimated AM index vs. N and mean square estimation error vs. N .

Signal Processing Method	Steady State			Transient State		
	PM	AM	Discr.	PM	AM	Discr.
Spectral Estimation	X	X	-	-	-	-
Instantaneous Frequency	X	-	-	X	-	-
Spectrogram	X	X	X	X	X	-
Pseudo WD	X	X	X	X	X	X
Parameter Estimation	X	X	X	-	-	-

Table 4.1: Summarized performances of the discussed signal processing methods in steady and transient state: Columns PM / AM indicate the capability of detecting the modulation and Discr. the capability of discriminating PM and AM.

estimated modulation index $E[\hat{k}_2]$ with respect to the data record length where N varies from 64 to 512. It can be seen that the relative error is always inferior to 0.5% which signifies a low estimation bias. Fig. 4.36(b) shows the obtained MSE for the AM modulation index. It decreases approximately proportional to $1/N$.

4.5 Summary

In this chapter, the previously presented signal processing methods were applied to the faulty stator current models with PM and AM. The signatures of the faulty current signals with the non-parametric analysis methods have been derived through theoretical calculus and simulations. Hence, the different methods and their performances can be compared. Evaluation criteria for the different methods are the capability to detect and distinguish AM and PM in steady or transient state. The performances of the parametric and non-parametric methods are summarized in Table 4.1.

The first analysis method, spectral estimation, was found to be useful only for detection purposes in steady state. The two types of modulation cannot be distinguished under the particular conditions of this application. Since spectral

estimation supposes stationary signals, it cannot be used during transients.

Instantaneous frequency estimation can effectively be used in steady and transient state. Since AM has no effect on the IF, only PM can be detected. The extraction of fault indicators is possible employing e.g. the spectrogram.

The direct use of the spectrogram itself yields acceptable results in steady state. AM and PM can be detected and discriminated if a priori knowledge about the modulation frequency is available. Since the performance of the spectrogram depends heavily on the window length, the latter must be chosen with respect to the modulation period. During transients, PM and AM can be detected with an adequate window length but their discrimination is nearly impossible with the considered signals. In general, the spectrogram suffers from a lack of time and frequency resolution.

The Wigner Distribution and PWD overcome this problem since they offer good time-frequency resolution. Certain undesirable interferences can be controlled by smoothing. It has been shown through theoretical demonstrations and simulations that PM and AM lead to characteristic outer interferences that can be used for detection and discrimination. Since the WD perfectly localizes linear chirp signals it performs well in steady state and during linear transients.

Finally, a parameter estimation approach based on the AM and PM signal models was presented for use with stationary signals. Maximum likelihood estimation leads to a practically realizable estimator. Two methods for numerical optimization were effectively used. The fixed grid search and the evolution strategy offer tradeoffs between computation time and accuracy. The estimated PM and AM modulation indices can be directly used as fault indicators. The estimator performs well even for short data records. Note that in this work, the parameter estimation approach has only been used for stationary signals. However, the models can theoretically be extended to take into account transient signals.

Chapter 5

Experimental Results

Contents

5.1	Introduction	144
5.2	Load Torque Oscillations	145
5.2.1	Spectral Estimation	145
5.2.2	Instantaneous Frequency - Steady State	147
5.2.3	Instantaneous Frequency - Transient State	148
5.2.4	Pseudo Wigner Distribution - Steady State	153
5.2.5	Pseudo Wigner Distribution - Transient State	157
5.2.6	Parameter Estimation	161
5.3	Load Unbalance	162
5.3.1	Spectral Estimation	162
5.3.2	Instantaneous Frequency - Steady State	164
5.3.3	Instantaneous Frequency - Transient State	166
5.3.4	Pseudo Wigner Distribution - Steady State	169
5.3.5	Pseudo Wigner Distribution - Transient State	171
5.3.6	Parameter Estimation	173
5.4	Dynamic Eccentricity	174
5.4.1	Spectral Estimation	174
5.4.2	Instantaneous Frequency - Steady State	176
5.4.3	Instantaneous Frequency - Transient State	177
5.4.4	Pseudo Wigner Distribution - Steady State	177
5.4.5	Pseudo Wigner Distribution - Transient State	180
5.4.6	Parameter Estimation	182
5.5	On-line Monitoring	182
5.5.1	Load Torque Oscillations - Steady State	183
5.5.2	Load Unbalance - Steady State	185

5.5.3	Load Torque Oscillations - Transient State	186
5.5.4	Load Unbalance - Transient State	186
5.6	Mechanical Fault Diagnosis	187
5.6.1	Steady State	187
5.6.2	Transient State	189
5.7	Summary	190

5.1 Introduction

The following chapter presents experimental results to illustrate the previously derived fault signatures. The experimental setup is detailed in appendix C. The machine under test is a 400 V, 5.5 kW, three phase induction motor with $p = 2$ and 36 Nm nominal torque. It is coupled to a DC motor used as load. The induction motor is supplied by a standard industrial inverter operating in open loop condition. Thus, the current signals are not influenced by current, torque or speed control. The DC machine is connected to a resistor through a DC/DC converter which controls the DC motor armature current.

The armature current reference signal is a DC level plus possible oscillations generated by a voltage controlled oscillator (VCO) through a speed or position measurement. Thereto, position or speed dependent torque oscillations are generated. Measured signals include the three line currents, three stator voltages, torque and shaft speed. Data acquisition is performed by a 24 bit board at 25.6 kHz sampling frequency. This high sampling frequency is chosen to include several inverter switching frequency harmonics at $k \cdot 3000$ Hz. The experimental setup is schematically depicted in Fig. 5.1.

Each mentioned signal processing method is tested with experimental signals resulting from different faults. The following faults are studied:

- Load torque oscillations of amplitude Γ_c , generated through control of the DC motor armature current
- Load unbalance produced by a mass that is eccentrically fixed on a shaft-mounted disc. This mass generates torque oscillations $\Gamma_{osc}(t)$ through its weight with respect to the rotor position i.e. oscillations at shaft rotational frequency:

$$\Gamma_{osc}(t) = \Gamma_c \cos(\theta_r) = \Gamma_c \cos(2\pi f_r t) \quad (5.1)$$

where $\Gamma_c = mgr_m$ with m the mass, g is the acceleration of gravity and r_m the distance of the mass to the rotational centre. A second effect of the unbalance is a centrifugal force. However, this force does not contribute to torque. If bearing clearances are important, an additional dynamic eccentricity could be introduced by the mass. Varying m and r_m , four different levels of load unbalance are studied with $\Gamma_c = 0.04, 0.06, 0.07, 0.10$ Nm.

- Dynamic eccentricity with $\delta_d \approx 40\%$

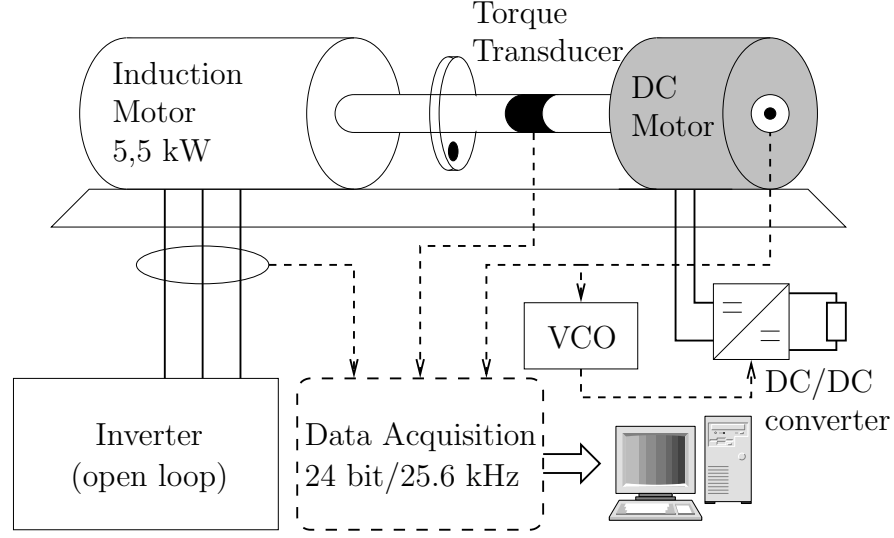


Figure 5.1: Scheme of experimental setup

In general, three different average load conditions are studied: 10%, 50% and 80% load. The full nominal load could not be tested due to current limitations of the DC motor.

5.2 Load Torque Oscillations

The first studied fault are load torque oscillations at shaft rotational frequency produced through control of the DC motor armature current. This somehow artificial fault is chosen for validation of the theoretical considerations from chapter 2. Moreover, it can be supposed that a number of realistic faults such as shaft misalignment, load unbalance, eccentricity, gearbox or bearing faults produce torque oscillations. For each average load level, signals with increasing load torque oscillation amplitude Γ_c are recorded in order to test the indicator behavior. The smallest value $\Gamma_c = 0.03$ Nm corresponds to approximately 0.1% of the nominal load torque whereas the highest value $\Gamma_c = 0.22$ Nm is about 6% of the nominal torque. The torque oscillation amplitudes were determined by measurements. The acquired signal length is $N = 507904$ samples, corresponding to 19.84 s acquisition time. For indicator calculations, the three line currents are segmented into blocks and analyzed independently.

5.2.1 Spectral Estimation

First, classical spectral estimation techniques will be used for analysis of stationary signals. This provides results with the method of reference for subsequent comparison with more advanced techniques. For visualization of the spectra, the averaged periodogram is calculated using segments of length $N_w = 63488$ (equivalent 2.48 s) windowed by a Hanning window. The segments overlap by $N_w/2$. The obtained stator current spectra with load torque oscillations are shown in Fig. 5.2 compared to spectra from a healthy motor. The load torque oscillation amplitude

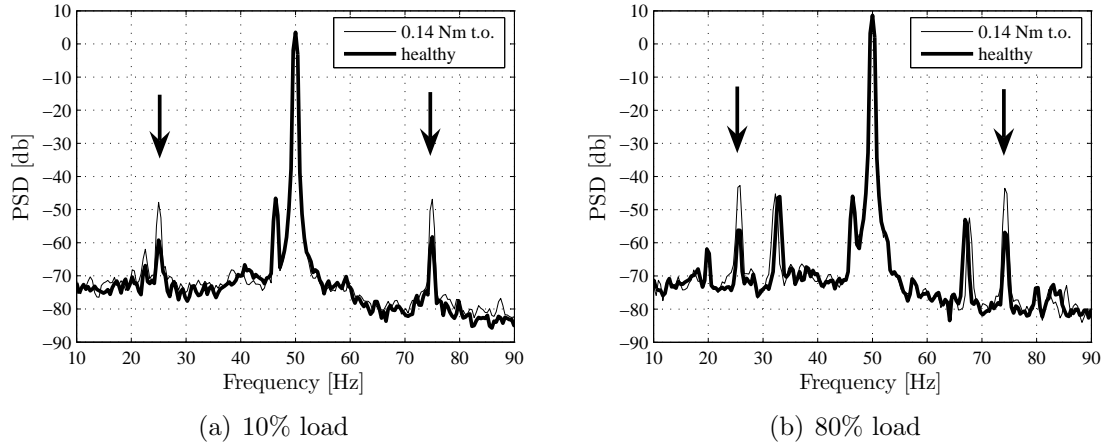


Figure 5.2: PSD of stator current with load torque oscillation $\Gamma_c = 0.14$ Nm vs. healthy case.

is $\Gamma_c = 0.14$ Nm. Two operating states with average load levels 10% and 80% and supply frequency $f_s = 50$ Hz are displayed. First, sidebands at $f_s \pm f_r \approx 50 \pm 25$ Hz can already be recognized with the healthy machine. Inaccurate alignment, a natural level of eccentricity or torque oscillations due to the coupling can explain this phenomenon.

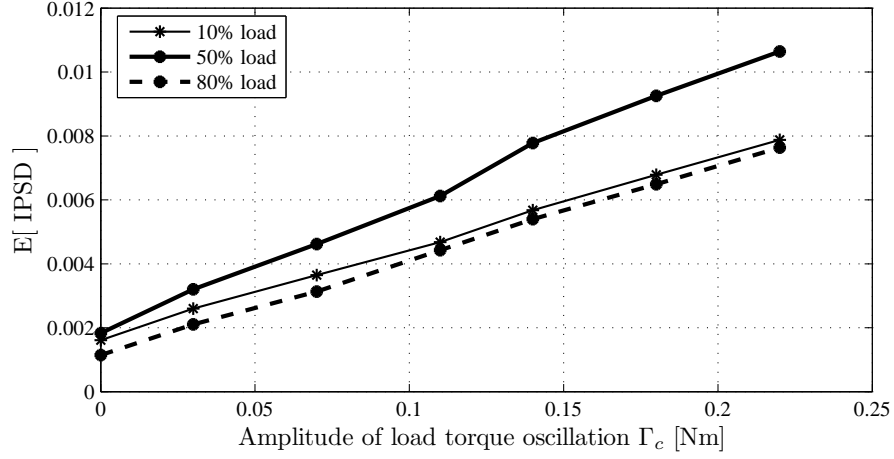
Healthy and faulty spectrum comparison shows a rise of sideband components at $f_s \pm f_r \approx 50 \pm 25$ Hz in each case. This confirms the preceding theoretical considerations. The amplitude of these components increases by approximately 10 dB at 10% load and 12 dB at 80% load. The greater increase with higher load can be explained by a stronger rotor current component I_{rt} .

Apart from the fundamental and the sidebands, other frequencies appear in the stator current spectrum. With 80% load, sidebands of relatively strong amplitude appear at $f_s \pm 18$ Hz. Additional experimental verifications with different load levels showed that the location of these sidebands can be characterized by $f_s \pm 14sf_s$. Their exact origin is unknown but they have also been observed with another induction motor from the same manufacturer in [Blö03]. Therefore, a relation to the motor design can be supposed. It can also be noted that their amplitude does not vary with the fault.

The fault indicator IPSD is derived for different torque oscillation amplitudes. Each data record is first downsampled to 200 Hz and then divided into blocks of 512 samples. IPSD is calculated on each block from each phase current, resulting in a total of 21 estimations. The average indicator value $E[\text{IPSD}]$ and the standard deviation σ_{IPSD} are given in Table 5.1. The average indicator values are also displayed graphically in Fig. 5.3 versus the measured load torque oscillation amplitude Γ_c . The average indicator values show an approximately linear evolution with respect to Γ_c , equivalent to the fault severity. This confirms the theoretical result that the PM modulation index is proportional to Γ_c . Note that the indicator is sensitive to very small values of Γ_c , e.g. 0.03 Nm corresponds to approximately 0.1% of the nominal torque.

Table 5.1: Average fault indicator IPSD ($\times 10^{-3}$) and standard deviation σ_{IPSD} ($\times 10^{-3}$) for load torque oscillations.

	10% load		50% load		80% load	
	$E[\text{IPSD}]$	σ_{IPSD}	$E[\text{IPSD}]$	σ_{IPSD}	$E[\text{IPSD}]$	σ_{IPSD}
healthy	1.60	0.15	1.83	0.38	1.14	0.17
0.03 Nm	2.60	0.18	3.20	0.22	2.11	0.20
0.07 Nm	3.64	0.23	4.62	0.25	3.13	0.20
0.11 Nm	4.68	0.32	6.12	0.23	4.42	0.22
0.14 Nm	5.68	0.31	7.78	0.48	5.40	0.17
0.18 Nm	6.78	0.27	9.25	0.40	6.49	0.21
0.22 Nm	7.88	0.43	10.64	0.54	7.63	0.13

**Figure 5.3:** Average fault indicator IPSD vs. load torque oscillation amplitude Γ_c .

The average indicator values also depend on the average load level due to the indicator normalization with respect to the fundamental amplitude which is $I_{st} + I_{rt}$ in the stator current model. A correct normalization would include only the rotor current amplitude I_{rt} but the value of the latter cannot be extracted from the stator current signal. Similar observation have been made in [Oba03a]. Nevertheless, the obtained results show that a simple threshold based decision with IPSD allows an effective fault detection.

5.2.2 Instantaneous Frequency - Steady State

This subsection presents results obtained with instantaneous frequency (IF) estimation. The stator current signal is a multicomponent signal due to the presence of numerous supply frequency harmonics. In order to obtain an approximation of a monocomponent signal, the current is lowpass filtered with cutoff frequency 100 Hz and downsampled to 200 Hz. Then, the corresponding analytical signal is calculated through the Hilbert transform. The subsequent IF estimation is realized using the simple and fast phase difference estimator.

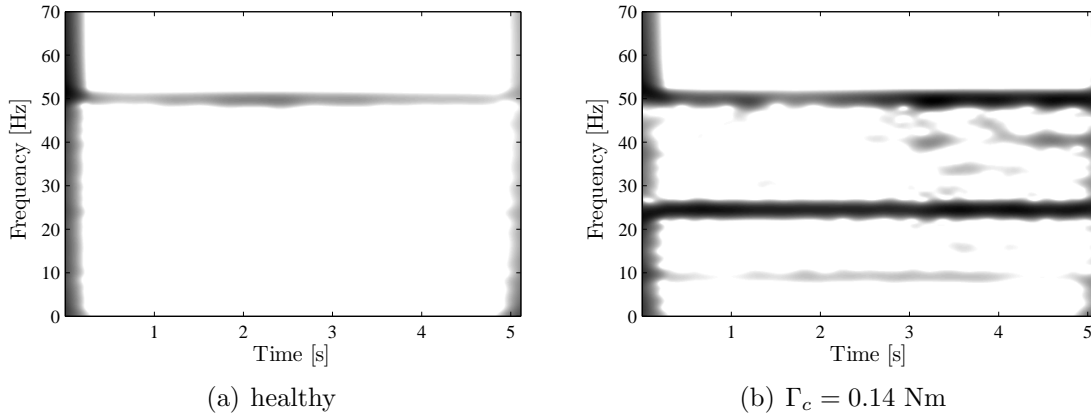


Figure 5.4: Spectrogram of stator current IF with load torque oscillation $\Gamma_c = 0.14$ Nm vs. healthy case, 50% load.

Since the IF oscillations are of small amplitude, an appropriate IF postprocessing must follow. In steady state, the IF power spectral density can be analyzed. An alternative is the IF spectrogram, suitable for steady state and transients. For illustration, the IF spectrogram of steady state stator current signals is displayed in Fig. 5.4 for the healthy case and load torque oscillations with $\Gamma_c = 0.14$ Nm. A fault-related component at $f_r \approx 25$ Hz can clearly be noticed when a fault is present. It should be noted that the IF DC level has been removed prior to the spectrogram calculation.

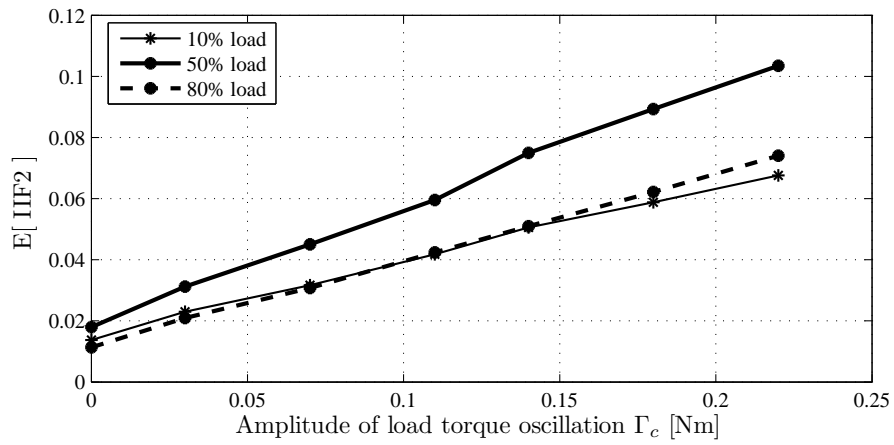
For further analysis of the collected data, the fault indicator IIF2 is calculated for all cases. As before, the analysis is carried out on data records of length 512 samples. For each level of torque oscillation and average load, 21 samples are analyzed. Table 5.2 summarizes the obtained average fault indicator IIF2 and its standard deviation. The average values are graphically displayed in Fig. 5.2 with respect to the load torque oscillation amplitude Γ_c . It can be noticed that these curves are similar to the spectrum-based indicator IPSD. The average fault indicator evolves approximately linearly with respect to Γ_c and even the smallest level of torque oscillation can be detected. As before, the indicator values with 50% load are higher than with 10% or 80% load. This time, no indicator normalization with respect to the fundamental is used but recall that the IF oscillation amplitudes depend on $C(I_{st}, I_{rt})$ (see equation (4.32)). This could explain the indicator variations with respect to load.

5.2.3 Instantaneous Frequency - Transient State

In the next and subsequent sections, transient stator current signals are considered. They are obtained during motor startup and braking between standstill and nominal supply frequency. The frequency sweep rate is 10 Hz per second i.e. the startup takes 5 seconds. For the following analysis, the transient between $f_s = 10$ Hz and 48 Hz is extracted. For illustration, a transient stator current signal during motor startup is displayed in Fig. 5.6 together with its PWD. The original signal has been

Table 5.2: Average fault indicator IIF2 ($\times 10^{-3}$) and standard deviation σ_{IIF2} ($\times 10^{-3}$) for load torque oscillations.

	10% load		50% load		80% load	
	$E[\text{IIF2}]$	σ_{IIF2}	$E[\text{IIF2}]$	σ_{IIF2}	$E[\text{IIF2}]$	σ_{IIF2}
healthy	13.8	1.5	18.0	2.6	11.3	1.2
0.03 Nm	23.0	1.8	31.2	1.8	20.9	1.7
0.07 Nm	31.7	2.5	45.0	2.2	30.8	1.4
0.11 Nm	41.8	3.1	59.5	1.9	42.4	2.5
0.14 Nm	50.6	2.9	75.0	3.8	51.0	1.4
0.18 Nm	58.8	2.7	89.3	3.6	62.2	2.2
0.22 Nm	67.6	4.0	103.5	4.9	74.0	1.4

**Figure 5.5:** Average fault indicator IIF2 vs. load torque oscillation amplitude Γ_c .

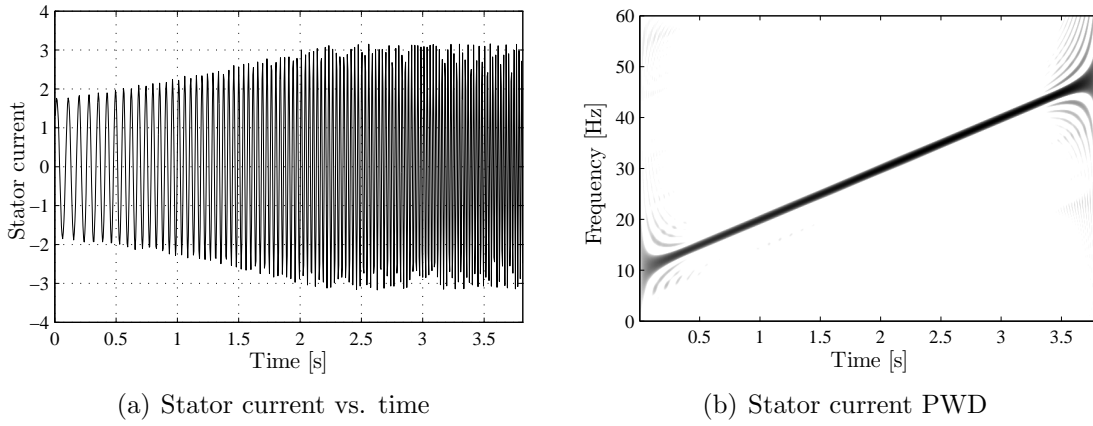


Figure 5.6: Example of transient stator current during motor startup and its PWD.

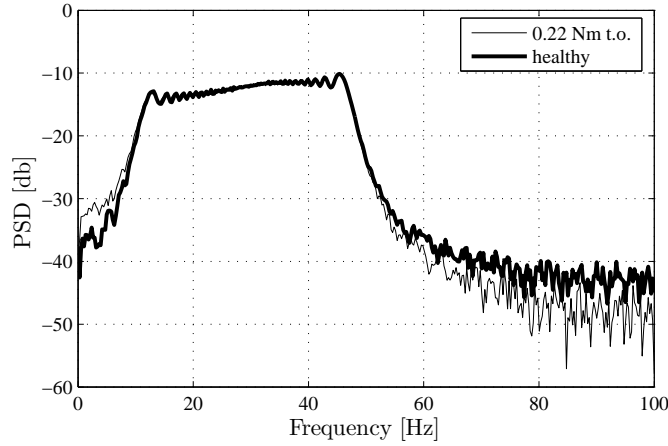


Figure 5.7: PSD of stator current during speed transient with load torque oscillation $\Gamma_c = 0.22$ Nm vs. healthy case.

lowpass filtered and downsampled to 200 Hz.

The PSD of a healthy and faulty transient signal is displayed in Fig. 5.7. This example illustrates that spectral estimation is not appropriate for transient signal analysis. The broad peak due to the time-varying supply frequency masks all other phenomena. The faulty and healthy case cannot be distinguished.

Therefore, IF estimation is tested during the speed transients. For illustration, a transient stator current IF is shown in Fig. 5.8 for the healthy case and with a relatively strong load torque oscillation $\Gamma_c = 0.5$ Nm. It can be noted that the average IF value shows a linear evolution during the motor startup. When load torque oscillations are present, the IF oscillations increase. The oscillation frequency is approximately half the supply frequency which corresponds to the shaft rotational frequency f_r [Blö05c] [Blö05a].

Again, the IF spectrogram is used for further analysis. With a smaller load torque oscillation $\Gamma_c = 0.22$ Nm, the spectrograms depicted in Fig. 5.9 are obtained during a motor startup. Besides the strong DC level in the spectrogram, time

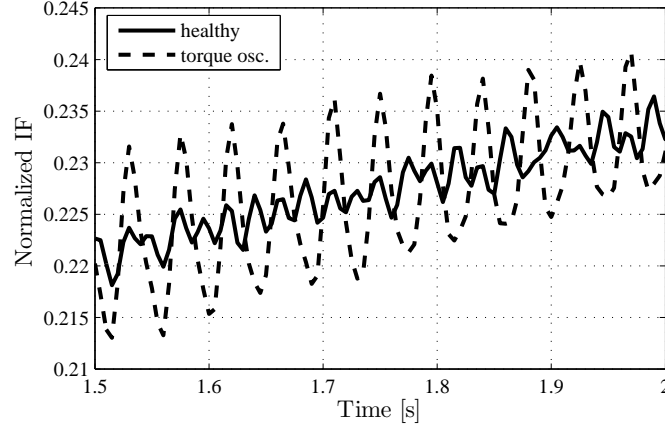


Figure 5.8: Example of transient stator current IF with strong load torque oscillation ($\Gamma_c = 0.5$ Nm) vs. healthy case, 25% load.

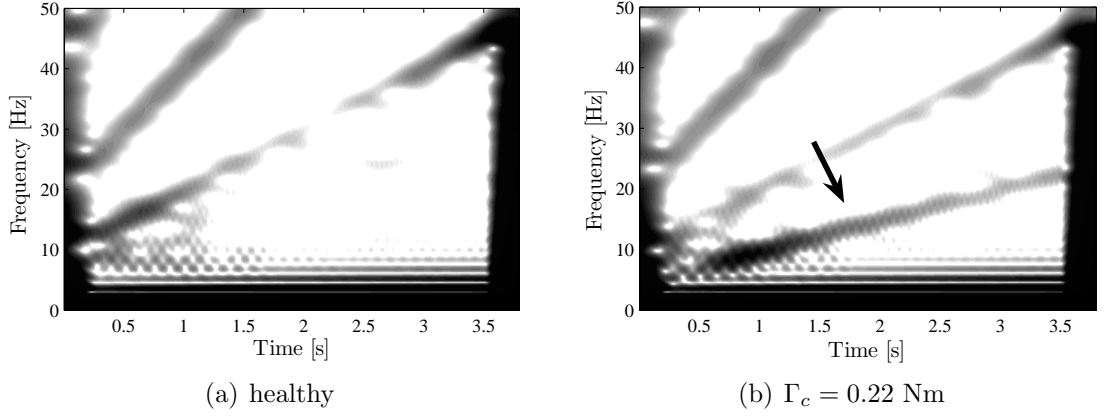


Figure 5.9: Spectrogram of transient stator current IF with load torque oscillation $\Gamma_c = 0.22$ Nm vs. healthy case, 10% load.

varying components can already be noticed in the healthy case (Fig. 5.9(a)). They correspond to the supply frequency $f_s(t)$ and its second harmonic. Comparing the spectrogram of the healthy IF to the one with load torque oscillations (Fig. 5.9(b)), a fault-related component at $f_r(t)$ becomes visible.

For indicator calculation during transients, modifications must be made to IIF2. The indicator IIF2 has been designed proportional to the PM modulation index β . However, since $\beta \propto \Gamma_c / f_c^2$, β is not constant during transients. In order to obtain an indicator IIF2' proportional to Γ_c , IIF2 must be multiplied by the squared fault frequency. The indicator IIF2' suitable for transient analysis is therefore:

$$\text{IIF2}'[n] = \text{IIF2}[n] \cdot \left(\hat{f}_c[n] \right)^2 \quad \hat{f}_c[n] = \frac{\text{IF}_i[n]}{p} \quad (5.2)$$

The estimate of $f_c[n]$ is obtained as the instantaneous frequency of the stator current $\text{IF}_i[n]$ divided by the pole pair number i.e. $\hat{f}_c[n]$ is the shaft rotational frequency at no load. The indicators $\text{IIF2}'(t)$ corresponding to the previous signals are shown in Fig. 5.10. The healthy and the faulty case can be clearly distinguished

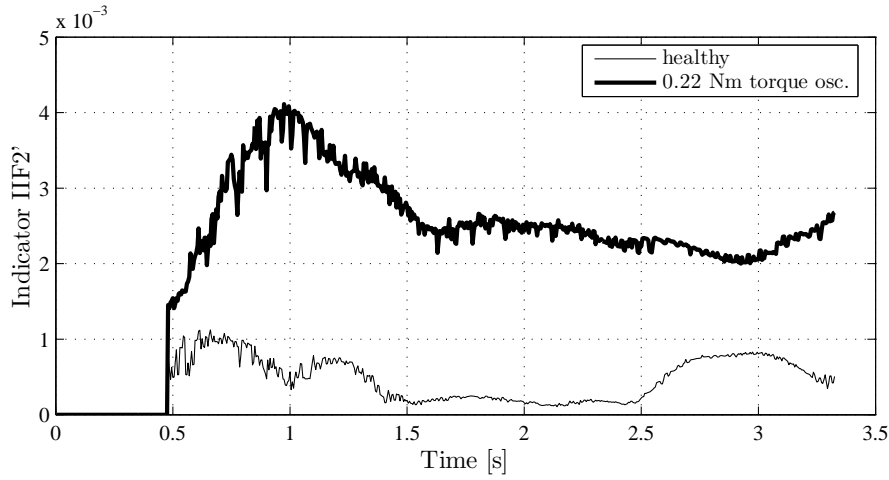


Figure 5.10: Fault indicator $IIF2'(t)$ during motor startup with load torque oscillation $\Gamma_c = 0.22$ Nm vs. healthy case, 10% load.

Table 5.3: Average fault indicator $IIF2' (\times 10^{-3})$ and standard deviation $\sigma_{IIF2'} (\times 10^{-3})$ for load torque oscillations during speed transients.

	10% load		50% load		80% load	
	$E[IIF2']$	$\sigma_{IIF2'}$	$E[IIF2']$	$\sigma_{IIF2'}$	$E[IIF2']$	$\sigma_{IIF2'}$
healthy	0.42	0.07	0.47	0.09	0.45	0.06
0.03 Nm	0.64	0.04	0.61	0.04	0.47	0.10
0.07 Nm	0.84	0.20	0.78	0.06	0.70	0.09
0.11 Nm	1.11	0.23	0.98	0.09	0.79	0.10
0.14 Nm	1.79	0.16	1.23	0.08	1.01	0.11
0.18 Nm	2.16	0.25	1.34	0.05	1.21	0.13
0.22 Nm	2.46	0.31	1.61	0.17	1.32	0.17

during the whole startup. Note that the indicator values are not calculated at the beginning and the end of the data record in order to avoid border effects in the spectrogram. The employed normalization with respect to f_c leads to indicator values that are relatively independent from the supply frequency.

Next, transients with different Γ_c and varying average load are studied. For each analyzed data record, one fault indicator value $IIF2'$ is obtained by taking the mean of $IIF2'[n]$. In each case, three motor accelerations and three decelerations are analyzed. The obtained average indicator values and their standard deviations are given in Table 5.3.

The average indicator values are graphically represented in Fig. 5.11. The indicator with respect to the average load and Γ_c behavior is different from steady state. First, $IIF2'$ is in general higher with small load. This can be explained by the experimental setup that produces the load torque oscillations. During the speed transients, the average load current reference is constant. Since the DC motor voltage is small at low speed and the resistor value is constant, the current control saturates at low speed and high loads. Therefore, the small load torque oscillations cannot be correctly produced at higher load and the indicator values are therefore

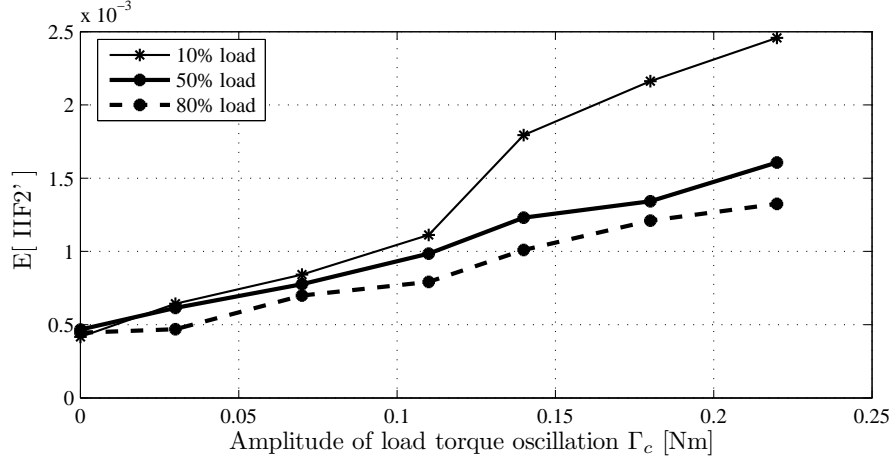


Figure 5.11: Average fault indicator IIF2' vs. load torque oscillation amplitude Γ_c during speed transients.

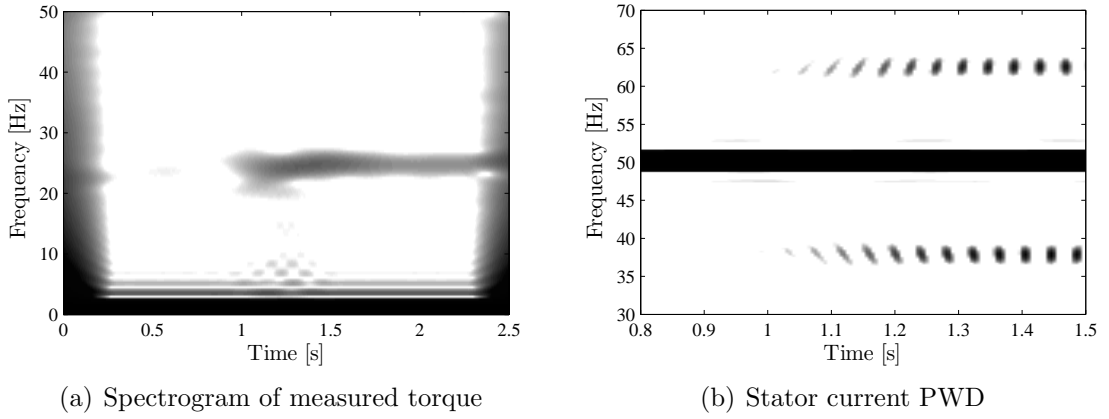


Figure 5.12: Spectrogram of measured torque and PWD of stator current with appearing load torque oscillation $\Gamma_c = 0.05$ Nm, 25% load.

smaller. For $\Gamma_c = 0.03$ Nm and 80% load, no clear change in the indicator value with respect to the healthy case is visible due to the saturation.

5.2.4 Pseudo Wigner Distribution - Steady State

In this section, the stationary current signals are analyzed using the PWD. For illustration purposes, the load torque oscillation starts in the middle of one data record. Fig. 5.12(a) shows the spectrogram of the measured load torque. At $t = 1$ s, the torque oscillation at $f_r \approx 25$ Hz is switched on. The corresponding stator current PWD is displayed in Fig. 5.12(b). Oscillating sidebands appear around the fundamental frequency in consequence of the torque oscillation. The sidebands are located at $f_s \pm f_r/2 \approx 50 \pm 12.5$ Hz. They oscillate at $f_r \approx 25$ Hz and a phase shift between upper and lower sideband can be recognized. This corroborates the theoretical considerations from the previous chapters.

The two proposed fault indicators IWD1 and IWD2 are tested on the experi-

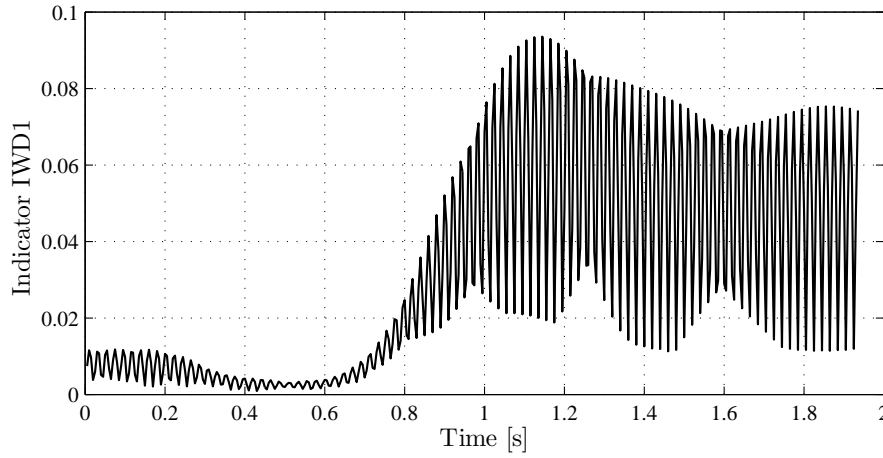


Figure 5.13: Fault indicator $IWD1(t)$ for data record with appearing load torque oscillation $\Gamma_c = 0.05$ Nm, 25% load.

mental stator current signal with appearing load torque oscillation. $IWD1$ is shown with respect to time in Fig. 5.13. The indicator jumps to considerably higher values when the torque oscillation appears. Note that the time instant of the jump does not correspond exactly to the previous figures since the indicator is not calculated for the beginning and the end of the data record. The fault indicator oscillates since it represents the total sideband energy at each time instant.

The second fault indicator $IWD2$ is displayed in Fig. 5.14. Recall that it reflects the oscillating sideband energy and the phase shift between the upper and lower sideband signal. Since $IWD2$ is complex valued, the absolute value and phase are separately displayed. The absolute value of $IWD2$ (Fig. 5.14(a)) shows a considerable jump in consequence of the fault. Before the apparition of the fault, the phase is close to π but with a high variance. This is related to the small amplitudes of the sideband signals and therefore a higher noise sensitivity. With the load torque oscillation, the phase is more stable with a reduced variance. These examples demonstrate the effectiveness of both PWD based indicators with experimental stator current signals.

As before, the indicators have been tested on data with different levels of torque oscillation and average load. For $IWD1$, Table 5.4 shows the average indicator values together with their standard deviation. The average values are also graphically represented in Fig. 5.15 with respect to the load torque oscillation amplitude. The indicator behaves similar to IPSD or IIF2 in steady state.

The corresponding results with the indicator $IWD2$ are shown in Table 5.5. The absolute value and the argument are given separately whereas the standard deviations have been omitted. Figure 5.16 represents the obtained indicator values in the complex plane for 10% and 50% average load. With increasing Γ_c , the absolute value of the indicators also increases. It can be noticed that the average load influences on the indicator argument. With 50% load, the argument is closest to π whereas values around 130° are obtained with 10% and 80% load.

Further tests with a modified indicator $IWD2$ were carried out: Previously, the amplitudes and the phase shift of the two sideband signals were extracted using

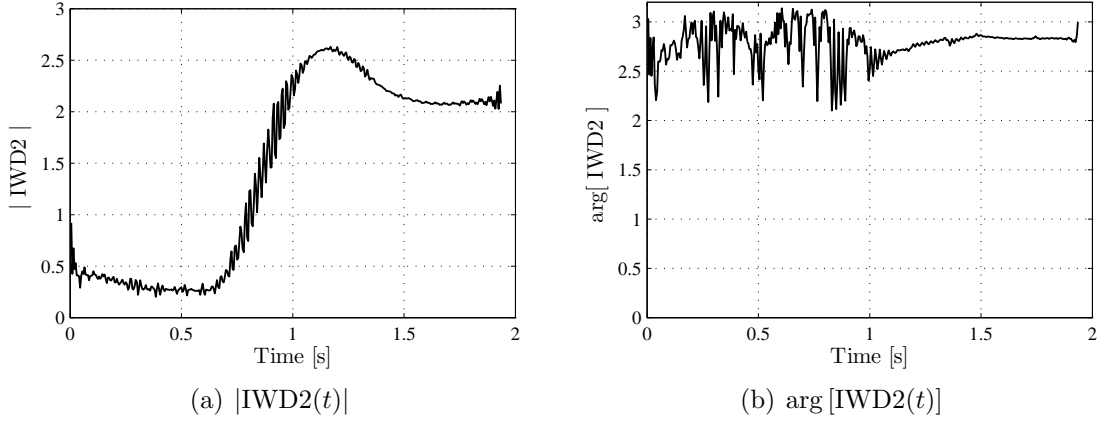


Figure 5.14: Absolute value and argument of fault indicator $IWD2(t)$ for data record with appearing load torque oscillation $\Gamma_c = 0.05$ Nm, 25% load.

Table 5.4: Average fault indicator $IWD1$ ($\times 10^{-3}$) and standard deviation σ_{IWD1} ($\times 10^{-3}$) for load torque oscillations.

	10% load		50% load		80% load	
	$E[IWD1]$	σ_{IWD1}	$E[IWD1]$	σ_{IWD1}	$E[IWD1]$	σ_{IWD1}
healthy	1.88	0.16	2.15	0.32	1.43	0.21
0.03 Nm	2.90	0.19	3.67	0.21	2.68	0.23
0.07 Nm	4.02	0.25	5.30	0.26	3.96	0.23
0.11 Nm	5.17	0.35	7.01	0.23	5.46	0.29
0.14 Nm	6.26	0.32	8.85	0.47	6.65	0.19
0.18 Nm	7.46	0.27	10.51	0.43	8.02	0.27
0.22 Nm	8.63	0.44	12.16	0.60	9.54	0.16

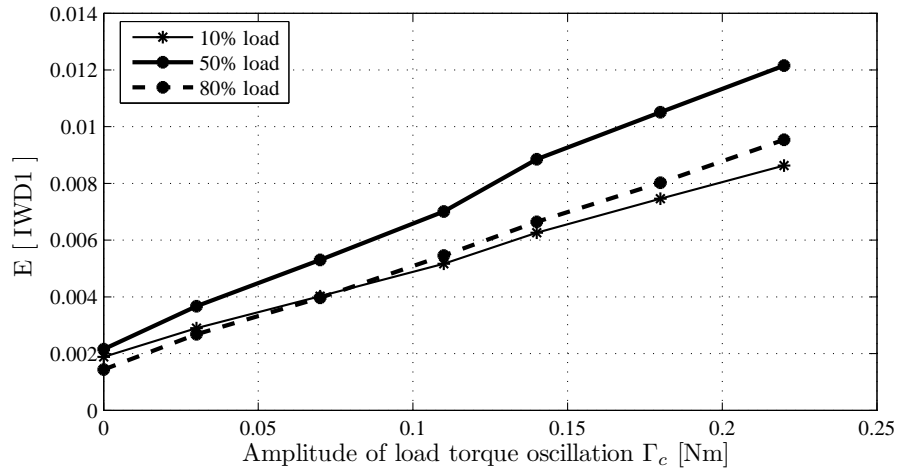


Figure 5.15: Average fault indicator $IWD1$ vs. load torque oscillation amplitude Γ_c .

Table 5.5: Average fault indicator IWD2 (absolute value $A = E[|IWD2|]$ and argument $\varphi = E[\angle IWD2]$ in $^\circ$) for load torque oscillations.

	10% load		50% load		80% load	
	A	φ	A	φ	A	φ
healthy	30.0	106.3	32.7	146.1	21.3	135.2
0.03 Nm	45.2	124.3	54.2	162.6	39.0	135.8
0.07 Nm	62.4	123.0	78.0	162.9	57.4	135.6
0.11 Nm	79.8	129.4	103.0	164.6	79.0	135.1
0.14 Nm	96.4	128.7	129.9	162.7	96.1	132.0
0.18 Nm	114.7	123.0	154.4	164.6	116.0	135.1
0.22 Nm	132.4	122.2	178.3	164.8	137.8	135.3

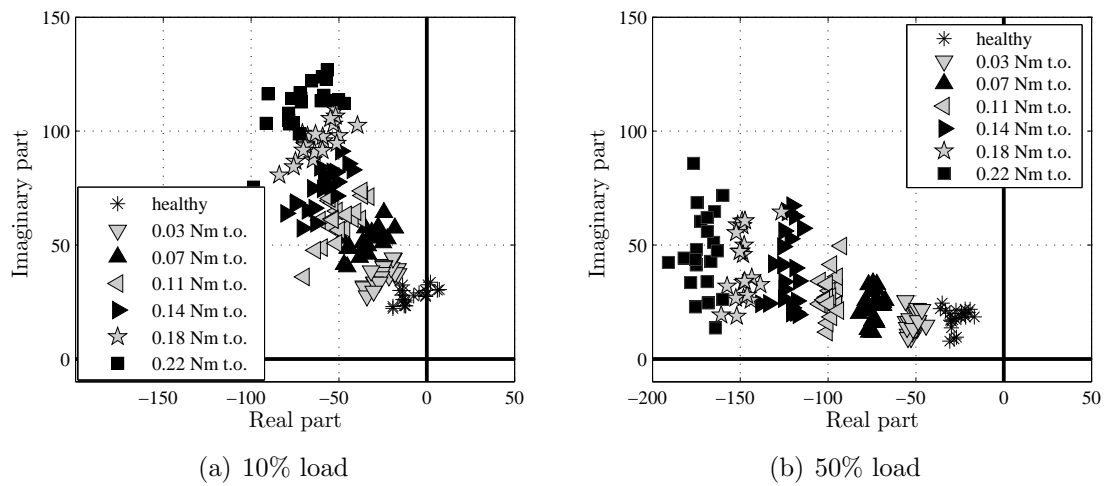


Figure 5.16: Complex representation of fault indicator IWD2 with load torque oscillations, 10% and 50% load.

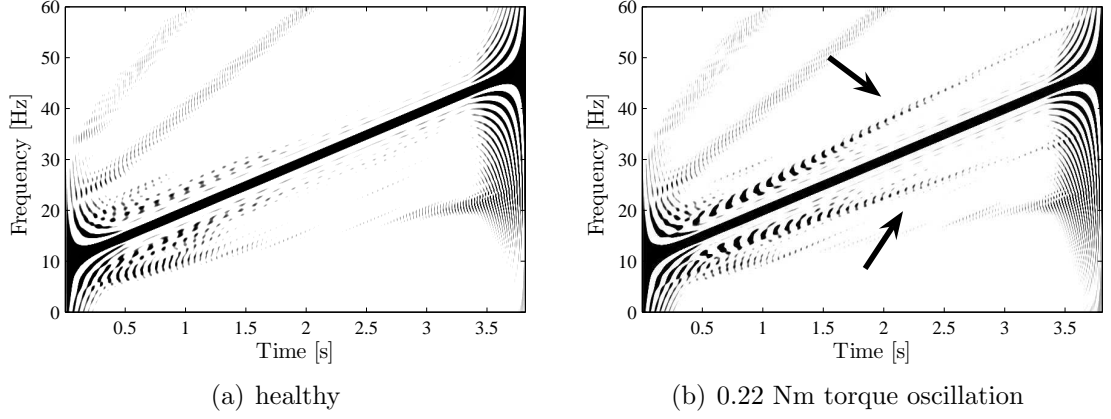


Figure 5.17: PWD of transient stator current in healthy case and with load torque oscillation, 10% load.

the Hilbert transform. In steady state, the Fourier transform can provide the same information. The equivalent tests after implementation showed very similar results compared to extraction with the Hilbert transform. Theoretically, the Fourier transform based extraction should show a better insensitivity with respect to noise or other perturbations since the oscillating energy can be extracted from a well determined frequency interval.

5.2.5 Pseudo Wigner Distribution - Transient State

The previously considered transient signals are also analyzed with the PWD. Figure 5.17 shows an example of the stator current PWD during a motor startup. Comparing the healthy case to 0.22 Nm load torque oscillations, the characteristic interference signature becomes visible around the time-varying fundamental frequency. Since the fault frequency is also time variable, the sideband location and their oscillation frequency depend on time [Blö05c] [Blö05a].

For indicator calculation during transients with constant torque oscillation Γ_c , the previously used indicators must be modified since the PM modulation index β depends on the time-varying fault frequency f_c . Similar to IIF2', IWD1' and IWD2' are obtained by multiplication with the squared estimate of f_c :

$$\text{IWD1}'[n] = \text{IWD1}[n] \cdot \left(\hat{f}_c[n]\right)^2 \quad \text{IWD2}'[n] = \text{IWD2}[n] \cdot \left(\hat{f}_c[n]\right)^2 \quad (5.3)$$

where $\hat{f}_c[n] = \hat{f}_s[n]/p$. The modified indicator $\text{IWD1}'(t)$ is displayed in Fig. 5.18 during a motor startup. The healthy and the faulty case can clearly be distinguished. The same can be recognized with the fault indicator $\text{IWD2}'$ which is shown in Fig. 5.19. The change is particularly visible in the absolute indicator value. The phase shows significant fluctuations in the healthy case due to a low amplitude of the sideband signals. With the load torque oscillation, the phase difference is always close to π .

The complete analysis results of load torque oscillations during transients are given in Table 5.6 for the indicator $\text{IWD1}'$. The average indicator values with

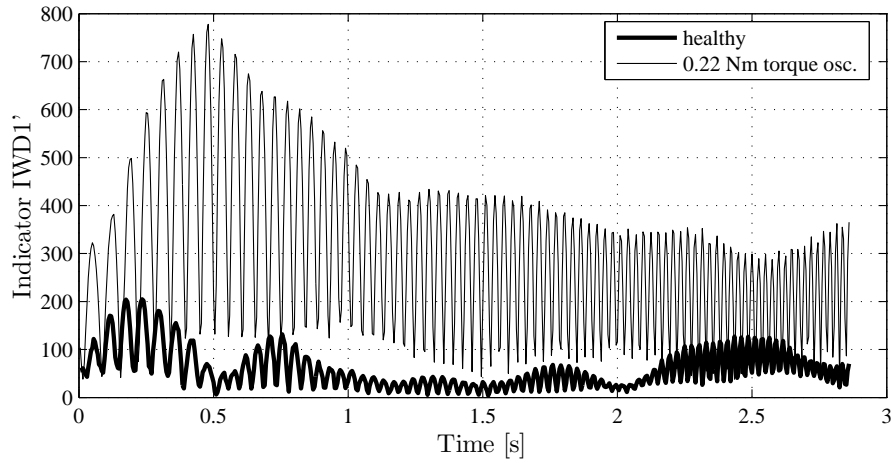


Figure 5.18: Fault indicator $IWD1'(t)$ during motor startup with load torque oscillation $\Gamma_c = 0.22$ Nm vs. healthy case, 10% load.

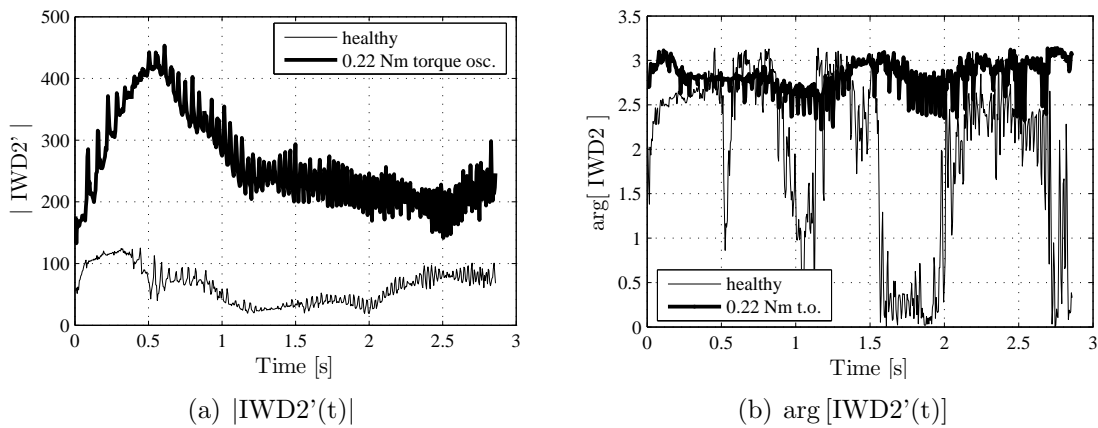
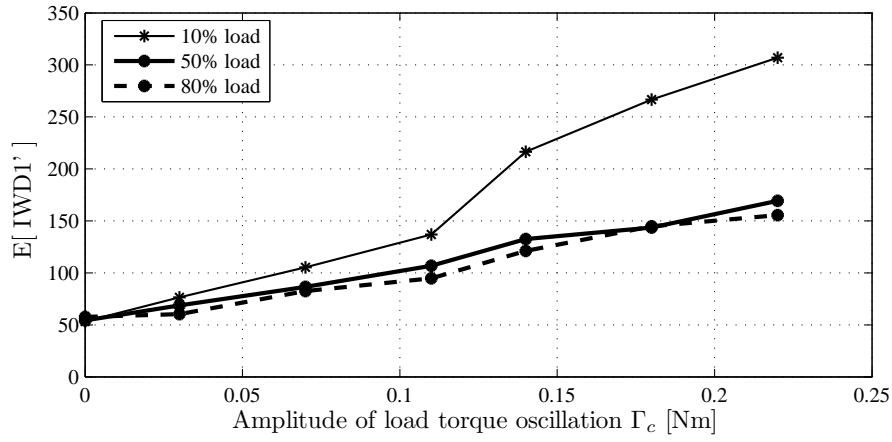


Figure 5.19: Absolute value and argument of fault indicator $IWD2'(t)$ during motor startup with load torque oscillation $\Gamma_c = 0.22$ Nm vs. healthy case, 10% load.

Table 5.6: Average fault indicator $IWD1'$ and standard deviation $\sigma_{IWD1'}$ for load torque oscillations during speed transients.

	10% load		50% load		80% load	
	$E[IWD1']$	$\sigma_{IWD1'}$	$E[IWD1']$	$\sigma_{IWD1'}$	$E[IWD1']$	$\sigma_{IWD1'}$
healthy	53.2	6.5	54.4	9.9	57.7	6.5
0.03 Nm	76.4	7.0	68.8	5.0	60.4	9.5
0.07 Nm	105.3	10.3	86.5	4.6	82.5	10.8
0.11 Nm	136.9	12.4	106.8	10.1	94.8	12.1
0.14 Nm	216.5	7.5	132.5	7.2	121.1	10.9
0.18 Nm	266.7	9.3	143.6	6.2	144.8	15.2
0.22 Nm	306.9	7.1	169.3	14.9	155.5	20.7

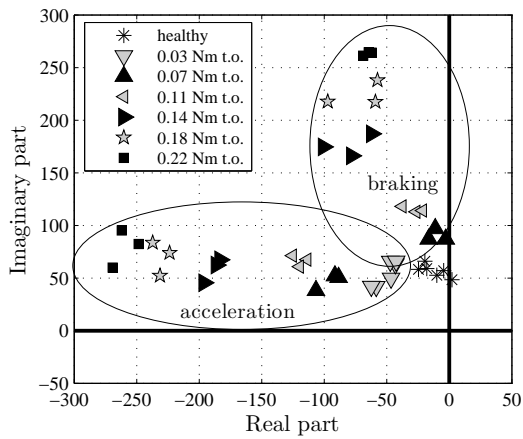
**Figure 5.20:** Average fault indicator $IWD1'$ vs. load torque oscillation amplitude Γ_c during speed transients.

respect to Γ_c are shown in Fig. 5.20. They are very similar to the indicator values obtained with IIF2'.

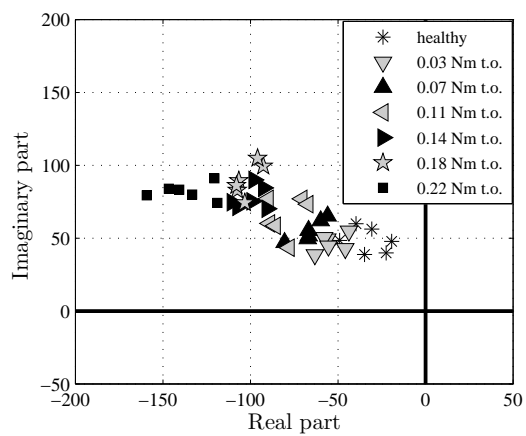
The results with the second PWD based indicator $IWD2'$ are given in Table 5.7. The results are separated into the acceleration and the braking phase. The evolution of the absolute value A corresponds to the previous results. For certain load levels, different phase angles φ between acceleration and braking can be noticed. The difference is particularly significant for 10% load. This can also be seen in Fig. 5.21 where the obtained indicator values are represented in the complex plane. At 10% load (see Fig. 5.21(a)), the obtained indicators have approximately the same absolute value but their phase angle differs significantly depending on acceleration or braking. This effect cannot be recognized at 50% load (see Fig. 5.21(b)). It can be supposed that the angle values close to $\pi/2$ during braking at small load are related to a relatively high motor braking torque. At high load level, the motor does not need to provide negative torque in contrary to small load. The negative torque might lead to such indicator values. In any case, the absolute indicator value clearly reflects the amplitude of the load torque oscillation during speed transients.

Table 5.7: Average fault indicator IWD2' (absolute value $A = E[|IWD2'|]$ and argument $\varphi = E[\angle IWD2']$ in $^\circ$) for load torque oscillations during speed transients.

		10% load		50% load		80% load	
		A	φ	A	φ	A	φ
acceleration	healthy	64.6	108.8	68.3	125.8	57.5	90.7
	0.03 Nm	71.8	141.2	75.2	142.1	56.8	106.4
	0.07 Nm	106.8	153.6	85.2	136.1	75.8	133.8
	0.11 Nm	136.9	150.9	110.0	139.3	86.8	126.5
	0.14 Nm	197.7	162.7	127.6	139.3	109.6	127.8
	0.18 Nm	241.4	163.2	137.6	141.3	128.0	122.4
	0.22 Nm	272.1	163.1	148.9	146.7	131.1	132.6
braking	healthy	53.1	94.3	49.9	121.1	69.0	100.4
	0.03 Nm	78.7	124.2	68.0	135.6	69.8	112.4
	0.07 Nm	91.1	96.4	88.1	144.1	91.2	120.2
	0.11 Nm	118.7	103.8	97.5	143.0	103.1	116.3
	0.14 Nm	194.0	114.5	125.5	144.8	124.2	118.9
	0.18 Nm	236.2	107.6	135.0	136.6	149.7	112.8
	0.22 Nm	271.3	103.9	170.1	151.0	164.4	113.2



(a) 10% load



(b) 50% load

Figure 5.21: Complex representation of fault indicator IWD2' with load torque oscillations during speed transients, 10% and 50% load.

Table 5.8: Average estimated PM modulation index $E[\hat{\theta}_3]$ ($\times 10^{-3}$) and standard deviation $\sigma_{\hat{\theta}_3}$ ($\times 10^{-3}$) for load torque oscillations, $N_b = 64$.

	10% load		50% load		80% load	
	$E[\hat{\theta}_3]$	$\sigma_{\hat{\theta}_3}$	$E[\hat{\theta}_3]$	$\sigma_{\hat{\theta}_3}$	$E[\hat{\theta}_3]$	$\sigma_{\hat{\theta}_3}$
healthy	1.83	1.52	2.30	1.63	1.66	1.53
0.03 Nm	2.77	1.48	3.49	1.40	2.55	1.44
0.07 Nm	3.61	1.56	4.86	1.37	3.57	1.43
0.11 Nm	4.50	1.65	6.46	1.68	4.60	1.37
0.14 Nm	5.38	1.38	7.84	1.28	5.50	1.32
0.18 Nm	6.20	1.59	9.19	1.41	6.65	1.47
0.22 Nm	7.16	1.43	10.68	1.41	7.92	1.36

Table 5.9: Average estimated AM modulation index $E[\hat{\kappa}_2]$ ($\times 10^{-3}$) and standard deviation $\sigma_{\hat{\kappa}_2}$ ($\times 10^{-3}$) for load torque oscillations, $N_b = 64$.

	10% load		50% load		80% load	
	$E[\hat{\kappa}_2]$	$\sigma_{\hat{\kappa}_2}$	$E[\hat{\kappa}_2]$	$\sigma_{\hat{\kappa}_2}$	$E[\hat{\kappa}_2]$	$\sigma_{\hat{\kappa}_2}$
healthy	1.49	2.39	1.33	2.49	1.26	2.31
0.03 Nm	1.74	2.29	1.29	2.47	1.49	2.47
0.07 Nm	2.30	2.45	1.43	2.44	1.89	2.42
0.11 Nm	2.57	2.43	1.62	2.33	2.31	2.23
0.14 Nm	2.95	2.36	1.84	2.30	2.68	2.19
0.18 Nm	3.77	2.51	1.89	2.28	3.07	2.35
0.22 Nm	4.27	2.48	2.03	2.33	3.60	2.14

5.2.6 Parameter Estimation

The last employed method is signal parameter estimation. Using the same signals as before, the PM and AM modulation are estimated as fault indicators. The estimates are obtained on blocks of length $N_b = 64$ samples with the previously described estimation procedures. The evolution strategy is used for optimization in the PM case. Table 5.8 shows the obtained average PM modulation indices with their standard deviation, Table 5.9 gives the same information for the AM indices. The average indicator values are also graphically displayed in Fig. 5.22.

The PM modulation index shows an approximately linear evolution with respect to Γ_c . It resembles to the previously obtained indicators based on non-parametric methods. On the contrary, the AM modulation index shows only a slight rise. Moreover, its characteristics are different from the previously obtained indicators e.g. the indicator values with 50% load are smaller than with 10% or 80%. This signifies, that the considered load torque oscillations mainly lead to phase modulations of the stator current. The PM modulation index is a suitable fault indicator in this case.

Since the data record length N_b was only 64 samples in this example, the standard deviation is higher than with the spectrum based indicator where $N_b = 512$. Tests with the PM estimator and increased data record length demonstrated

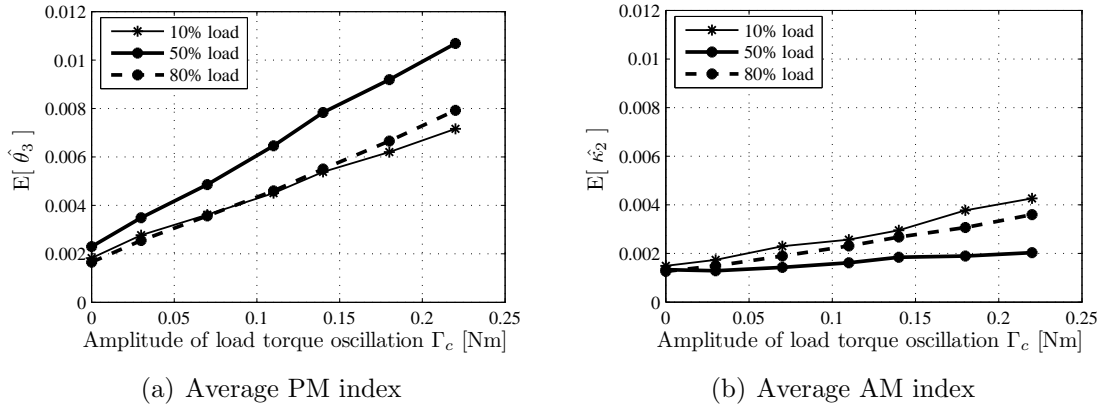


Figure 5.22: Average PM and AM modulation indices with respect to load torque oscillation amplitude Γ_c , $N_b = 64$.

however a significant reduction.

Another optimization procedure, the fixed grid search, was tested with $N_b = 64$. The obtained estimates for the PM modulation index showed approximately the same standard deviation. The relatively high variance is therefore due to noise or other non-stationary phenomena and not related to the optimization procedure. Hence, a satisfactory performance of the evolution strategy with experimental signals can be remarked.

Finally, ROC curves can be calculated in order to demonstrate the detection performance of a threshold based decision using the PM modulation index. The ROC are displayed in Fig. 5.23 for 10% and 80% average load. Detection of the smallest load torque oscillation $\Gamma_c = 0.03$ Nm is difficult whereas the detection performance approaches the ideal case with higher Γ_c .

5.3 Load Unbalance

In order to study a more realistic fault producing torque oscillations, a load unbalance is introduced. The same signal processing methods as before are applied in the following to signals recorded under equivalent conditions.

In order to verify that the load unbalance creates torque oscillations, the measured load torque is analyzed and the amplitude component amplitude at f_r is determined. The obtained values are given in Table 5.10. It can be noticed that an increase in unbalance does not necessarily lead to higher measured load torque oscillations. For example, with theoretical $\Gamma_c = 0.07$ Nm, the measured values are always lower than with $\Gamma_c = 0.06$ Nm.

5.3.1 Spectral Estimation

First, classical spectral analysis is used to analyze the stator current signals with load unbalance. Stator current spectra corresponding to the smallest level of unbalance with $\Gamma_c = 0.04$ Nm are shown in Fig. 5.24 in comparison to the healthy case.

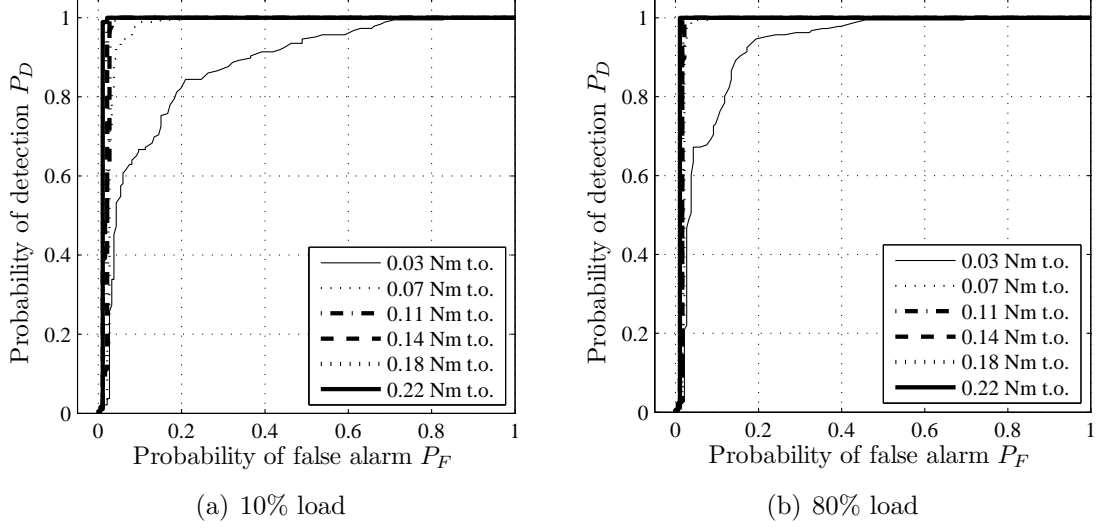


Figure 5.23: Experimental ROC for threshold based detection of load torque oscillations using the estimated PM modulation index, $N_b = 64$.

Table 5.10: Measured oscillating torque with load unbalance under different load conditions, $f_s = 50$ Hz.

Theoretical load torque oscillation [Nm]	Measured Γ_c [Nm]		
	10% load	50% load	80% load
healthy	0.012	0.009	0.007
0.04	0.039	0.036	0.043
0.06	0.041	0.062	0.066
0.07	0.033	0.038	0.041
0.10	0.050	0.060	0.053

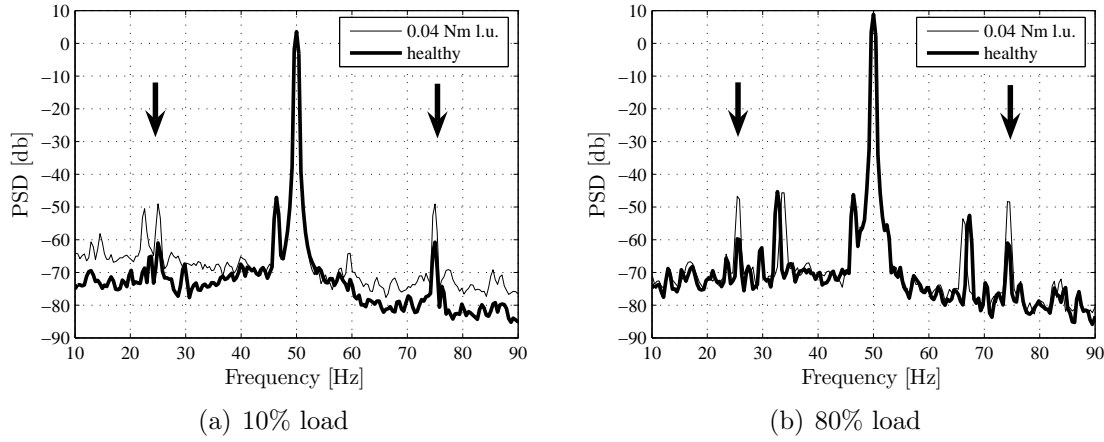


Figure 5.24: PSD of stator current with load unbalance $\Gamma_c = 0.04$ Nm vs. healthy case.

As before, the sidebands at $f_s \pm f_r$ show a considerable increase. Moreover, the fault seems to provoke a slight increase of the noise floor at small load. However, this effect disappears with increasing load.

The obtained fault indicators IPSD together with their standard deviations are given for 4 levels of unbalance in Table 5.11. The average indicator values are also displayed in Fig. 5.25 with respect to the theoretical load torque oscillation amplitude Γ_c . First, it can be noticed that all cases of load unbalance can clearly be distinguished from the healthy case, independent from the load condition. However, the fault indicator does not evolve linearly with respect to the theoretical Γ_c . The corresponding measured load torque confirmed this tendency: a higher level of unbalance does not lead to higher values of oscillating torque in this experimental setup. However, the obtained indicator values correspond approximately to the measured torque oscillation amplitudes. The nonlinearity between unbalance and measured Γ_c could be related to high levels of vibration during the test, resulting from considerable centrifugal forces at nominal speed.

The obtained indicator values can be compared to those with load torque oscillations generated by the DC motor current control (see Table 5.1). The first three levels of unbalance lead to higher indicator values compared to the corresponding load torque oscillations. The indicator values with the highest level of unbalance $\Gamma_c = 0.10$ Nm correspond relatively well to the equivalent load torque oscillation.

5.3.2 Instantaneous Frequency - Steady State

Using the same procedure as before with load torque oscillations, the stator current IF is estimated and processed using the spectrogram. For illustration, Fig. 5.26 shows the IF spectrogram of a healthy current signal in comparison to one with load unbalance of theoretical $\Gamma_c = 0.1$ Nm. The supply frequency is $f_s = 50$ Hz and the machine is loaded at 50%. Since the average IF value has not been removed prior to the spectrogram calculation, a DC level can be recognized. Due to its strong amplitude, even the sidelobes of the DC component are visible. With load

Table 5.11: Average fault indicator IPSD ($\times 10^{-3}$) and standard deviation σ_{IPSD} ($\times 10^{-3}$) for load unbalance.

	10% load		50% load		80% load	
	$E[\text{IPSD}]$	σ_{IPSD}	$E[\text{IPSD}]$	σ_{IPSD}	$E[\text{IPSD}]$	σ_{IPSD}
healthy	1.20	0.11	1.17	0.20	0.68	0.10
0.04 Nm	4.46	0.47	4.79	0.32	3.13	0.15
0.06 Nm	4.81	0.19	5.86	0.31	4.06	0.28
0.07 Nm	4.13	0.32	4.85	0.27	3.26	0.13
0.10 Nm	4.53	0.24	5.25	0.27	3.47	0.09

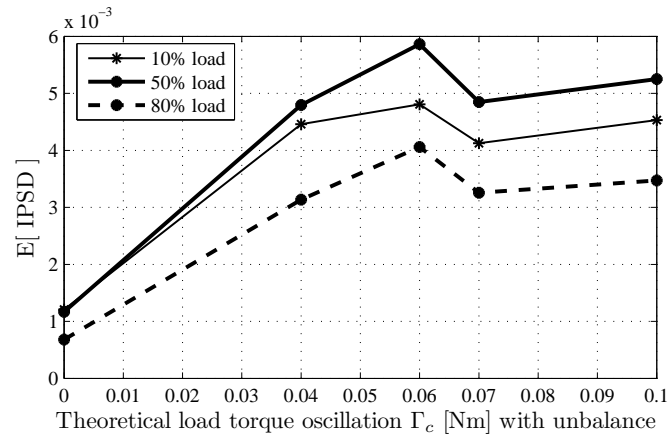


Figure 5.25: Average fault indicator IPSD vs. theoretical load torque oscillation amplitude Γ_c with load unbalance

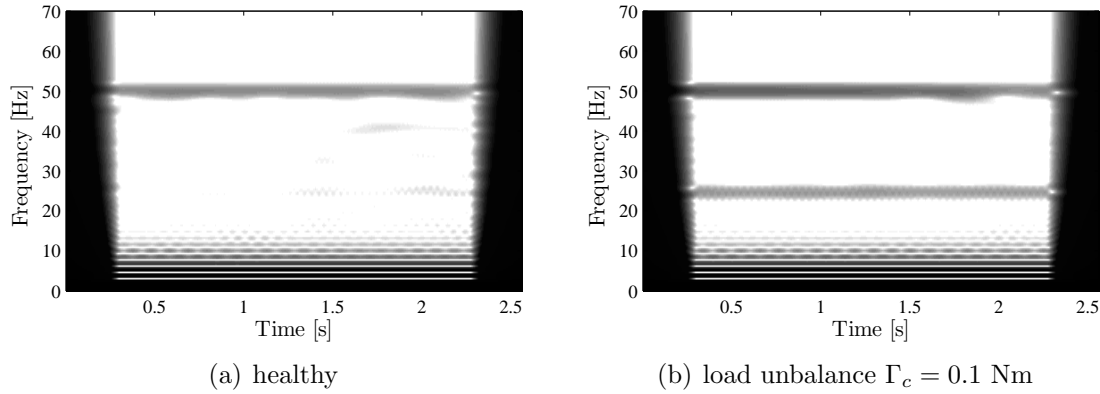


Figure 5.26: Spectrogram of stator current IF in healthy case and with load unbalance ($\Gamma_c = 0.1$ Nm), 50% load.

Table 5.12: Average fault indicator IIF2 ($\times 10^{-3}$) and standard deviation σ_{IIF2} ($\times 10^{-3}$) for load unbalance.

	10% load		50% load		80% load	
	$E[\text{IIF2}]$	σ_{IIF2}	$E[\text{IIF2}]$	σ_{IIF2}	$E[\text{IIF2}]$	σ_{IIF2}
healthy	10.9	1.1	12.3	1.6	7.5	0.8
0.04 Nm	43.3	3.7	47.0	2.8	31.8	1.4
0.06 Nm	42.8	2.2	56.4	2.8	39.0	2.4
0.07 Nm	38.7	3.3	47.3	2.4	32.7	0.8
0.10 Nm	39.8	2.2	50.5	2.4	33.8	0.8

unbalance, the spectrogram shows a component at shaft rotational frequency f_r which is not visible in the healthy case. This signature is identical to the previously studied load torque oscillations, therefore suggesting a very similar effect.

The IF based fault indicator IIF2 is then calculated on signals with different average load and level of unbalance. The obtained results are shown in Table 5.12 and graphically represented in Fig. 5.27. The obtained curves are very similar to the spectrum based indicator IPSD which again validates the IF analysis as alternative method for this fault.

5.3.3 Instantaneous Frequency - Transient State

Next, transient signals with load unbalance are analyzed using the instantaneous frequency. The stator currents during motor startup and braking are extracted from data records and analyzed using the appropriate indicator. As before, the frequency varies linearly from 10 to 48 Hz.

The fault indicator IIF2' is shown with respect to time in Fig. 5.28. With a load unbalance of theoretical amplitude $\Gamma_c = 0.1$ Nm, the indicator is at a higher level than in the healthy case. However, two regions with nearly equal indicator value exist: at the beginning of the data record and around 1.7 s which corresponds to approximately 30 Hz supply frequency. At low speed and supply frequency, the

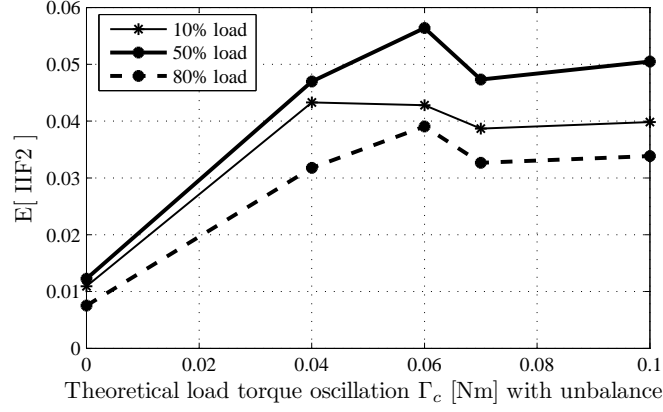


Figure 5.27: Average fault indicator IIF2 vs. theoretical load torque oscillation amplitude Γ_c with load unbalance.

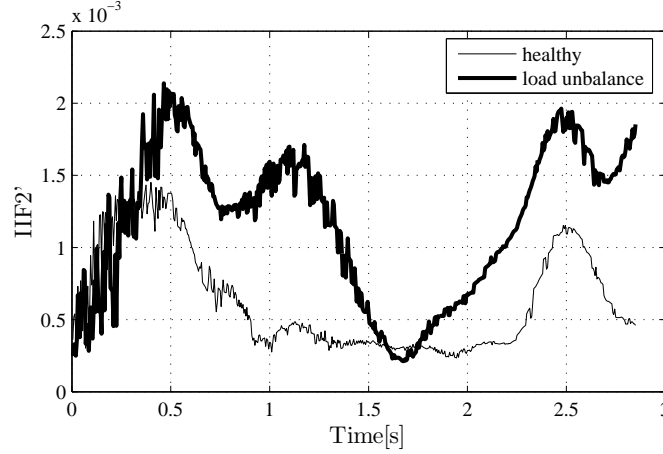


Figure 5.28: Fault indicator $IIF2'(t)$ during motor startup with load unbalance of theoretical $\Gamma_c = 0.1$ Nm.

interval in the spectrogram from which energy values are considered is relatively small and close to the DC level. This signifies that noise or the sidelobes of the DC level may strongly influence the indicator value, especially if the latter is small. The low indicator value around $f_s = 30$ Hz is probably related to mechanical resonance phenomena. Additional tests in steady state with varying supply frequency confirmed very low indicator values in a frequency range from 30 to 40 Hz with this experimental setup [Ped06]. Moreover, abnormal vibrations were recognized for these supply frequencies.

The obtained average indicator values for different load levels and unbalances are given in Table 5.13 together with their standard deviation. The average values are also shown in Fig. 5.29 with respect to the theoretical torque oscillation amplitude generated by the unbalance. Again, the evolution of the fault indicator is not linear with respect to the theoretical value of Γ_c . The fault detection is more difficult than in steady state since the relative indicator variations are smaller.

Table 5.13: Average fault indicator IIF2' ($\times 10^{-3}$) and standard deviation $\sigma_{\text{IIF2}'}$ ($\times 10^{-3}$) for load unbalance during speed transients.

	no load		50% load		80% load	
	$E[\text{IIF2}']$	$\sigma_{\text{IIF2}'}$	$E[\text{IIF2}']$	$\sigma_{\text{IIF2}'}$	$E[\text{IIF2}']$	$\sigma_{\text{IIF2}'}$
healthy	0.37	0.08	0.49	0.09	0.47	0.11
0.04 Nm	0.58	0.10	0.70	0.07	0.74	0.03
0.06 Nm	0.56	0.08	0.71	0.16	0.64	0.13
0.10 Nm	0.79	0.12	1.03	0.13	0.97	0.07

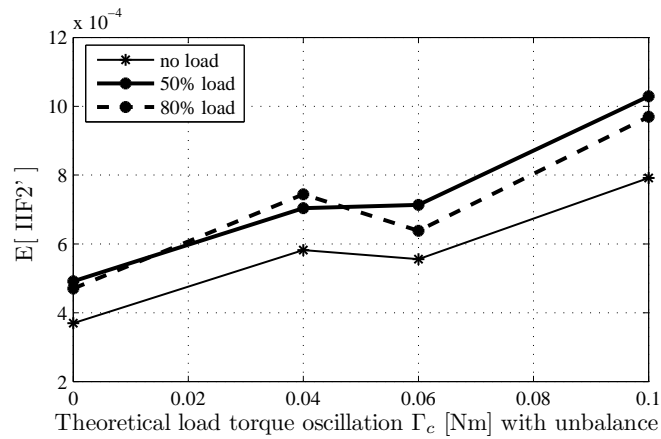


Figure 5.29: Average fault indicator IIF2' vs. theoretical load torque oscillation amplitude Γ_c with load unbalance during speed transients.

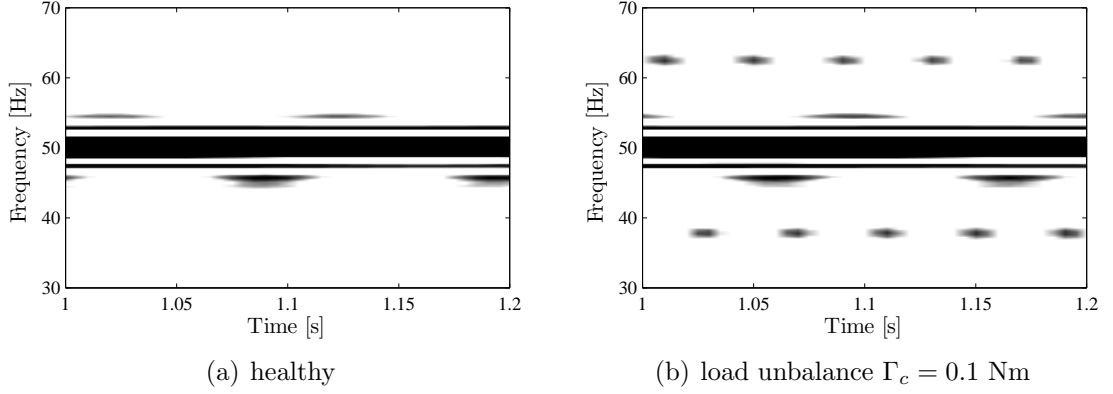


Figure 5.30: PWD of stator current in healthy case and with load unbalance ($\Gamma_c = 0.1$ Nm), 50% load.

Table 5.14: Average fault indicator IWD1 ($\times 10^{-3}$) and standard deviation σ_{IWD1} ($\times 10^{-3}$) for load unbalance.

	10% load		50% load		80% load	
	$E[\text{IWD1}]$	σ_{IWD1}	$E[\text{IWD1}]$	σ_{IWD1}	$E[\text{IWD1}]$	σ_{IWD1}
healthy	1.44	0.10	1.46	0.18	0.90	0.09
0.04 Nm	4.98	0.40	5.52	0.33	4.08	0.19
0.06 Nm	5.29	0.21	6.69	0.34	5.14	0.32
0.07 Nm	4.61	0.31	5.55	0.31	4.23	0.11
0.10 Nm	4.99	0.24	5.99	0.31	4.41	0.13

5.3.4 Pseudo Wigner Distribution - Steady State

The PWD is first used for stator current analysis in steady state. Figure 5.30 displays a zoom on the stator current PWD in healthy conditions and with load unbalance. The unbalance leads to sideband components at $f_s \pm f_r/2 \approx 50 \pm 12.5$ Hz. They oscillate at fault characteristic frequency $f_r \approx 25$ Hz. The phase shift between upper and lower sideband component is approximately π . Thus, it becomes clear that the load unbalance causes the same fault signature in the PWD as the load torque oscillations.

The PWD based fault indicators are then calculated on all recorded signals. Table 5.14 displays the average indicator values for IWD1 together with their standard deviation. Figure 5.31 displays the average indicator value with respect to the theoretical load torque oscillation amplitude Γ_c generated by the unbalance. Again, the general indicator evolution is very similar to IPSD or IIF2 in steady state.

The results with the second indicator IWD2 are displayed in Table 5.15. The absolute indicator values correspond to the previously obtained results with the other indicators. The phase angles with unbalance are between 130° and 160° , similar to the load torque oscillations. As before, the phase angles are closest to π with 50% load.

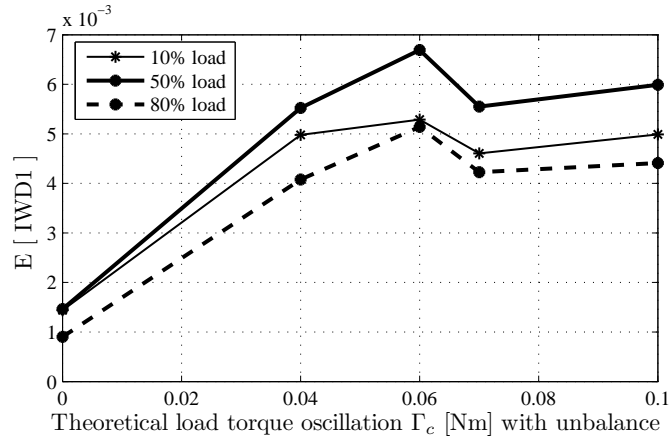
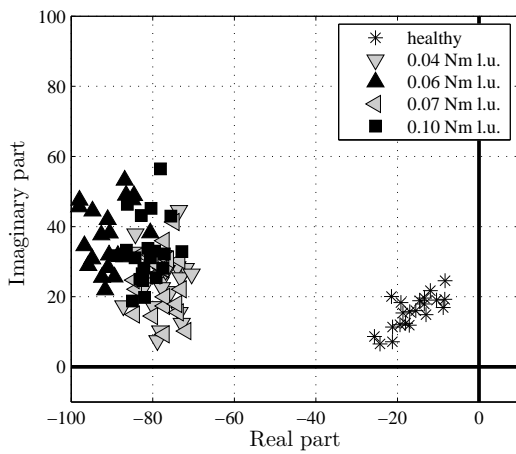


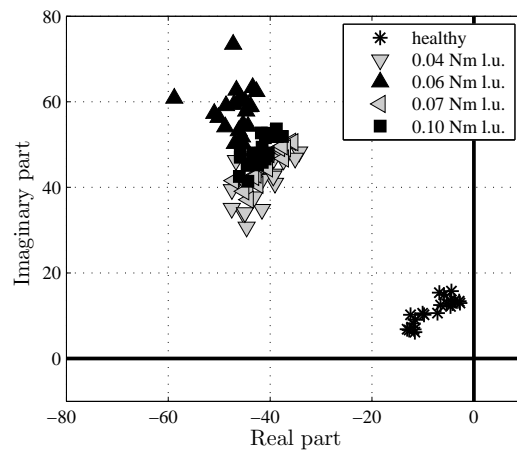
Figure 5.31: Average fault indicator IWD1 vs. theoretical load torque oscillation amplitude Γ_c with load unbalance.

Table 5.15: Average fault indicator IWD2 (absolute value $A = E[|IWD2|]$ and argument $\varphi = E[\angle IWD2]$ in $^\circ$) for load unbalance.

	10% load		50% load		80% load	
	A	φ	A	φ	A	φ
healthy	23.7	106.7	23.4	135.7	14.4	124.9
0.04 Nm	81.9	145.7	81.5	162.7	59.1	135.4
0.06 Nm	81.4	129.1	98.5	157.8	74.7	128.9
0.07 Nm	72.6	139.2	82.0	163.1	61.2	132.2
0.10 Nm	76.9	125.8	88.2	158.2	63.9	131.3



(a) 50% load



(b) 80% load

Figure 5.32: Complex representation of fault indicator IWD2 with load unbalance, 50% and 80% load.

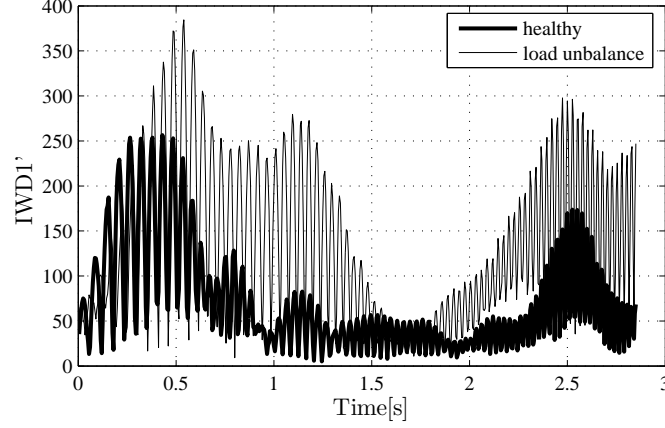


Figure 5.33: Fault indicator $IWD1'(t)$ during motor startup with load unbalance of theoretical $\Gamma_c = 0.1$ Nm.

Table 5.16: Average fault indicator $IWD1'$ and standard deviation $\sigma_{IWD1'}$ for load unbalance during speed transients.

	no load		50% load		80% load	
	$E[IWD1']$	$\sigma_{IWD1'}$	$E[IWD1']$	$\sigma_{IWD1'}$	$E[IWD1']$	$\sigma_{IWD1'}$
healthy	49.5	5.5	56.7	10.5	54.8	11.7
0.04 Nm	72.6	5.3	76.8	7.7	82.3	2.3
0.06 Nm	67.3	5.0	77.9	18.0	74.7	14.1
0.10 Nm	98.8	6.0	111.3	17.0	108.5	5.2

5.3.5 Pseudo Wigner Distribution - Transient State

Both PWD based indicators are also tested during speed transients. The same signals as before are used to calculate the indicators. Indicator $IWD1'$ is shown with respect to time for a data record with load unbalance $\Gamma_c = 0.1$ Nm in Fig. 5.33. With load unbalance, the indicator amplitude takes higher values, except at low speed and around 30 Hz supply frequency. This behavior is identical to the indicator $IIF2'(t)$ (see Fig. 5.28). The average values of $IWD1'$ are shown in Table 5.16 as well as in Fig. 5.34. Again, the obtained results are similar to $IIF2'$.

For illustration of the transient performance of $IWD2'$, Fig. 5.35 shows the absolute value and phase during a motor startup with load unbalance. The absolute value is similar to the amplitude of $IWD1'(t)$. It is interesting to note that the phase is stable and relatively close to π with load unbalance, except when the absolute value is low.

The complete results with the second indicator $IWD2'$ are displayed in Table 5.17. Acceleration and braking phase are separated since the angles at small load are again significantly different. This can also be recognized in the complex representation of the indicator in Fig. 5.36. At no load, the obtained indicators during acceleration and braking are well distinct with phase angles close to $\pi/2$ during braking. The tests with load unbalance are in general related to a higher absolute indicator value compared to the healthy case. Nevertheless, the fault de-

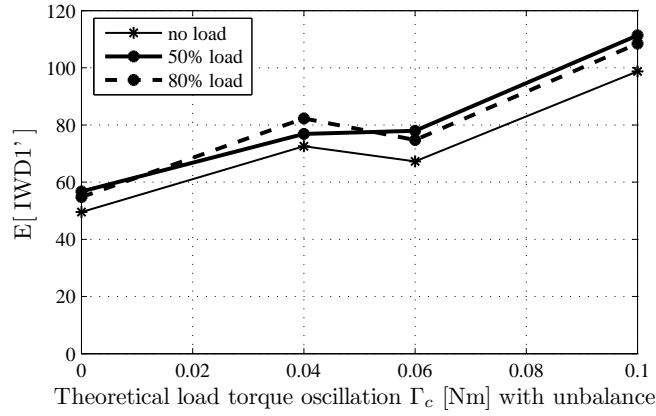


Figure 5.34: Average fault indicator $IWD1'$ vs. theoretical load torque oscillation amplitude Γ_c with load unbalance during speed transients.

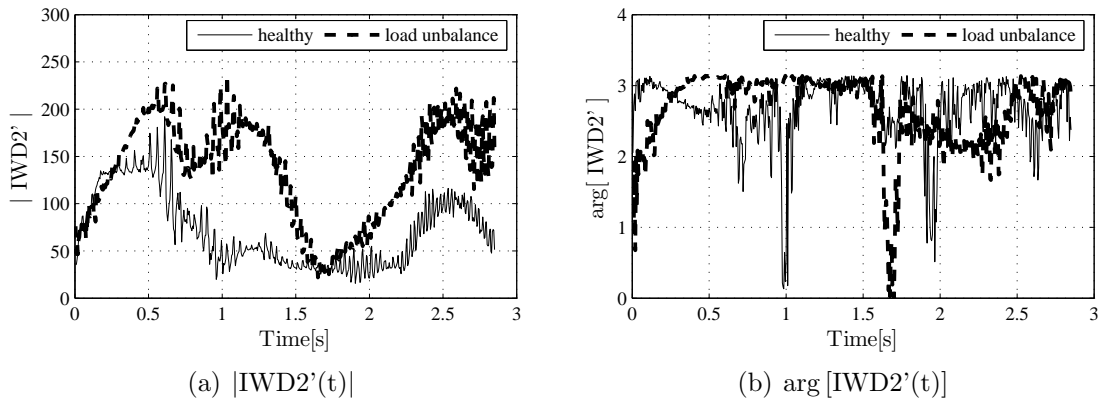


Figure 5.35: Absolute value and argument of fault indicator $IWD2'(t)$ during motor startup with load unbalance of theoretical $\Gamma_c = 0.1$ Nm.

Table 5.17: Average fault indicator IWD2' (absolute value $A = E[|IWD2'|]$ and argument $\varphi = E[\angle IWD2']$ in $[\circ]$) for load unbalance during speed transients.

		no load		50% load		80% load	
		A	φ	A	φ	A	φ
acceleration	healthy	58.7	116.8	69.1	135.9	70.4	129.6
	0.04 Nm	76.4	132.6	87.0	149.3	85.1	144.7
	0.06 Nm	73.9	128.4	95.2	142.1	89.2	139.2
	0.10 Nm	101.1	137.7	130.2	151.7	105.9	140.1
braking	healthy	48.4	82.4	53.4	124.1	47.6	111.4
	0.04 Nm	73.7	91.6	74.4	130.6	78.9	150.8
	0.06 Nm	67.9	94.4	64.3	133.5	64.2	120.4
	0.10 Nm	97.2	97.9	96.1	142.8	105.7	157.0

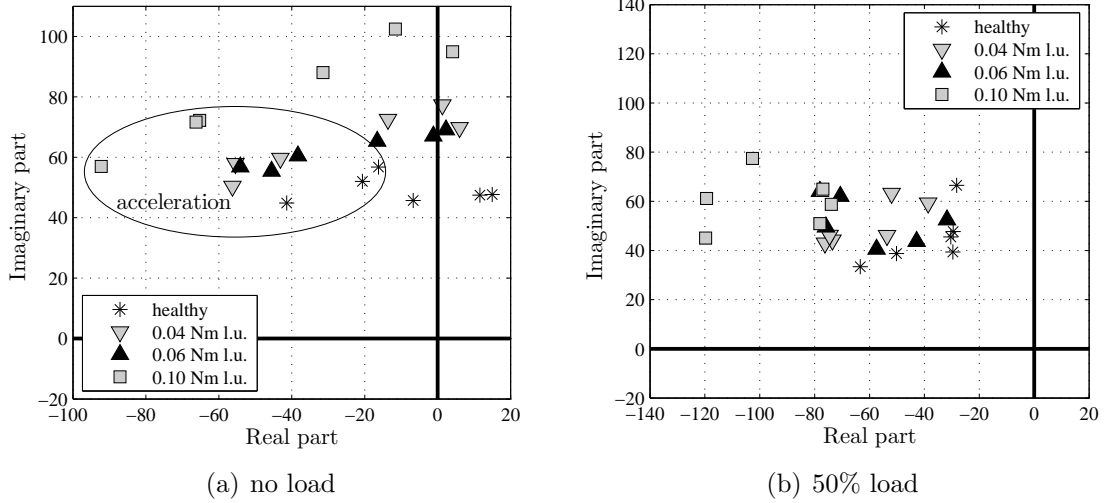


Figure 5.36: Complex representation of fault indicator IWD2' with load unbalance during speed transients, no load and 50% load.

tection is more difficult during transients since some data records show relative high absolute values even in the healthy case.

5.3.6 Parameter Estimation

As with load torque oscillations, the PM and AM modulation indices are estimated. The data record length is $N_b = 64$ samples. For PM estimation, the evolution strategy is used for optimization. The obtained results are displayed in Tables 5.18 and 5.19. The average indices are shown with respect to the theoretical torque oscillation amplitude in Fig. 5.37.

First, it can be noticed that the obtained PM indices reflect the previously obtained fault indicators with non-parametric methods. This points to a predominance of torque oscillations in the case of load unbalance. The AM indices show

Table 5.18: Average estimated PM modulation index $E[\hat{\theta}_3]$ ($\times 10^{-3}$) and standard deviation $\sigma_{\hat{\theta}_3}$ ($\times 10^{-3}$) for load unbalance, $N_b = 64$.

	10% load		50% load		80% load	
	$E[\hat{\theta}_3]$	$\sigma_{\hat{\theta}_3}$	$E[\hat{\theta}_3]$	$\sigma_{\hat{\theta}_3}$	$E[\hat{\theta}_3]$	$\sigma_{\hat{\theta}_3}$
healthy	1.63	1.55	1.88	1.58	1.41	1.51
0.04 Nm	4.80	1.54	4.99	1.45	3.59	1.46
0.06 Nm	4.69	1.54	5.96	1.44	4.25	1.44
0.07 Nm	4.24	1.51	5.06	1.49	3.69	1.46
0.10 Nm	4.34	1.46	5.44	1.53	3.74	1.59

Table 5.19: Average estimated AM modulation index $E[\hat{\kappa}_2]$ ($\times 10^{-3}$) and standard deviation $\sigma_{\hat{\kappa}_2}$ ($\times 10^{-3}$) for load torque oscillations, $N_b = 64$.

	10% load		50% load		80% load	
	$E[\hat{\kappa}_2]$	$\sigma_{\hat{\kappa}_2}$	$E[\hat{\kappa}_2]$	$\sigma_{\hat{\kappa}_2}$	$E[\hat{\kappa}_2]$	$\sigma_{\hat{\kappa}_2}$
healthy	1.36	2.37	1.23	2.34	1.15	2.24
0.04 Nm	2.38	2.50	1.49	2.37	1.78	2.46
0.06 Nm	2.49	2.41	1.73	2.44	2.43	2.49
0.07 Nm	2.14	2.20	1.49	2.10	1.97	2.27
0.10 Nm	2.51	2.30	1.62	2.42	2.07	2.36

a slight rise but no significant evolution. Moreover, the standard deviation of the AM indices is high and is in some cases equal or higher than the AM index value itself. It can be concluded that the PM modulation index is an effective fault indicator for detection of load unbalance. This is also confirmed by the corresponding ROC curves, displayed in Fig. 5.38.

5.4 Dynamic Eccentricity

The healthy induction motor is replaced by a motor with 40% dynamic airgap eccentricity. First, the measured load torque is analyzed in order to corroborate experimentally the hypothesis that eccentricity leads to oscillating torque components at frequency f_r (see section 2.5.5). The obtained torque spectra are displayed in Fig. 5.39 for three different load levels together with the corresponding healthy case. It can clearly be seen that the oscillating torque component at $f_r \approx 25$ Hz increases when dynamic eccentricity is present.

5.4.1 Spectral Estimation

The corresponding stator current spectra with dynamic eccentricity are shown in Fig. 5.40 in comparison to the healthy case. The amplitude of sidebands at $f_s \pm f_r$ increases with the fault. It becomes clear that the spectral signature of airgap eccentricity is identical to load torque oscillations or load unbalance. Therefore, spectral estimation can be used for fault detection purposes but the discrimination

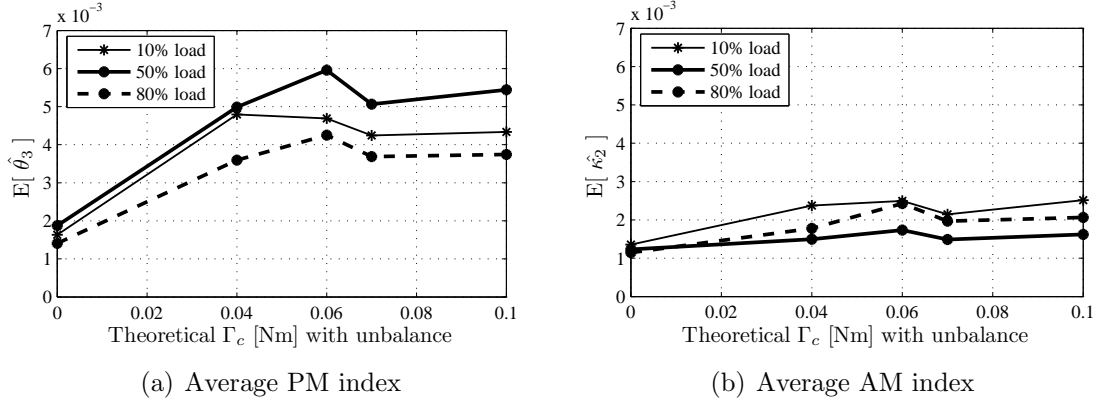


Figure 5.37: Average PM and AM modulation indices with respect to theoretical torque oscillation amplitude Γ_c with unbalance, $N_b = 64$.

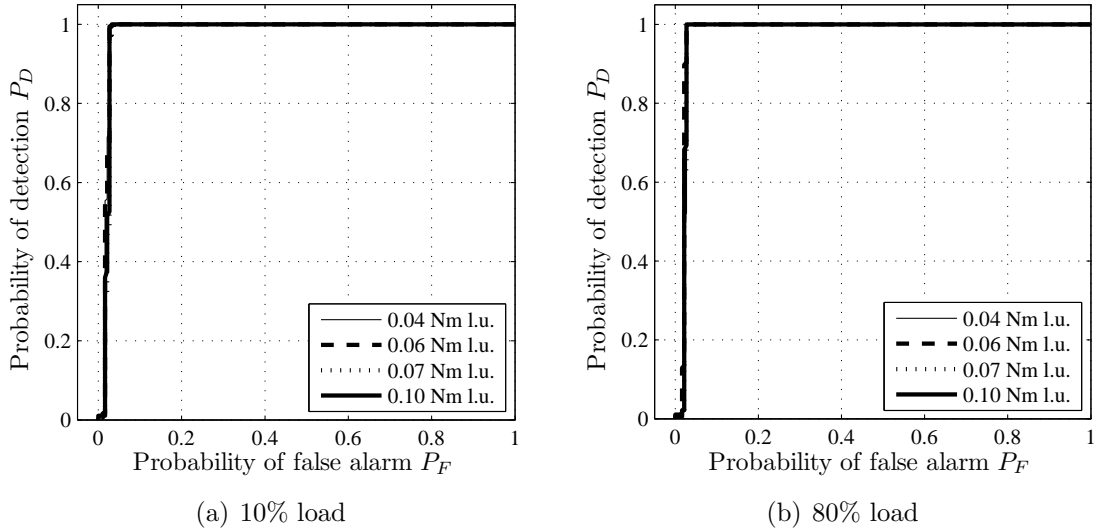


Figure 5.38: Experimental ROC for threshold based detection of load unbalance using the estimated PM modulation index, $N_b = 64$.

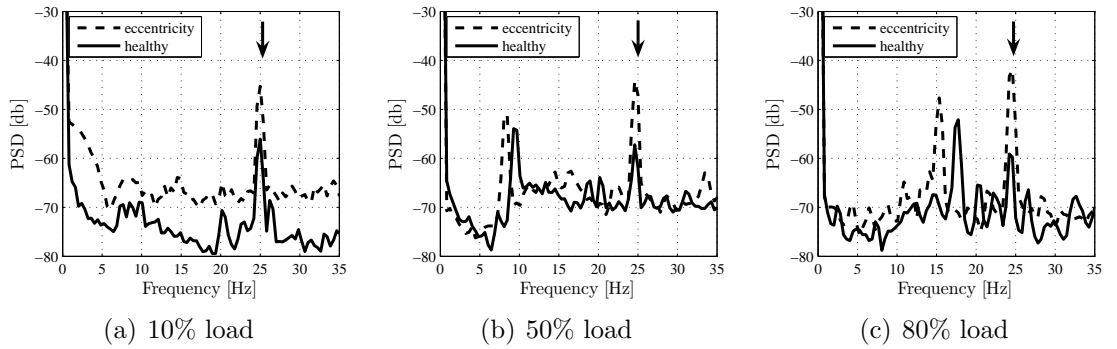


Figure 5.39: PSD of measured torque with 40% dynamic eccentricity vs. healthy case.

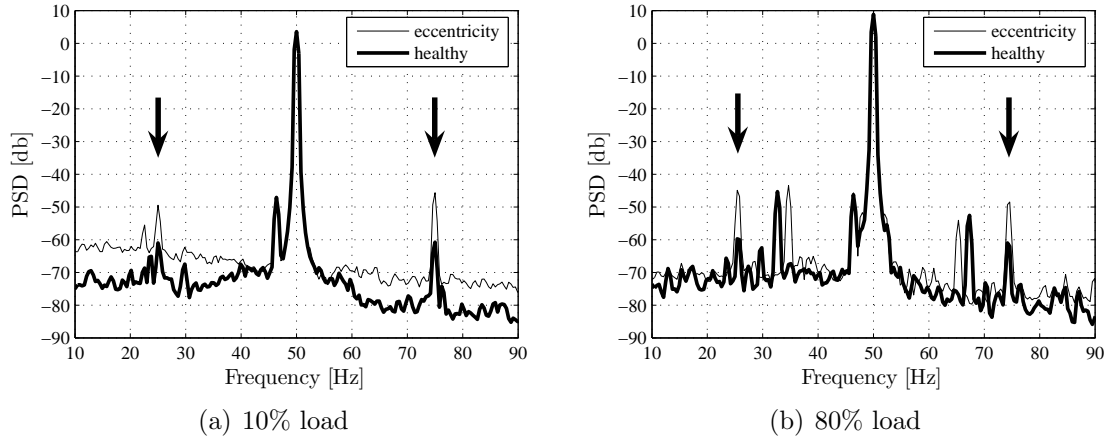


Figure 5.40: PSD of stator current with 40% dynamic eccentricity vs. healthy case.

Table 5.20: Average fault indicator IPSD ($\times 10^{-3}$) and standard deviation σ_{IPSD} ($\times 10^{-3}$) for 40% dynamic eccentricity.

	10% load		50% load		80% load	
	$E[\text{IPSD}]$	σ_{IPSD}	$E[\text{IPSD}]$	σ_{IPSD}	$E[\text{IPSD}]$	σ_{IPSD}
healthy	1.20	0.11	1.17	0.20	0.68	0.10
dynamic eccentricity	5.67	0.45	3.70	0.35	3.49	0.16

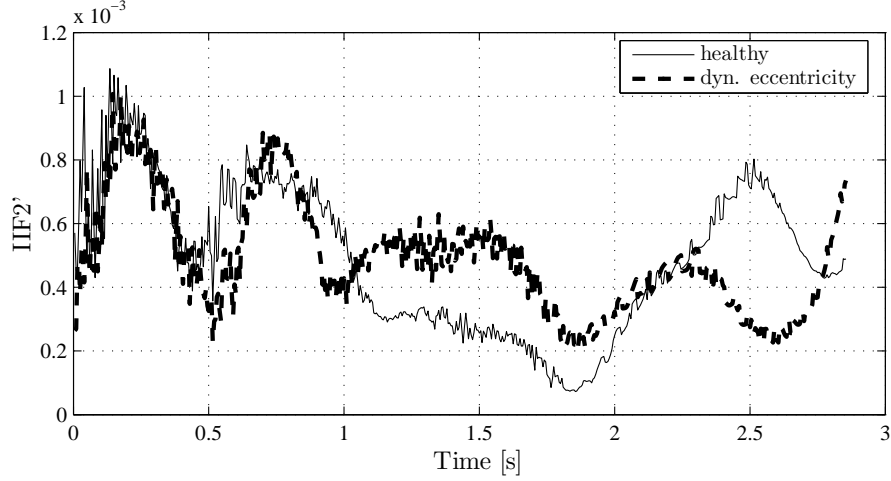
of eccentricity from torque oscillations is impossible. The obtained fault indicator values are given in Table 5.20. It is interesting to note that contrary to load unbalance or torque oscillations, the indicator is highest at small load with dynamic eccentricity. This confirms similar observations in [Dor97].

5.4.2 Instantaneous Frequency - Steady State

The stator current IF with dynamic eccentricity is analyzed using the fault indicator IIF2. The results are shown in Table 5.21. The indicator IIF2 shows a significant rise with dynamic eccentricity. This can be explained by the eccentricity related load torque oscillations since a pure AM should not influence the stator current IF. The fact that IIF2 takes only into account stator current PM can also be seen by observing the relative indicator variation compared to IPSD. With eccentricity, the relative indicator variation with IIF2 between the healthy and faulty case is smaller than with IPSD. Consider e.g. 80% average load: IPSD shows an increase by 5.13 with dynamic eccentricity whereas IIF2 increases only by 3.5. With the previously analyzed load torque oscillations, IPSD and IIF2 increased approximately in the same proportions (compare Tables 5.1 and 5.2). This points to the fact that dynamic eccentricity leads to other modulations besides pure PM.

Table 5.21: Average fault indicator IIF2 ($\times 10^{-3}$) and standard deviation σ_{IIF2} ($\times 10^{-3}$) for 40% dynamic eccentricity.

	10% load		50% load		80% load	
	$E[\text{IIF2}]$	σ_{IIF2}	$E[\text{IIF2}]$	σ_{IIF2}	$E[\text{IIF2}]$	σ_{IIF2}
healthy	10.9	1.1	12.3	1.6	7.5	0.8
dynamic eccentricity	38.2	4.2	28.1	2.8	26.5	1.3

**Figure 5.41:** Fault indicator IIF2' with dynamic eccentricity during speed transient.

5.4.3 Instantaneous Frequency - Transient State

The motor with dynamic eccentricity is tested during transients with the same speed variations as before. The IF based indicator IIF2' is displayed in Fig. 5.41 during a startup with a healthy motor compared to dynamic eccentricity. The indicator does not show a significantly higher level during the whole startup.

The calculated indicator values for all load levels are displayed in Table 5.22. Again, it can be seen that the indicator IIF2' is not sensitive to dynamic eccentricity during transients.

5.4.4 Pseudo Wigner Distribution - Steady State

Next, the steady state stator current signals are analyzed with the PWD. The PWD of the stator current with dynamic eccentricity is displayed in Fig. 5.42 in

Table 5.22: Average fault indicator IIF2' ($\times 10^{-3}$) and standard deviation $\sigma_{\text{IIF2}'}$ ($\times 10^{-3}$) for dynamic eccentricity during speed transients.

	10% load		50% load		80% load	
	$E[\text{IIF2}']$	$\sigma_{\text{IIF2}'}$	$E[\text{IIF2}']$	$\sigma_{\text{IIF2}'}$	$E[\text{IIF2}']$	$\sigma_{\text{IIF2}'}$
healthy	0.37	0.08	0.49	0.09	0.47	0.11
dynamic eccentricity	0.47	0.04	0.66	0.05	0.44	0.03

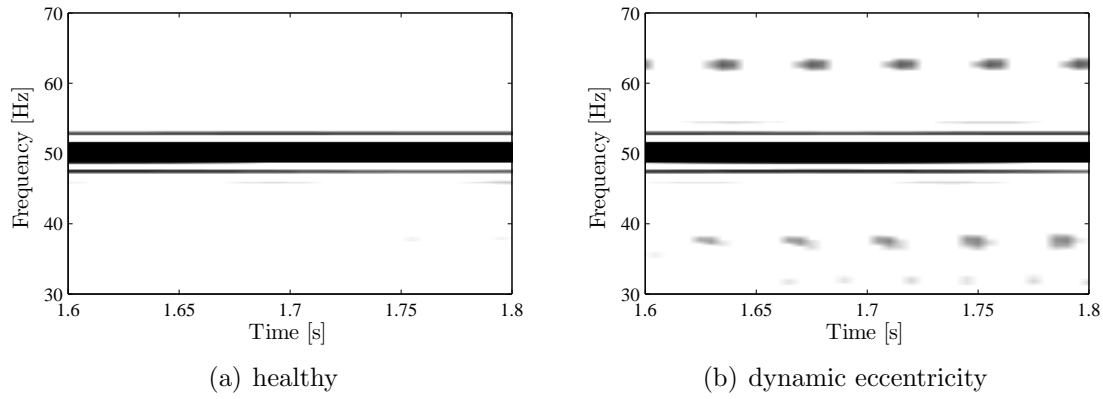


Figure 5.42: PWD of stator current in healthy case and with dynamic eccentricity, 10% load.

Table 5.23: Average fault indicator IWD1 ($\times 10^{-3}$) and standard deviation σ_{IWD1} ($\times 10^{-3}$) for 40% dynamic eccentricity.

	10% load		50% load		80% load	
	$E[\text{IWD1}]$	σ_{IWD1}	$E[\text{IWD1}]$	σ_{IWD1}	$E[\text{IWD1}]$	σ_{IWD1}
healthy	1.44	0.10	1.46	0.18	0.90	0.09
dynamic eccentricity	6.32	0.37	4.33	0.36	4.47	0.18

comparison to the healthy case. With dynamic eccentricity, oscillating sidebands at $f_s \pm f_r/2 \approx 50 \pm 12.5$ Hz are visible. The sidebands oscillate approximately at f_r . Moreover, it can be recognized that their phase shift is closer to 0 than with the previously observed load torque oscillations. Therefore, the observed signature resembles more to the PWD of AM signals, derived in section 4.3.3.

The PWD based fault indicator IWD1 has been calculated and it is shown in Table 5.23. The indicator shows a significant rise with dynamic eccentricity. The relative indicator variation is greater than with IIF2 since IWD1 takes into account AM and PM. For example, IWD1 increases approximately by 5 with 80% average load, which is close to the relative variation of IPSD.

The obtained values with indicator IWD2 are displayed in Table 5.24. Again, the absolute value of IWD2 shows a significant rise with dynamic eccentricity. The observed phase values are of particular interest since they are close to $\pi/2$. This points to the fact that both AM and PM are present on the stator current. Pure AM would lead to phase angles close to 0 whereas it should be close to π with pure PM. These results corroborate the theoretical developments in section 2.5 on the effects of airgap eccentricity on the stator current.

The results with IWD2 can also be visualized by plotting the indicator in the complex plane. The obtained indicator estimates are shown in Fig. 5.43 with 10% and 50% average load. The same observations regarding the angle and absolute indicator values can be made.

Table 5.24: Average fault indicator IWD2 (absolute value $A = E[|IWD2|]$ and argument $\varphi = E[\angle IWD2]$ in $^\circ$) for 40% dynamic eccentricity.

	10% load		50% load		80% load	
	A	φ	A	φ	A	φ
healthy	23.7	106.7	23.4	135.7	14.4	124.9
dynamic eccentricity	98.5	81.8	64.4	93.8	64.7	86.3

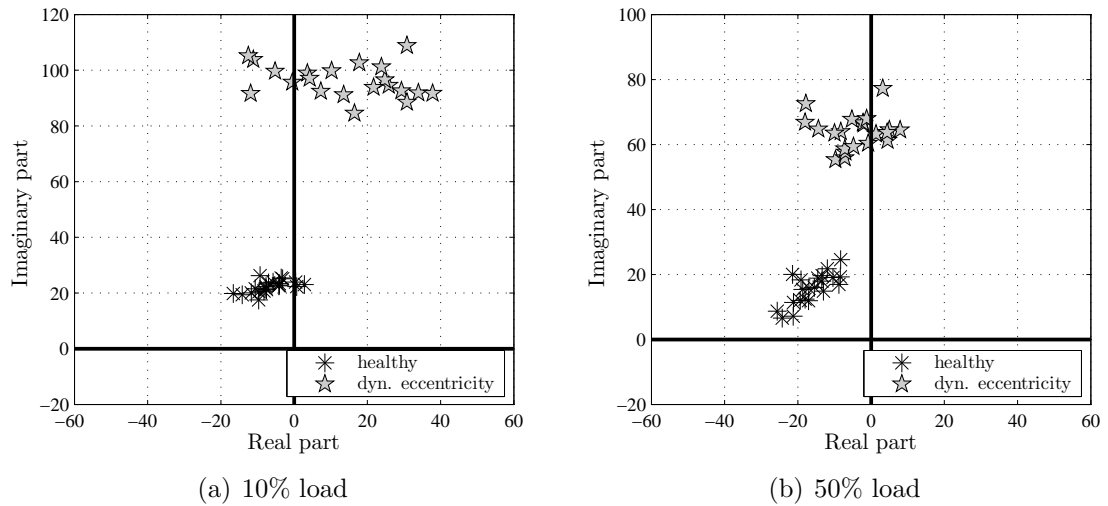


Figure 5.43: Complex representation of fault indicator IWD2 with dynamic eccentricity, 10% and 50% load.

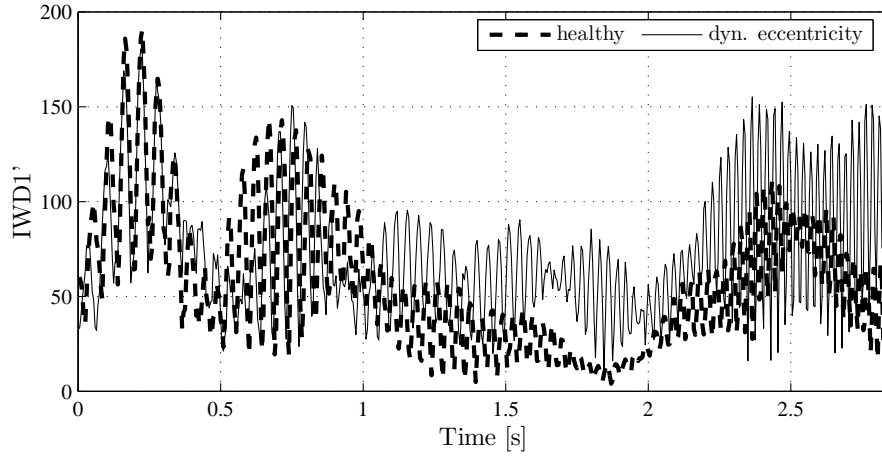


Figure 5.44: Fault indicator $IWD1'$ with dynamic eccentricity during motor startup, 10% load.

Table 5.25: Average fault indicator $IWD1'$ ($\times 10^{-3}$) and standard deviation $\sigma_{IWD1'}$ ($\times 10^{-3}$) for dynamic eccentricity during speed transients.

	no load		50% load		80% load	
	$E[IWD1']$	$\sigma_{IWD1'}$	$E[IWD1']$	$\sigma_{IWD1'}$	$E[IWD1']$	$\sigma_{IWD1'}$
healthy	6.17	0.90	7.33	1.89	6.71	2.43
dynamic eccentricity	7.74	0.47	9.72	1.02	7.18	1.05

5.4.5 Pseudo Wigner Distribution - Transient State

The PWD based indicators are also tested with dynamic eccentricity during speed transients. Figure 5.44 displays for example $IWD1'(t)$ during a motor startup with 10% load. At the beginning of the data record, the healthy and faulty signals lead to the same indicator values. Later, a higher amplitude with dynamic eccentricity can be noticed. It is interesting to compare this result to the indicator $IIF2'(t)$ in Fig. 5.41. $IWD1'(t)$ shows significantly higher values with eccentricity compared to the healthy case than $IIF2'(t)$. A probable explanation is the presence of eccentricity related AM which cannot be detected by IF based indicators.

The average indicator values $IWD1'$ with all tested load levels are shown in Table 5.25. The relative indicator variations are much smaller compared to load torque oscillations or load unbalance during transients. This makes detection of dynamic eccentricity difficult in non-stationary conditions.

The second indicator $IWD2'(t)$ is shown with respect to time for a motor startup in Fig. 5.45. The absolute values are in general very similar. However, the phase is in general smaller with dynamic eccentricity and drops to values smaller than $\pi/2$ between 1.7 and 2.3 seconds. This is the only sign pointing to the presence of the fault.

The average absolute values and phase angles for $IWD2'$ are given in Table 5.26. The absolute value shows in most cases an increase and the phase angles are generally smaller with eccentricity. However, the detection of dynamic eccentricity during transients is significantly harder than in steady state.

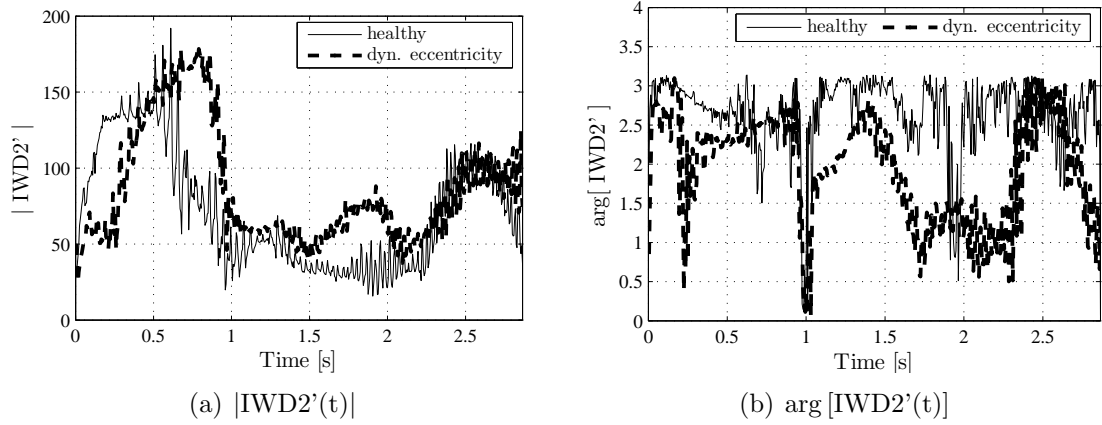


Figure 5.45: Absolute value and argument of fault indicator $IWD2'(t)$ with dynamic eccentricity during motor startup.

Table 5.26: Average fault indicator $IWD2'$ (absolute value $A = E[|IWD2'|]$ and argument $\varphi = E[\angle IWD2']$ in $^\circ$) for dynamic eccentricity during speed transients.

		10% load		50% load		80% load	
		A	φ	A	φ	A	φ
acceleration	healthy	58.7	116.8	69.1	135.9	70.4	129.6
	dynamic eccentricity	72.5	110.1	91.1	102.3	66.7	86.4
braking	healthy	48.4	82.4	53.4	124.1	47.6	111.4
	dynamic eccentricity	72.8	57.4	81.7	101.5	65.2	82.4

Table 5.27: Average estimated PM modulation index $E[\hat{\theta}_3]$ ($\times 10^{-3}$) and standard deviation $\sigma_{\hat{\theta}_3}$ ($\times 10^{-3}$) for dynamic eccentricity, $N_b = 64$.

	10% load		50% load		80% load	
	$E[\hat{\theta}_3]$	$\sigma_{\hat{\theta}_3}$	$E[\hat{\theta}_3]$	$\sigma_{\hat{\theta}_3}$	$E[\hat{\theta}_3]$	$\sigma_{\hat{\theta}_3}$
healthy	1.63	1.55	1.87	1.59	1.41	1.51
dynamic eccentricity	4.30	1.70	3.19	1.60	3.04	1.58

Table 5.28: Average estimated AM modulation index $E[\hat{\kappa}_2]$ ($\times 10^{-3}$) and standard deviation $\sigma_{\hat{\kappa}_2}$ ($\times 10^{-3}$) for dynamic eccentricity, $N_b = 64$.

	10% load		50% load		80% load	
	$E[\hat{\kappa}_2]$	$\sigma_{\hat{\kappa}_2}$	$E[\hat{\kappa}_2]$	$\sigma_{\hat{\kappa}_2}$	$E[\hat{\kappa}_2]$	$\sigma_{\hat{\kappa}_2}$
healthy	1.36	2.37	1.23	2.34	1.15	2.24
dynamic eccentricity	4.79	2.45	3.00	2.14	3.18	2.29

5.4.6 Parameter Estimation

Finally, parameter estimation techniques are tested in steady state with dynamic eccentricity. Using data records of length $N_b = 64$ samples as before, the results displayed in Tables 5.27 and 5.28 are obtained. As expected, the average PM index shows a significant rise due to an increased level of torque oscillations. In addition, the AM index also increases significantly and reaches values approximately equal to the PM index. This important result confirms that dynamic eccentricity leads simultaneously to amplitude and phase modulation of the stator current. The previous parameter estimation results with torque oscillations and load unbalance did not lead to significantly higher AM indices. Therefore, the parameter estimation approach is an effective tool not only for fault detection but also discrimination of eccentricity and torque oscillations.

5.5 On-line Monitoring

Two of the discussed methods, spectral estimation and the PWD, have also been implemented on a low cost DSP board (ADSP-21161) for on-line monitoring. The principal reason are often stated concerns about computation time with time-frequency methods. The DSP implementation demonstrates the feasibility of on-line monitoring using time-frequency methods on a standard processor. This has also been shown in [Raj05] for rotor fault detection in brushless DC motors.

One stator current signal is continuously sampled and processed by the DSP. The three fault indicators IPSD, IWD1 and IWD2 are then calculated on data records of length 512 samples (≈ 2.7 s). Note that the phase extraction for IWD2 has not been implemented, i.e. $IWD2 = |IWD2|$ in this section. Additional details on the implementation are given in appendix C and [Blö07]. Load torque oscillations and load unbalance are first studied in steady state and then during speed transients.

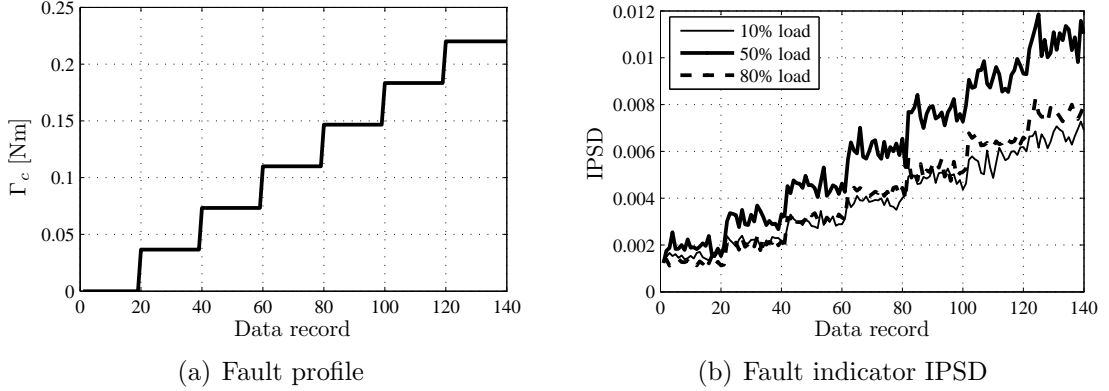


Figure 5.46: Fault profile for Γ_c and indicator IPSD response vs. data record.

5.5.1 Load Torque Oscillations - Steady State

In order to test the indicators with different fault severity in steady state, the load torque oscillation amplitude Γ_c successively increases from $\Gamma_c = 0$ to 0.22 Nm. Each fault level is maintained during 20 data records. The fault profile is shown in Fig. 5.46(a).

The obtained spectrum based indicator IPSD is displayed in Fig. 5.46(b). Three load levels are tested at supply frequency $f_s = 50$ Hz. It can be noticed that the indicator follows the fault profile. Even small torque oscillation can be detected. The indicator dependence on the average load corresponds to the previous results.

The stator current PM modulation index depends on the frequency of the considered torque oscillation according to (2.70): $\beta \propto 1/f_c^2$. Therefore, the fault indicator IPSD should depend on f_c in the same way. For verification, the same test are conducted at supply frequency $f_s = 25$ Hz. Theoretically, the fault indicator should be 4 times higher than with $f_s = 50$ Hz. Fig. 5.47 shows IPSD with $f_s = 25$ Hz compared to (4IPSD) with $f_s = 50$ Hz, for two different load levels. With higher torque oscillation amplitudes, the two curves are approximately at the same level which corroborates the theoretical assumption. At low values for Γ_c the indicators differ more due to inherent torque oscillations and/or eccentricity in the healthy case.

Next, the two PWD based indicators are tested in steady state at constant supply frequency $f_s = 50$ Hz. The obtained results with the considered fault profiles are shown in Fig. 5.48. Due to slight differences in normalization, the amplitudes do not correspond exactly to the previous off-line results. For IWD2, a Fourier transform based extraction method is used instead of the Hilbert transform. Both indicators show an approximately linear rise with respect to the amplitude of the load torque oscillation. The indicator IWD2 seems more sensitive to the increase of Γ_c than IWD1. A possible explanation is the more accurate analysis with respect to the fault frequency in case of IWD2. Recall that IWD1 is based on the total energy in the PWD in a given frequency interval, whereas IWD2 only considers the energy of pulsating components at fault frequency. It can also be noticed that IWD2 depends less on the average load level than IWD1.

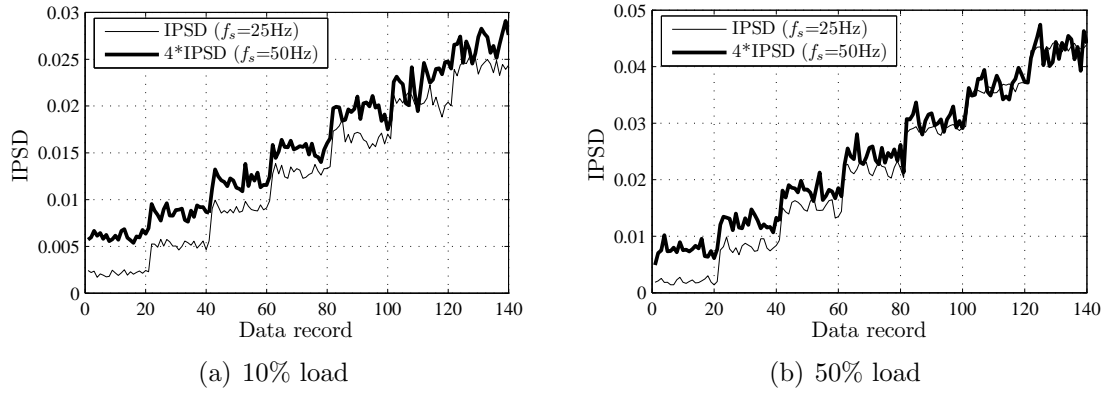


Figure 5.47: Comparison of fault indicator IPSD with $f_s = 25$ and 50 Hz.

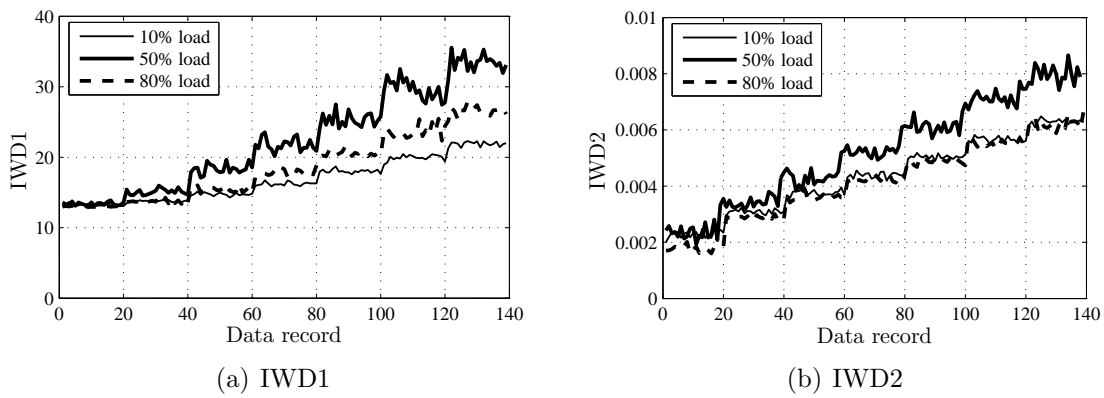


Figure 5.48: PWD based indicators IWD1 and IWD2 vs. data records, $f_s = 50$ Hz.

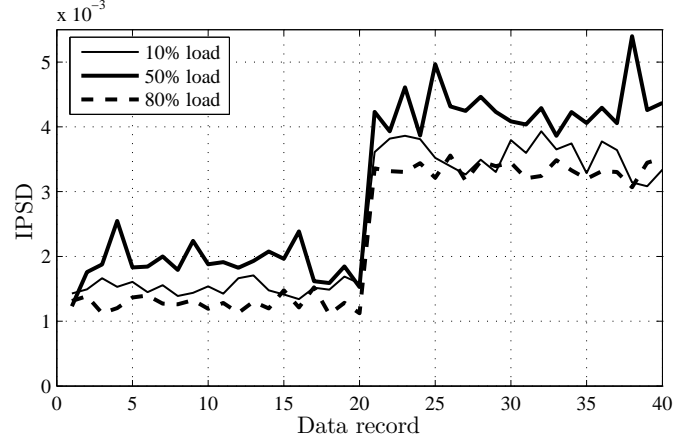


Figure 5.49: Fault indicator IPSD with load unbalance: data records 1-20 correspond to the healthy case, 21-40 to load unbalance with theoretical $\Gamma_c = 0.06$ Nm.

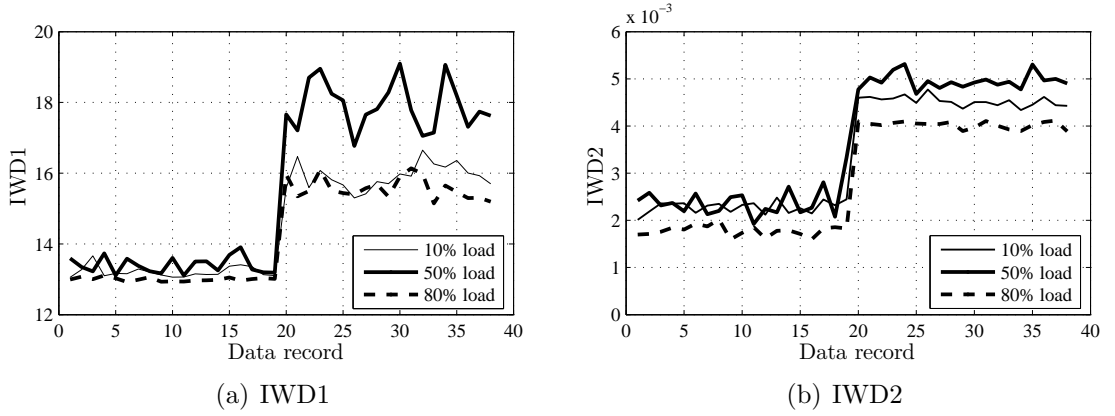


Figure 5.50: Fault indicators IWD1 and IWD2 with load unbalance: data records 1-20 correspond to the healthy case, 21-40 to load unbalance with theoretical $\Gamma_c = 0.06$ Nm.

5.5.2 Load Unbalance - Steady State

Next, the on-line monitoring scheme is also tested with a load unbalance of theoretical amplitude $\Gamma_c = 0.06$ Nm. Results with IPSD and three average load levels at $f_s = 50$ Hz are shown in Fig. 5.49. The data records 1-20 represent the healthy state whereas 21-40 are with load unbalance. The load unbalance leads to a clear rise in the indicator. The indicators also depend on the average load level but a simple threshold could however be used in this case for unbalance detection.

The results with the PWD based indicators IWD1 and IWD2 are shown in Fig. 5.50. Again, the indicator are sensitive to the unbalance. Due to the nature of the indicator IWD1, the relative fault sensitivity is higher with IWD2. Actually, since IWD1 considers all the energy in a certain frequency range in the PWD, it is more sensitive to noise and other phenomena. IWD2 however takes only into account the oscillating energy in the sideband signals and is therefore more accurate.

5.5.3 Load Torque Oscillations - Transient State

For indicator analysis during transients, the speed profile displayed in Fig. 5.51 is used in the following tests. During one speed cycle, the supply frequency f_s varies linearly from 20 Hz to 50 Hz during 20 data records and back to 20 Hz in the same way. At the start and at the end of one cycle, f_s is constant during 5 data records. This speed cycle is repeated three times: first without load torque oscillations, then with $\Gamma_c = 0.11$ Nm and $\Gamma_c = 0.22$ Nm. The lowest supply frequency is 20 Hz because of the DC machine voltage drop. Below this value, the DC motor armature current control is no more possible and therefore, the torque oscillations are not correctly produced.

The tests with the first fault indicator IWD1' gave the results displayed in Fig. 5.52(a) for two constant average load levels corresponding to 10% and 70% load. During the first speed cycle without any oscillating torque, the indicator shows variations and is therefore still speed dependent with higher indicator values at higher motor speed. When the first level of torque oscillation is applied from data record 50 on, the indicator jumps to a higher value. During the second speed cycle, the indicator value still depends on the speed but the relative variations between $f_s = 20$ Hz and $f_s = 50$ Hz are much smaller. The same behavior can be observed during the third speed cycle with a higher oscillating torque. The indicator IWD1' is therefore still speed dependent. A simple threshold cannot clearly distinguish between the healthy case and $\Gamma_c = 0.11$ Nm (0.3% of nominal torque). However, for a given speed or supply frequency, the fault indicator is always higher in the presence of the torque oscillation. With stronger oscillations ($\Gamma_c = 0.22$ Nm or 0.6% of nominal torque), the discrimination is possible for all considered speeds.

The results obtained with the second indicator IWD2' are shown in Fig. 5.52(b) for the same two load levels. It can be noted that IWD2' is less varying during the first speed cycle compared to IWD1'. The behaviour during the following cycles with torque oscillation shows higher indicator values at low speed whereas the indicator is approximately constant above a certain minimal supply frequency (about 30 Hz). It can further be observed that the relative variation of the mean indicator value between the healthy state and $\Gamma_c = 0.22$ Nm is smaller than with IWD1' i.e. IWD1' is more sensitive to variations of Γ_c . The opposite behavior has been observed in steady state but this is probably due to the modifications for normalization with respect to the varying fault frequency.

5.5.4 Load Unbalance - Transient State

The two fault indicators IWD1' and IWD2' are tested with a load unbalance of theoretical amplitude $\Gamma_c = 0.1$ Nm. In this configuration, the DC motor is directly connected to the resistor without the DC/DC converter i.e. the load torque is no longer constant but proportional to speed during the transients. The chosen speed profile is identical to the preceding cases. At full speed, the load is 10% of the nominal load in these tests.

The obtained results with the two fault indicators are displayed in Fig. 5.53

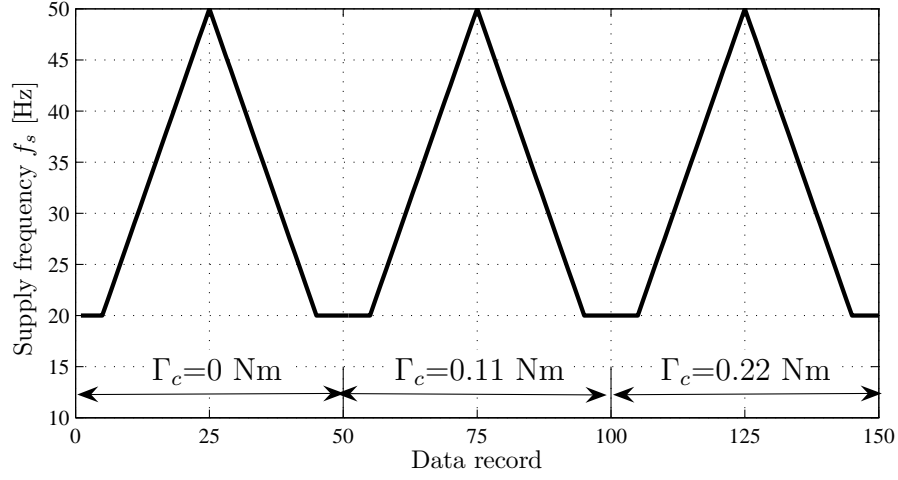


Figure 5.51: Considered speed profile: Supply frequency f_s vs. data records and corresponding torque oscillation amplitude Γ_c .

for the healthy drive and with a load unbalance. It can be noticed with the two indicators that the healthy and faulty case can be distinguished at low speed and full speed. However, at certain supply frequencies around 35 Hz, this is not clearly possible. This can be related to the previously observed phenomena with unbalance during transients. In this experimental setup, indicator values with load unbalance are always close to the healthy case for a certain supply frequency range.

Nevertheless, the mean indicator value increased during one speed cycle by 28% with IWD1' and by 52% with IWD2'. This demonstrates that realistic mechanical faults can be detected during transients using time-frequency methods.

5.6 Mechanical Fault Diagnosis

The last section in this chapter addresses shortly the problem of mechanical fault diagnosis. When a mechanical fault is detected by a high indicator value, it can be useful for a monitoring system to provide additional information about the origin of the fault. In this work, the mechanical faults are assumed to have two effects on the drive: load torque and speed oscillations and/or airgap eccentricity. Depending on the nature of the fault, one of the effects may prevail. For example, load unbalance or shaft misalignment should mainly produce load torque oscillations if bearing clearances are small.

Since both phenomena lead to different stator current modulations, methods capable of discriminating PM and AM can provide valuable information for fault diagnosis. In the following, examples with the previously presented signal processing methods are discussed.

5.6.1 Steady State

In steady state, the reference method for stator current based fault detection is current spectrum analysis. It has been shown through theoretical developments

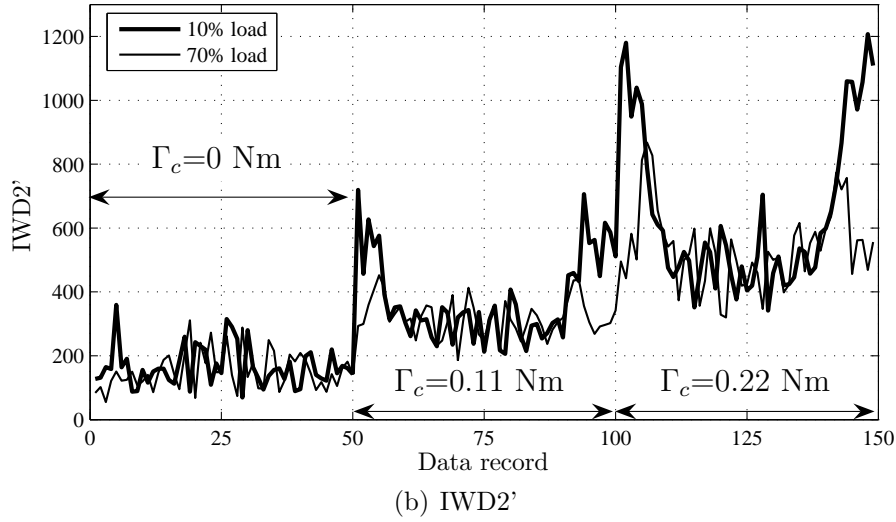
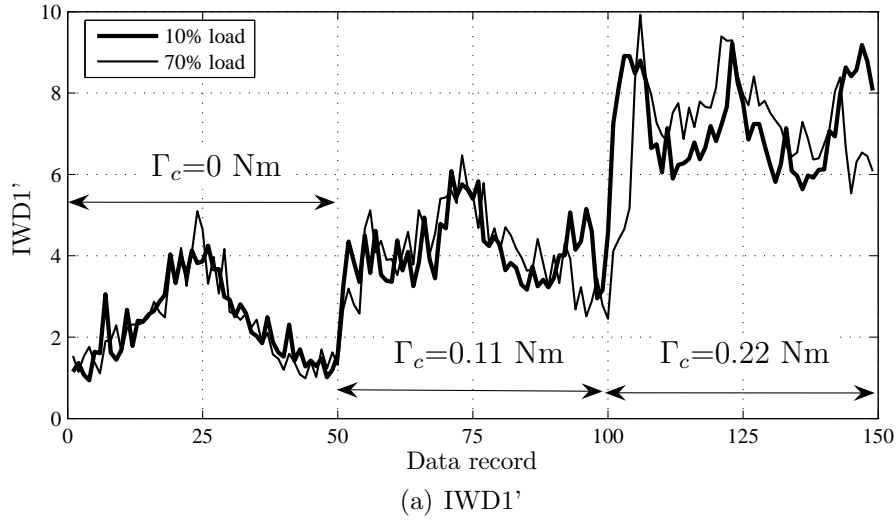


Figure 5.52: Fault indicators IWD1' and IWD2' vs. data records during speed transients with load torque oscillations.

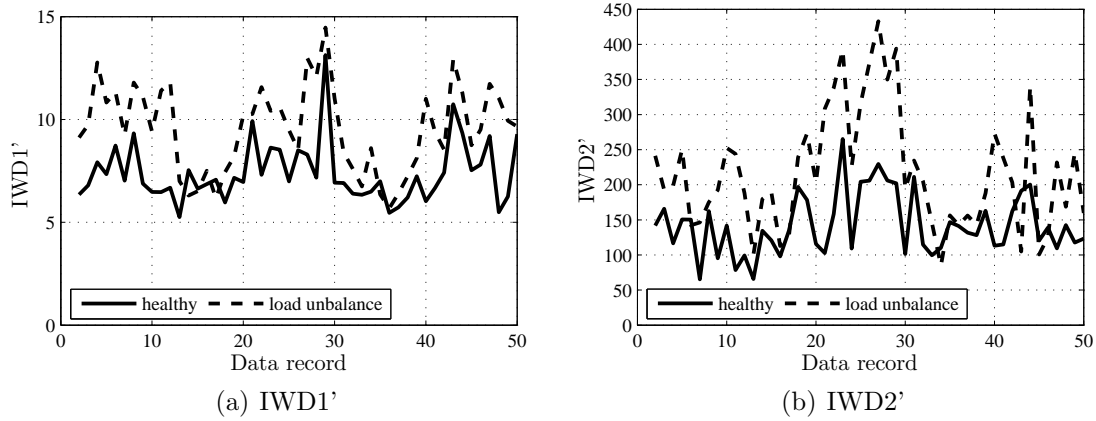


Figure 5.53: Fault indicators IWD1' and IWD2' vs. data records during speed transients with load unbalance of theoretical amplitude $\Gamma_c = 0.1$ Nm.

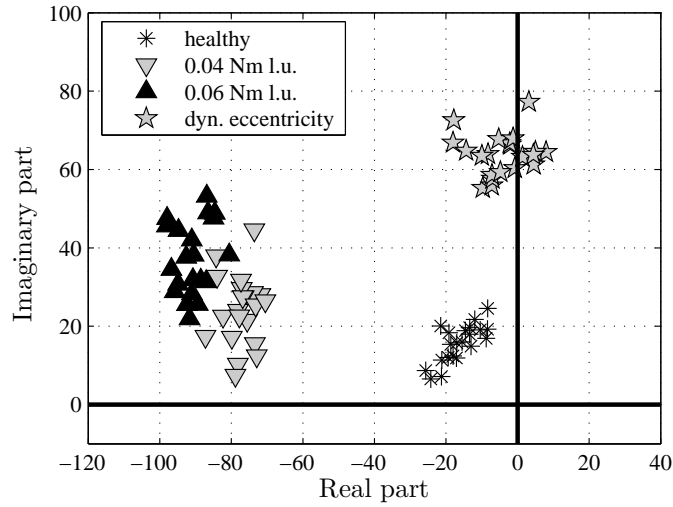


Figure 5.54: Complex representation of fault indicator IWD2 with load unbalance and 40% dynamic eccentricity, 50% average load.

and experimental results that PM and AM cannot be distinguished using spectrum analysis in this application. The reason are very small modulation indices.

However, it was shown that PM and AM have different signatures on the Wigner Distribution through the phase shift between the upper and lower sideband. Recall that a phase shift close to π characterizes PM whereas values close to 0 point to AM. Since the fault indicator IWD2 provides this information, it can be suitable for distinguishing different mechanical faults. Consider for example IWD2 with load unbalance and dynamic eccentricity. Figure 5.54 shows the obtained indicator values in the complex plane. It can be recognized that the healthy and faulty state differ by the absolute indicator value. Dynamic eccentricity leads to indicator values with a phase angle close to $\pi/2$ whereas load unbalance provokes phase angles closer to π . The reason is that load unbalance creates torque oscillations and therefore PM prevails, whereas dynamic eccentricity leads to AM and PM due to the eccentric airgap and as well as oscillating torques. The nature of the two mechanical failures can therefore be distinguished [Blö06c].

The second approach capable of providing this information in a more direct way is signal parameter estimation. This method yields directly the PM and AM modulation indices. The average indices are given in Table 5.29 for various faults and three average load conditions. Every fault leads to a considerable rise of the PM modulation index. With load unbalance and torque oscillations, the AM modulation index shows only a slight rise and is always significantly smaller than the PM index. Airgap eccentricity however causes the AM modulation index to take values approximately equal to the PM index. Hence, both fault types can be distinguished with the parameter estimation approach.

5.6.2 Transient State

During speed transients, the proposed parameter estimation approach can no longer be used since stationary signals have been supposed. Thus, the only method capa-

Table 5.29: Average estimated PM and AM modulation indices ($\times 10^{-3}$) for some cases of load torque oscillation, load unbalance and dynamic eccentricity, $N_b = 64$.

	10% load		50% load		80% load	
	PM	AM	PM	AM	PM	AM
healthy	1.63	1.36	1.87	1.23	1.41	1.15
0.03 Nm torque oscillation	2.77	1.74	3.49	1.29	2.55	1.49
0.11 Nm torque oscillation	4.50	2.57	6.46	1.62	4.60	2.31
0.22 Nm torque oscillation	7.16	4.27	10.68	2.03	7.92	3.60
0.04 Nm load unbalance	4.80	2.38	4.99	1.49	3.59	1.78
0.10 Nm load unbalance	4.34	2.51	5.44	1.62	3.74	2.07
40% dynamic eccentricity	4.30	4.79	3.19	3.00	3.04	3.18

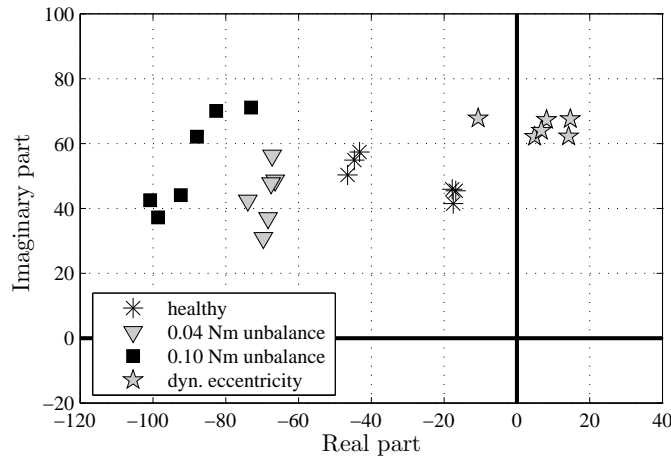


Figure 5.55: Complex representation of fault indicator IWD2' during speed transients with load unbalance and 40% dynamic eccentricity, 50% average load.

ble of discriminating PM and AM during transients is the indicator IWD2'. The latter is displayed in Fig. 5.55 for a motor startup with dynamic eccentricity and load unbalance. In this case, a discrimination between AM and PM is possible due to different phase angles. However, the results with dynamic eccentricity during speed transients have shown that a univocal fault detection is not always possible. Therefore, the presented results cannot be generalized.

5.7 Summary

This chapter presented experimental results for stator current based monitoring of mechanical faults. Three fault types were introduced: load torque oscillations generated by control of the DC motor armature current, load unbalance and dynamic eccentricity. The employed signal processing methods for stator current analysis are spectral estimation and signal parameter estimation in steady state whereas

instantaneous frequency estimation and the Pseudo Wigner Distribution are used in steady state and during speed transients. In all cases, suitable fault indicators were automatically extracted from the stator current signal only without using other information.

The faulty stator current analysis allowed to corroborate several important theoretical results from chapter 2:

- Load torque oscillations lead to phase modulations of the stator current. This has been shown through instantaneous frequency analysis, the PWD and parameter estimation.
- Dynamic eccentricity causes amplitude modulations of the stator current. The PWD and signal parameter estimation provided this result.
- Torque measurements have shown that dynamic eccentricity leads to an increase of oscillating torque at rotational frequency f_r as predicted in 2.5.5. Consequently, phase modulations were also found on the stator current with dynamic eccentricity.
- Load unbalance causes also oscillating torques at frequency f_r . This effect was found to be predominant on the stator current in contrast to assumptions by R. Obaid, T. Habetler et al. in [Oba03b] [Oba03c]. They suppose that load unbalance mainly leads to increased dynamic airgap eccentricity. However, experimental results in this chapter showed that load unbalance principally causes phase modulations of the stator current.

During the study of torque oscillations, the oscillating torque amplitude Γ_c was varied to test different fault severities. The proposed fault indicators showed in general a linear behavior with respect to Γ_c and they were sensitive to very small oscillations. Suitable indicator normalization reduced the indicator dependence on speed and average load level. Therefore, these indicators proved to be appropriate tools for fault detection. During speed transients, fault detection is more difficult but nevertheless possible in most cases with the proposed indicators.

The tests with load unbalance revealed a non-linear indicator behavior with respect to the degree of unbalance. The measured load torque confirmed that the oscillating torque amplitude is not proportional to the degree of unbalance. Moreover, the unbalance effect depends on the motor speed. Hence, these results demonstrate the complexity and difficulty of accurate physical fault effect modeling.

The feasibility of on-line stator current based monitoring using time-frequency methods was demonstrated through a DSP implementation of the PWD based algorithms. Fault indicators are continuously calculated and allow an automatic and permanent monitoring.

For the first time in condition monitoring, the capacity of some signal processing methods to distinguish PM and AM has been used for diagnosis purposes. Signal parameter estimation and the PWD show different signatures with the two modulations. Therefore, the predominance of torque oscillations or airgap eccentricity can be detected.

Chapter 6

Conclusions and Suggestions for Further Work

The literature survey on stator current analysis for mechanical fault detection and diagnosis in electric drives revealed, on the one hand, a lack of adapted analytical stator current models. On the other hand, the most common monitoring strategies use stator current spectrum estimation which requires stationary signals. This requirement is incompatible with variable speed drives where the stator current frequency varies with respect to time.

The first part of this work concentrated on analytical stator current modeling in presence of mechanical failures. Two consequences of mechanical faults were considered: First, periodic load torque and speed oscillations and secondly airgap eccentricity. Using the magnetomotive force and permeance wave approach, two models accounting for the two fault effects were obtained. Both show modulations of the fundamental supply frequency at fault characteristic frequency. However, the modulation types are different: While load torque and speed oscillations lead to stator current phase modulation, airgap eccentricity was shown to produce amplitude modulation. This important result influences the choice of adapted signal processing methods. Moreover, the result signifies that fault diagnosis is possible if the analysis method can distinguish amplitude from phase modulation.

In addition, the effects of airgap eccentricity on the motor output torque were studied with the analytical approach. Airgap eccentricity was shown to increase oscillating torque components at shaft rotational frequency. To the author's knowledge, the stator current models and the theoretical justifications of torque oscillations resulting from eccentricity have not been mentioned in literature before.

Following a discussion of suitable signal processing methods and their theoretical signatures, tests were carried out on an experimental setup. The theoretical results from the first part could be validated. Load torque oscillations produced typical PM signatures on the stator current. The proposed indicators showed to be very sensitive since even small load torque oscillation amplitudes (0.1% of nominal torque) could be detected under any load condition. Tests with variable load torque oscillation amplitude demonstrated that the indicators are proportional to the fault severity. In steady state, the time-frequency methods performed similar to the spectrum based indicator which is the method of reference. The application

of time-frequency analysis during speed transients was also successfully tested. A more realistic fault, load unbalance, produced similar effects as the load torque oscillations. Detection is possible in steady state and during transients. Only the fault severity was difficult to evaluate in this case due to nonlinear relations between theoretical and measured torque oscillations with load unbalance.

Experimental study of dynamic eccentricity first confirmed the increase in oscillating torques as predicted by theory. The measured stator current signals showed AM and PM modulations at the same time which corroborates again the preceding theoretical work. Two methods, parameter estimation and the Wigner Distribution, are capable of distinguishing small AM from PM. They revealed fault signatures with dynamic eccentricity differing from those with load unbalance or torque oscillations. This additional information allows a more accurate fault diagnosis which is not possible using the classical spectrum based approach.

The practical feasibility of on-line monitoring by stator current time-frequency analysis was demonstrated. The algorithms that have previously been tested off-line only were then implemented on a low cost DSP. One stator current signal is continuously processed and fault indicators are derived. Tests in steady state and during speed transients with load unbalance and torque oscillations successfully confirmed the off-line results.

It can be concluded that this work provides an original contribution to condition monitoring of mechanical failures in variable speed drives. Significant aspects are the developed analytical stator current models, choice of adequate signal processing methods and their successful application.

Future work could further generalize the parameter estimation approach. It proved to be effective for detection and diagnosis in steady state but the models and estimators have not been adapted to speed transients. Since the generalization would necessarily lead to more model parameters, fast and accurate optimization becomes more important. It would be interesting to test other evolutionary optimization algorithms such as particle swarm optimization or differential evolution and to compare them to the methods discussed in this work. Moreover, a DSP implementation of these methods would demonstrate their practical feasibility.

Another aspect is the chosen frequency range for stator current analysis. Since the fundamental is the strongest component in the current signal, this work focussed on the low frequency range around the supply frequency. However, other strong components in higher frequency range such as rotor slot harmonics or harmonics from pulse width modulation should show similar fault signatures and could therefore be used for monitoring.

Since the proposed methods were only tested on two realistic faults, more experimental verifications would be of great interest. The study of other realistic mechanical failures such as shaft misalignment, gearbox faults, bearing faults, different degrees of static and dynamic eccentricity would provide valuable information for generalized mechanical fault monitoring.

In this work, the electric drive has been considered in open-loop conditions without current or speed control. However, most variable speed drives in practical applications operate with speed and current controllers. This has to be considered in a practical monitoring system. Depending on the bandwidth of the controllers,

the stator current modulations will be attenuated. However, other quantities such as voltages could contain the fault relevant information in these cases. More thorough studies are necessary to incorporate condition monitoring in closed-loop drive systems.

Appendix A

Addition of Coil Voltages for Phase and Amplitude Modulation of the Airgap Flux Density

A.1 Addition of PM Coil Voltages

In order to obtain the total induced voltage in a winding phase, the phase modulated induced coil voltages must be added. Consider for example two series connected adjacent coils spaced by an angle θ_d . The sum $x(t)$ of the two induced voltages can be written in a general form according to (2.68):

$$\begin{aligned} x(t) = & V_s \cos(\omega_s t - \varphi_{\Phi,s}) + V_r \cos(\omega_s t + \beta' \cos(\omega_c t) - \varphi_{\Phi,r}) \\ & + V_s \cos(\omega_s t - \varphi_{\Phi,s} - \theta_d) + V_r \cos(\omega_s t + \beta' \cos(\omega_c t) - \varphi_{\Phi,r} - \theta_d) \end{aligned} \quad (\text{A.1})$$

Using simply $\cos \alpha + \cos \beta = 2 \cos \frac{\alpha+\beta}{2} \cos \frac{\alpha-\beta}{2}$, the following expression is obtained:

$$\begin{aligned} x(t) = & 2V_s \cos\left(\frac{\theta_d}{2}\right) \cos\left(\omega_s t - \varphi_{\Phi,s} - \frac{\theta_d}{2}\right) \\ & + 2V_r \cos\left(\frac{\theta_d}{2}\right) \cos\left(\omega_s t + \beta' \cos(\omega_c t) - \varphi_{\Phi,r} - \frac{\theta_d}{2}\right) \end{aligned} \quad (\text{A.2})$$

This relation demonstrates that the sum of two PM signals is another PM signal with a different initial phase angle. The sinusoidal phase modulation is preserved. Therefore, the total induced voltage in phase winding is also a PM signal with the same modulation term.

A.2 Addition of AM Coil Voltages

Consider two series connected adjacent coils spaced by an angle θ_d . The total induced voltage is the sum of two amplitude modulated signals according to equation

(2.98). Without loss of generality, the sum $x(t)$ can be rewritten:

$$\begin{aligned} x(t) = & [1 + a_1 \cos \omega_r t] \cos \Omega_i t + [a_2 \sin \omega_r t] \sin \Omega_i t \\ & + [1 + a_1 \cos (\omega_r t - \theta_d)] \cos (\Omega_i t - m_i \theta_d) + [a_2 \sin (\omega_r t - \theta_d)] \sin (\Omega_i t - m_i \theta_d) \end{aligned} \quad (\text{A.3})$$

After multiplication of the sine and cosine terms using:

$$\cos \alpha \cos \beta = \frac{1}{2} \cos (\alpha + \beta) + \frac{1}{2} \cos (\alpha - \beta) \quad (\text{A.4})$$

$$\sin \alpha \sin \beta = \frac{1}{2} \cos (\alpha - \beta) - \frac{1}{2} \cos (\alpha + \beta) \quad (\text{A.5})$$

the following expression is obtained:

$$\begin{aligned} x(t) = & \cos \Omega_i t + \cos (\Omega_i t - m_i \theta_d) \\ & + \frac{1}{2} a_1 \cos (\Omega_i + \omega_r) t + \frac{1}{2} a_1 \cos (\Omega_i - \omega_r) t \\ & + \frac{1}{2} a_1 \cos (\Omega_i t + \omega_r t - m_i \theta_d - \theta_d) + \frac{1}{2} a_1 \cos (\Omega_i t - \omega_r t - m_i \theta_d + \theta_d) \quad (\text{A.6}) \\ & + \frac{1}{2} a_2 \cos (\Omega_i - \omega_r) t - \frac{1}{2} a_2 \cos (\Omega_i + \omega_r) t \\ & + \frac{1}{2} a_2 \cos (\Omega_i t - \omega_r t - m_i \theta_d + \theta_d) - \frac{1}{2} a_2 \cos (\Omega_i t + \omega_r t - m_i \theta_d - \theta_d) \end{aligned}$$

The terms with equal pulsation are added using $\cos \alpha + \cos \beta = 2 \cos \frac{\alpha + \beta}{2} \cos \frac{\alpha - \beta}{2}$:

$$\begin{aligned} x(t) = & 2 \cos \left(\Omega_i t - m_i \frac{\theta_d}{2} \right) \cos \left(m_i \frac{\theta_d}{2} \right) \\ & + (a_1 - a_2) \cos \left(\Omega_i t + \omega_r t - (m_i + 1) \frac{\theta_d}{2} \right) \cos (m_i + 1) \frac{\theta_d}{2} \quad (\text{A.7}) \\ & + (a_1 + a_2) \cos \left(\Omega_i t - \omega_r t - (m_i - 1) \frac{\theta_d}{2} \right) \cos (m_i - 1) \frac{\theta_d}{2} \end{aligned}$$

Then, $\cos (\alpha + \beta) = \cos \alpha \cos \beta - \sin \alpha \sin \beta$ is used to isolate the carrier frequency in the modulation terms:

$$\begin{aligned} x(t) = & 2 \cos \left(\Omega_i t - m_i \frac{\theta_d}{2} \right) \cos \left(m_i \frac{\theta_d}{2} \right) \\ & + (a_1 - a_2) \cos \left[(m_i + 1) \frac{\theta_d}{2} \right] \\ & \left[\cos \left(\Omega_i t - m_i \frac{\theta_d}{2} \right) \cos \left(\omega_r t - \frac{\theta_d}{2} \right) - \sin \left(\Omega_i t - m_i \frac{\theta_d}{2} \right) \sin \left(\omega_r t - \frac{\theta_d}{2} \right) \right] \\ & + (a_1 + a_2) \cos \left[(m_i - 1) \frac{\theta_d}{2} \right] \\ & \left[\cos \left(\Omega_i t - m_i \frac{\theta_d}{2} \right) \cos \left(\omega_r t - \frac{\theta_d}{2} \right) + \sin \left(\Omega_i t - m_i \frac{\theta_d}{2} \right) \sin \left(\omega_r t - \frac{\theta_d}{2} \right) \right] \end{aligned} \quad (\text{A.8})$$

Rewriting this expression using $\cos \alpha - \cos \beta = -2 \sin \frac{\alpha+\beta}{2} \sin \frac{\alpha-\beta}{2}$:

$$\begin{aligned}
 x(t) = & \cos \left(\Omega_i t - m_i \frac{\theta_d}{2} \right) \\
 & \left\{ 2 \cos \left(m_i \frac{\theta_d}{2} \right) + \cos \left(\omega_r t - \frac{\theta_d}{2} \right) \left[2a_1 \cos \frac{m_i \theta_d}{2} \cos \frac{\theta_d}{2} + 2a_2 \sin \frac{m_i \theta_d}{2} \sin \frac{\theta_d}{2} \right] \right\} \\
 & + \sin \left(\Omega_i t - m_i \frac{\theta_d}{2} \right) \sin \left(\omega_r t - \frac{\theta_d}{2} \right) \left[2a_2 \cos \frac{m_i \theta_d}{2} \cos \frac{\theta_d}{2} + 2a_1 \sin \frac{m_i \theta_d}{2} \sin \frac{\theta_d}{2} \right]
 \end{aligned} \tag{A.9}$$

This expression shows that the sum of the two considered AM signals is another AM signal with the same structure: the sum of a double-sideband AM signal with residual carrier and a double-sideband suppressed-carrier AM signal. As in the original signals, the two carrier components and the two modulating components are in quadrature.

It has been demonstrated that the suppressed-carrier component in the original signal is in general of smaller amplitude than the component with residual carrier i.e. $a_1 > a_2$. This is also true for the signal $x(t)$. Consider for simplification a machine with $m_i = p = 2$: The angle of one phase belt in a single layer winding is $2\pi/12 = \pi/6$. The angle θ_d between adjacent coils is therefore smaller than $\pi/6$. Consequently, the term $\cos \theta_d \cos \frac{\theta_d}{2}$ will also be smaller than $\sin \theta_d \sin \frac{\theta_d}{2}$. Therefore, the first term in square brackets from equation (A.9) will always be greater than the second term.

Appendix B

Elements of the Fisher information matrix

B.1 Monocomponent PM signal

The following equations specify the matrix elements in (4.69).

$$\begin{aligned} f_{11} &= \frac{N}{\sigma^2} \\ f_{22} &= \frac{\theta_1^2}{\sigma^2} N \\ f_{23} &= \frac{\theta_1^2}{\sigma^2} \sum_{n=0}^{N-1} \cos(2\pi\theta_4 n + \theta_5) \\ f_{24} &= \frac{\theta_1^2}{\sigma^2} (-2\pi\theta_3) \sum_{n=0}^{N-1} n \sin(2\pi\theta_4 n + \theta_5) \\ f_{25} &= \frac{\theta_1^2}{\sigma^2} (-\theta_3) \sum_{n=0}^{N-1} \sin(2\pi\theta_4 n + \theta_5) \\ f_{26} &= \frac{\theta_1^2}{\sigma^2} \frac{N(N-1)}{2} \\ f_{33} &= \frac{\theta_1^2}{\sigma^2} \sum_{n=0}^{N-1} \cos^2(2\pi\theta_4 n + \theta_5) \\ f_{34} &= \frac{\theta_1^2}{\sigma^2} (-2\pi\theta_3) \sum_{n=0}^{N-1} \frac{1}{2} n \sin(4\pi\theta_4 n + 2\theta_5) \\ f_{35} &= \frac{\theta_1^2}{\sigma^2} (-\theta_3) \sum_{n=0}^{N-1} \frac{1}{2} \sin(4\pi\theta_4 n + 2\theta_5) \\ f_{36} &= \frac{\theta_1^2}{\sigma^2} (2\pi) \sum_{n=0}^{N-1} n \cos(2\pi\theta_4 n + \theta_5) \end{aligned}$$

$$f_{44} = \frac{\theta_1^2}{\sigma^2} (2\pi\theta_3)^2 \sum_{n=0}^{N-1} n^2 \sin^2 (2\pi\theta_4 n + \theta_5)$$

$$f_{45} = \frac{\theta_1^2}{\sigma^2} 2\pi\theta_3^2 \sum_{n=0}^{N-1} n \sin^2 (2\pi\theta_4 n + \theta_5)$$

$$f_{46} = \frac{\theta_1^2}{\sigma^2} (2\pi)^2 (-\theta_3) \sum_{n=0}^{N-1} n^2 \sin (2\pi\theta_4 n + \theta_5)$$

$$f_{55} = \frac{\theta_1^2}{\sigma^2} \theta_3^2 \sum_{n=0}^{N-1} \sin^2 (2\pi\theta_4 n + \theta_5)$$

$$f_{56} = \frac{\theta_1^2}{\sigma^2} (-2\pi\theta_3) \sum_{n=0}^{N-1} n \sin (2\pi\theta_4 n + \theta_5)$$

$$f_{66} = \frac{\theta_1^2}{\sigma^2} (2\pi)^2 \frac{N(N-1)(2N-1)}{6}$$

Appendix C

Description of the Experimental Setup

This appendix provides more details about the experimental setup and particularly on the DSP implementation.

C.1 General Description of the Test Rig

A schematic representation of the experimental setup used for off-line analysis is displayed in Fig. 5.1. A photo of the setup is shown in Fig. C.1 where the supply rig and the machines can be distinguished.

The motor under test is a standard industrial induction motor whose characteristics are given in Table C.1. The DC motor acts as a load and it is coupled to the induction machine via a rotating torque transducer. The DC motor nameplate data can also be found in Table C.1. It should be noted that the rated power of the DC motor is inferior to the induction motor. Consequently, the experimental tests were carried out at a maximum of 80% load. Several induction motors of the same type but with different faults are available in addition to a healthy machine:

- Motors with 1, 2 or 3 broken rotor bars
- Motor with rewound stator for simulation of stator short-circuits
- Motor with 40% dynamic eccentricity
- Motor with damaged bearings

The two machines and the coupling can be observed on Fig. C.2.

The induction machine is supplied by a variable speed drive (Leroy Somer UMV4301) operating in open loop condition without current or speed control. The chosen switching frequency is 3 kHz. The DC motor is connected to a resistor through a DC/DC converter. The latter is obtained by using two legs of a Semi-kron inverter. A photo of the inverter together with the current control circuit is displayed in Fig. C.3.

The following physical quantities are measured:



Figure C.1: Photo of the test rig

Table C.1: Characteristics of induction and DC motor

Induction motor	LS132S T	DC motor	MS1321 M33
Rated power	5.5 kW	Rated power	3.9 kW
Rated speed	1445 rpm	Rated speed	1450 rpm
Voltage	400 V	Voltage	260 V
Frequency	50 Hz	Current	17.6 A
Connection	Y		
Current	11.2 A		
$\cos \varphi$	0.8		
Number of rotor bars	28		

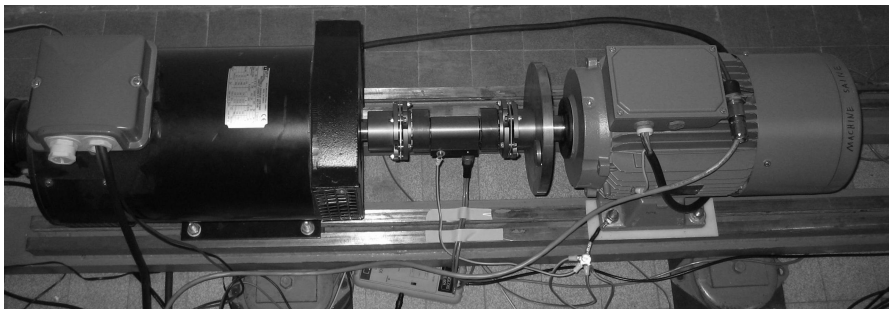


Figure C.2: Photo of induction motor and DC motor

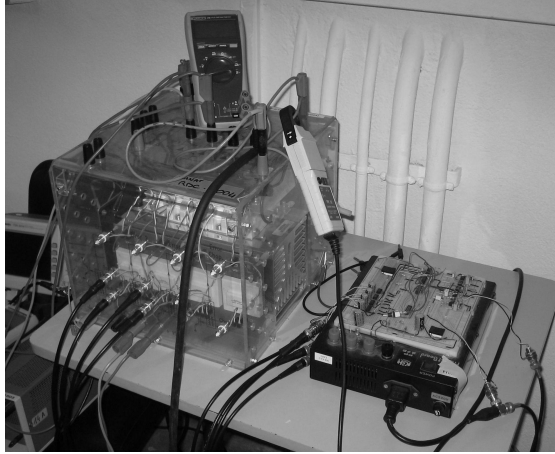


Figure C.3: DC/DC converter for DC motor current control

- 3 line currents
- 3 inverter output voltages
- torque
- speed

These signals are acquired through a data acquisition board (NI4472) at 25.6 kHz with 24 bit resolution. The board has 8 channels with a separate AD-converter each. Anti-aliasing filters are also included. The following signal processing is done off-line using Matlab software and the graphical user interface *AnsiSud* (Analyse de signaux pour la surveillance et le diagnostic).

The three studied fault types, load torque oscillations, mechanical load unbalance and airgap eccentricity, have already been presented in 5.1.

C.2 DSP Implementation

Two different detection algorithms based on stator current time-frequency analysis have been implemented on a DSP. The DSP is a low-cost Analog Devices ADSP-21161 (21161N EZ-Kit lite), mainly designed for audio applications. The inputs include anti-aliasing filters, followed by 24-bit AD-converters with a minimum sampling rate of 48 kHz. As the fault signatures appear around the fundamental supply frequency of 50 Hz, a lower sampling rate would be advantageous but cannot be realized with this hardware. Therefore, a preprocessing stage with filtering and downsampling is implemented numerically before the calculation of the WD.

C.2.1 Downsampling

The stator current is sampled at 48 kHz. However, relevant fault frequencies with the two pole pair machine are at a maximum frequency of 1.5 times the supply frequency f_s which leads approximately to 75 Hz for the considered machine in

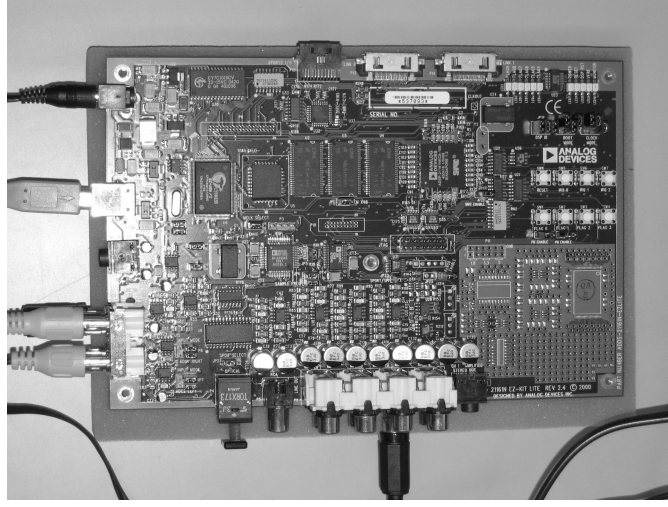


Figure C.4: Photo of DSP board with ADSP-21161

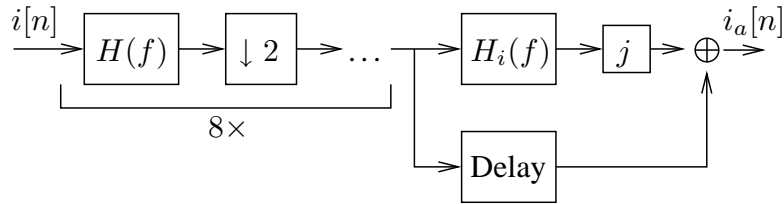


Figure C.5: Preprocessing of stator current signal: lowpass filter $H(f)$, decimation and Hilbert filter $H_i(f)$

nominal conditions. As a consequence, a real-time downsampling stage is implemented to decrease the sampling frequency by a factor $2^8 = 256$ i.e. the new sampling frequency is 187.5 Hz. The implementation of a single lowpass filter with normalized cut-off frequency $1/(2 \cdot 256)$ followed by a 256-fold decimator (takes one sample out of 256) would require a high filter order and a significant amount of memory for storage. It is more efficient to implement a scheme as depicted in Fig. C.5 with 8 decimation stages in cascade, each including the same filter $H(f)$ with a normalized cut-off frequency 0.25 followed by a 2-fold decimator. Main benefits are a low global order, small time delay and computational cost.

More precisely, the implemented lowpass filter $H(f)$ is an elliptic IIR filter of order 14. Its normalized cut-off frequency at -3 dB is 0.227 so that after the last downsampling stage, frequencies between 0 and 85.03 Hz can be analyzed without significant attenuation.

C.2.2 Hilbert Filtering

The Wigner Distribution should be calculated on the complex, analytical current signal in order to avoid interferences [Fla99]. The analytical current signal $i_a[n]$ is obtained from the real current signal $i[n]$ by means of the Hilbert transform $H\{\cdot\}$ according to:

$$i_a[n] = i[n] + jH\{i[n]\} \quad (\text{C.1})$$

The Hilbert transform is realized using a Hilbert filter with the following frequency response:

$$H_i(f) = \begin{cases} -j & \text{for } 0 \leq f \leq \frac{1}{2} \\ j & \text{for } -\frac{1}{2} \leq f < 0 \end{cases} \quad (\text{C.2})$$

Its impulse response $h_i[n]$ is:

$$h_i[n] = \frac{2 \sin^2(\pi n/2)}{\pi n} = \begin{cases} 0 & \text{if } n \text{ is even} \\ \frac{2}{\pi n} & \text{if } n \text{ is odd} \end{cases} \quad (\text{C.3})$$

In practice, the Hilbert filter is implemented as a finite impulse response filter of order $N_i=257$. In order to respect causality, the symmetric impulse response must be shifted by $(N_i - 1)/2$. The filter output is therefore delayed by 128 samples corresponding to 0.688 s. The analytical signal $i_a[n]$ is obtained by multiplication of the filter output with j and addition of the delayed real signal $i[n]$ (see Fig. C.5).

C.2.3 Discrete Implementation of the WD

The discrete WD $\text{DWD}_x[n, m]$ of a signal $x[n]$ of length N can be calculated according to the following formula [Fla99]:

$$\text{DWD}_x[n, m] = 2 \sum_{k=-(N-1)}^{N-1} p[k] x[n+k] x^*[n-k] e^{-j4\pi mk/N} \quad (\text{C.4})$$

where $p[k]$ is a window function. This expression can be efficiently implemented using an FFT algorithm (see [Aug96] for a sample algorithm). In this work, the DWD is calculated on data records of length $N = 512$. The window function $p[k]$ is a 127 point Hamming window.

The result of the calculation would be a (512×512) matrix requiring a considerable amount of memory for storage. However, the DWD can be calculated for each time bin n independently and the fault indicator can be directly derived for this time bin. This offers the advantage that no storage of the complete DWD is necessary, only the fault indicator is retained.

Bibliography

- [Abr64] M. Abramowitz, I. A. Stegun, *Handbook of Mathematical Functions with Formulas, Graphs, and Mathematical Tables*, Dover Publications, New York, ninth ed., 1964.
- [AK84] F. M. Abdel-Kader, “The Characteristic Performance of Induction Motors with Eccentricity”, *Electric Machines and Power Systems*, vol. 9, pp. 61–70, 1984.
- [Alb87] P. F. Albrecht, J. C. Appiarius, E. P. Cornell, D. W. Houghtaling, R. M. McCoy, E. L. Owen, D. K. Sharma, “Assessment of the reliability of motors in utility applications - Part 1”, *IEEE Transactions on Energy Conversion*, vol. EC-2, no. 3, pp. 396–406, Sep. 1987.
- [Alg95] P. L. Alger, *Induction Machines - Their Behavior and Uses*, Gordon and Breach, Basel, Switzerland, 2nd ed., 1995.
- [Ali06] A. A. Ali, *Modélisation des machines synchrones à aimants permanents destinées à la traction ferroviaire pour la simulation de défauts statoriques*, Ph.D. thesis, Institut National Polytechnique de Toulouse, Toulouse, France, Jan. 2006.
- [Ark05] M. Arkan, H. Çaliş, M. E. Tağluk, “Bearing and misalignment fault detection in induction motors by using the space vector angular fluctuation signal”, *Electrical Engineering (Archiv für Elektrotechnik)*, vol. 87, no. 4, pp. 197–206, Jun. 2005.
- [Att03] H. B. Attia, *Détection et localisation de défauts mécaniques d’un entraînement électrique à vitesse variable*, Ph.D. thesis, Institut National Polytechnique de Toulouse, Toulouse, France, Mar. 2003.
- [Aug96] F. Auger, P. Flandrin, P. Gonçalvès, O. Lemoine, “Time-Frequency Toolbox”, CNRS / Rice University, France, 1995/1996, URL <http://tftb.nongnu.org>.
- [Bäc96] T. Bäck, *Evolutionary Algorithms in Theory and Practice*, Oxford University Press, New York, 1996.
- [Bed63] E. Bedrosian, “A Product Theorem for Hilbert Transforms”, *Proceedings of the IEEE*, vol. 51, no. 5, pp. 868–869, May 1963.

- [Ben00] M. E. H. Benbouzid, "A review of induction motors signature analysis as a medium for faults detection", *IEEE Transactions on Industrial Electronics*, vol. 47, no. 5, pp. 984–993, Oct. 2000.
- [Ben03] M. E. H. Benbouzid, G. B. Kliman, "What stator current processing-based technique to use for induction motor rotor faults diagnosis?", *IEEE Transactions on Energy Conversion*, vol. 18, no. 2, pp. 238–244, Jun. 2003.
- [Bey02] H.-G. Beyer, H.-P. Schwefel, "Evolution strategies: A comprehensive introduction", *Natural Computing*, vol. 1, no. 1, pp. 3–52, Mar. 2002.
- [Big94] R. Bigret, J. L. Féron, *Diagnostic - maintenance - disponibilité des machines tournantes*, Masson, Paris, 1994.
- [Blö03] M. Blödt, *Diagnostic d'un entraînement électrique à base de machine asynchrone - Etude de l'influence des défauts de roulement sur le courant statorique*, Master's thesis, ENSIEG - INP Grenoble/Universität Karlsruhe (TH), France/Germany, Sep. 2003.
- [Blö04] M. Blödt, P. Granjon, B. Raison, G. Rostaing, "Models for Bearing Damage Detection in Induction Motors Using Stator Current Monitoring", in *Proc. IEEE International Symposium on Industrial Electronics (ISIE '04)*, pp. 383–388, Ajaccio, France, May 2004.
- [Blö05a] M. Blödt, M. Chabert, J. Faucher, B. Dagues, "Diagnostic de défauts mécaniques d'un entraînement asynchrone à vitesse variable", in *Conférence des Jeunes Chercheurs en Génie Electrique (JCGE '05)*, Montpellier, France, Jun. 2005.
- [Blö05b] M. Blödt, M. Chabert, J. Faucher, B. Dagues, "Mechanical load fault detection in induction motors by stator current time-frequency analysis", in *Proc. IEEE International Electric Machines and Drives Conference (IEMDC '05)*, San Antonio, Texas, May 2005.
- [Blö05c] M. Blödt, M. Chabert, J. Regnier, J. Faucher, B. Dagues, "Detection of Mechanical Load Faults in Induction Motors at Variable Speed Using Stator Current Time-Frequency Analysis", in *Proc. IEEE International Symposium on Diagnostics for Electric Machines, Power Electronics and Drives (SDEMPED '05)*, Vienna, Austria, Sep. 2005.
- [Blö06a] M. Blödt, M. Chabert, J. Regnier, J. Faucher, "Maximum-Likelihood Parameter Estimation for Current-Based Mechanical Fault Detection in Induction Motors", in *Proc. IEEE International Conference on Audio, Signal and Speech Processing (ICASSP '06)*, Toulouse, France, May 2006.
- [Blö06b] M. Blödt, J. Regnier, M. Chabert, J. Faucher, "Fault Indicators for Stator Current Based Detection of Torque Oscillations in Induction Motors at Variable Speed Using Time-Frequency Analysis", in *Proc. IEE Third International Conference on Power Electronics, Machines and Drives (PEMD '06)*, Dublin, Ireland, Apr. 2006.

- [Blö06c] M. Blödt, J. Regnier, J. Faucher, “Distinguishing Load Torque Oscillations and Eccentricity Faults in Induction Motors Using Stator Current Wigner Distribution”, in *Proc. IEEE Industry Applications Society Annual Meeting 2006*, Tampa, Florida, Oct. 2006.
- [Blö07] M. Blödt, D. Bonacci, J. Regnier, M. Chabert, J. Faucher, “On-line Monitoring of Mechanical Faults in Variable-Speed Induction Motor Drives Using the Wigner Distribution”, *accepted for publication in IEEE Transactions on Industrial Electronics*, 2007.
- [Boa92a] B. Boashash, “Estimating and interpreting the instantaneous frequency of a signal - Part 1: Fundamentals”, *Proceedings of the IEEE*, vol. 80, no. 4, pp. 520–538, Apr. 1992.
- [Boa92b] B. Boashash, “Estimating and interpreting the instantaneous frequency of a signal - Part 2: Algorithms and Applications”, *Proceedings of the IEEE*, vol. 80, no. 4, pp. 540–568, Apr. 1992.
- [Boa03] B. Boashash, *Time Frequency Signal Analysis and Processing - A Comprehensive Reference*, Elsevier, Oxford, UK, 1st ed., 2003.
- [Bon93] A. H. Bonnett, “Cause and analysis of anti-friction bearing failures in AC induction motors”, in *Proc. Pulp and Paper Industry Technical Conference*, pp. 36–46, Jun. 1993.
- [Bro99] I. N. Bronstein, K. A. Semendjajew, G. Musiol, H. Mühlig, *Taschenbuch der Mathematik*, Verlag Harri Deutsch, Frankfurt am Main, Germany, 4th ed., 1999.
- [Cab96] M. F. Cabanas, M. G. Melero, J. G. Aleixandre, M. G. Muñoz, J. Solares, “Effects of Shaft Misalignment on the Current, Axial Flux, and Airgap Torque of Induction Motors”, in *Proc. ELECTRIMACS’96*, pp. 1045–1050, Saint Nazaire, France, Sep. 1996.
- [Cam86] J. R. Cameron, W. T. Thomson, “Vibration and current monitoring for detecting airgap eccentricities in large induction motors”, *IEE Proceedings*, vol. 133, no. 3, pp. 155–163, May 1986.
- [Car93] A. J. M. Cardoso, E. S. Saraiva, “Computer-aided detection of airgap eccentricity in operating three-phase induction motors by Park’s vector approach”, *IEEE Transactions on Industry Applications*, vol. 29, no. 5, pp. 897–901, Sep./Oct. 1993.
- [Cas03] F. Castanié, *Analyse spectrale*, Hermes, Paris, 2003.
- [Cou93] L. W. Couch, *Digital and analog communication systems*, Prentice Hall, New Jersey, 4th ed., 1993.
- [Dau92] I. Daubechies, *Ten Lectures on Wavelets*, Society for Industrial and Applied Mathematics (SIAM), Philadelphia, Pennsylvania, 1992.

- [Del84] W. Deleroi, “Der Stabbruch im Käfigläufer eines Asynchronmotors”, *Archiv für Elektrotechnik*, vol. 67, pp. 91–99, 1984.
- [Dev02] V. Devanneaux, *Modélisation des machines asynchrones triphasées à cage d’écureuil en vue de la surveillance et le diagnostic*, Ph.D. thesis, Institut National Polytechnique de Toulouse, Toulouse, France, Dec. 2002.
- [Did04] G. Didier, *Modélisation et diagnsotic de la machine asynchrone en présence de défaillances*, Ph.D. thesis, Université Henri Poincaré, Nancy, France, Oct. 2004.
- [Dor93] D. G. Dorrell, *Calculation of Unbalanced Magnetic Pull in Cage Induction Machines*, Ph.D. thesis, University of Cambridge, Cambridge, United Kingdom, May 1993.
- [Dor94] D. G. Dorrell, “The influence of rotor eccentricity on the output torque of cage induction motors”, in *Proc. International Conference on Electrical Machines (ICEM ’94)*, vol. 1, pp. 35–40, Paris, France, 1994.
- [Dor97] D. G. Dorrell, W. T. Thomson, S. Roach, “Analysis of airgap flux, current, and vibration signals as a function of the combination of static and dynamic airgap eccentricity in 3-phase induction motors”, *IEEE Transactions on Industry Applications*, vol. 33, no. 1, pp. 24–34, Jan./Feb. 1997.
- [Ell71] A. J. Ellison, S. J. Yang, “Effects of rotor eccentricity on acoustic noise from induction machines”, *IEE Proceedings*, vol. 118, no. 1, pp. 174–184, Jan. 1971.
- [Eng95] R. H. Engelmann, W. H. Middelndorf, *Handbook of Electric Motors*, Marcel Dekker, New York, 1995.
- [Fey65a] R. P. Feynman, R. B. Leighton, M. Sands, *The Feynman Lectures on Physics - Volume I*, Addison-Wesley, Reading, Massachusetts, 1965.
- [Fey65b] R. P. Feynman, R. B. Leighton, M. Sands, *The Feynman Lectures on Physics - Volume II*, Addison-Wesley, Reading, Massachusetts, 1965.
- [Fla98] P. Flandrin, *Temps-fréquence*, Hermes, Paris, 2nd ed., 1998.
- [Fla99] P. Flandrin, *Time-Frequency/Time-Scale Analysis*, Academic Press, San Diego, 1999.
- [Gab46] D. Gabor, “Theory of communication”, *Journal IEE*, vol. 93, no. 3, pp. 429–457, Nov. 1946.
- [Gho99] M. Ghogho, A. K. Nandi, A. Swami, “Cramer-Rao Bounds and Maximum Likelihood Estimation for Random Amplitude Phase-Modulated Signals”, *IEEE Transactions on Signal Processing*, vol. 47, no. 11, pp. 2905–2916, Nov. 1999.

- [Gul03] H. Guldemir, "Detection of airgap eccentricity using line current spectrum of induction motors", *Electric Power Systems Research*, vol. 64, no. 2, pp. 109–117, Feb. 2003.
- [Han03] Y. Han, Y. H. Song, "Condition monitoring techniques for electrical equipment - a survey", *IEEE Transactions on Power Delivery*, vol. 18, no. 1, pp. 4–13, Jan. 2003.
- [Har78] F. Harris, "On the Use of Windows for Harmonic Analysis with the Discrete Fourier Transform", *Proceedings of the IEEE*, vol. 66, no. 1, pp. 51–83, Jan. 1978.
- [Hel77] B. Heller, V. Hamata, *Harmonic Field Effects in Induction Machines*, Elsevier, Amsterdam, Netherlands, 1977.
- [Hes92] H. Hesse, "Air gap permeance in doubly-slotted asynchronous machines", *IEEE Transactions on Energy Conversion*, vol. 7, no. 3, pp. 491–499, Sep. 1992.
- [IEE85] IEEE motor reliability working group, "Report on large motor reliability survey of industrial and commercial installations", *IEEE Transactions on Industry Applications*, vol. IA-21, no. 4, pp. 853–872, Jul./Aug. 1985.
- [Kay88] S. M. Kay, *Modern Spectral Estimation: Theory and Application*, Prentice Hall, Englewood Cliffs, New Jersey, 1988.
- [Kay93] S. M. Kay, *Fundamentals of Statistical Signal Processing: Estimation Theory*, Prentice Hall, Upper Saddle River, New Jersey, 1993.
- [Kay98] S. M. Kay, *Fundamentals of Statistical Signal Processing: Detection Theory*, Prentice Hall, Upper Saddle River, New Jersey, 1998.
- [Kir83] S. Kirkpatrick, C. Gelatt, M. P. Vecchi, "Optimization by Simulated Annealing", *Science*, vol. 220, no. 4598, pp. 671–680, May 1983.
- [Kli88] G. B. Kliman, R. A. Koegl, J. Stein, R. D. Endicott, M. W. Madden, "Noninvasive detection of broken rotor bars in operating induction motors", *IEEE Transactions on Energy Conversion*, vol. 3, no. 4, pp. 873–879, Dec. 1988.
- [Kni05] A. M. Knight, S. P. Bertani, "Mechanical Fault Detection in a Medium-Sized Induction Motor Using Stator Current Monitoring", *IEEE Transactions on Energy Conversion*, vol. 20, no. 4, pp. 753–760, Dec. 2005.
- [Kos69] M. Kostenko, L. Piotrovsky, *Electrical Machines - Vol. 2: Alternating Current Machines*, Mir Publishers, Moscow, 1969.
- [Kra04] C. Kral, T. G. Habetler, R. G. Harley, "Detection of mechanical imbalances of induction machines without spectral analysis of time-domain signals", *IEEE Transactions on Industry Applications*, vol. 40, no. 4, pp. 1101–1106, Jul./Aug. 2004.

- [Kuč70] J. Kučera, “Vliv excentrického uložení rotoru ve statoru na asynchronní motor (Influence of Eccentric Seating of the Rotor in the Stator of an Induction Motor)”, *Elektrotechnický Obzor*, vol. 59, no. 6, pp. 281–284, 1970.
- [Leg96] S. F. Legowski, A. H. M. S. Ula, A. M. Trzynadlowski, “Instantaneous power as a medium for the signature analysis of induction motors”, *IEEE Transactions on Industry Applications*, vol. 32, no. 4, pp. 904–909, Jul./Aug. 1996.
- [Ler60] R. Lerner, “A matched filter detection system for complicated Doppler shifted signals”, *IEEE Transactions on Information Theory*, vol. 6, no. 3, pp. 373–385, Jun. 1960.
- [LG61] M. Liwschitz-Garik, C. C. Whipple, *Alternating-Current Machines*, D. van Nostrand, Princeton, New Jersey, 2nd ed., 1961.
- [Mal00] S. Mallat, *Une exploration des signaux en ondelettes*, Editions de l’Ecole Polytechnique, Paris, 2nd ed., 2000.
- [Max00] J. Max, J.-L. Lacoume, *Méthodes et techniques de traitement du signal*, Dunod, Paris, 5th ed., 2000.
- [Mec97] W. Mecklenbräuker, F. Hlawatsch, eds., *The Wigner Distribution — Theory and Applications in Signal Processing*, Elsevier, Amsterdam (The Netherlands), 1997.
- [Mor92] J. Morel, *Vibrations des machines et diagnostic de leur état mécanique*, Dunod, Editions Eyrolles, 1992.
- [Nan99] S. Nandi, H. A. Toliyat, “Condition monitoring and fault diagnosis of electrical machines - a review”, in *Proc. IEEE Industry Applications Society Annual Meeting, 1999*, vol. 1, pp. 197–204, Phoenix, AZ, Oct. 1999.
- [Nan01] S. Nandi, S. Ahmed, H. A. Toliyat, “Detection of rotor slot and other eccentricity related harmonics in a three phase induction motor with different rotor cages”, *IEEE Transactions on Energy Conversion*, vol. 16, no. 3, pp. 253–260, Sep. 2001.
- [Nan02] S. Nandi, R. M. Bharadwaj, H. A. Toliyat, “Performance Analysis of a Three-Phase Induction Motor Under Mixed Eccentricity Condition”, *IEEE Transactions on Energy Conversion*, vol. 17, no. 3, pp. 392–399, Sep. 2002.
- [Nut66] A. H. Nuttall, E. Bedrosian, “On the quadrature approximation to the Hilbert transform of modulated signals”, *Proceedings of the IEEE*, vol. 54, no. 10, pp. 1458–1459, Oct. 1966.
- [Oba00] R. R. Obaid, T. G. Habetler, D. J. Gritter, “A simplified technique for detecting mechanical faults using stator current in small induction motors”, in *Proc. IEEE Industry Applications Society Annual Meeting, 2000*, pp. 479–483, Rome, Italy, Oct. 2000.

- [Oba03a] R. R. Obaid, T. G. Habetler, “Current-based algorithm for mechanical fault detection in induction motors with arbitrary load conditions”, in *Proc. IEEE Industry Applications Society Annual Meeting, 2003*, pp. 1347–1351, Salt Lake City, USA, Oct. 2003.
- [Oba03b] R. R. Obaid, T. G. Habetler, “Effect of Load on Detecting Mechanical Faults in Small Induction Motors”, in *Proc. IEEE International Symposium on Diagnostics for Electric Machines, Power Electronics and Drives (SDEMPED '03)*, Atlanta, USA, Aug. 2003.
- [Oba03c] R. R. Obaid, T. G. Habetler, R. M. Tallam, “Detecting load unbalance and shaft misalignment using stator current in inverter-driven induction motors”, in *Proc. IEEE International Electric Machines and Drives Conference (IEMDC'03)*, vol. 3, pp. 1454–1458, Madison, USA, Jun. 2003.
- [Obe65] K. Oberretl, “Die Oberfeldtheorie des Käfigmotors unter Berücksichtigung der durch die Ankerrückwirkung verursachten Statoroberströme und der parallelen Wicklungszweige”, *Electrical Engineering (Archiv für Elektrotechnik)*, vol. 49, no. 6, pp. 343–364, Nov. 1965.
- [Pap65] A. Papoulis, *Probability, Random Variables, and Stochastic Processes*, McGraw-Hill, Kogakusha, 1965.
- [Ped06] A. Pedro, *Etude des signatures fréquentielles de défauts de roulement d'un moteur asynchrone par analyse du courant statorique*, Mémoire CNAM, Conservatoire National des Arts et Metiers (CNAM) Midi-Pyrénées, Toulouse, France, Mar. 2006.
- [Pic97] B. Picinbono, “On Instantaneous Amplitude and Phase of Signals”, *IEEE Transactions on Signal Processing*, vol. 45, no. 3, pp. 552–560, Mar. 1997.
- [Raj05] S. Rajagopalan, J. A. Restrepo, J. M. Aller, T. G. Habetler, R. G. Harley, “Wigner-Ville Distributions for Detection of Rotor Faults in Brushless DC (BLDC) Motors Operating Under Non-Stationary Conditions”, in *Proc. IEEE International Symposium on Diagnostics for Electric Machines, Power Electronics and Drives (SDEMPED '05)*, Vienna, Austria, Sep. 2005.
- [Ric54] R. Richter, *Elektrische Maschinen - Band IV : Die Induktionsmaschinen*, Birkhäuser Verlag, Basel, 2nd ed., 1954.
- [Rif74] D. C. Rife, R. R. Boorstyn, “Single-tone parameter estimation from discrete-time observations”, *IEEE Transactions on Information Theory*, vol. 20, no. 5, pp. 591–598, Sep. 1974.
- [Rih66] A. W. Rihaczek, E. Bedrosian, “Hilbert transforms and the complex representation of real signals”, *Proceedings of the IEEE*, vol. 54, no. 3, pp. 434–435, Mar. 1966.

- [Rus96] J. Rusek, "Reflection of eccentricities in spectral composition of currents of induction machines", in *Proc. International Conference on Electrical Machines (ICEM '96)*, pp. 470–475, Vigo, Spain, Sep. 1996.
- [Sal97] G. Salles, *Surveillance et diagnostic des défauts de la charge d'un entraînement par machine asynchrone*, Ph.d. thesis, Université Lyon 1, Lyon, France, 1997.
- [Sal98] G. Salles, G. Grellet, F. Filippetti, H. Yahoui, "Study of monitoring load failure of an actuator system", *The European Physical Journal - Applied Physics*, vol. 4, no. 3, pp. 203–211, Dec. 1998.
- [Sal00] G. Salles, F. Filippetti, C. Tassoni, G. Grellet, G. Franceschini, "Monitoring of induction motor load by neural network techniques", *IEEE Transactions on Power Electronics*, vol. 15, no. 4, pp. 762–768, Jul. 2000.
- [Sch95a] R. R. Schoen, T. G. Habetler, "Effects of time-varying loads on rotor fault detection in induction machines", *IEEE Transactions on Industry Applications*, vol. 31, no. 4, pp. 900–906, Jul./Aug. 1995.
- [Sch95b] R. R. Schoen, T. G. Habetler, F. Kamran, R. Bartheld, "Motor bearing damage detection using stator current monitoring", *IEEE Transactions on Industry Applications*, vol. 31, no. 6, pp. 1274–1279, Nov./Dec. 1995.
- [Sch95c] H.-P. Schwefel, *Evolution and Optimum Seeking*, John Wiley & Sons, New York, 1995.
- [Sch97] R. R. Schoen, T. G. Habetler, "Evaluation and Implementation of a System to Eliminate Arbitrary Load Effects in Current-Based Monitoring of Induction Machines", *IEEE Transactions on Industry Applications*, vol. 33, no. 6, pp. 1571–1577, Nov./Dec. 1997.
- [Ség96] G. Séguier, F. Notelet, *Electrotechnique industrielle*, Lavoisier, Paris, 1996.
- [Sta04a] J. Stack, T. G. Habetler, R. G. Harley, "Bearing Fault Detection via Autoregressive Stator Current Modeling", *IEEE Transactions on Industry Applications*, vol. 40, no. 3, pp. 740–747, May/Jun. 2004.
- [Sta04b] J. Stack, T. G. Habetler, R. G. Harley, "Fault Classification and Fault Signature Production for Rolling Element Bearings in Electric Machines", *IEEE Transactions on Industry Applications*, vol. 40, no. 3, pp. 735–739, May/Jun. 2004.
- [Tav87] P. J. Tavner, J. Penman, *Condition Monitoring of Electrical Machines*, Research Studies Press, England, 1987.
- [Tho88] W. T. Thomson, J. R. Cameron, A. B. Dow, "On-line Diagnostics of Large Induction Motors", in R. Belmans, K. J. Binns, W. Geysen, A. Vandemput, eds., *Vibrations and Audible Noise in Alternating Current Machines*, Kluwer Academic Publishers, Dordrecht, The Netherlands, 1988.

- [Tho94] W. T. Thomson, "On-line current monitoring to detect electrical and mechanical faults in three-phase induction motor drives", in *Proc. International Conference on Life Management of Power Plants*, pp. 66–73, Dec. 1994.
- [Tho99a] W. T. Thomson, A. Barbour, "An industrial case study of on-line current monitoring and finite element analysis to diagnose airgap eccentricity problems in large high voltage 3-phase induction motors", in *Proc. IEE International Conference on Electric Machines and Drives*, pp. 242–246, May 1999.
- [Tho99b] W. T. Thomson, A. Barbour, "The on-line prediction of airgap eccentricity levels in large (MW range) 3-phase induction motors", in *Proc. IEE International Conference on Electric Machines and Drives*, pp. 383–385, May 1999.
- [Tho99c] W. T. Thomson, D. Rankin, D. G. Dorrell, "On-line current monitoring to diagnose airgap eccentricity in large three-phase induction motors - Industrial case histories verify the predictions", *IEEE Transactions on Energy Conversion*, vol. 14, no. 4, pp. 1372 – 1378, Dec. 1999.
- [Tho03] W. T. Thomson, M. Fenger, "Case histories of current signature analysis to detect faults in induction motor drives", in *Proc. IEEE International Electric Machines and Drives Conference (IEMDC '03)*, vol. 3, pp. 1459–1465, Jun. 2003.
- [Tim89] P. L. Timár, *Noise and Vibration of Electrical Machines*, Elsevier, North-Holland, 1989.
- [Tre01] H. L. van Trees, *Detection, Estimation and Modulation Theory: Part I*, John Wiley & Sons, New York, 2001.
- [Vas93] P. Vas, *Parameter estimation, condition monitoring and diagnosis of electrical machines*, Clarendon Press, Oxford, 1993.
- [Ver82] S. P. Verma, R. Natarajan, "Effects of Eccentricity in Induction Machines", in *Proc. International Conference on Electrical Machines (ICEM '82)*, vol. 3, pp. 930–933, Budapest, Hungary, Sep. 1982.
- [Vil48] J. Ville, "Théorie et applications de la notion de signal analytique", *Câbles et Transmissions*, vol. 2, no. 1, pp. 61–74, 1948.
- [Wig32] E. Wigner, "On the Quantum Correction for Thermodynamic Equilibrium", *Physical Review*, vol. 40, no. 5, pp. 749–759, Jun. 1932.
- [Yan81] S. J. Yang, *Low-noise electrical motors*, Clarendon Press, Oxford, 1981.